



Universität Hamburg
DER FORSCHUNG | DER LEHRE | DER BILDUNG



Max-Planck-Institut für
Struktur und Dynamik der Materie

Nonequilibrium materials engineering in correlated systems via light-matter coupling

Dissertation
zur Erlangung des Doktorgrades
an der Fakultät für Mathematik, Informatik und Naturwissenschaften
Fachbereich Physik
der Universität Hamburg

vorgelegt von
Mona Helen Alexandra Kalthoff
aus Wuppertal

Hamburg
2022

Gutachter/innen der Dissertation:	Dr. Michael Sentef Prof. Dr. Michael Potthoff
Zusammensetzung der Prüfungskommission:	Dr. Michael Sentef Prof. Dr. Michael Potthoff Prof. Dr. Henning Moritz Prof. Dr. Dante Kennes Prof. Dr. Andrew Millis Prof. Dr. Daniela Pfannkuche
Vorsitzender der Prüfungskommission:	Prof. Dr. Daniela Pfannkuche
Datum der Disputation:	13. Juni 2022
Vorsitzender Fach-Promotionsausschusses PHYSIK:	Prof. Dr. Wolfgang J. Parak
Leiter des Fachbereichs PHYSIK:	Prof. Dr. Günter H. W. Sigl
Dekan der Fakultät MIN:	Prof. Dr. Heinrich Graener

Eidesstattliche Versicherung

Hiermit versichere ich an Eides statt, die vorliegende Dissertationsschrift selbst verfasst und keine anderen als die angegebenen Hilfsmittel und Quellen benutzt zu haben.
Die eingereichte schriftliche Fassung entspricht der auf dem elektronischen Speichermedium.
Die Dissertation wurde in der vorgelegten oder einer ähnlichen Form nicht schon einmal in einem früheren Promotionsverfahren angenommen oder als ungenügend beurteilt.



Hamburg, den 25.4.2022

Preface

The work leading up to this cumulative dissertation was conducted from October 2018 to April 2022 at the Max Planck Institute for the Structure and Dynamics of Matter and the University of Hamburg under the supervision of Dr. Michael Sentef and Prof. Dr. Dante Kennes, as well as at the Center for Computational Quantum Physics at the Simons Foundation's Flatiron Institute, New York City, under the supervision of Prof. Dr. Andrew Millis. This thesis is based on the publications presented in Sec. 3, in which we investigate non-equilibrium phenomena in driven magnetic systems.

Contents

1	Abstract	1
2	Zusammenfassung	3
3	List of Publications	5
3.1	Declaration of contribution	5
4	Introduction	7
4.1	Nonequilibrium phenomena in magnetic materials	10
5	Nonequilibrium phase transition	11
5.1	Spin wave theory	11
5.1.1	The Holstein–Primakoff representation	12
5.1.2	The Dyson–Maleev representation	16
5.1.3	Diagonalizing the bilinear Hamiltonian H'_0	17
5.1.4	The interaction term	20
5.1.5	The staggered magnetization	26
5.2	The Boltzmann formalism	27
5.3	The noninteracting steady state and the time evolution	30
5.4	Computational remarks	31
5.5	Linearized kinetic equation	46
5.5.1	The nonequilibrium condensed steady state	48
5.5.2	Long time limit of the kinetic equation	52
6	Light-cone spreading of correlations	59
6.1	The dual charge/spin Hamiltonian and dynamical localization	59
7	Entanglement dynamics	71
8	Comprehensive discussion	79
	Appendix	97
A	Mathematical details of the magnon interactions	97
B	Numerical implementation of the density of states	101
	Acknowledgements	103

1 | Abstract

The investigation of nonequilibrium phenomena in strongly correlated systems is an intense and increasingly important field of research, both from a theoretical and from an experimental perspective. Experimental advances regarding the creation of ultrashort laser pulses and large field intensities are making it feasible to avoid the decoherences that historically have made the dynamics in driven solid state systems hard to access. However, many of the powerful analytical and numerical equilibrium methods are not applicable in a nonequilibrium setup, largely because of the increasing mixing of energy scales due to the external driving. It is therefore essential to gain a deeper theoretical understanding of systems far from equilibrium. In particular, driven dissipative systems allow for the formation of nonequilibrium steady states and the possibility of phase transitions between them. Here, we present theoretical results on driven quantum spin systems that help to gain an understanding of the different control knobs for driving such nonequilibrium phase transitions. This is of great interest because it paves the way to optically control the properties of quantum many body states.

A numerical method that has been shown to generate reliable results for periodically driven, one dimensional systems is the time-dependent density matrix renormalization group (t-DMRG). By simulating the dynamics of a quantum chain with Luttinger liquid and charge-density wave phases under both continuous and pulsed laser driving with t-DMRG calculations, we show that the drive causes a light-cone spreading of density-density correlations with a Floquet-engineered propagation velocity through the system. At large time scales, the employed continuous, off-resonant, large frequency driving protocol leads to the formation of a Floquet steady state with negligible heating. Strikingly, the formation of a discontinuity in form of a kink at the edge of the light cone is observed. This kink shows similarities with the discontinuity that has been analytically shown to exist in quenched systems, which indicates that dynamical quantum criticality can be achieved in Floquet-driven systems. These results directly connect to the field of time-resolved spectroscopy, aiming at measuring correlations in strongly correlated materials.

Emergent nonequilibrium states of matter prominently feature a high degree of many-body entanglement, which may have a significant effect on the macroscopic finite-temperature behavior of the systems in question. This makes the identification of entanglement in driven quantum systems an important area of research. A quantity that has been shown to act as an *entanglement witness* is the Quantum Fisher Information (QFI), which can be used to discriminate criticality at nonzero temperatures from thermal behavior. We investigate the QFI in an interaction-quenched one dimensional XXZ quantum chain, transitioning from from adiabatic to nonadiabatic dynamics.

In order to identify critical behavior in a driven-dissipative spin system with magnon interactions we study the nonequilibrium steady states of a two-dimensional Heisenberg antiferromagnet which is driven by a high frequency laser and coupled to a reservoir. The interplay between interactions and the flow of energy due to drive and dissipation is crucial to describe the resulting steady state system. We demonstrate a nonthermal transition that is characterized by a qualitative change in the magnon distribution, from subthermal at low drive to a generalized

1 Abstract

Bose-Einstein form including a nonvanishing condensate fraction at high drive and find that this transition shows static and dynamical critical scaling. An analysis of the linearized kinetic equation and its spectrum of eigenvalues allows us to draw conclusions about the role of hydrodynamic slow modes in the critical behavior near the transition point. Understanding these mechanisms that determine the critical behavior could help understand nonthermal pathways for controlling emergent properties of driven quantum materials.

2 | Zusammenfassung

Die Untersuchung von Nicht-Gleichgewichtsphänomenen in stark korrelierten Systemen ist ein breites und zunehmend an Bedeutung gewinnendes Forschungsgebiet, sowohl aus theoretischer als auch aus experimenteller Sicht. Experimentelle Fortschritte bei der Erzeugung ultrakurzer Laserpulse und großer Feldstärken machen es möglich, Dekohärenzen zu vermeiden, die in der Vergangenheit die Messung der Dynamik angetriebener Festkörpersysteme erschwert haben. Allerdings sind viele der mächtigen analytischen und numerischen Methoden der Gleichgewichtsphysik in einem Nichtgleichgewichtskontext nicht anwendbar, was vor allem auf die zunehmende Vermischung der Energieskalen aufgrund des externen Antriebs zurückzuführen ist. Daher ist es wichtig, ein tieferes theoretisches Verständnis von Systemen fernab des Gleichgewichts zu erlangen. Besonders interessant sind in diesem Zusammenhang getriebene dissipative Systeme, da sie die Ausbildung von stationären Nichtgleichgewichtszuständen ermöglichen, zwischen denen es zu dynamischen Phasenübergängen kommen kann. In dieser Dissertation stellen wir theoretische Ergebnisse zu angetriebenen Quantenspinsystemen vor, die zum Verständnis der verschiedenen Mechanismen zur Steuerung solcher Nichtgleichgewichtsphasenübergänge beitragen. Dies ist von großem Interesse, da es den Weg zur optischen Kontrolle der Eigenschaften von Quantenvielkörperzuständen ebnet.

Eine numerische Methode, die nachweislich zuverlässige Ergebnisse für periodisch angetriebene, eindimensionale Systeme liefert, ist die zeitabhängige Dichte-Matrix-Renormierungsgruppe (t-DMRG). Wir nutzen t-DMRG-Berechnungen um die Dynamik einer Quantenkette, die einen Phasenübergang zwischen einer Luttinger-Flüssigkeit und einer Ladungsdichtewelle aufweist, sowohl unter kontinuierlichem als auch unter gepulstem Treiben zu simulieren. Dabei wird deutlich, dass es unter dem Treiben zu einer lichtkegelförmigen Ausbreitung von Dichte-Dichte-Korrelationen mit Floquet-modelierter Ausbreitungsgeschwindigkeit kommt. Auf großen Zeitskalen führt das verwendete kontinuierliche, nicht-resonante, hochfrequente Antriebsprotokoll zur Bildung eines stationären Floquet-Zustandes mit vernachlässigbarer Aufheizung. Eine Auffälligkeit ist die Bildung einer Diskontinuität in Form eines Knicks am Rande des Lichtkegels. Dieser Knick weist Ähnlichkeiten mit der Diskontinuität auf, die analytisch in gequenchten Systemen nachgewiesen wurde, was darauf hindeutet, dass dynamische Quantenkritikalität in Floquet-getriebenen Systemen erreicht werden kann. Diese Ergebnisse stehen in direktem Zusammenhang mit dem Forschungsgebiet der zeitaufgelösten Spektroskopie, die darauf abzielt, Korrelationen in niedrigdimensionalen Materialien zu messen.

Emergente Nichtgleichgewichtszustände der Materie zeichnen sich durch eine hohe Vielteilchenverschränkung aus, die einen erheblichen Einfluss auf das makroskopische Verhalten von Systemen bei endlichen Temperaturen haben kann. Dies macht die Identifizierung von Verschränkungen in angetriebenen Quantensystemen zu einem wichtigen Forschungsgegenstand. Eine Größe die nachweislich dynamische Verschränkungen *bezeugt*, ist die quanten Fisher information (QFI), die zur Unterscheidung von Kritikalität bei endlichen Temperaturen und thermischem Verhalten verwendet werden kann. Wir untersuchen die QFI in einer eindimensionalen XXZ-Quantenkette, deren Wechselwirkungen sprunghaft verstärkt werden, und zeigen einen Übergang von adiabatis-

cher zu nichtadiabatischer Dynamik.

Um kritisches Verhalten in einem angetriebenen dissipativen Spinsystem mit wechselwirkenden Spinwellen zu identifizieren, untersuchen wir die stationären Nichtgleichgewichtszustände eines zweidimensionalen Heisenberg-Antiferromagneten, der durch einen Hochfrequenzlaser getrieben wird und an ein Reservoir gekoppelt ist. Das Zusammenspiel zwischen Wechselwirkungen und dem Energiefluss aufgrund von Antrieb und Dissipation ist entscheidend für die Beschreibung des resultierenden Systems stationärer Zustände. Wir zeigen einen nicht-thermischen Übergang, der durch eine qualitative Änderung der Magnonenverteilung charakterisiert ist. Bei niedrigem Antrieb zeigt das Quantensystem subthermisches Verhalten, während ein starkes Treiben zu einer verallgemeinerten Bose-Einstein-Form mit einem nicht-verschwindenden Kondensatanteil führt. Der Übergang zwischen diesen Phasen zeigt kritisches Skalierungsverhalten, sowohl in statischen als auch in dynamischen Messgrößen. Eine Analyse der linearisierten kinetischen Gleichung und ihres Eigenwertspektrums erlaubt Rückschlüsse auf die Rolle der hydrodynamischen langsamen Moden im kritischen Verhalten nahe dem Übergangspunkt. Das Verständnis der Mechanismen, die die Nichtgleichgewichtsdynamik und das kritische Verhalten des Spinsystems bestimmen, könnte dazu beitragen neue, nicht-thermische Wege zur Kontrolle von getriebenen Quantenmaterialien zu verstehen.

3 | List of Publications

This cumulative dissertation is based on publications **I**, **II** and **III**. These publications are listed chronologically below, but they are presented starting with publication **II** - the paper investigating a driven-dissipative quantum antiferromagnet - in this thesis. In chapter **5** we provide a derivation of the vertices encoding spin wave interactions in the two-dimensional antiferromagnet using spin wave theory and proceed by introducing the Boltzmann formalism, which we use to simulate the interacting magnon system under drive and dissipation. The following analysis of the properties of the eigenvalues and the kinetic equation is not part of publication **II**, but a corresponding publication is currently in preparation.

In both publication **I** and manuscript **III** we are employing t-DMRG calculations in order to simulate a one-dimensional XXZ spin chain under the influence of a nonequilibrium drive. Publication **I** is presented in chapter **6**, where the spin-flip terms are periodically driven and we demonstrate a light-cone-like spread of correlations through the quantum chain. Here, we also introduce how the XXZ spin chain can be mapped onto a half-filled chain of spinless fermions through the Jordan-Wigner transformation. In chapter **7** we present results on using the quantum Fisher information as a nonequilibrium entanglement witness, which is the main focus of manuscript **III**.

- I** **Mona H. Kalthoff**, Dante M. Kennes and Michael A. Sentef, "Floquet-engineered light-cone spreading of correlations in a driven quantum chain" *Physical Review B* 100 (16), 165125, Oct 2019, DOI: [10.1103/PhysRevB.100.165125](https://doi.org/10.1103/PhysRevB.100.165125)
- II** **Mona H. Kalthoff**, Dante M. Kennes, Andrew. J. Millis, Michael A. Sentef, "Nonequilibrium phase transition in a driven-dissipative quantum antiferromagnet" Accepted at *Physical Review Research*, Apr. 2022, <http://arxiv.org/abs/2107.03841>
- III** Denitsa R. Baykusheva, **Mona H. Kalthoff**, Damian Hofmann, Martin Claassen, Dante M. Kennes, Michael A. Sentef, Matteo Mitrano "Witnessing Nonequilibrium Entanglement Dynamics in a Quenched Quantum Chain", in preparation

3.1 Declaration of contribution

- I** M. H. Kalthoff modified the t-DMRG code written by D.M. Kennes, performed all simulations and created all plots. All authors participated in the planning of the project, the analysis of the data and the writing of the paper.
- II** M. H. Kalthoff wrote the code and did the analytics needed to implement the magnon interactions with the assistance of M. A. Sentef. All authors participated in the planning of the project, the writing of the paper and the analysis of the data. The full code is available at <https://github.com/MonaHKa/Boltzmann-simulation>

3 *List of Publications*

- III M. H. Kalthoff modified the t-DMRG code written by D.M. Kennes, wrote the script to extract the QFI from the correlations and plotted the DMRG data. All authors participated in the discussions and the analysis of the data. The main draft of the paper was written by D. R. Baykusheva and M. Mitrano, M. H. Kalthoff contributed the section about the DMRG data and the Jordan-Wigner transformation.

4 | Introduction

Understanding the dynamics and phase transitions of driven solid state systems far from equilibrium is a crucial aspect of modern physics with many possible applications in future technologies, such as quantum computing, the creation of memory devices and the engineering of quantum materials with desired properties [1]. However, even some of the most basic questions in the field remain to be answered and a schematic framework to explain nonequilibrium phenomena is yet to be developed [2]. In quantum materials, an equilibrium ground state is determined by the interactions between many intertwined degrees of freedom, such as spin, charge, orbitals and the lattice [3, 4]. Our general understanding of the equilibrium properties of strongly correlated materials and their phase transitions has majorly advanced over the last century, largely due to powerful equilibrium methods, such as mean field theory and renormalization group techniques [2]. Conceptually, these theoretical frameworks make use of the separable hierarchy of energy scales in equilibrium systems, which allows the formation of a theory that starts from a microscopic picture and correctly describes the long wavelength behavior of a system by integrating out fluctuations at each intermediate energy scale [5]. Introducing perturbations in an equilibrium system does not necessarily mean that the system needs to be seen in a nonequilibrium context, in fact measurements of equilibrium systems are in general performed by applying an external force, which introduces a localized change in the system and then studying the response function of the system [6]. As long as the external force is sufficiently weak for the response of the system to be linear, the perturbation does not majorly influence the separability of energy scales.

However, the abundance of interactions and energy scales involved in strongly correlated materials leads to a variety of many-body states far beyond the linear response regime, so that even slight external perturbations introduce the possibility of a rich spectrum of new phases of matter [7]. Controlling these phase transitions through ultrafast light matter interaction is a vibrant field of research with many open questions, since the study of nonequilibrium systems is more challenging, both from an experimental and a theoretical point of view [8]. A major reason for this is that external perturbations can lead to a mixing of energy scales, such that the framework in which systems in equilibrium are understood is no longer applicable. Two major points of research are:

1. How can we understand new nonequilibrium phenomena, like exotic topological states, that have no counterpart in equilibrium? Do these new, transient nonequilibrium states of matter have properties that are robust, in the same way that equilibrium phase properties are robust?
2. How can we reproduce phenomena that do exist but that are hard to realize in equilibrium, in a feasible nonequilibrium setup? Can we, for example, use light-matter-interaction to increase the temperature at which a material becomes superconducting?

Progress in this field has been largely driven by the improvement of experimental techniques such as the manipulations of ultracold gases in optical lattices created by standing laser waves [9, 10]

4 Introduction

as well as ultrafast measurements in solid state systems [11–13], where laser pulses on femto- and even attosecond timescales allow the study of systems undergoing phase transitions far from equilibrium and to access transient states that have no analogue in equilibrium. Examples for such phase transitions are light induced superconductivity [14–17], insulator-to-metal transitions [18–21] and photoinduced melting of orbital order [22, 23].

In general, nonequilibrium problems fall into two categories. The first one is a quench where there is a sudden change to the system properties. Theoretically, this can be achieved by an instantaneous change in the Hamiltonian parameters, which corresponds to experimentally hitting a system with a short pulse [24]. In particular, ultrafast laser spectroscopy allows to access time and angle resolved information about the relaxation of a system after excitation with periodic and pulsed electric fields [25]. Then one may ask how the system relaxes, which transient states it evolves through and whether or not the resulting steady state corresponds to thermal equilibrium [26]. It has been shown that such an instantaneous change in the system parameters can indeed lead to dynamical phase transitions and nonequilibrium critical behavior [27–29] that persists on timescales that are larger than the duration of the pump pulse due to a critical slowing down of the relaxation dynamics close to critical points [30, 31].

In recent times, the field has moved from describing relaxation dynamics after a laser pulse towards the growing field of dressed-state dynamics and light-induced states of matter during the laser pulse [32]. This is particularly interesting because driven systems have a quasi energy spectrum which can be tailored by the external drive, known as Floquet engineering of desired system properties [33–36]. There are multiple advantages in exposing a system to a high frequency drive with frequencies larger than the intrinsic time and energy scales in the system, one of them being that under such driving conditions the long time physics can be described by a renormalized Hamiltonian that is averaged over one period of the drive [3, 37]. One phenomenon resulting from this renormalized description is known as *dynamical localization* because, at this level of perturbation theory, the averaging leads to an effective hopping amplitude which is reduced with regard to the equilibrium value, meaning the electrons are more localized [38]. Moreover, Floquet theory [39] provides an effective analytical tool to describe the stationary states and the corresponding quasienergy-spectrum of periodically driven systems [40] because it applies to time-periodic systems in analogy to Bloch theory for spatially periodic systems.

A feature systems with periodic lattice potentials that is observed experimentally during the periodic driving, is the formation of so called Floquet-Bloch-Bands that repeat in both momentum and energy [41, 42]. These findings are particularly notable since the interactions of the degrees of freedom in quantum materials with light lead to an increased decoherence due to additional scattering mechanisms, and high field intensities are required to overcome these decoherences [3, 43]. Another important aspect is that solid state systems may absorb energy from the driving field, which leads to a growing number of excitations in the system which cause an increase in its local entropy density so that the system is driven towards the infinite temperature limit with no local correlations [44, 45]. While this is less of a problem when studying ultracold atoms in optical lattices [9, 10] due to the almost perfect decoupling from the environment [46], it is a major challenge in solid-state physics, where strong correlations make probes prone to heating and eventually melting. However, this runaway heating can be significantly slowed down or avoided by choosing a high frequency driving protocol that is detuned from the excitation energies of the system [47–49] or has a with quasi-periodic time dependence [50]. Moreover, even though Floquet theory strictly assumes an infinite drive, meaning a drive which has been turned

on in the infinitely distant past [36, 51, 52], it has been shown that the framework of Floquet theory is still largely applicable for systems which are exposed to pulses with finite duration [53], as long as a certain hierarchy between the pump and the probe pulse as well as the period of the laser is maintained [54].

In one dimension, the time-dependent density matrix renormalization group (t-DMRG) [55] is a versatile numerical tool to simulate quantum chains which are exposed to such a ramped or pulsed high frequency periodic drive [47]. Amongst other applications, it can be used to obtain information about the spread of correlations, which in quantum many body systems is restricted to a maximum velocity, namely the Lieb-Robinson bound [56], analogously to the speed of light bounding the velocity with which information can spread in relativistic quantum field theory [24, 46, 57, 58]. One major part of this thesis is an investigation on how this light-cone-like spread of electronic correlations in an infinite quantum chain exposed to modulated periodic driving can be described using Floquet-renormalized effective Hamiltonian parameters, and how drives that are ramped up over a short time interval can lead to kink-like discontinuity, which resembles the discontinuity observed in the context of dynamical phase transitions after quantum quenches.

While the study of periodically driven systems is a vast field of research with many open questions on its own, the coupling of such a driven system to a reservoir leads to further rich physical phenomenology and in particular allows the formation of a nonequilibrium steady state. This is of great interest, because the effective Hamiltonians obtained through Floquet theory can only be used to describe dynamics in systems where dissipation is negligible, which is a challenge to realize experimentally [59]. In contrast, it is a flow of energy that characterizes a nonequilibrium steady state obtained by a drive that adds energy to the system, a redistribution of energy due to the interaction dynamics within the system and a dissipation into a bath such that energy can go out of the system as well [60–63]. The interplay between these factors determining the flow of energy through a system can potentially drive the system through phase transitions that do not have an analogue in equilibrium, where phase transitions are commonly characterized through an order parameter that indicates the breaking or recovery of symmetries [64]. Distinct from these *symmetry breaking* phase transitions, which have been shown to also exist in nonequilibrium setups [65–67], there can be another type of phase transition in a nonequilibrium steady state, whose main feature is a qualitative change in the low frequency distribution of the collective excitations [68]. Such phase transitions are exclusive to nonequilibrium scenarios, because in equilibrium the shape of the distribution function is determined through thermodynamics.

Another feature of equilibrium phase transitions is, that the behavior in the vicinity of critical points obeys well defined scaling laws with universal exponents [69, 70]. However, it is a priori less clear if phase transitions in driven quantum systems share universal critical behavior distinct from equilibrium [71–75], and while it has been shown that some universality arguments may persist out of equilibrium, there are indications that the out of equilibrium dynamics in strongly correlated systems go beyond what can be captured by a theory of universal critical exponents [2, 24, 76]. Theoretically, the question of whether universality persists in nonequilibrium has been mostly addressed in the context of global quenches, so understanding the role of critical exponents in driven-dissipative systems is an important open point of research which is relevant for many experimental setups.

4.1 Nonequilibrium phenomena in magnetic materials

Nonequilibrium phenomena in magnetic materials are of particular interest because magnetically ordered ensembles of magnetic moments can host collective excitations that are quantized spin waves, commonly referred to as magnons [77, 78]. Controlling the magnetization and the dynamic excitations of quantum materials is of fundamental technological importance, for example for information transport and processing [79] as well as for the creation of devices which store and manipulate data [13]. Over the last decade multiple ultrafast thermal and nonthermal pathways to optically control magnetism have been discovered [1, 80]. One example of a novel state of matter in magnetic materials is Bose-Einstein condensation (BEC) of magnons, in which an excitation with a pulse causes the distribution of excitations to form a single coherent macroscopic quantum state in which the lowest energy excited state is macroscopically populated [81–83]. The most prominent example of materials in which such BEC of magnons has been observed are thin, ferromagnetic yttrium iron garnet (YIG) films [83–90]. Magnon–magnon interactions have been shown to be essential for many phenomena in magnetic materials, like magnon thermalization and Bose-Einstein condensation [79, 91, 92].

In this thesis we investigate magnon interactions in a nonequilibrium system where the crucial physics is determined by the interplay of the interactions as well as the particle addition and dissipation processes. In particular, we study the nonequilibrium steady states of a driven-dissipative Heisenberg Antiferromagnet using a semiclassical magnon Boltzmann equation [93, 94] and thereby treating interactions among the excitations on a microscopic level. This adds a new direction to past theoretical approaches for the study of spin systems that feature condensates, which have been based on semi-phenomenological continuum approximations using Landau-Lifshitz-Gilbert equations [95, 96], Gross-Pitaevskii equations [82, 84, 97] or field theoretical analyses [65, 75]. We identify an intrinsically nonequilibrium phase transition characterized by a qualitative change in the magnon distribution function and showing characteristic scaling behavior between an ordered low drive state and a disordered phase with a finite condensate fraction. This work is complimentary to the existing largely experimental literature on BEC of magnons, which concerns systems with very long relaxation times, where a population of magnons is transiently induced and then thermalizes into a Bose condensed state, because we focus on a system where the drive strength is varied and the competition between the effects of the particle addition and removal processes as well as the magnon interactions qualitatively changes the system properties. Furthermore our work bears interesting relationships with exciton-polariton condensates [73, 98, 99] and possible extensions of our numeric method to ferromagnetic materials and polariton systems are being discussed.

5 | Nonequilibrium phase transition

In this chapter, we focus on the identification of critical behavior, and in particular a nonequilibrium phase transition in a two-dimensional Heisenberg antiferromagnet which is driven by high-frequency light and coupled to a dissipative reservoir. The general motivation for investigating a nonequilibrium phase transition in the driven-dissipative Heisenberg model were recent theory results demonstrating a dynamical phase transition involving nonthermal magnon populations in the antiferromagnetic phase of the two-dimensional Hubbard model upon laser driving [68]. However, these results were obtained in a one loop non-interacting magnon theory. In this project, we investigate the effects of magnon-magnon interactions on the dynamical phase transition using an interacting spin-wave theory with a large spin expansion and a Boltzmann formalism. In particular, we are interested in whether the redistribution of energy amongst magnon modes due to scattering transfers energy to places where it can be relaxed more easily and therefore makes the phase transition disappear. What we find is that the dynamic phase transition survives the inclusion of interactions, but that the influence of magnon-magnon scattering leads to qualitative and quantitative changes with respect to the noninteracting results. Crucially, magnon-magnon scattering is shown to lead to a high drive steady state in the driven-dissipative system that can be characterized by a generalized Bose-Einstein distribution with a condensate fraction at zero momentum.

Section 5.1 provides a summary of the standard Holstein-Primakoff spin wave theory, which is used to implement magnon interactions in the code simulating a driven-dissipative system with magnon-magnon scattering. We proceed by introducing the Boltzmann formalism in section 5.2 before briefly summarizing the findings leading up to this project in chapter 5.3 and presenting computational details in section 5.4, such that researchers interested in similar problems can understand the theoretical and numerical background of the simulation used to obtain the results presented in publication II. In section 5.5 we proceed to present so far unpublished results on the linearized kinetic equation, its eigenvalues and possible implications for the slow modes in the system.

5.1 Spin wave theory

In order to investigate the effect of magnon interactions on the steady states in a driven-dissipative square lattice Heisenberg antiferromagnet, we consider the Hamiltonian

$$\mathcal{H}_{\text{Heis}} = \sum_{ij} J_{ij} \left\{ \frac{1}{2} (S_i^+ S_j^- + S_i^- S_j^+) + \Delta S_i^z S_j^z \right\} \quad \text{with } J_{ij} > 0 \quad (5.1)$$

where the local spin operators S_i satisfy $S^2 = S(S+1)$ and the coupling strength J_{ij} is taken to be positive to ensure an antiferromagnetic ground state. The spin magnitude S also determines the magnitude of quantum fluctuations in the system, which for sufficiently large spin length is ordered. By including the Hamiltonian parameter Δ , we allow for anisotropies of the exchange

interaction. While this model is isotropic at $\Delta = 1$, spin rotation symmetry is broken for $\Delta > 1$ yielding the antiferromagnetic Ising model for $\Delta \rightarrow \infty$. While the ferromagnetic ($J_{ij} < 0$) ground state is well known, defining a ground state is more difficult in the antiferromagnetic case and dependent on both the dimensionality and the anisotropy [100, 101].

We restricting the system to nearest neighbor interactions by defining the the exchange coupling to be

$$J_{ij} = \begin{cases} J & \text{if } \mathbf{R}_i + \boldsymbol{\delta} = \mathbf{R}_j \\ 0 & \text{otherwise} \end{cases}, \quad (5.2)$$

where $\boldsymbol{\delta}$ are the unit vectors connecting a given site with its nearest neighbors and J determines the energy scale. The coordination number z states how many of these vectors $\boldsymbol{\delta}$ exist for each lattice point, i.e. how many nearest neighbors there are. On a two-dimensional square lattice, the coordination number is $z = 4$ and the unit vectors are given by

$$\boldsymbol{\delta} \in \{+\mathbf{x}, -\mathbf{x}, +\mathbf{y}, -\mathbf{y}\}, \quad (5.3)$$

where for simplicity we have set the lattice constant to be $a = 1$. Classically, the spins would favor alternating spin orientations, but while the Néel state is an eigenstate of $H_{ZZ} = J \sum_{\langle ij \rangle} S_i^z S_j^z$, it is not an eigenstate of the general Hamiltonian

$$\mathcal{H}_{\text{HAFM}} = J \sum_{\langle ij \rangle} \left\{ \frac{1}{2} (S_i^+ S_j^- + S_i^- S_j^+) + \Delta S_i^z S_j^z \right\}, \quad (5.4)$$

where the sum $\langle ij \rangle$ runs over nearest neighbors on the square lattice. Spin waves, i.e. magnons can be described as bosons and there are different expansions around the Néel state that map the local spin operators onto bosonic operators. Two of the most common expansions are the Holstein–Primakoff transformation and the Dyson–Maleev representation, which will be explained in detail in the following.

5.1.1 The Holstein–Primakoff representation

The Holstein–Primakoff representation maps the spin Hamiltonian given in Eq. (5.1) onto a hermitian bosonic Hamiltonian. Both representations consider two sublattices, one where the magnetic moments are pointing up and one where the magnetic moments are pointing down. The formalisms assume bipartite lattices, meaning that next neighbors always belong to different sublattices, as displayed in Fig. 5.1.

The Holstein–Primakoff transformation on one sublattice is given by

$$S_i^+ = \sqrt{2S} \sqrt{1 - \frac{a_i^\dagger a_i}{2S}} a_i \quad (5.5a)$$

$$S_i^- = \sqrt{2S} a_i^\dagger \sqrt{1 - \frac{a_i^\dagger a_i}{2S}} \quad (5.5b)$$

$$S_i^z = S - a_i^\dagger a_i \quad (5.5c)$$

and on the other sublattice by

$$S_j^+ = \sqrt{2S} b_j^\dagger \sqrt{1 - \frac{b_j^\dagger b_j}{2S}} \quad (5.6a)$$

$$S_j^- = \sqrt{2S} \sqrt{1 - \frac{b_j^\dagger b_j}{2S}} b_j \quad (5.6b)$$

$$S_j^z = -S + b_j^\dagger b_j, \quad (5.6c)$$

where both a and b are bosonic operators that follow the commutation rules

$$[a_i, a_{i'}^\dagger] = \delta_{ii'} \quad (5.7a)$$

$$[\beta_j, \beta_{j'}^\dagger] = \delta_{jj'} \quad (5.7b)$$

$$[a_i^{(\dagger)}, b_j^{(\dagger)}] = 0. \quad (5.7c)$$

Under the assumption that the spin S is large, we can Taylor expand the square roots in the expressions above, yielding

$$S_i^+ = \sqrt{2S} \left(1 - \frac{a_i^\dagger a_i}{4S} \right) a_i + \mathcal{O}\left(\frac{1}{S}\right) \quad (5.8a)$$

$$S_i^- = \sqrt{2S} a_i^\dagger \left(1 - \frac{a_i^\dagger a_i}{4S} \right) + \mathcal{O}\left(\frac{1}{S}\right) \quad (5.8b)$$

and the analogous for S_j^+ and S_j^- . At this point it becomes apparent that while the exact Hamiltonian is not maintained due to the expansion, the hermitian nature of the Hamiltonian is conserved as $(S_i^+)^{\dagger} = S_i^-$. The lattice has N sites, i.e. $N/2$ sites on each sublattice, so we use

$$\sum_{\langle ij \rangle} 1 = \sum_{i \in A} \sum_{\text{bonds attached to } i} 1 = \frac{Nz}{2} \quad (5.9)$$

where the number of the bonds attached to i is z and $\sum_{i \in A} = N/2$ (only the A sublattice).

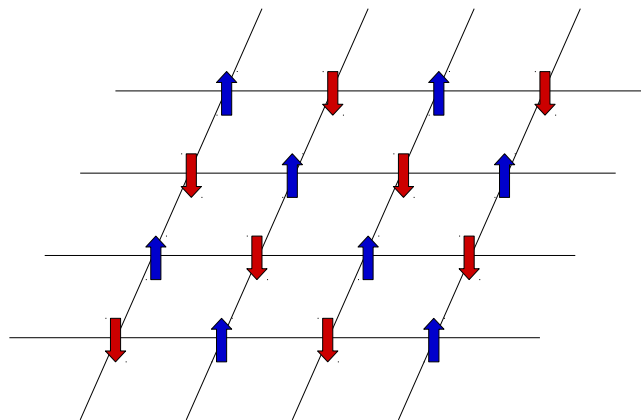


Figure 5.1: Schematic display of a bipartite lattice in the Néel state with magnetic moments pointing up (blue) only directly neighboring magnetic moments pointing down (blue) and vice versa.

With this, we can evaluate the components of the Hamiltonian in Eq. (5.1) as

$$J\Delta \sum_{\langle ij \rangle} S_i^z S_j^z = -J\Delta S^2 \frac{Nz}{2} + J\Delta S z \left(\sum_i a_i^\dagger a_i + \sum_j b_j^\dagger b_j \right) - J\Delta \sum_{\langle ij \rangle} \{ a_i^\dagger a_i b_j^\dagger b_j \} \quad (5.10a)$$

$$\frac{J}{2} \sum_{\langle ij \rangle} S_i^+ S_j^- = \frac{J}{2} \sum_{\langle ij \rangle} \left\{ 2S a_i b_j - \frac{a_i b_j^\dagger b_j b_j}{2} - \frac{a_i^\dagger a_i a_i b_j}{2} + \frac{a_i^\dagger a_i a_i b_j^\dagger b_j b_j}{8S} \right\} \quad (5.10b)$$

$$\frac{J}{2} \sum_{\langle ij \rangle} S_i^- S_j^+ = \frac{J}{2} \sum_{\langle ij \rangle} \left\{ 2S a_i^\dagger b_j^\dagger - \frac{a_i^\dagger a_i^\dagger a_i b_j^\dagger}{2} - \frac{a_i^\dagger b_j^\dagger b_j^\dagger b_j}{2} + \frac{a_i^\dagger a_i^\dagger a_i b_j^\dagger b_j^\dagger b_j}{8S} \right\}, \quad (5.10c)$$

such that the full Hamiltonian is given by

$$\mathcal{H}_{\text{HP}} = E'_0 + H'_0 + V'_{\text{HP}} + V''_{\text{HP}} \quad (5.11a)$$

$$E'_0 = -\frac{Nz}{2} \Delta JS (S+1) \quad (5.11b)$$

$$H'_0 = JSz\Delta \left(\sum_i a_i a_i^\dagger + \sum_j b_j^\dagger b_j \right) + JS \sum_{\langle ij \rangle} (a_i^\dagger b_j^\dagger + a_i b_j) \quad (5.11c)$$

$$V'_{\text{HP}} = -J \sum_{\langle ij \rangle} \left\{ \Delta a_i^\dagger a_i b_j^\dagger b_j + \frac{1}{4} (a_i b_j^\dagger b_j b_j + a_i^\dagger a_i a_i b_j + a_i^\dagger a_i^\dagger a_i b_j^\dagger + a_i^\dagger b_j^\dagger b_j^\dagger b_j) \right\} \quad (5.11d)$$

$$V''_{\text{HP}} = \frac{J}{16S} \sum_{\langle ij \rangle} \{ a_i^\dagger a_i^\dagger a_i b_j^\dagger b_j^\dagger b_j + a_i^\dagger a_i a_i b_j^\dagger b_j b_j \}. \quad (5.11e)$$

Since we are using the Holstein-Primakoff transformation in the limit of large S , we will neglect V''_{HP} in the following. Fourier transforming the boson operators into momentum space via

$$a_i = \sqrt{\frac{2}{N}} \sum_{\mathbf{k}} e^{-i\mathbf{k}\mathbf{R}_i} a_{\mathbf{k}} \quad (5.12a)$$

$$b_j = \sqrt{\frac{2}{N}} \sum_{\mathbf{k}} e^{+i\mathbf{k}\mathbf{R}_j} b_{\mathbf{k}}, \quad (5.12b)$$

where \mathbf{k} runs over the (antiferromagnetic-)Brillouin zone, yields the momentum space representation of \mathcal{H}_{HP} . We define the Fourier transform with opposite signs in the exponent to facilitate the notation and restrict the indices to positive \mathbf{k} . This implies that a -bosons and b -bosons carry opposite momenta. Transforming the number operators on a given sublattice gives

$$\sum_i a_i^\dagger a_i = \frac{N}{2} \sum_i \sum_{\mathbf{k}_1, \mathbf{k}_2} e^{+i\mathbf{k}_1 \mathbf{R}_i} a_{\mathbf{k}_1}^\dagger e^{-i\mathbf{k}_2 \mathbf{R}_i} a_{\mathbf{k}_2} \quad (5.13a)$$

$$= \sum_{\mathbf{k}_1, \mathbf{k}_2} a_{\mathbf{k}_1}^\dagger a_{\mathbf{k}_2} \left(\frac{N}{2} \sum_i e^{+i(\mathbf{k}_1 - \mathbf{k}_2) \mathbf{R}_i} \right) \quad (5.13b)$$

$$= \sum_{\mathbf{k}_1, \mathbf{k}_2} a_{\mathbf{k}_1}^\dagger a_{\mathbf{k}_2} \delta(\mathbf{k}_1 - \mathbf{k}_2) \quad (5.13c)$$

$$= \sum_{\mathbf{k}} a_{\mathbf{k}}^\dagger a_{\mathbf{k}}, \quad (5.13d)$$

and, following the same steps,

$$\sum_j b_j^\dagger b_j = \sum_{\mathbf{k}} b_{\mathbf{k}}^\dagger b_{\mathbf{k}}. \quad (5.14)$$

For the mixed quadratic operators, we get

$$\sum_{\langle ij \rangle} a_i^\dagger b_j^\dagger = \frac{N}{2} \sum_i \sum_{\mathbf{k}_1, \mathbf{k}_2} \sum_{\boldsymbol{\delta}} e^{i\mathbf{k}_1 \mathbf{R}_i} a_{\mathbf{k}_1}^\dagger e^{-i\mathbf{k}_2 (\mathbf{R}_i + \boldsymbol{\delta})} b_{\mathbf{k}_2}^\dagger \quad (5.15a)$$

$$= \sum_{\mathbf{k}_1, \mathbf{k}_2} \sum_{\boldsymbol{\delta}} e^{-i\mathbf{k}_2 \boldsymbol{\delta}} a_{\mathbf{k}_1}^\dagger b_{\mathbf{k}_2}^\dagger \left(\frac{N}{2} \sum_i e^{i\mathbf{R}_i (\mathbf{k}_1 - \mathbf{k}_2)} \right) \quad (5.15b)$$

$$= \sum_{\mathbf{k}} a_{\mathbf{k}}^\dagger b_{\mathbf{k}}^\dagger \sum_{\boldsymbol{\delta}} e^{-i\mathbf{k} \boldsymbol{\delta}} \quad (5.15c)$$

where $\boldsymbol{\delta}$ runs over the unit vectors given in Eq. (5.3). In two dimensions we have

$$\sum_{\boldsymbol{\delta}} e^{-i\mathbf{k} \boldsymbol{\delta}} \stackrel{2d}{=} e^{-ik_x} + e^{-ik_y} + e^{ik_x} + e^{ik_y} \quad (5.16a)$$

$$= 2 [\cos(k_x) + \cos(k_y)], \quad (5.16b)$$

and more generally we can define the function

$$\gamma_{\mathbf{k}} = \frac{1}{z} \sum_{\boldsymbol{\delta}} e^{i\mathbf{k} \boldsymbol{\delta}} \quad (5.17a)$$

$$= \frac{1}{d} \sum_{\eta=1}^d \cos(k_\eta a), \quad (5.17b)$$

where d is the number of dimensions and a is the lattice constant. This allows us to write the mixed operator products as

$$\sum_{\langle ij \rangle} a_i^\dagger b_j^\dagger = z \sum_{\mathbf{k}} \gamma_{\mathbf{k}} a_{\mathbf{k}}^\dagger b_{\mathbf{k}}^\dagger \quad (5.18a)$$

$$\sum_{\langle ij \rangle} a_i b_j = z \sum_{\mathbf{k}} \gamma_{\mathbf{k}} a_{\mathbf{k}} b_{\mathbf{k}}. \quad (5.18b)$$

In order to transform the interaction part V'_{HP} , as defined in Eq. (5.11d), into momentum space, we compute

$$\sum_{\langle ij \rangle} a_i^\dagger a_i b_j^\dagger b_j = \left(\frac{2}{N} \right)^2 \sum_{\mathbf{k}_1 \mathbf{k}_2 \mathbf{k}_3 \mathbf{k}_4} \sum_{\langle ij \rangle} e^{i\mathbf{k}_1 \mathbf{R}_i} a_1^\dagger e^{-i\mathbf{k}_2 \mathbf{R}_i} a_2 e^{-i\mathbf{k}_3 \mathbf{R}_j} b_3^\dagger e^{i\mathbf{k}_4 \mathbf{R}_j} b_4 \quad (5.19a)$$

$$= \left(\frac{2}{N} \right)^2 \sum_{\mathbf{k}_1 \mathbf{k}_2 \mathbf{k}_3 \mathbf{k}_4} \sum_i \sum_{\boldsymbol{\delta}} e^{i(\mathbf{k}_1 - \mathbf{k}_2) \mathbf{R}_i} e^{-i\mathbf{k}_3 (\mathbf{R}_i + \boldsymbol{\delta})} e^{i\mathbf{k}_4 (\mathbf{R}_i + \boldsymbol{\delta})} a_1^\dagger a_2 b_3^\dagger b_4 \quad (5.19b)$$

$$= \frac{2}{N} \sum_{\mathbf{k}_1 \mathbf{k}_2 \mathbf{k}_3 \mathbf{k}_4} \sum_{\boldsymbol{\delta}} e^{i\boldsymbol{\delta} (\mathbf{k}_4 - \mathbf{k}_3)} \frac{2}{N} \sum_i e^{i(\mathbf{k}_1 - \mathbf{k}_2 - \mathbf{k}_3 + \mathbf{k}_4) \mathbf{R}_i} a_1^\dagger a_2 b_3^\dagger b_4 \quad (5.19c)$$

$$= \frac{2z}{N} \sum_{\mathbf{k}_1 \mathbf{k}_2 \mathbf{k}_3 \mathbf{k}_4} \gamma_{(4-3)} \delta(\mathbf{k}_1 - \mathbf{k}_2 - \mathbf{k}_3 + \mathbf{k}_4) a_1^\dagger a_2 b_3^\dagger b_4 \quad (5.19d)$$

$$= \frac{2z}{N} \sum_{\mathbf{k}_1 \mathbf{k}_2 \mathbf{k}_3 \mathbf{k}_4} \gamma_{(2-4)} \delta(\mathbf{k}_1 + \mathbf{k}_2 - \mathbf{k}_3 - \mathbf{k}_4) a_1^\dagger a_3 b_4^\dagger b_2, \quad (5.19e)$$

where all delta-functions in this context are to be taken modulo a reciprocal lattice vector of the antiferromagnetic Brillouin zone. Similarly, we can transform

$$\sum_{\langle ij \rangle} a_i^\dagger a_i a_j b_j = \frac{2z}{N} \sum_{\mathbf{k}_1 \mathbf{k}_2 \mathbf{k}_3 \mathbf{k}_4} \gamma_{(2)} \delta(\mathbf{k}_1 + \mathbf{k}_2 - \mathbf{k}_4 - \mathbf{k}_3) a_1^\dagger a_3 a_4 b_2 \quad (5.20a)$$

$$\sum_{\langle ij \rangle} a_i^\dagger a_i^\dagger a_i b_j^\dagger = \frac{2z}{N} \sum_{\mathbf{k}_1 \mathbf{k}_2 \mathbf{k}_3 \mathbf{k}_4} \gamma_{(4)} \delta(\mathbf{k}_1 + \mathbf{k}_2 - \mathbf{k}_3 - \mathbf{k}_4) a_1^\dagger a_2^\dagger a_3 b_4^\dagger \quad (5.20b)$$

$$\sum_{\langle ij \rangle} a_i b_j^\dagger b_j b_j = \frac{2z}{N} \sum_{\mathbf{k}_1 \mathbf{k}_2 \mathbf{k}_3 \mathbf{k}_4} \gamma_{(2-3-4)} \delta(\mathbf{k}_1 + \mathbf{k}_2 - \mathbf{k}_3 - \mathbf{k}_4) a_1 b_2^\dagger b_3 b_4 \quad (5.20c)$$

$$\sum_{\langle ij \rangle} a_i^\dagger b_j^\dagger b_j^\dagger b_j = \frac{2z}{N} \sum_{\mathbf{k}_1 \mathbf{k}_2 \mathbf{k}_3 \mathbf{k}_4} \gamma_{(2-3-4)} \delta(\mathbf{k}_1 + \mathbf{k}_2 - \mathbf{k}_3 - \mathbf{k}_4) a_1^\dagger b_3^\dagger b_4^\dagger b_2. \quad (5.20d)$$

Transforming the components of the real space Hamiltonian in Eq. (5.11) in momentum space yields

$$H'_0 = JSz \sum_{\mathbf{k}} \left[\Delta (a_{\mathbf{k}} a_{\mathbf{k}}^\dagger + b_{\mathbf{k}}^\dagger b_{\mathbf{k}}) + \gamma_{\mathbf{k}} (a_{\mathbf{k}}^\dagger b_{\mathbf{k}}^\dagger + a_{\mathbf{k}} b_{\mathbf{k}}) \right] \quad (5.21)$$

for the bilinear Hamiltonian and

$$\begin{aligned} V'_{\text{HP}} = & -J \frac{2z}{N} \sum_{\mathbf{k}_1 \mathbf{k}_2 \mathbf{k}_3 \mathbf{k}_4} \delta(\mathbf{k}_1 + \mathbf{k}_2 - \mathbf{k}_3 - \mathbf{k}_4) \Delta \gamma_{(2-4)} a_1^\dagger a_3 b_4^\dagger b_2 \\ & - J \frac{2z}{N} \sum_{\mathbf{k}_1 \mathbf{k}_2 \mathbf{k}_3 \mathbf{k}_4} \delta(\mathbf{k}_1 + \mathbf{k}_2 - \mathbf{k}_3 - \mathbf{k}_4) \frac{1}{4} \left(\gamma_{(2)} a_1^\dagger a_3 a_4 b_2 + \gamma_{(1)} a_1^\dagger b_3^\dagger b_4^\dagger b_2 \right) \\ & - J \frac{2z}{N} \sum_{\mathbf{k}_1 \mathbf{k}_2 \mathbf{k}_3 \mathbf{k}_4} \delta(\mathbf{k}_1 + \mathbf{k}_2 - \mathbf{k}_3 - \mathbf{k}_4) \frac{1}{4} \left(\gamma_{(4)} a_1^\dagger a_2^\dagger a_3 b_4^\dagger + \gamma_{(1)} a_1 b_2^\dagger b_3 b_4 \right) \end{aligned} \quad (5.22)$$

for the magnon scattering. Here we have used that

$$\sum_{\mathbf{k}_1 \mathbf{k}_2 \mathbf{k}_3 \mathbf{k}_4} \delta(\mathbf{k}_1 + \mathbf{k}_2 - \mathbf{k}_3 - \mathbf{k}_4) \gamma_{(2-3-4)} = \sum_{\mathbf{k}_1 \mathbf{k}_2 \mathbf{k}_3 \mathbf{k}_4} \delta(\mathbf{k}_1 + \mathbf{k}_2 - \mathbf{k}_3 - \mathbf{k}_4) \gamma_{(1)}. \quad (5.23)$$

5.1.2 The Dyson-Maleev representation

Just like the Holstein-Primakoff representation, the Dyson-Maleev representation uses a transformation on two sublattices, namely

$$S_i^z = S - a_i^\dagger a_i \quad (5.24a)$$

$$S_i^+ = \sqrt{2S} \left(1 - \frac{a_i^\dagger a_i}{2S} \right) a_i \quad (5.24b)$$

$$S_i^- = \sqrt{2S} a_i^\dagger \quad (5.24c)$$

and

$$S_j^z = -S + b_j^\dagger b_j \quad (5.25a)$$

$$S_j^+ = \sqrt{2S} b_j^\dagger \left(1 - \frac{b_j^\dagger b_j}{2S} \right) \quad (5.25b)$$

$$S_j^- = \sqrt{2S} b_j \quad (5.25c)$$

to map the spin Hamiltonian in Eq. (5.1) onto a bosonic Hamiltonian. The major difference between the Holstein-Primakoff representation and the Dyson-Maleev representation is that the Dyson-Maleev representation maintains the full Hamiltonian because there is no need for a truncation of a power series. However, in contrast to the Holstein-Primakoff representation, it is not hermitian because

$$(S_i^+)^{\dagger} \neq S_i^- . \quad (5.26)$$

Following the same steps as described in section 5.1.1, we can divide the Hamiltonian into a ground state energy, a bilinear Hamiltonian and a term encoding the magnon interaction, yielding

$$\mathcal{H}_{\text{DM}} = E'_0 + H'_0 + V'_{\text{DM}} \quad (5.27a)$$

$$E'_0 = -\frac{Nz}{2} \Delta JS (S + 1) \quad (5.27b)$$

$$H'_0 = JSz \Delta \left(\sum_i a_i a_i^{\dagger} + \sum_j b_j^{\dagger} b_j \right) + JS \sum_{\langle ij \rangle} (a_i^{\dagger} b_j^{\dagger} + a_i b_j) \quad (5.27c)$$

$$V'_{\text{DM}} = -J \sum_{\langle ij \rangle} \left[\Delta a_i^{\dagger} a_i b_j^{\dagger} b_j + \frac{1}{2} (a_i^{\dagger} a_i a_i b_j + a_i^{\dagger} b_j^{\dagger} b_j^{\dagger} b_j) \right] \quad (5.27d)$$

where both E'_0 and H'_0 are identical to the Holstein-Primakoff Hamiltonian. However, the term encoding the magnon scattering is different, and its momentum space representation is given by

$$\begin{aligned} V'_{\text{DM}} = & -J \frac{2z}{N} \sum_{\mathbf{k}_1 \mathbf{k}_2 \mathbf{k}_3 \mathbf{k}_4} \delta(\mathbf{k}_1 + \mathbf{k}_2 - \mathbf{k}_3 - \mathbf{k}_4) \Delta \gamma_{(2-4)} a_1^{\dagger} a_3 b_4^{\dagger} b_2 \\ & - J \frac{2z}{N} \sum_{\mathbf{k}_1 \mathbf{k}_2 \mathbf{k}_3 \mathbf{k}_4} \delta(\mathbf{k}_1 + \mathbf{k}_2 - \mathbf{k}_3 - \mathbf{k}_4) \frac{1}{2} \left(\gamma_{(2)} a_1^{\dagger} a_3 a_4 b_2 + \gamma_{(1)} a_1^{\dagger} b_3^{\dagger} b_4^{\dagger} b_2 \right) . \end{aligned} \quad (5.28)$$

5.1.3 Diagonalizing the bilinear Hamiltonian H'_0

The bilinear Hamiltonian, which is identical in the two previously discussed formalisms, can be written as the matrix equation

$$H'_0 = JSz \sum_{\mathbf{k}} \begin{bmatrix} a_{\mathbf{k}} & b_{\mathbf{k}}^{\dagger} \end{bmatrix} \begin{bmatrix} \Delta & -\gamma_{\mathbf{k}} \\ \gamma_{\mathbf{k}} & \Delta \end{bmatrix} \begin{bmatrix} a_{\mathbf{k}}^{\dagger} \\ -b_{\mathbf{k}} \end{bmatrix} . \quad (5.29)$$

where the eigenvalues of the matrix are given by $\pm \sqrt{\Delta^2 - \gamma_{\mathbf{k}}^2}$. We define

$$\lambda_{\mathbf{k}} = \sqrt{\Delta^2 - \gamma_{\mathbf{k}}^2} , \quad (5.30)$$

which allows us to write the diagonal Hamiltonian as

$$H'_0 = JSz \sum_{\mathbf{k}} \begin{bmatrix} a_{\mathbf{k}} & b_{\mathbf{k}}^{\dagger} \end{bmatrix} \begin{bmatrix} \lambda_{\mathbf{k}} & 0 \\ 0 & -\lambda_{\mathbf{k}} \end{bmatrix} \begin{bmatrix} a_{\mathbf{k}}^{\dagger} \\ -b_{\mathbf{k}} \end{bmatrix} \quad (5.31a)$$

$$= JSz \sum_{\mathbf{k}} \lambda_{\mathbf{k}} \left(a_{\mathbf{k}} a_{\mathbf{k}}^{\dagger} + b_{\mathbf{k}}^{\dagger} b_{\mathbf{k}} \right). \quad (5.31b)$$

Figure 5.2 displays $\lambda_{\mathbf{k}}$ for three different anisotropies Δ along high symmetry cuts through the antiferromagnetic Brillouin zone and it is visible, that while the system is gapless in the isotropic case, a gap opens at $\Delta > 1$. Note that the derivative of $\lambda_{\mathbf{k}}$ perpendicular to the Brillouin zone boundary (BZB) is independent of the value of Δ , as it is required for a dispersion. In general, we know that

$$\lim_{\mathbf{k} \rightarrow 0} \gamma_{\mathbf{k}} = 1 \quad (5.32a)$$

$$\lim_{\mathbf{k} \rightarrow \text{BZB}} \gamma_{\mathbf{k}} = 0 \quad (5.32b)$$

and therefore

$$\lim_{\mathbf{k} \rightarrow 0} \lambda_{\mathbf{k}} = \sqrt{\Delta^2 - 1} \quad (5.33a)$$

$$\lim_{\mathbf{k} \rightarrow \text{BZB}} \lambda_{\mathbf{k}} = \Delta. \quad (5.33b)$$

In order to eliminate off-diagonal terms in the corrections to the bilinear Hamiltonian, we write a and b in terms of the Bogoliubov operators

$$a_{\mathbf{k}} = u_{\mathbf{k}} \alpha_{\mathbf{k}} + v_{\mathbf{k}} \beta_{\mathbf{k}}^{\dagger} \quad (5.34a)$$

$$b_{\mathbf{k}} = u_{\mathbf{k}} \beta_{\mathbf{k}} + v_{\mathbf{k}} \alpha_{\mathbf{k}}^{\dagger}. \quad (5.34b)$$

Just like the original operators a and b , the Bogoliubov operators $\alpha_{\mathbf{k}}^{(\dagger)}$ and $\beta_{\mathbf{k}}^{(\dagger)}$ are canonical bosonic annihilation (creation) operators and therefore need to obey the same bosonic commutation laws. Assuming $u_{\mathbf{k}}$ and $v_{\mathbf{k}}$ to be real without loss of generality, we evaluate the commutators

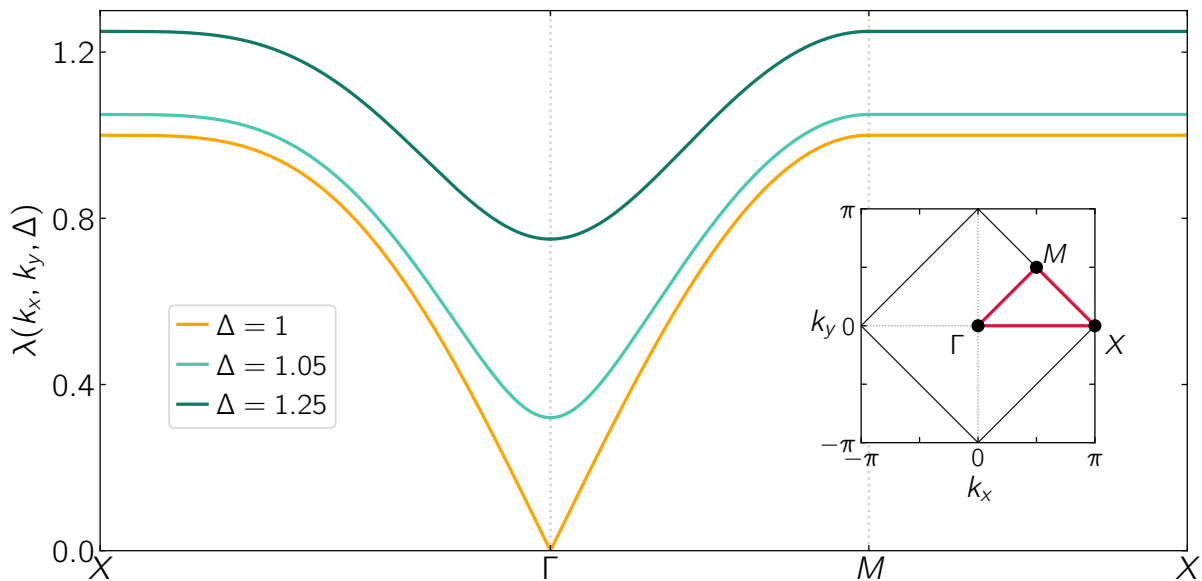


Figure 5.2: Magnon dispersion $\lambda_{\mathbf{k}}$ for three different values of Δ along high symmetry cuts (shown in the inset, red) through the antiferromagnetic Brillouin zone. For $\Delta > 1$ a gap opens at Γ , which corresponds to the center of the Brillouin zone

$$1 \stackrel{!}{=} [a_{\mathbf{k}}, a_{\mathbf{k}}^\dagger] = u_{\mathbf{k}}^2 [\alpha_{\mathbf{k}}, \alpha_{\mathbf{k}}^\dagger] + v_{\mathbf{k}}^2 [\beta_{\mathbf{k}}^\dagger, \beta_{\mathbf{k}}] = u_{\mathbf{k}}^2 - v_{\mathbf{k}}^2 \quad (5.35a)$$

$$1 \stackrel{!}{=} [b_{\mathbf{k}}, b_{\mathbf{k}}^\dagger] = u_{\mathbf{k}}^2 [\beta_{\mathbf{k}}, \beta_{\mathbf{k}}^\dagger] + v_{\mathbf{k}}^2 [\alpha_{\mathbf{k}}^\dagger, \alpha_{\mathbf{k}}] = u_{\mathbf{k}}^2 - v_{\mathbf{k}}^2 \quad (5.35b)$$

and find that the Bogoliubov factors $u_{\mathbf{k}}$ and $v_{\mathbf{k}}$ need to satisfy

$$u_{\mathbf{k}}^2 - v_{\mathbf{k}}^2 \stackrel{!}{=} 1. \quad (5.36)$$

In order to write the momentum space Hamiltonian in Eq. (5.21) in terms of these operators, we compute

$$\gamma_{\mathbf{k}} a_{\mathbf{k}} b_{\mathbf{k}} = \gamma_{\mathbf{k}} \left[u_{\mathbf{k}}^2 \alpha_{\mathbf{k}} \beta_{\mathbf{k}} + v_{\mathbf{k}}^2 \alpha_{\mathbf{k}}^\dagger \beta_{\mathbf{k}}^\dagger + u_{\mathbf{k}} v_{\mathbf{k}} (\alpha_{\mathbf{k}} \alpha_{\mathbf{k}}^\dagger + \beta_{\mathbf{k}}^\dagger \beta_{\mathbf{k}}) \right] \quad (5.37a)$$

$$\gamma_{\mathbf{k}} \alpha_{\mathbf{k}}^\dagger \beta_{\mathbf{k}}^\dagger = \gamma_{\mathbf{k}} \left[u_{\mathbf{k}}^2 \alpha_{\mathbf{k}}^\dagger \beta_{\mathbf{k}}^\dagger + v_{\mathbf{k}}^2 \alpha_{\mathbf{k}} \beta_{\mathbf{k}} + u_{\mathbf{k}} v_{\mathbf{k}} (\alpha_{\mathbf{k}} \alpha_{\mathbf{k}}^\dagger + \beta_{\mathbf{k}}^\dagger \beta_{\mathbf{k}}) \right] \quad (5.37b)$$

$$\Delta a_{\mathbf{k}} a_{\mathbf{k}}^\dagger = \Delta \left[u_{\mathbf{k}}^2 \alpha_{\mathbf{k}} \alpha_{\mathbf{k}}^\dagger + v_{\mathbf{k}}^2 \beta_{\mathbf{k}}^\dagger \beta_{\mathbf{k}} + u_{\mathbf{k}} v_{\mathbf{k}} (\alpha_{\mathbf{k}} \beta_{\mathbf{k}} + \alpha_{\mathbf{k}}^\dagger \beta_{\mathbf{k}}^\dagger) \right] \quad (5.37c)$$

$$\Delta b_{\mathbf{k}}^\dagger b_{\mathbf{k}} = \Delta \left[u_{\mathbf{k}}^2 \beta_{\mathbf{k}}^\dagger \beta_{\mathbf{k}} + v_{\mathbf{k}}^2 \alpha_{\mathbf{k}} \alpha_{\mathbf{k}}^\dagger + u_{\mathbf{k}} v_{\mathbf{k}} (\alpha_{\mathbf{k}} \beta_{\mathbf{k}} + \alpha_{\mathbf{k}}^\dagger \beta_{\mathbf{k}}^\dagger) \right], \quad (5.37d)$$

which yields the Hamiltonian

$$\begin{aligned} H'_0 = & \left[2\gamma_{\mathbf{k}} u_{\mathbf{k}} v_{\mathbf{k}} + \Delta (u_{\mathbf{k}}^2 + v_{\mathbf{k}}^2) \right] (\alpha_{\mathbf{k}} \alpha_{\mathbf{k}}^\dagger + \beta_{\mathbf{k}}^\dagger \beta_{\mathbf{k}}) \\ & + \left[2\Delta u_{\mathbf{k}} v_{\mathbf{k}} + \gamma_{\mathbf{k}} (u_{\mathbf{k}}^2 + v_{\mathbf{k}}^2) \right] (\alpha_{\mathbf{k}} \beta_{\mathbf{k}} + \alpha_{\mathbf{k}}^\dagger \beta_{\mathbf{k}}^\dagger). \end{aligned} \quad (5.38)$$

Identifying this with the bilinear Hamiltonian in Eq. (5.31b), we set

$$2\gamma_{\mathbf{k}} u_{\mathbf{k}} v_{\mathbf{k}} + \Delta (u_{\mathbf{k}}^2 + v_{\mathbf{k}}^2) \stackrel{!}{=} \lambda_{\mathbf{k}} \quad (5.39a)$$

$$2\Delta u_{\mathbf{k}} v_{\mathbf{k}} + \gamma_{\mathbf{k}} (u_{\mathbf{k}}^2 + v_{\mathbf{k}}^2) \stackrel{!}{=} 0. \quad (5.39b)$$

This determines two further criteria that need to be satisfied by $u_{\mathbf{k}}$ and $v_{\mathbf{k}}$, namely

$$u_{\mathbf{k}}^2 + v_{\mathbf{k}}^2 \stackrel{!}{=} \frac{\Delta}{\lambda_{\mathbf{k}}} \quad (5.40a)$$

$$u_{\mathbf{k}} v_{\mathbf{k}} \stackrel{!}{=} -\frac{\gamma_{\mathbf{k}}}{2\lambda_{\mathbf{k}}}. \quad (5.40b)$$

One choice of Bogoliubov factors that meets all the requirements from Eq. (5.36) and Eq. (5.40) is given by

$$u_{\mathbf{k}} = \sqrt{\frac{\Delta + \lambda_{\mathbf{k}}}{2\lambda_{\mathbf{k}}}} \quad (5.41a)$$

$$v_{\mathbf{k}} = -\text{sign}(\gamma_{\mathbf{k}}) \sqrt{\frac{\Delta - \lambda_{\mathbf{k}}}{2\lambda_{\mathbf{k}}}}. \quad (5.41b)$$

The Bogoliubov transformation implies a new ground state, which is defined by

$$\alpha_{\mathbf{k}} |\Phi_{\text{GS}}\rangle = 0 \quad (5.42)$$

and defines the vacuum at temperature $T = 0$.

5.1.4 The interaction term

The magnon interactions are contained in the interaction term V , whose momentum space representations are given in Eq. (5.22) for the Holstein-Primakoff representation and in Eq. (5.28) for the Dyson-Maleev representation. Both terms have the four-operator products

$$\{a_1^\dagger a_3 b_4^\dagger b_2, a_1^\dagger a_3 a_4 b_2, a_1^\dagger b_3^\dagger b_4^\dagger b_2\} \quad (5.43)$$

in common, the products

$$\{a_1^\dagger b_4^\dagger a_2^\dagger a_3, b_2^\dagger b_3 a_1 b_4\} \quad (5.44)$$

are unique to the Holstein-Primakoff representation. Writing these products in terms of the Bogoliubov operators, as defined in Eq. (5.34), and normal ordering the result yields lengthy expressions given in appendix A, starting at Eq. (A.2). Each of the products has terms with two delta-functions, which do not depend on the Bogoliubov operators and therefore contribute to the magnon vacuum. Furthermore, the products consist of terms that contain one delta-function and that are bilinear in the Bogoliubov operators. These terms contribute to the bilinear Hamiltonian. The terms which are not multiplied by a delta-function and which have products of four Bogoliubov operators will lead to the vertices which we use to implement the magnon interactions in our simulation. To simplify the notation, we will now split up each of the five terms in Eq. (5.43) and Eq. (5.44) with the prefactors $\gamma_{\mathbf{k}}$ from the momentum space representation of the magnon interactions in Eq (5.22), in these three categories, meaning we define

$$\mathcal{P}_1 = \sum_{\mathbf{k}_1 \mathbf{k}_2 \mathbf{k}_3 \mathbf{k}_4} \Delta \delta(\mathbf{k}_1 + \mathbf{k}_2 - \mathbf{k}_3 - \mathbf{k}_4) \gamma_{(2-4)} a_1^\dagger a_3 b_4^\dagger b_2 = \mathcal{P}_1^E + \mathcal{P}_1^{\text{bilinear}} + \mathcal{P}_1^V, \quad (5.45)$$

where \mathcal{P}^E is the contribution to the ground state energy, $\mathcal{P}^{\text{bilinear}}$ is the contribution to the bilinear Hamiltonian and \mathcal{P}^V is the contribution to the magnon interactions. The analogous definitions for the remaining products are

$$\mathcal{P}_2 = \sum_{\mathbf{k}_1 \mathbf{k}_2 \mathbf{k}_3 \mathbf{k}_4} \delta(\mathbf{k}_1 + \mathbf{k}_2 - \mathbf{k}_3 - \mathbf{k}_4) \gamma_{(2)} a_1^\dagger a_3 a_4 b_2 = \mathcal{P}_2^E + \mathcal{P}_2^{\text{bilinear}} + \mathcal{P}_2^V \quad (5.46a)$$

$$\mathcal{P}_3 = \sum_{\mathbf{k}_1 \mathbf{k}_2 \mathbf{k}_3 \mathbf{k}_4} \delta(\mathbf{k}_1 + \mathbf{k}_2 - \mathbf{k}_3 - \mathbf{k}_4) \gamma_{(1)} a_1^\dagger b_3^\dagger b_4^\dagger b_2 = \mathcal{P}_3^E + \mathcal{P}_3^{\text{bilinear}} + \mathcal{P}_3^V \quad (5.46b)$$

$$\mathcal{P}_4 = \sum_{\mathbf{k}_1 \mathbf{k}_2 \mathbf{k}_3 \mathbf{k}_4} \delta(\mathbf{k}_1 + \mathbf{k}_2 - \mathbf{k}_3 - \mathbf{k}_4) \gamma_{(4)} a_1^\dagger a_2^\dagger a_3 b_4^\dagger = \mathcal{P}_4^E + \mathcal{P}_4^{\text{bilinear}} + \mathcal{P}_4^V \quad (5.46c)$$

$$\mathcal{P}_5 = \sum_{\mathbf{k}_1 \mathbf{k}_2 \mathbf{k}_3 \mathbf{k}_4} \delta(\mathbf{k}_1 + \mathbf{k}_2 - \mathbf{k}_3 - \mathbf{k}_4) \gamma_{(1)} a_1 b_2^\dagger b_3 b_4 = \mathcal{P}_5^E + \mathcal{P}_5^{\text{bilinear}} + \mathcal{P}_5^V. \quad (5.46d)$$

The first contribution to the magnon vacuum is given by

$$\mathcal{P}_1^E = \sum_{\mathbf{k}_1 \mathbf{k}_2 \mathbf{k}_3 \mathbf{k}_4} \Delta \delta(\mathbf{k}_1 + \mathbf{k}_2 - \mathbf{k}_3 - \mathbf{k}_4) \gamma_{(2-4)} \left[v_1^2 v_2^2 \delta(\mathbf{k}_1 - \mathbf{k}_3) \delta(\mathbf{k}_2 - \mathbf{k}_4) \right] \quad (5.47a)$$

$$\begin{aligned} &+ \sum_{\mathbf{k}_1 \mathbf{k}_2 \mathbf{k}_3 \mathbf{k}_4} \Delta \delta(\mathbf{k}_1 + \mathbf{k}_2 - \mathbf{k}_3 - \mathbf{k}_4) \gamma_{(2-4)} [u_1 u_2 v_1 v_2 \delta(\mathbf{k}_1 - \mathbf{k}_4) \delta(\mathbf{k}_2 - \mathbf{k}_3)] \\ &= \sum_{\mathbf{k}_1 \mathbf{k}_2} \Delta \left(v_1^2 v_2^2 + \gamma_{(2-1)} u_1 u_2 v_1 v_2 \right) \end{aligned} \quad (5.47b)$$

and the first correction to the bilinear Hamiltonian yields

$$\begin{aligned} \mathcal{P}_1^{\text{bilinear}} = & \sum_{\mathbf{k}_1 \mathbf{k}_2} \Delta \left[v_2^2 (u_1^2 + v_1^2) + 2 \gamma_{(2-1)} u_1 u_2 v_1 v_2 \right] (\alpha_1^\dagger \alpha_1 + \beta_1^\dagger \beta_1) \\ & + \sum_{\mathbf{k}_1 \mathbf{k}_2} \Delta \left[2 u_1 v_1 v_2^2 + \gamma_{(2-1)} u_2 v_2 (u_1^2 + v_1^2) \right] (\alpha_1^\dagger \beta_1^\dagger + \alpha_1 \beta_1). \end{aligned} \quad (5.48)$$

Analogously, we get

$$\mathcal{P}_2^{\text{E}} = \sum_{\mathbf{k}_1 \mathbf{k}_2} 2 v_1^2 u_2 v_2 \gamma_{(2)} \quad (5.49a)$$

$$\begin{aligned} \mathcal{P}_2^{\text{bilinear}} = & \sum_{\mathbf{k}_1 \mathbf{k}_2} \left[2 u_1 v_1 v_2^2 \gamma_{(1)} \right] (\alpha_1^\dagger \alpha_1 + \beta_1^\dagger \beta_1) + \sum_{\mathbf{k}_1 \mathbf{k}_2} \left[2 u_2 v_2 \gamma_{(2)} \right] (u_1^2 \alpha_1^\dagger \alpha_1 + v_1^2 \beta_1^\dagger \beta_1) \\ & + \sum_{\mathbf{k}_1 \mathbf{k}_2} \left[2 u_1 v_1 u_2 v_2 \gamma_{(2)} \right] (\alpha_1^\dagger \beta_1^\dagger + \alpha_1 \beta_1) + \sum_{\mathbf{k}_1 \mathbf{k}_2} \left[2 v_2^2 \gamma_{(1)} \right] (v_1^2 \alpha_1^\dagger \beta_1^\dagger + u_1^2 \alpha_1 \beta_1) \end{aligned} \quad (5.49b)$$

and

$$\mathcal{P}_3^{\text{E}} = \sum_{\mathbf{k}_1 \mathbf{k}_2} 2 v_1^2 u_2 v_2 \gamma_{(2)} \quad (5.50a)$$

$$\begin{aligned} \mathcal{P}_3^{\text{bilinear}} = & \sum_{\mathbf{k}_1 \mathbf{k}_2} \left[2 u_1 v_1 v_2^2 \gamma_{(1)} \right] (\alpha_1^\dagger \alpha_1 + \beta_1^\dagger \beta_1) + \sum_{\mathbf{k}_1 \mathbf{k}_2} \left[2 u_2 v_2 \gamma_{(2)} \right] (v_1^2 \alpha_1^\dagger \alpha_1 + u_1^2 \beta_1^\dagger \beta_1) \\ & + \sum_{\mathbf{k}_1 \mathbf{k}_2} \left[2 u_1 v_1 u_2 v_2 \gamma_{(2)} \right] (\alpha_1^\dagger \beta_1^\dagger + \alpha_1 \beta_1) + \sum_{\mathbf{k}_1 \mathbf{k}_2} \left[2 v_2^2 \gamma_{(1)} \right] (u_1^2 \alpha_1^\dagger \beta_1^\dagger + v_1^2 \alpha_1 \beta_1). \end{aligned} \quad (5.50b)$$

The products that are unique to the Holstein-Primakoff formalism yield

$$\mathcal{P}_4^{\text{E}} = \sum_{\mathbf{k}_1 \mathbf{k}_2} 2 v_1^2 u_2 v_2 \gamma_{(2)} \quad (5.51a)$$

$$\begin{aligned} \mathcal{P}_4^{\text{bilinear}} = & \sum_{\mathbf{k}_1 \mathbf{k}_2} \left[2 u_1 v_1 v_2^2 \gamma_{(1)} \right] (\alpha_1^\dagger \alpha_1 + \beta_1^\dagger \beta_1) + \sum_{\mathbf{k}_1 \mathbf{k}_2} \left[2 u_2 v_2 \gamma_{(2)} \right] (u_1^2 \alpha_1^\dagger \alpha_1 + v_1^2 \beta_1^\dagger \beta_1) \\ & + \sum_{\mathbf{k}_1 \mathbf{k}_2} \left[2 u_1 v_1 u_2 v_2 \gamma_{(2)} \right] (\alpha_1^\dagger \beta_1^\dagger + \alpha_1 \beta_1) + \sum_{\mathbf{k}_1 \mathbf{k}_2} \left[2 v_2^2 \gamma_{(1)} \right] (u_1^2 \alpha_1^\dagger \beta_1^\dagger + v_1^2 \alpha_1 \beta_1) \end{aligned} \quad (5.51b)$$

and

$$\mathcal{P}_5^{\text{E}} = \sum_{\mathbf{k}_1 \mathbf{k}_2} 2 v_1^2 u_2 v_2 \gamma_{(2)} \quad (5.52a)$$

$$\begin{aligned} \mathcal{P}_5^{\text{bilinear}} = & \sum_{\mathbf{k}_1 \mathbf{k}_2} \left[2 u_1 v_1 v_2^2 \gamma_{(1)} \right] (\alpha_1^\dagger \alpha_1 + \beta_1^\dagger \beta_1) + \sum_{\mathbf{k}_1 \mathbf{k}_2} \left[2 u_2 v_2 \gamma_{(2)} \right] (v_1^2 \alpha_1^\dagger \alpha_1 + u_1^2 \beta_1^\dagger \beta_1) \\ & + \sum_{\mathbf{k}_1 \mathbf{k}_2} \left[2 u_1 v_1 u_2 v_2 \gamma_{(2)} \right] (\alpha_1^\dagger \beta_1^\dagger + \alpha_1 \beta_1) + \sum_{\mathbf{k}_1 \mathbf{k}_2} \left[2 v_2^2 \gamma_{(1)} \right] (v_1^2 \alpha_1^\dagger \beta_1^\dagger + u_1^2 \alpha_1 \beta_1). \end{aligned} \quad (5.52b)$$

Collecting the contributions to the ground state energy, it is easy to see that the corrections to E'_0 , as defined in Eq. (5.11b) are the same for both formalisms, because $\mathcal{P}_2^{\text{E}} = \mathcal{P}_3^{\text{E}} = \mathcal{P}_4^{\text{E}} = \mathcal{P}_5^{\text{E}}$. Overall, we obtain

$$E_0 = E'_0 - \frac{2Jz}{N} \sum_{\mathbf{k}_1 \mathbf{k}_2} \Delta \left(v_1^2 v_2^2 + \gamma_{(2-1)} u_1 u_2 v_1 v_2 \right) + 2 v_1^2 u_2 v_2 \gamma_{(2)} \quad (5.53a)$$

$$= E'_0 - \frac{2Jz}{N} \sum_{\mathbf{k}_1 \mathbf{k}_2} \Delta \left[\frac{(\Delta - \lambda_1)(\Delta - \lambda_2)}{4\lambda_1 \lambda_2} + \frac{\gamma_{(2-1)} \gamma_{(1)} \gamma_{(2)}}{4\lambda_1 \lambda_2} \right] - \frac{\gamma_{(2)}^2}{\lambda_2} \left[\frac{\Delta - \lambda_1}{2\lambda_1} \right], \quad (5.53b)$$

5 Nonequilibrium phase transition

where we have used the properties of the Bogoliubov factors in Eq. (5.40). To compute integrals in momentum space, it is useful to recall that \mathbf{k} only runs over the antiferromagnetic Brillouin zone and not the full Brillouin zone, which means the corresponding integrals read

$$\sum_{\mathbf{k}} 1 = \frac{N}{2(2\pi)^2} \int_{-\pi}^{\pi} dk^x \int_{-\pi}^{\pi} dk^y = \frac{N}{2} \quad (5.54)$$

and correspondingly

$$\sum_{\mathbf{k}_1 \mathbf{k}_2} 1 = \frac{N}{2(2\pi)^2} \int_{-\pi}^{\pi} dk_1^x \int_{-\pi}^{\pi} dk_1^y \frac{N}{2(2\pi)^2} \int_{-\pi}^{\pi} dk_2^x \int_{-\pi}^{\pi} dk_2^y = \frac{N^2}{4}. \quad (5.55)$$

Furthermore, recalling the definition of $\gamma_{\mathbf{k}}$ in Eq. (5.17b) and the trigonometric addition formulas allows to write

$$\sum_{\mathbf{k}_2} \gamma_{(2-1)} f(\mathbf{k}_2) \propto \int_{-\pi}^{\pi} \int_{-\pi}^{\pi} dk_2^x dk_2^y \frac{\cos(k_2^x) \cos(k_1^x) + \cos(k_2^y) \cos(k_1^y)}{2} f(k_2^x, k_2^y) \quad (5.56a)$$

$$+ \frac{\sin(k_1^x)}{2} \int_{-\pi}^{\pi} \int_{-\pi}^{\pi} dk_2^x dk_2^y \sin(k_2^x) f(k_2^x, k_2^y) \quad (5.56b)$$

$$+ \frac{\sin(k_1^y)}{2} \int_{-\pi}^{\pi} \int_{-\pi}^{\pi} dk_2^x dk_2^y \sin(k_2^y) f(k_2^x, k_2^y), \quad (5.56c)$$

where both Eq. (5.56b) and Eq. (5.56c) are zero for any given function $f(k_2^x, k_2^y)$ that satisfies $f(k_2^x, k_2^y) = f(-k_2^x, -k_2^y)$. Similarly, we get

$$\sum_{\mathbf{k}_2} \gamma_{(2)} \gamma_{(1)} f(\mathbf{k}_2) \propto \int_{-\pi}^{\pi} \int_{-\pi}^{\pi} dk_2^x dk_2^y \frac{\cos(k_2^x) \cos(k_1^x) + \cos(k_2^y) \cos(k_1^y)}{4} f(k_2^x, k_2^y) \quad (5.57a)$$

$$+ \int_{-\pi}^{\pi} \int_{-\pi}^{\pi} dk_2^x dk_2^y \frac{\cos(k_2^x) \cos(k_1^y) + \cos(k_2^y) \cos(k_1^x)}{4} f(k_2^x, k_2^y)$$

$$\propto \int_{-\pi}^{\pi} \int_{-\pi}^{\pi} dk_2^x dk_2^y \frac{\cos(k_2^x) \cos(k_1^x) + \cos(k_2^y) \cos(k_1^y)}{2} f(k_2^x, k_2^y), \quad (5.57b)$$

where in Eq. (5.57b) we have used that we can swap k_2^x and k_2^y since $f(k_2^x, k_2^y) = f(k_2^y, k_2^x)$. So we see, that

$$\sum_{\mathbf{k}_2} \gamma_{(2)} \gamma_{(1)} f(\mathbf{k}_2) = \sum_{\mathbf{k}_2} \gamma_{(2-1)} f(\mathbf{k}_2) \quad \forall \quad f(k_2^x, k_2^y) = f(-k_2^x, -k_2^y) = f(k_2^y, k_2^x). \quad (5.58)$$

Since we know that

$$\gamma(k_2^x, k_2^y) = \gamma(-k_2^x, -k_2^y) = \gamma(k_2^y, k_2^x) \quad (5.59a)$$

$$\lambda(k_2^x, k_2^y) = \lambda(-k_2^x, -k_2^y) = \lambda(k_2^y, k_2^x) \quad (5.59b)$$

we can write the magnon vacuum as

$$E_0 = E'_0 - \frac{Jz\Delta}{2N} \sum_{\mathbf{k}_1 \mathbf{k}_2} \frac{(\Delta - \lambda_1)(\Delta - \lambda_2)}{\lambda_1 \lambda_2} \left[1 + (\Delta + \lambda_1)(\Delta + \lambda_2) - \frac{2(\Delta + \lambda_2)}{\Delta} \right] \quad (5.60a)$$

$$= E'_0 - \frac{Jz\Delta}{2N} \sum_{\mathbf{k}_1 \mathbf{k}_2} \left[1 + (\Delta^2 - 1) \left(\frac{\Delta^2}{\lambda_1 \lambda_2} - \frac{2\lambda_2}{\lambda_1} \right) - \frac{2\lambda_2}{\Delta} + \lambda_1 \lambda_2 \right] \quad (5.60b)$$

$$= E'_0 - \frac{Jz\Delta}{2N} \left[\frac{N^2}{4} - \frac{2}{\Delta} \sum_{\mathbf{k}} \lambda_{\mathbf{k}} + \left(\sum_{\mathbf{k}} \lambda_{\mathbf{k}} \right)^2 + (\Delta^2 - 1) \sum_{\mathbf{k}_1 \mathbf{k}_2} \left(\frac{\Delta^2}{\lambda_1 \lambda_2} - \frac{2\lambda_2}{\lambda_1} \right) \right] \quad (5.60c)$$

$$= E'_0 - \frac{Jz\Delta}{2N} \left[\left(\frac{N}{2} - \sum_{\mathbf{k}} \lambda_{\mathbf{k}} \right)^2 + (\Delta^2 - 1) \sum_{\mathbf{k}_1 \mathbf{k}_2} \left(\frac{\Delta^2}{\lambda_1 \lambda_2} - \frac{2\lambda_2}{\lambda_1} \right) \right], \quad (5.60d)$$

where it becomes apparent, that in the isotropic case of $\Delta = 1$, Eq. (5.60d) further simplifies to

$$E_0^{\text{isotropic}} = -\frac{JNz}{2} \left[S(S+1) + \frac{1}{4} \left(1 - \frac{2}{N} \sum_{\mathbf{k}} \lambda_{\mathbf{k}} \right)^2 \right], \quad (5.61)$$

which corresponds to the result in Ref. [102].

Just like the corrections to the ground state energy, the corrections to the bilinear Hamiltonian H'_0 (see Eq. (5.31b)) are independent of whether one uses the Holstein-Primakoff or the Dyson-Maleev Formalism because $\mathcal{P}_2^{\text{bilinear}} + \mathcal{P}_3^{\text{bilinear}} = \mathcal{P}_4^{\text{bilinear}} + \mathcal{P}_5^{\text{bilinear}}$, namely

$$\begin{aligned} H_0 = H'_0 &- \frac{2Jz}{N} \sum_{\mathbf{k}_1 \mathbf{k}_2} \Delta \left[v_2^2 (u_1^2 + v_1^2) + 2\gamma_{(1)}\gamma_{(2)} u_1 u_2 v_1 v_2 \right] (\alpha_1^\dagger \alpha_1 + \beta_1^\dagger \beta_1) \\ &- \frac{2Jz}{N} \sum_{\mathbf{k}_1 \mathbf{k}_2} \left[2u_1 v_1 v_2^2 \gamma_{(1)} + u_2 v_2 \gamma_{(2)} (u_1^2 + v_1^2) \right] (\alpha_1^\dagger \alpha_1 + \beta_1^\dagger \beta_1) \\ &- \frac{2Jz}{N} \sum_{\mathbf{k}_1 \mathbf{k}_2} \Delta \left[2u_1 v_1 v_2^2 + \gamma_{(1)}\gamma_{(2)} u_2 v_2 (u_1^2 + v_1^2) \right] (\alpha_1^\dagger \beta_1^\dagger + \alpha_1 \beta_1) \\ &- \frac{2Jz}{N} \sum_{\mathbf{k}_1 \mathbf{k}_2} \left[2u_1 v_1 u_2 v_2 \gamma_{(2)} + v_2^2 \gamma_{(1)} (u_1^2 + v_1^2) \right] (\alpha_1^\dagger \beta_1^\dagger + \alpha_1 \beta_1). \end{aligned} \quad (5.62)$$

Using the properties of the Bogoliubov factors, this can be written as

$$\begin{aligned} H_0 = H'_0 &+ \frac{2Jz}{N} \sum_{\mathbf{k}_2} \left[\left(\frac{\Delta^2 - \lambda_2^2}{2\lambda_2} \right) - \Delta \left(\frac{\Delta - \lambda_2}{2\lambda_2} \right) \right] \sum_{\mathbf{k}_1} \left(\frac{\Delta}{\lambda_1} \right) (\alpha_1^\dagger \alpha_1 + \beta_1^\dagger \beta_1) \\ &+ \frac{2Jz}{N} \sum_{\mathbf{k}_2} \left[\left(\frac{\Delta - \lambda_2}{2\lambda_2} \right) - \Delta \left(\frac{\Delta^2 - \lambda_2^2}{2\lambda_2} \right) \right] \sum_{\mathbf{k}_1} \left(\frac{\Delta^2 - \lambda_1^2}{\lambda_1} \right) (\alpha_1^\dagger \alpha_1 + \beta_1^\dagger \beta_1) \\ &+ \frac{2Jz}{N} \sum_{\mathbf{k}_2} \left(\frac{\Delta^2 - \lambda_2^2}{2\lambda_2} \right) \sum_{\mathbf{k}_1} \frac{(1 - \Delta^2) \gamma_{(1)}}{\lambda_1} (\alpha_1^\dagger \beta_1^\dagger + \alpha_1 \beta_1), \end{aligned} \quad (5.63)$$

where the terms that mix the two sublattices $(\alpha_1^{(\dagger)} \beta_1^{(\dagger)})$ cancel out for the isotropic system and we obtain

$$H_0^{\text{isotropic}} = H'_0 + \frac{Jz}{2} \left[1 - \frac{2}{N} \sum_{\mathbf{k}_2} \lambda_2 \right] \sum_{\mathbf{k}_1} \lambda_1 (\alpha_1^\dagger \alpha_1 + \beta_1^\dagger \beta_1) \quad (5.64a)$$

$$= JSz \left[1 + \frac{1}{2S} \left(1 - \frac{2}{N} \sum_{\mathbf{k}'} \lambda_{\mathbf{k}'} \right) \right] \sum_{\mathbf{k}} \lambda_{\mathbf{k}} (\alpha_{\mathbf{k}}^\dagger \alpha_{\mathbf{k}} + \beta_{\mathbf{k}}^\dagger \beta_{\mathbf{k}}), \quad (5.64b)$$

which also corresponds to Ref. [102]. To simplify notation we define

$$H_0^{\text{isotropic}} = \sum_{\mathbf{k}} \omega_{\mathbf{k}} (\alpha_{\mathbf{k}}^\dagger \alpha_{\mathbf{k}} + \beta_{\mathbf{k}}^\dagger \beta_{\mathbf{k}}) \quad (5.65)$$

with

$$\omega_{\mathbf{k}} = JSz \left[1 + \frac{1}{2S} \left(1 - \frac{2}{N} \sum_{\mathbf{k}'} \lambda_{\mathbf{k}'} \right) \right] \lambda_{\mathbf{k}}, \quad (5.66)$$

and we can numerically evaluate the constant

$$1 - \frac{2}{N} \sum_{\mathbf{k}'} \lambda_{\mathbf{k}'} = 1 - \frac{2}{N} \sum_{\mathbf{k}} \sqrt{1 - \left(\frac{\cos(k_x) + \cos(k_y)}{2} \right)^2} = 0.157947421. \quad (5.67)$$

Assuming an isotropic system with $S = 1/2$, this yields

$$\left[1 + \frac{1}{2S} \left(1 - \frac{2}{N} \sum_{\mathbf{k}'} \lambda_{\mathbf{k}'} \right) \right] = 1.157947421 \quad \forall \quad \Delta = 1, S = \frac{1}{2}. \quad (5.68)$$

Considering the limits $\mathbf{k} \rightarrow 0$ and $\mathbf{k} \rightarrow \text{BZB}$ in Eq. (5.32) and Eq. (5.33), we see that

$$\omega_{\max} = JSz \left[1 + \frac{1}{2S} \left(1 - \frac{2}{N} \sum_{\mathbf{k}'} \lambda_{\mathbf{k}'} \right) \right] \Delta \quad (5.69)$$

at the Brillouin zone boundary. In the system with an anisotropy (Eq. (5.63), $\Delta \neq 1$), the off-diagonal terms that do not only renormalize the overall energy scale but also change the dispersion itself, are proportional to $(1 - \Delta^2) (\gamma_{(\mathbf{k})} / \lambda_{\mathbf{k}})$. This term goes like

$$\lim_{\mathbf{k} \rightarrow \mathbf{0}} \frac{(1 - \Delta^2) \gamma_{(\mathbf{k})}}{\lambda_{\mathbf{k}}} = -\sqrt{\Delta^2 - 1} \quad (5.70a)$$

$$\lim_{\mathbf{k} \rightarrow \text{BZB}} \frac{(1 - \Delta^2) \gamma_{(\mathbf{k})}}{\lambda_{\mathbf{k}}} = 0. \quad (5.70b)$$

The vanishing of the off-diagonal terms at the Brillouin zone boundary for arbitrary anisotropies is a direct consequence of the symmetry due to the bipartite lattice. Only if a hopping between next-nearest neighbors is introduced, $\gamma_{(\mathbf{k})}$ does not vanish at the boundary and the off-diagonal terms remain finite at $\Delta \neq 0$. However, at the center of the Brillouin zone the off-diagonal term only vanishes at the Heisenberg-Point $\Delta = 1$, meaning spin rotational symmetry, i.e. the same symmetry that conserves magnons with $k \rightarrow 0$ and causes them to be massless (Goldstone modes), is strictly required for the Hamiltonian to be bilinear at this level of perturbation theory. At $\Delta > 1$ spin rotational symmetry is broken and a gap opens (see Fig 5.2), meaning there are further corrections to the dispersion.

The difference between the Holstein-Primakoff formalism and the Dyson-Maleev formalism manifests itself in the term that encodes the magnon interactions. We define

$$\begin{aligned} V = -\frac{2Jz}{N} \sum_{\mathbf{k}_1 \mathbf{k}_2 \mathbf{k}_3 \mathbf{k}_4} \delta(\mathbf{k}_1 + \mathbf{k}_2 - \mathbf{k}_3 - \mathbf{k}_4) \times & \left[\tilde{\mathcal{V}}_{1234}^{(2:2)} \left(\alpha_1^\dagger \alpha_3 \beta_4^\dagger \beta_2 \right) \right. \\ & + \mathcal{V}_{1234}^{(2:2)} \left(\alpha_1^\dagger \alpha_2^\dagger \alpha_3 \alpha_4 + \beta_3^\dagger \beta_4^\dagger \beta_1 \beta_2 \right) \\ & + \tilde{\mathcal{V}}_{1234}^{(3:1)} \left(\alpha_1^\dagger \alpha_2^\dagger \alpha_4 \beta_3^\dagger + \alpha_3 \beta_4^\dagger \beta_1 \beta_2 \right) \\ & + \mathcal{V}_{1234}^{(3:1)} \left(\alpha_2^\dagger \beta_3^\dagger \beta_4^\dagger \beta_1 + \alpha_1^\dagger \alpha_3 \alpha_4 \beta_2 \right) \\ & \left. + \mathcal{V}_{1234}^{(4:0)} \left(\alpha_1^\dagger \alpha_2^\dagger \beta_3^\dagger \beta_4^\dagger + \alpha_3 \alpha_4 \beta_1 \beta_2 \right) \right] \end{aligned} \quad (5.71)$$

and in the Holstein-Primakoff formalism, the vertices \mathcal{V} are given by

$$\begin{aligned} \tilde{\mathcal{V}}_{1\alpha^+ 2\beta^- 3\alpha^- 4\beta^+}^{\text{HP}(2:2)} &= \Delta\gamma_{(2-4)} [u_1 u_2 u_3 u_4 + v_1 v_2 v_3 v_4] + \Delta\gamma_{(2-3)} [u_1 u_2 v_3 v_4 + u_3 u_4 v_1 v_2] \\ &\quad + \frac{1}{2} \left\{ \gamma_{(1)} [u_3 v_1 v_2 v_4 + u_1 u_2 u_4 v_3] + \gamma_{(2)} [u_1 u_2 u_3 v_4 + u_4 v_1 v_2 v_3] \right\} \\ &\quad + \frac{1}{2} \left\{ \gamma_{(3)} [u_2 u_3 u_4 v_1 + u_1 v_2 v_3 v_4] + \gamma_{(4)} [u_2 v_1 v_3 v_4 + u_1 u_3 u_4 v_2] \right\} \end{aligned} \quad (5.72a)$$

$$\begin{aligned} \mathcal{V}_{1\alpha^+ 2\alpha^+ 3\alpha^- 4\alpha^-}^{\text{HP}(2:2)} &= \Delta\gamma_{(2-4)} u_1 u_3 v_2 v_4 \\ &\quad + \frac{1}{4} \left[\gamma_{(2)} (u_2 v_1 v_3 v_4 + u_1 u_3 u_4 v_2) + \gamma_{(4)} (u_4 v_1 v_2 v_3 + u_1 u_2 u_3 v_4) \right] \end{aligned} \quad (5.72b)$$

$$\begin{aligned} \tilde{\mathcal{V}}_{1\alpha^+ 2\alpha^+ 3\beta^+ 4\alpha^-}^{\text{HP}(3:1)} &= \Delta\gamma_{(2-3)} [u_1 u_3 u_4 v_2 + u_2 v_1 v_3 v_4] \\ &\quad + \frac{1}{2} \left\{ \gamma_{(2)} [u_2 u_3 v_1 v_4 + u_1 u_4 v_2 v_3] \right\} \\ &\quad + \frac{1}{4} \left\{ \gamma_{(3)} [v_1 v_2 v_3 v_4 + u_1 u_2 u_3 u_4] + \gamma_{(4)} [u_3 u_4 v_1 v_2 + u_1 u_2 v_3 v_4] \right\} \end{aligned} \quad (5.72c)$$

$$\begin{aligned} \mathcal{V}_{1\alpha^+ 2\beta^- 3\alpha^- 4\alpha^-}^{\text{HP}(3:1)} &= \Delta\gamma_{(2-4)} [u_4 v_1 v_2 v_3 + u_1 u_2 u_3 v_4] \\ &\quad + \frac{1}{2} \left\{ \gamma_{(4)} [u_2 u_4 v_1 v_3 + u_1 u_3 v_2 v_4] \right\} \\ &\quad + \frac{1}{4} \left\{ \gamma_{(2)} [v_1 v_2 v_3 v_4 + u_1 u_2 u_3 u_4] + \gamma_{(1)} [u_1 u_2 v_3 v_4 + u_3 u_4 v_1 v_2] \right\} \end{aligned} \quad (5.72d)$$

$$\begin{aligned} \mathcal{V}_{1\alpha^+ 2\alpha^+ 3\beta^+ 4\beta^+}^{\text{HP}(4:0)} &= \Delta\gamma_{(2-4)} u_1 u_4 v_2 v_3 \\ &\quad + \frac{1}{4} \left[\gamma_{(2)} (u_1 v_2 v_3 v_4 + u_2 u_3 u_4 v_1) + \gamma_{(4)} (u_3 v_1 v_2 v_4 + u_1 u_2 u_4 v_3) \right] \end{aligned} \quad (5.72e)$$

while the vertices in the Dyson Maleev formalism yield

$$\begin{aligned} \tilde{\mathcal{V}}_{1\alpha^+ 2\beta^- 3\alpha^- 4\beta^+}^{\text{DM}(2:2)} &= \Delta\gamma_{(2-4)} (u_1 u_2 u_3 u_4 + v_1 v_2 v_3 v_4) + \Delta\gamma_{(2-3)} (u_1 u_2 v_3 v_4 + v_1 v_2 u_3 u_4) \\ &\quad + \gamma_{(2)} (u_1 u_2 u_3 v_4 + u_4 v_1 v_2 v_3) + \gamma_{(1)} (u_1 u_2 u_4 v_3 + u_3 v_1 v_2 v_4) \end{aligned} \quad (5.73a)$$

$$\mathcal{V}_{1\alpha^+ 2\alpha^+ 3\alpha^- 4\alpha^-}^{\text{DM}(2:2)} = \Delta\gamma_{(2-4)} u_1 u_3 v_2 v_4 + \frac{1}{2} \gamma_{(2)} [u_2 v_1 v_3 v_4 + u_1 u_3 u_4 v_2] \quad (5.73b)$$

$$\tilde{\mathcal{V}}_{1\alpha^+ 2\alpha^+ 3\beta^+ 4\alpha^-}^{\text{DM}(3:1)} = \Delta\gamma_{(2-3)} (u_1 u_3 u_4 v_2 + u_2 v_1 v_3 v_4) + \gamma_{(2)} (u_1 u_4 v_2 v_3 + u_2 u_3 v_1 v_4) \quad (5.73c)$$

$$\begin{aligned} \mathcal{V}_{1\alpha^+ 2\beta^- 3\alpha^- 4\alpha^-}^{\text{DM}(3:1)} &= \Delta\gamma_{(2-4)} (u_1 u_2 u_3 v_4 + u_4 v_1 v_2 v_3) \\ &\quad + \frac{1}{2} \left[\gamma_{(1)} (u_3 u_4 v_1 v_2 + u_1 u_2 v_3 v_4) + \gamma_{(2)} (v_1 v_2 v_3 v_4 + u_1 u_2 u_3 u_4) \right] \end{aligned} \quad (5.73d)$$

$$\mathcal{V}_{1\alpha^+ 2\alpha^+ 3\beta^+ 4\beta^+}^{\text{DM}(4:0)} = \Delta\gamma_{(2-4)} u_1 u_4 v_2 v_3 + \frac{1}{2} \gamma_{(2)} [u_1 v_2 v_3 v_4 + u_2 u_3 u_4 v_1] . \quad (5.73e)$$

All components \mathcal{P}^V used to construct these vertices, can be found in appendix A. At the quadratic level, α and β annihilate the ground state. This means that $\alpha^\dagger \alpha^\dagger \beta^\dagger \beta^\dagger$ is the only term that changes the ground state. The vertices in both formalisms are closely related by a symmetry transformation [103]. In particular, we find

$$\mathcal{V}_{\mathbf{k}_\alpha^+ 2\alpha^+ 3\alpha^- 4\alpha^-}^{(2:2)\text{HP}} = \frac{1}{2} \left(\mathcal{V}_{\mathbf{k}_\alpha^+ 2\alpha^+ 3\alpha^- 4\alpha^-}^{(2:2)\text{DM}} + \mathcal{V}_{3\alpha^+ 4\alpha^+ \mathbf{k}_\alpha^- 2\alpha^-}^{(2:2)\text{DM}} \right) \quad (5.74a)$$

$$\tilde{\mathcal{V}}_{1\alpha^+ 2\beta^- 3\alpha^- 4\beta^+}^{\text{HP}(2:2)} = \frac{1}{2} \left(\tilde{\mathcal{V}}_{1\alpha^+ 2\beta^- 3\alpha^- 4\beta^+}^{\text{DM}(2:2)} + \tilde{\mathcal{V}}_{3\alpha^+ 4\beta^- 1\alpha^- 2\beta^+}^{\text{DM}(2:2)} \right), \quad (5.74b)$$

which we use in the code presented in Sec. 5.4 to ensure that the vertices remain nonnegative, meaning that small deviations from an equilibrium state decay back into equilibrium and do not amplify.

5.1.5 The staggered magnetization

The staggered magnetization m is defined as the expectation value of the staggered magnetization operator [101] given by

$$m = \frac{1}{N} \sum_i \langle \Phi_{\text{GS}} | S_i^z | \Phi_{\text{GS}} \rangle \quad (5.75a)$$

$$S_{\text{stag}} = \sum_{i \in A} S_i^z - \sum_{j \in B} S_j^z. \quad (5.75b)$$

Writing this operator in terms of the Bogoliubov operators in Eq. (5.34) yields

$$\sum_{i \in A} S_i^z = \sum_i (S - a_i^\dagger a_i) \quad (5.76a)$$

$$= \frac{NS}{2} - \sum_{\mathbf{k} \in BZA} a_{\mathbf{k}}^\dagger a_{\mathbf{k}} \quad (5.76b)$$

$$= \frac{NS}{2} - \sum_{\mathbf{k} \in BZA} \left[v_{\mathbf{k}}^2 + u_{\mathbf{k}}^2 \alpha_{\mathbf{k}}^\dagger \alpha_{\mathbf{k}} + v_{\mathbf{k}}^2 \beta_{\mathbf{k}}^\dagger \beta_{\mathbf{k}} + u_{\mathbf{k}} v_{\mathbf{k}} (\alpha_{\mathbf{k}}^\dagger \beta_{\mathbf{k}}^\dagger + \alpha_{\mathbf{k}} \beta_{\mathbf{k}}) \right], \quad (5.76c)$$

and, following the same steps,

$$- \sum_{j \in B} S_j^z = \frac{NS}{2} - \sum_{\mathbf{k} \in BZB} \left[v_{\mathbf{k}}^2 + v_{\mathbf{k}}^2 \alpha_{\mathbf{k}}^\dagger \alpha_{\mathbf{k}} + u_{\mathbf{k}}^2 \beta_{\mathbf{k}}^\dagger \beta_{\mathbf{k}} + u_{\mathbf{k}} v_{\mathbf{k}} (\alpha_{\mathbf{k}}^\dagger \beta_{\mathbf{k}}^\dagger + \alpha_{\mathbf{k}} \beta_{\mathbf{k}}) \right]. \quad (5.77)$$

We can now write the staggered magnetization operator as

$$S_{\text{stag}} = NS - \sum_{\mathbf{k} \in BZA} \left[2v_{\mathbf{k}}^2 + (v_{\mathbf{k}}^2 + u_{\mathbf{k}}^2) (\alpha_{\mathbf{k}}^\dagger \alpha_{\mathbf{k}} + \beta_{\mathbf{k}}^\dagger \beta_{\mathbf{k}}) + 2u_{\mathbf{k}} v_{\mathbf{k}} (\alpha_{\mathbf{k}}^\dagger \beta_{\mathbf{k}}^\dagger + \alpha_{\mathbf{k}} \beta_{\mathbf{k}}) \right]. \quad (5.78)$$

In order to compute the staggered magnetization we recall that $\langle \Phi_{\text{GS}} | \alpha_{\mathbf{k}}^\dagger \beta_{\mathbf{k}}^\dagger | \Phi_{\text{GS}} \rangle = 0$ and $\langle \Phi_{\text{GS}} | \alpha_{\mathbf{k}} \beta_{\mathbf{k}} | \Phi_{\text{GS}} \rangle = 0$, as well as that the expectation values of the occupation operators $\alpha_{\mathbf{k}}^\dagger \alpha_{\mathbf{k}}$ and $\beta_{\mathbf{k}}^\dagger \beta_{\mathbf{k}}$ at a given temperature T are given by

$$\langle \Phi_{\text{GS}} | \alpha_{\mathbf{k}}^\dagger \alpha_{\mathbf{k}} | \Phi_{\text{GS}} \rangle = \langle \Phi_{\text{GS}} | \beta_{\mathbf{k}}^\dagger \beta_{\mathbf{k}} | \Phi_{\text{GS}} \rangle = n_T(\mathbf{k}), \quad (5.79)$$

where $n(T, \mathbf{k})$ is a thermal distribution with

$$n_T(\mathbf{k}) = \frac{1}{\exp\left[\frac{\omega_{\mathbf{k}}}{T}\right] - 1}. \quad (5.80)$$

We will from now on refer to Eq. 5.80 as *thermal distribution*, assuming there is no chemical potential μ . For $\mu \neq 0$ we will specify the chemical potential separately. Now we can write the staggered magnetization as

$$m(T) = S - \frac{2}{N} \sum_{\mathbf{k} \in BZA} \left[v_{\mathbf{k}}^2 + (v_{\mathbf{k}}^2 + u_{\mathbf{k}}^2) n_T(\mathbf{k}) \right] \quad (5.81)$$

and recall that we can write the Bogoliubov operators as functions of the magnon mode energy $\omega_{\mathbf{k}}$, namely

$$v_{\mathbf{k}}^2 = \frac{1}{2} \left(\frac{\Delta}{\lambda_{\mathbf{k}}} - 1 \right) = \frac{1}{2} \left(\frac{\omega_{\max}}{\omega_{\mathbf{k}}} - 1 \right) \quad (5.82a)$$

$$u_{\mathbf{k}}^2 + v_{\mathbf{k}}^2 = \frac{\Delta}{\lambda_{\mathbf{k}}} = \frac{\omega_{\max}}{\omega_{\mathbf{k}}}. \quad (5.82b)$$

With this, we obtain

$$m(T) = S - \frac{2}{N} \sum_{\mathbf{k} \in BZA} \left\{ \frac{1}{2} \left(\frac{\omega_{\max}}{\omega_{\mathbf{k}}} - 1 \right) + \left[\left(\frac{\omega_{\max}}{\omega_{\mathbf{k}}} \right) n_T(\mathbf{k}) \right] \right\} \quad (5.83a)$$

$$= \left(S + \frac{1}{2} \right) - \frac{2}{N} \sum_{\mathbf{k} \in BZA} \left\{ \frac{1}{2} \left(\frac{\omega_{\max}}{\omega_{\mathbf{k}}} \right) + \left[\left(\frac{\omega_{\max}}{\omega_{\mathbf{k}}} \right) n_T(\mathbf{k}) \right] \right\} \quad (5.83b)$$

$$= \left(S + \frac{1}{2} \right) - \frac{2\omega_{\max}}{N} \sum_{\mathbf{k} \in BZA} \left\{ \frac{1}{\omega_{\mathbf{k}}} \left[n_T(\mathbf{k}) + \frac{1}{2} \right] \right\}. \quad (5.83c)$$

The numerical value for a thermal distribution with $S = 1/2$, $\Delta = 1$ and $T = 0$ is $m = 0.303398$. Note that for sufficiently small spin S the staggered magnetization mathematically becomes negative. The physical interpretation behind this is that quantum and thermal fluctuations increase for shorter spin length and are eventually large enough to destabilize the ordered state. At this point there is no long range order, so the definition of the staggered magnetization in the magnon picture becomes invalid. We can use the density of states summed over the two magnon branches, namely

$$\rho(\omega) = 2 \int d^2k \delta(\omega - \omega_{\mathbf{k}}). \quad (5.84)$$

and the distribution function of energy ω , which is given by

$$n(\omega) = \int d^2k n_{\mathbf{k}} \delta(\omega - \omega_{\mathbf{k}}) / \rho(\omega) \quad (5.85)$$

to write the staggered magnetization as

$$m(S, n(\omega)) = S + \frac{1}{2} - \omega_{\max} \sum_{m=1}^{\omega_{\max}} \frac{\rho(\omega_m)}{\omega_m} \left(n(\omega_m) + \frac{1}{2} \right), \quad (5.86)$$

where $n(\omega)$ is not restricted to the subspace of thermal distributions.

5.2 The Boltzmann formalism

We use the interaction vertices \mathcal{V} , which are derived in Sec. 5.1.4 in a semiclassical Boltzmann approach. The distribution of magnons in a branch α at a given momentum \mathbf{k} is given by

$$\frac{dn^\alpha(\mathbf{k})}{dt} = 2\pi \left(\frac{2Jz}{N} \right)^2 \left(\tilde{\mathcal{S}}_\alpha^{(2:2)}(\mathbf{k}) + \mathcal{S}_\alpha^{(2:2)}(\mathbf{k}) + \tilde{\mathcal{S}}_\alpha^{(3:1)}(\mathbf{k}) + \mathcal{S}_\alpha^{(3:1)}(\mathbf{k}) + \mathcal{S}_\alpha^{(4:0)}(\mathbf{k}) \right), \quad (5.87)$$

where the scattering integrals \mathcal{S} are corresponding to the self energy diagrams of the different scattering processes. In particular, the vertices for processes in which two magnons scatter into

5 Nonequilibrium phase transition

two other magnons are given by

$$\begin{aligned} \mathcal{V}^{(2:2)} = & -\frac{2Jz}{N} \sum_{\mathbf{k}_1 \mathbf{k}_2 \mathbf{k}_3 \mathbf{k}_4} \delta(\mathbf{k}_1 + \mathbf{k}_2 - \mathbf{k}_3 - \mathbf{k}_4) \times \left[\tilde{\mathcal{V}}_{1_\alpha^+ 2_\beta^- 3_\alpha^- 4_\beta^+}^{(2:2)} \alpha_1^\dagger \alpha_3 \beta_4^\dagger \beta_2 \right] \\ & -\frac{2Jz}{N} \sum_{\mathbf{k}_1 \mathbf{k}_2 \mathbf{k}_3 \mathbf{k}_4} \delta(\mathbf{k}_1 + \mathbf{k}_2 - \mathbf{k}_3 - \mathbf{k}_4) \times \left[\mathcal{V}_{1_\alpha^+ 2_\alpha^+ 3_\alpha^- 4_\alpha^-}^{(2:2)} \alpha_1^\dagger \alpha_2^\dagger \alpha_3 \alpha_4 + \mathcal{V}_{1_\beta^- 2_\beta^- 3_\beta^+ 4_\beta^+}^{(2:2)} \beta_3^\dagger \beta_4^\dagger \beta_1 \beta_2 \right] \end{aligned} \quad (5.88)$$

and the corresponding α -scattering integrals are

$$\begin{aligned} \tilde{\mathcal{S}}_\alpha^{(2:2)}(\mathbf{k}) = & \sum_{\mathbf{k}_2 \mathbf{k}_3 \mathbf{k}_4} \delta_{\mathbf{k} + \mathbf{k}_2 - \mathbf{k}_3 - \mathbf{k}_4} \delta(\omega_{\mathbf{k}} + \omega_{\mathbf{k}_2} - \omega_{\mathbf{k}_3} - \omega_{\mathbf{k}_4}) \tilde{\mathcal{V}}_{\mathbf{k}_\alpha^+ 4_\beta^- 3_\alpha^- 2_\beta^+}^{(2:2)} \tilde{\mathcal{V}}_{3_\alpha^+ 2_\beta^- \mathbf{k}_\alpha^- 4_\beta^+}^{(2:2)} \times \\ & \left[(1 + n_{\mathbf{k}}^\alpha) (1 + n_{\mathbf{k}_2}^\beta) n_{\mathbf{k}_3}^\alpha n_{\mathbf{k}_4}^\beta - (1 + n_{\mathbf{k}_3}^\alpha) (1 + n_{\mathbf{k}_4}^\beta) n_{\mathbf{k}}^\alpha n_{\mathbf{k}_2}^\beta \right], \end{aligned} \quad (5.89)$$

where both magnon branches are involved in the scattering process, and

$$\begin{aligned} \mathcal{S}_\alpha^{(2:2)}(\mathbf{k}) = & \sum_{\mathbf{k}_2 \mathbf{k}_3 \mathbf{k}_4} \delta_{\mathbf{k} + \mathbf{k}_2 - \mathbf{k}_3 - \mathbf{k}_4} \delta(\omega_{\mathbf{k}_1} + \omega_{\mathbf{k}_2} - \omega_{\mathbf{k}} - \omega_{\mathbf{k}_4}) \mathcal{V}_{\mathbf{k}_\alpha^+ 2_\alpha^+ 3_\alpha^- 4_\alpha^-}^{(2:2)} \mathcal{V}_{3_\alpha^+ 4_\alpha^+ \mathbf{k}_\alpha^- 2_\alpha^-}^{(2:2)} \times \\ & \left[(1 + n_{\mathbf{k}}^\alpha) (1 + n_{\mathbf{k}_2}^\alpha) n_{\mathbf{k}_3}^\alpha n_{\mathbf{k}_4}^\alpha - n_{\mathbf{k}}^\alpha n_{\mathbf{k}_2}^\alpha (1 + n_{\mathbf{k}_3}^\alpha) (1 + n_{\mathbf{k}_4}^\alpha) \right], \end{aligned} \quad (5.90)$$

where the scattering consists of α magnons only. The β scattering integrals can be written down analogously. All processes in the system can be visualized using self energy diagrams, the diagrams corresponding to Eq. (5.89) and Eq. (5.90) are displayed in Fig. 5.3.

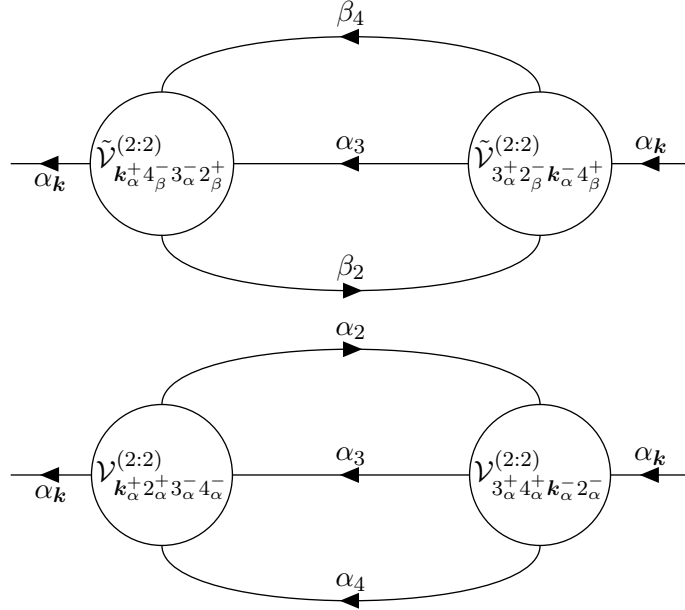


Figure 5.3: Self energy diagrams corresponding to Eq. (5.89) (above) and Eq.(5.90) (below).

Note that the difference of the occupations ensures that any thermal distribution, even with a possible chemical potential μ , which is given by

$$n(\mathbf{k}, \mu) = \frac{1}{\exp\left[\frac{\omega_{\mathbf{k}} - \mu}{T}\right] - 1}, \quad (5.91)$$

stays constant in time, meaning the thermal distribution is a steady state of the system with-

out drive and dissipation. This is because the delta function of the energies ensures that ($\omega_{\mathbf{k}_1} + \omega_{\mathbf{k}_2} = \omega_{\mathbf{k}_3} + \omega_{\mathbf{k}_4}$). At this point we find the Holstein-Primakoff model advantageous, since the hermitian nature of the Hamiltonian ensures that

$$\mathcal{V}_{\mathbf{k}_\alpha^+ 2_\alpha^+ 3_\alpha^- 4_\alpha^-}^{\text{HP}(2:2)} \times \mathcal{V}_{3_\alpha^+ 4_\alpha^+ \mathbf{k}_\alpha^- 2_\alpha^-}^{\text{HP}(2:2)} = \left(\mathcal{V}_{\mathbf{k}_\alpha^+ 2_\alpha^+ 3_\alpha^- 4_\alpha^-}^{\text{HP}(2:2)} \right)^2 \quad (5.92a)$$

$$\tilde{\mathcal{V}}_{1_\alpha^+ 2_\beta^- 3_\alpha^- 4_\beta^+}^{\text{HP}(2:2)} \times \tilde{\mathcal{V}}_{3_\alpha^+ 4_\beta^- 1_\alpha^- 2_\beta^+}^{\text{HP}(2:2)} = \left(\tilde{\mathcal{V}}_{1_\alpha^+ 2_\beta^- 3_\alpha^- 4_\beta^+}^{\text{HP}(2:2)} \right)^2, \quad (5.92b)$$

meaning that the vertex products are inherently nonnegative. This is in general not the case for the Dyson-Maleev vertex products, which may lead to an amplification of small deviations from the equilibrium distribution.

Analogously we can write down scattering integrals for processes where three magnons scatter into one magnon, like for example

$$\mathcal{S}_{\alpha\alpha\alpha\beta}^{(3:1)} = \sum_{\mathbf{k}_1 \mathbf{k}_2 \mathbf{k}_4} \delta_{\mathbf{k}_1 + \mathbf{k}_2 - \mathbf{k} - \mathbf{k}_4} \delta(\omega_{\mathbf{k}_1} - \omega_{\mathbf{k}_2} - \omega_{\mathbf{k}} - \omega_{\mathbf{k}_4}) \tilde{\mathcal{V}}_{\mathbf{k}_\alpha^+ 4_\alpha^+ 2_\beta^+ 1_\alpha^-}^{3:1} \mathcal{V}_{1_\alpha^+ 2_\beta^- \mathbf{k}_\alpha^- 4_\alpha^-}^{3:1} \times \quad (5.93)$$

$$\left[(1 + n_{\mathbf{k}}^\alpha) (1 + n_{\mathbf{k}_2}^\beta) (1 + n_{\mathbf{k}_4}^\alpha) n_{\mathbf{k}_1}^\alpha - (1 + n_{\mathbf{k}_1}^\alpha) n_{\mathbf{k}}^\alpha n_{\mathbf{k}_2}^\beta n_{\mathbf{k}_4}^\alpha \right].$$

However, we find that for an evenly spaced momentum grid which avoids the $\mathbf{k} = 0$ point, these integrals do not contribute to Eq.(5.87) because the two delta-functions $\delta(\omega_{\mathbf{k}_1} - \omega_{\mathbf{k}_2} - \omega_{\mathbf{k}_3} - \omega_{\mathbf{k}_4})$ and $\delta_{\mathbf{k}_1 + \mathbf{k}_2 - \mathbf{k}_3 - \mathbf{k}_4}$ are never satisfied at the same time. This is easy to show mathematically in the isotropic case, because we know that for small \mathbf{k} -vectors, the energy is proportional to the magnitude of the momentum vector so

$$\omega(\mathbf{k}_i) \sim v |\mathbf{k}_i| \quad \forall \quad |\mathbf{k}_i| \ll \pi \quad (5.94)$$

which means that

$$\omega_{\mathbf{k}_1} = \omega_{\mathbf{k}_2} - \omega_{\mathbf{k}} - \omega_{\mathbf{k}_4} \quad \Rightarrow \quad |\mathbf{k}_1| \approx |\mathbf{k}_2| + |\mathbf{k}_3| + |\mathbf{k}_4|. \quad (5.95)$$

Given that we know $\mathbf{k}_4 = \mathbf{k}_1 + \mathbf{k}_2 - \mathbf{k}_3$ from momentum conservation, the delta functions only

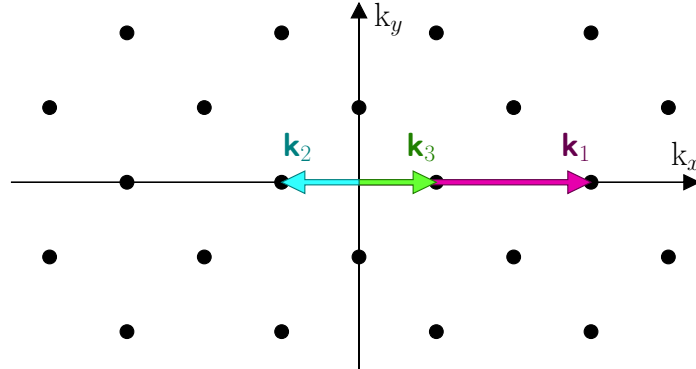


Figure 5.4: Schematic illustration of the momentum points in a subsection of the magnetic Brillouin zone around $\mathbf{k} = 0$. The three highlighted vectors are the smallest three vectors that fulfill $|\mathbf{k}_1| - |\mathbf{k}_2| - |\mathbf{k}_3| \approx |\mathbf{k}_1 + \mathbf{k}_2 - \mathbf{k}_3|$.

contribute at

$$|\mathbf{k}_1| \approx |\mathbf{k}_2| + |\mathbf{k}_3| + |\mathbf{k}_1 + \mathbf{k}_2 - \mathbf{k}_3| \quad (5.96a)$$

$$|\mathbf{k}_1| - |\mathbf{k}_2| - |\mathbf{k}_3| \approx |\mathbf{k}_1 + \mathbf{k}_2 - \mathbf{k}_3|. \quad (5.96b)$$

Using the uniformly distributed momentum points described in detail in publication [II](#) and partially shown in Fig. 5.4, we know that the smallest three vectors that fulfill this requirement satisfy

$$\mathbf{k}_1 = 3\mathbf{k}_4 \quad (5.97a)$$

$$\mathbf{k}_2 = -\mathbf{k}_4 \quad (5.97b)$$

$$\mathbf{k}_3 = \mathbf{k}_4 \quad (5.97c)$$

and that the deviation from zero of the argument of the energy delta function becomes larger as the magnitude of the vectors gets larger. So no matter how dense the \mathbf{k} -points are distributed, there is a deviation from zero as long as none of the \mathbf{k} -vectors is the null-vector. From Eq. (5.97) we also know that $\omega_2 = \omega_3 = \omega_4$, so the minimal energy in this finite grid is given by

$$\min(|\omega_{\mathbf{k}_1} - \omega_{\mathbf{k}_2} - \omega_{\mathbf{k}_3} - \omega_{\mathbf{k}_4}|) = |\omega_{\mathbf{k}_1} - 3\omega_{\mathbf{k}_2}| \quad \text{if } \mathbf{k}_4 \stackrel{!}{=} \mathbf{k}_1 + \mathbf{k}_2 - \mathbf{k}_3. \quad (5.98)$$

While the Taylor expansion in Eq. (5.94) is not accurate in case of a system with an anisotropy, where a gap opens for small momentum vectors, we find numerically that the scattering of three magnons into one magnon is kinetically forbidden for all $\Delta \geq 1$.

5.3 The noninteracting steady state and the time evolution

In order to study how the magnon interactions derived in the previous chapter influence the nonequilibrium steady states in a driven-dissipative system, we start from the results of a previous theoretical analysis of a half-filled large U Hubbard model coupled to a high frequency, off-resonant drive and a dissipative reservoir at zero temperature [68]. This analysis largely neglects magnon-magnon scattering and finds a steady state system which can be understood in terms of the differential equation

$$\partial_t n(\omega) = \gamma_{\text{in}}(1 + n(\omega)) - \gamma_{\text{out}} \left(n(\omega) + \left[\frac{n(\omega)}{n_{\tilde{T}}(\omega)} \right]^2 \right), \quad (5.99)$$

where $n_{\tilde{T}}(\omega)$ is a thermal distribution at temperature \tilde{T} without a chemical potential, as given in Eq. (5.80). In this notation, γ_{in} is proportional to the drive strength and γ_{out} regulates how magnons dissipate into the bath. The term describing the relaxation of magnons into the bath has a nonlinearity in order to allow for the formation of a steady state. This means magnons are created equally at all energies, but dissipate in an energy-dependent way where the dissipation is faster at low energies. Equation (5.99) obtains steady states that can be characterized by a dimensionless tuning parameter g , which is the ratio of in and out scattering, namely

$$g = \frac{\gamma_{\text{in}}}{\gamma_{\text{out}}}. \quad (5.100)$$

The analytic form of the steady states is given by

$$n(g, n_{\bar{T}}) = \frac{n_{\bar{T}}^2}{2} \cdot \left(g - 1 \pm \sqrt{(g-1)^2 + \frac{4g}{n_{\bar{T}}^2}} \right), \quad (5.101)$$

where only the + solution gives the desired physical result, which is displayed in Fig. 5.5 and reproduces all features from the noninteracting result. At $g = 1$, meaning $\gamma_{\text{in}} = \gamma_{\text{out}}$, the solution is $n(g, n_{\bar{T}}) = n_{\bar{T}}$, meaning a thermal distribution that diverges like $1/\omega$ as $\omega \rightarrow 0$. For weak and intermediate driving ($g < 1$, blue) the magnon modes at larger mode energies are not occupied and they go to a finite value as $\omega \rightarrow 0$. However, the distribution of spin waves diverges even faster than the thermal distribution when the drive is dominating ($g > 1$, red), so in this case the noninteracting theory predicts nonthermal, in fact superthermal magnons. We take this drive and dissipation and include it in our interacting Boltzmann simulation in order to study how this changes the noninteracting theory. In particular, we are interested in whether the redistribution of energy due to magnon interactions transfers the magnon occupation to energies where dissipation is faster and therefore changes the theory.

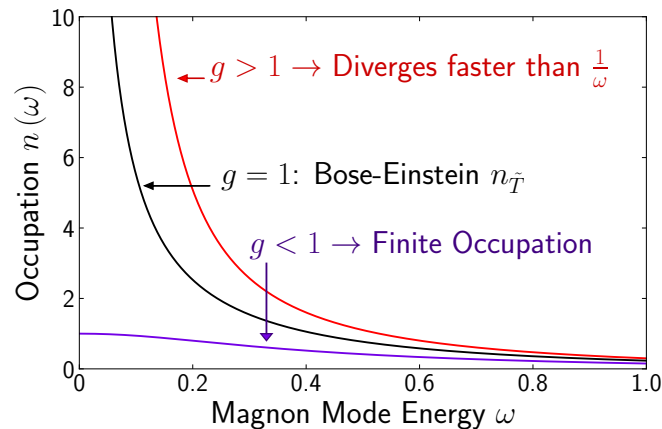


Figure 5.5: The steady states of the noninteracting analysis. At $g < 1$ the distribution of spin waves is finite for all ω , at $g = 1$ the distribution is thermal and therefore diverges like $1/\omega$ and at $g > 1$ the distribution diverges faster than $1/\omega$.

5.4 Computational remarks

Implementing the Boltzmann simulation for interacting magnons posed various computational challenges, and we describe our solutions to these in detail in the appendix of publication II. In particular, we need to avoid the $\mathbf{k} = 0$ momentum point because a Bose-Einstein distribution without a chemical potential diverges at the center of the Brillouin zone and can therefore not be treated numerically. Furthermore, we need to numerically ensure momentum and energy conservation at the same time over comparatively large timescales, and we found that a broadening of one of the delta functions in the scattering integrals \mathcal{S} leads to an accumulation of errors such that one of the quantities is not conserved. In order to avoid this, we map a uniformly distributed momentum grid onto an energy grid which is uniformly distributed as well. The full code is available at <https://github.com/MonaHKa/Boltzmann-simulation>

Nonequilibrium phase transition in a driven-dissipative quantum antiferromagnet

Mona H. Kalthoff,^{1,*} Dante M. Kennes,^{2,1,†} Andrew J. Millis,^{3,4,‡} and Michael A. Sentef^{1,§}

¹Max Planck Institute for the Structure and Dynamics of Matter, Center for Free Electron Laser Science (CFEL), Luruper Chaussee 149, 22761 Hamburg, Germany

²Institut für Theorie der Statistischen Physik, RWTH Aachen University, 52056 Aachen, Germany and JARA-Fundamentals of Future Information Technology, 52056 Aachen, Germany

³Department of Physics, Columbia University, 538 West 120th Street, New York, New York 10027, USA

⁴Center for Computational Quantum Physics, Flatiron Institute, 162 5th Avenue, New York, New York 10010, USA

(Dated: April 20, 2022)

A deeper theoretical understanding of driven-dissipative interacting systems and their nonequilibrium phase transitions is essential both to advance our fundamental physics understanding and to harness technological opportunities arising from optically controlled quantum many-body states. This paper provides a numerical study of dynamical phases and the transitions between them in the nonequilibrium steady state of the prototypical two-dimensional Heisenberg antiferromagnet with drive and dissipation. We demonstrate a nonthermal transition that is characterized by a qualitative change in the magnon distribution, from subthermal at low drive to a generalized Bose-Einstein form including a nonvanishing condensate fraction at high drive. A finite-size analysis reveals static and dynamical critical scaling at the transition, with a discontinuous slope of the magnon number versus driving field strength and critical slowing down at the transition point. Implications for experiments on quantum materials and polariton condensates are discussed.

I. INTRODUCTION

Nonequilibrium phase transitions in driven interacting quantum systems constitute a fundamental and largely open research problem^{1,2}. *Quenches*, i.e., abrupt changes in Hamiltonian parameters or initial conditions, followed by a time evolution, have been extensively studied and can lead to dynamical phase transitions^{3,4} characterized by qualitative modifications of the dynamical response as the quench magnitude is varied. A nonequilibrium steady state presents additional issues involving the flow and redistribution of energy: the drive adds energy, the dissipation removes energy, and the internal dynamics redistribute energy among modes^{5,6}. As the drive strength is varied, the competition between these effects can qualitatively change system properties in the same sense that changing temperature or a Hamiltonian parameter can drive a system through an equilibrium phase transition.

Equilibrium phase transitions are typically analyzed in terms of the onset or disappearance of order parameters that encode broken symmetries, for example, the staggered magnetization in an antiferromagnet that appears when the temperature is reduced below a critical temperature. We label such phase transitions as symmetry breaking transition in the following. In a nonequilibrium setting, an additional type of phase transition can exist that is characterized by a qualitative change in the low-frequency distribution of the collective excitations of a system. Such a transition cannot exist in equilibrium where the form of the distribution is fixed by equilibrium thermodynamics. We refer to the latter as a subthermal-to-superthermal transition. Phase transitions occurring in a nonequilibrium *steady state* are the subject of an interesting and growing literature⁷⁻¹⁵ but are less well understood. A deeper theoretical understanding of these

issues could open nonthermal pathways for controlling emergent properties of driven quantum materials².

Driven magnetic systems are of particular interest in this context, for both fundamental and technological reasons¹⁶. A specific focus of attention has been the possibility of magnon Bose-Einstein condensation (BEC), in which a system is excited by a radiation pulse and the resulting excitation distribution forms a single coherent macroscopic quantum state with the lowest energy excited state being macroscopically populated. The existing experimental literature on magnon BEC¹⁷⁻³² concerns systems with very long energy relaxation times, where a population of magnons is transiently induced (often by a short duration frequency-coherent excitation) and then evolves into a BEC^{16,33-35}. This physics is very similar to the Bose-Einstein condensation of excitons and exciton-polaritons which has been studied experimentally³⁶⁻⁴⁰ and theoretically⁴¹⁻⁴³. Theoretical analyses of the magnon case to date have been based on semi-phenomenological continuum approximations using Landau-Lifshitz-Gilbert equations^{44,45}, Gross-Pitaevskii equations^{18,26,27} or field theoretical analyses^{8,10,12-15,42,43}. Here, we focus on the distribution function of excitations.

In this work we aim to add a new dimension to the understanding of this field. We study a steady state system in which the crucial physics is the interplay of interactions and the flow of energy and particles from the drive through the system to a dissipative reservoir. We provide a precise microscopic treatment of the interaction among excitations, which is known^{35,46-57} to be crucial for the long time physics. Fig. 1 shows the behavior of the spin system under consideration as a function of the critical parameter g , which parametrizes the nonequilibrium excitation strength relative to dissipative losses and will be

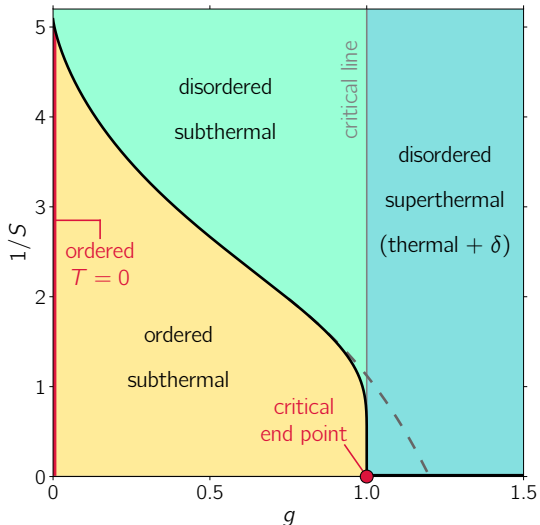


FIG. 1. **Nonequilibrium phase diagram of driven dissipative steady states.** Steady states as a function of drive strength g and quantum fluctuations, parametrized here by the inverse spin length $1/S$, but controlled in physical systems by many factors, including geometrical frustration. The red section along the vertical axis marks the antiferromagnetically ordered ground state at $T = 0$. The black curve separating the ordered (orange) from the disordered (green) subthermal phase is obtained by determining the value of $1/S$ at which the staggered magnetization (as defined in Eq. (A10)) vanishes for a given g . The grey vertical line at $g = 1$ separates the subthermal from the superthermal regime, which turns into a thermal distribution plus a δ function in the interacting system in the thermodynamic limit. The critical end point at $g = 1$, $1/S = 0$ is a specific feature of the Heisenberg antiferromagnet in two dimensions. The grey dashed curve indicates the expected behavior in three dimensions, or in the anisotropic xy or xzx (Ising, gapped) regimes in two dimensions.

introduced in more detail below. The figure displays two distinct phase transitions, namely an order-to-disorder phase transition, which is conceptually similar to known equilibrium transitions but occurs here for nonthermal distributions, and an intrinsically nonequilibrium subthermal to superthermal transition, which we study in this paper. This new phase transition is characterized by a qualitative change in the distribution function.

II. MODEL AND FORMALISM

A. Hamiltonian and kinetic equation

We study the driven-dissipative square-lattice Heisenberg antiferromagnet with nearest neighbor interactions,

described by the Hamiltonian

$$H_{Heis} = J \sum_{\langle ij \rangle} \left\{ \frac{1}{2} (S_i^+ S_j^- + S_i^- S_j^+) + S_i^z S_j^z \right\}, \quad (1)$$

with canonical spin operators \mathbf{S}_i at site i of the lattice. The Heisenberg Hamiltonian has two parameters, the exchange coupling strength J , which sets the energy scale and which we take to be positive so that the ground state is antiferromagnetic, and the spin magnitude $|S|$ which sets the strength of the quantum fluctuations and of the interactions between the spin waves. At $|S| = \infty$ the model is straightforwardly solvable and has a two-fold degenerate set of spin wave excitations (magnons) with dispersion $\omega_{\mathbf{k}}$. The primary object of interest will be the magnon distribution function $n_{\mathbf{k}}$ counting the number of magnons excited above the ground state into the mode with energy $\omega_{\mathbf{k}}$. Key to our analysis will be the interactions between magnons. Because we are interested in the qualitative effects of the interactions we use a standard Holstein-Primakoff method⁵⁸ to obtain the spin-wave interactions at leading nontrivial order in $1/|S|$ (See appendix A). The important points here are that the inter-spin-wave interactions conserve both total energy and the total number of spin waves and that their effect on the distribution may be studied using the Boltzmann equation with a collision integral \mathcal{S} derived via standard methods from the magnon-magnon interactions.

The Heisenberg model is an effective model describing the low energy physics of a more fundamental system of strongly correlated electrons moving in a periodic lattice potential such as the Hubbard model. These more fundamental models enable a calculation of the drive due to electromagnetic radiation and dissipation due to coupling with a reservoir. We specifically adopt the model studied in Ref. 59 in which the Heisenberg model is obtained as the low-energy limit of the half-filled large U Hubbard model. The drive emerges from a Floquet analysis of minimally coupled high frequency radiation detuned from the upper Hubbard band. The dissipation results from particle exchange with a reservoir, which we take to be at zero temperature. The particle exchange is virtual because of the Mott-Hubbard gap, but dissipation of energy and magnons into the reservoir are allowed.

Since we consider only a spatially uniform drive, we restrict our attention to a distribution function of energy ω (instead of momentum \mathbf{k}) defined⁶⁰ as $n(\omega) = \int d^2k n_{\mathbf{k}} \delta(\omega - \omega_{\mathbf{k}}) / \rho(\omega)$ with $\omega_{\mathbf{k}}$ the magnon energy and $n_{\mathbf{k}}$ the magnon distribution as a function of wavevector. The density of states summed over the two magnon branches is

$$\rho(\omega) = 2 \int d^2k \delta(\omega - \omega_{\mathbf{k}}). \quad (2)$$

We take the drive and dissipation from a previous analysis⁵⁹ of the driven-dissipative Hubbard model, specializing to the particular case of a high-frequency drive detuned from any charge excitations, and a dissipation

arising from particle exchange with a reservoir. Reference⁵⁹ found, using an approximation that neglected the magnon-magnon interactions, that the effect of a high frequency detuned drive is the addition of magnons to the system, such that the number of magnons in the mode with energy ω increases at the rate $\gamma_{\text{in}}(1+n(\omega))$. γ_{in} is proportional to the drive strength and the simple form of the in-scattering follows from the very high frequency, detuned drive. The calculation also implies a decay of magnons into the charge reservoir at a rate given by $\gamma_{\text{out}} \left(n(\omega) + \left(\frac{n(\omega)}{n_{\tilde{T}}(\omega)} \right)^2 \right)$ with $n_{\tilde{T}}(\omega) = 1/(e^{\frac{\omega}{\tilde{T}}} - 1)$ and parameters $\tilde{T} \approx 0.6J$. Note that \tilde{T} from Eq. (3) is not the equilibrium temperature of the system, but is a parameter describing the nonlinearity of the relaxation to the bath. The nonlinearity ensures a steady state at any drive amplitude. The key features of the out scattering are that the basic rate is determined by the particle-reservoir coupling and that the nonlinearity vanishes quadratically as $\omega_k \rightarrow 0$. The latter feature stems from the large charge gap and the vanishing of the charge-magnon coupling at low energies due to the Goldstone theorem.

This allows us to write down a kinetic equation that encodes magnon-magnon scattering through the collision integral \mathcal{S} as well as the effects of drive and dissipation

$$\partial_t n(\omega) = \gamma_{\text{in}}(1+n(\omega)) - \gamma_{\text{out}} \left(n(\omega) + \left(\frac{n(\omega)}{n_{\tilde{T}}(\omega)} \right)^2 \right) + \mathcal{S}[\{n(\omega)\}]. \quad (3)$$

B. Numerical implementation

We discretize the system and solve the resulting set of coupled nonlinear equations numerically by integrating forward in time from an initial condition until a steady state is reached. We choose a uniform $\ell \times \ell$ momentum space grid containing $N = \ell^2$ points shown in appendix D and therefore a discrete set of momentum points $\omega_{\mathbf{k}}$. We replace all momentum/frequency integrals by sums. The largest linear dimension ℓ used throughout the paper is $\ell = 120$, which is the default discretization parameter for the results shown below, unless otherwise indicated. The discretized momentum grid is chosen in a way such that $\mathbf{k} = 0$ is avoided because a Bose-Einstein distribution with $\mu = 0$ diverges as $\mathbf{k} \rightarrow 0$, implying that $\mathbf{k} = 0$ cannot be treated directly numerically (see appendix D, Figure 7). Below we employ a careful finite-size scaling analysis and extrapolation to infinite system size to extract information about $\mathbf{k} \rightarrow 0$ and possible Bose-Einstein condensation. In the numerical results presented here we fix the parameter \tilde{T} describing the nonlinear term in the dissipation to be $\tilde{T} = 0.6$ and set $\gamma_{\text{out}} = 0.002$, unless explicitly denoted otherwise. Our conclusions are independent of the specific parameter values.

As noted above, the collision integral \mathcal{S} conserves the

magnon number \mathcal{N} and energy \mathcal{E} which are discretized as

$$\mathcal{N} = \sum_{m=1}^{\omega_{\text{max}}} \rho(\omega_m) n(\omega_m) \quad (4a)$$

$$\mathcal{E} = \sum_{m=1}^{\omega_{\text{max}}} \rho(\omega_m) n(\omega_m) \omega_m, \quad (4b)$$

where $\rho(\omega_m)$ is the discretization of the density of states given in Eq. (2). We parametrize the drive strength via the dimensionless tuning parameter, that controls the excitation density,

$$g \equiv \frac{\gamma_{\text{in}}}{\gamma_{\text{out}}}, \quad (5)$$

and consider the qualitative form of the computed magnon distribution function.

III. RESULTS

A. Nonequilibrium phase diagram

Fig. 1 summarizes our findings in terms of a phase diagram in the plane defined by the amplitude of quantum fluctuations (inverse spin length $1/S$, vertical axis) and the drive strength (g , horizontal axis). In equilibrium ($g = 0$), increasing quantum fluctuations drives a transition to a quantum disordered state. Increasing the drive strength at a fixed value of quantum fluctuations produces two conceptually distinct effects.

The drive adds energy to the system, exciting magnons above the ground state and thereby weakening the order. For drive strengths less than a critical value (here, $g = 1$) the magnon distribution retains a subthermal form, with the magnon occupation $n(\omega)$ remaining finite as the magnon energy ω vanishes, in contrast to the $\sim T/\omega$ behavior of the thermal distribution. Although the distribution is subthermal, the increase in magnon number may be sufficient to drive the system into a disordered state, as indicated by the phase boundary in Fig. 1. This symmetry breaking phase transition is a nonequilibrium version of the standard equilibrium phase transition driven by raising temperature. Distinct from this transition Walldorf *et al.* also found a change in the magnon distribution from subthermal to superthermal, occurring as the relative drive strength was increased beyond the critical value $g = 1$ ⁵⁹. It is this subthermal-to-superthermal transition, which is characterized by a qualitative change in the distribution and is not directly related to the disappearance of a conventional order parameter, that we investigate here. Because the distribution function is at least thermal, in the two-dimensional Heisenberg-symmetry case studied in detail here, long-range order is necessarily destroyed at $g = 1$. However, in two-dimensional xy/xxz or in three-dimensional systems, the ordered phase may persist into the superthermal phase.

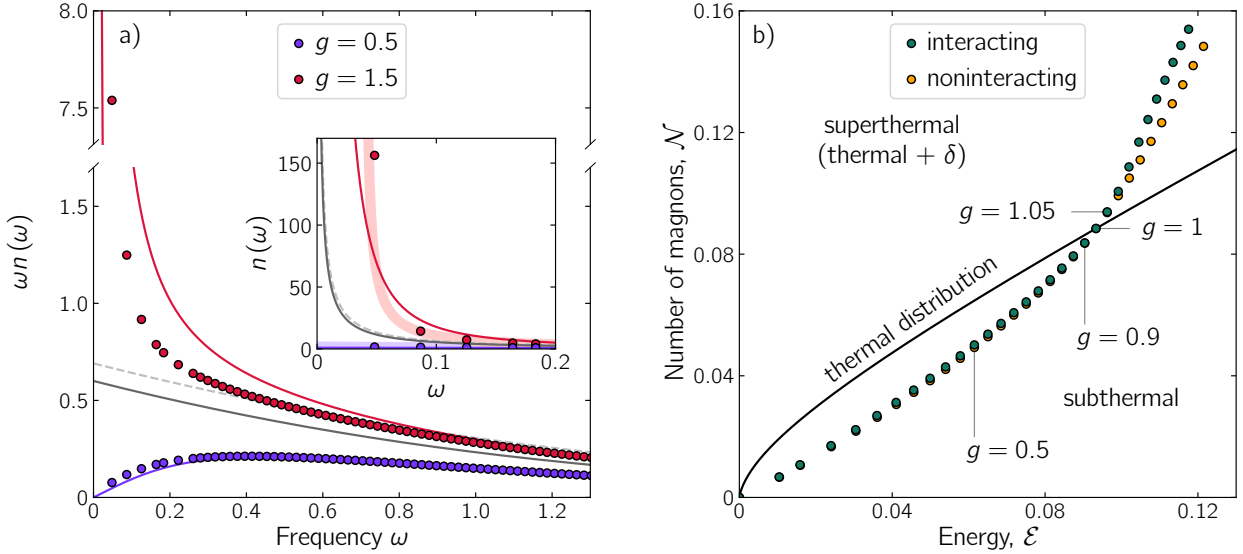


FIG. 2. **Nonequilibrium phase transition.** a) Interaction-induced changes of steady-state magnon occupation $n(\omega)$. Plotted is $\omega n(\omega)$ as a function of magnon frequency ω , in order to highlight the difference between subthermal ($\omega n(\omega) \rightarrow 0$ for $\omega \rightarrow 0$), thermal ($\omega n(\omega) \rightarrow \text{const}$), and superthermal ($\omega n(\omega) \rightarrow \infty$) regimes. The blue (red) data points show the interacting results for representative subthermal, $g = 0.5$ (superthermal, $g = 1.5$) cases, in comparison with the noninteracting results shown by blue (red) curves. The dark grey solid line indicates a thermal state at $g = 1$ and $T = 0.6$; the light grey dashed line is a best fit to the high-frequency part of the interacting distribution function at $g = 1.5$, and corresponds to a thermal state with an effective temperature $T > \bar{T}$. Inset: The same results plotted as $n(\omega)$ versus ω focussing on the low-frequency part to highlight that the interacting superthermal system shows a low-frequency divergence that is stronger than both the noninteracting system and the best thermal fit. b) Points: magnon number vs total energy curve defined from Eq. 4 with g as an implicit parameter for both noninteracting and interacting steady state. Solid black line: magnon-number vs. total energy relation obtained from Bose distribution with chemical potential $\mu = 0$ with temperature as implicit parameter. States below this critical Bose-Einstein condensation line have a lower number of magnons per energy than a thermal state. States above the critical line have a number of magnons that exceeds the maximal number in states with $\omega(\mathbf{k}) > 0$ that is compatible with the given system energy in a thermal state, implying the existence of a δ -function contribution at zero energy (condensate fraction) in the thermodynamic limit.

B. Nonequilibrium steady state

Fig. 2 (a) compares the magnon distribution function calculated with and without magnon-magnon scattering. We find that the clear qualitative difference between the subthermal and superthermal cases is still evident in the interacting case, confirming that the nonequilibrium phase transition is preserved under magnon-magnon scattering. In the subthermal steady state, the impact of magnon-magnon scattering is rather small, producing only a slight shift of magnon occupation towards lower frequencies. In striking contrast, the superthermal steady state is strongly affected by magnon-magnon scattering. At all but the lowest frequency the effect of the scattering is to drive the distribution close to a thermal distribution, but the occupancy at the lowest frequency is strongly enhanced relative to the noninteracting case (see inset of Fig. 2 (a)).

To interpret our results, we recall equilibrium BEC, where the occupancy is given by a Bose Einstein distribution with $\mu = 0$ and a δ -function at $\omega_k = 0$ describing

the condensate fraction. This distribution has a temperature that is fixed by the total energy; the number of uncondensed bosons is then uniquely determined by this temperature, and any excess over the uncondensed number makes up the condensate fraction. With this in mind we plot in Fig. 2 (b) the magnon number as a function of magnon energy with g as an implicit parameter, along with the magnon number-energy relation implied by the Bose distribution with chemical potential $\mu = 0$ and no condensate, with temperature as an implicit parameter. In ordinary BEC, decreasing the temperature decreases the energy moving the system to the left along a line at fixed \mathcal{N} . Crossing the solid line signals the BEC. In our system for $g < 1$ the number-energy trace remains below the solid line. At $g = 1$ the curves for both noninteracting and interacting systems cross the solid line, implying for $g > 1$ an excess of magnons. Importantly magnon-magnon interactions push the system even further away from the thermal distribution rather than towards it because magnon-magnon scattering tends to redistribute magnons towards lower energy, thus accommo-

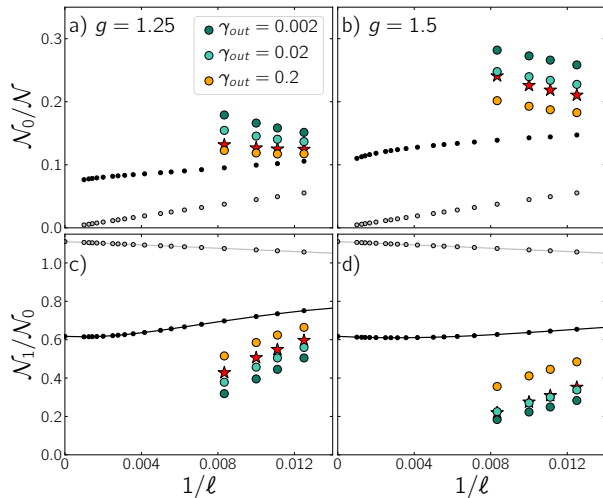


FIG. 3. **Finite-size scaling analysis revealing δ -function contribution at $g > 1$ in the thermodynamic limit.** (a), (b) Ratio of the magnon density at the lowest frequency and the total number of magnons in the system, $\mathcal{N}_0/\mathcal{N}$, and (c), (d) ratio of the magnon density at the second lowest frequency and the lowest frequency, $\mathcal{N}_1/\mathcal{N}_0$, for $g = 1.25$ (left panels) and $g = 1.5$ (right panels). Different colors correspond to different values of $\gamma_{\text{out}} = 0.002, 0.02, 0.2$ as indicated. Black points correspond to the noninteracting stationary state, gray points show thermal behavior ($g = 1$), and red stars correspond to the stationary state to which the interacting, closed system evolves when initialized with the respective noninteracting stationary state at given g .

dating more magnons per energy compared to the noninteracting steady state.

C. Finite size scaling analysis

To further interpret the data we present a finite-size scaling analysis. We define the magnon occupancy at the m -th frequency weighted by the discretized density of states, $\mathcal{N}_m = \rho(\omega_m)n(\omega_m)$. Fig. 3 (a) and (b) strongly suggest that the occupancy \mathcal{N}_0 of the the lowest frequency magnon mode remains a nonvanishing fraction of the overall number of magnons \mathcal{N} as the system size increases in any interacting system with $g > 1$. This is different from the case $g = 1$, which has no condensate, and where the contribution of the lowest frequency vanishes as the system size increases. Fig. 3 (c) and (d) shows that the ratio of the occupancy at the second smallest frequency to the occupancy at the smallest frequency, $\mathcal{N}_1/\mathcal{N}_0$, is decreasing as the system size increases. The decrease is apparently linear in $1/\ell$, but the system sizes available are not sufficient to allow for a precise determination. The combination of a nonvanishing $\mathcal{N}_0/\mathcal{N}$ and a vanishing $\mathcal{N}_1/\mathcal{N}_0$ in the thermodynamic limit strongly suggests the existence of a δ -function con-

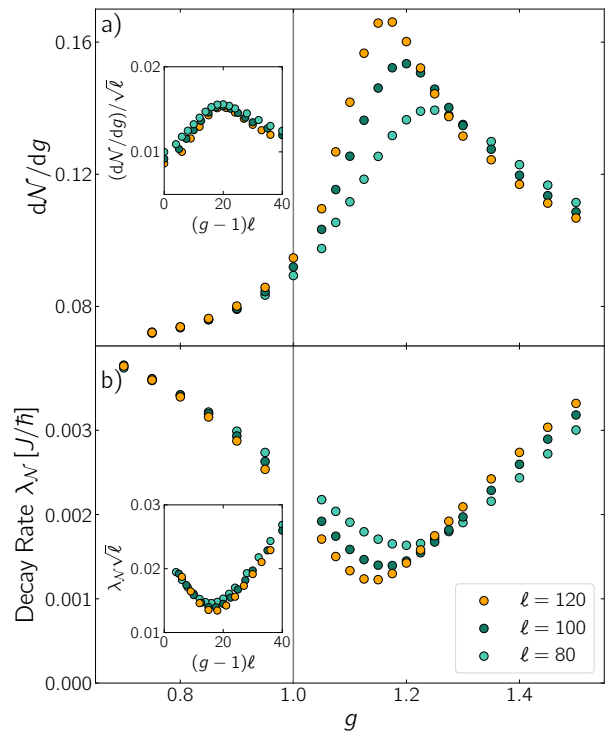


FIG. 4. **Static and dynamical critical behavior in the interacting driven-dissipative steady state.** (a) Rate of change of magnon number \mathcal{N} as a function of g . Inset: Scaling behavior with linear system size collapses the data points onto a single curve. (b) Rate of decay of total magnon number \mathcal{N} towards the stationary state, plotted as a function of g for different system sizes as indicated. Inset: Scaling behavior with linear system size consistent with collapse onto a single curve, suggesting critical slowing down as $g \rightarrow 1$. (for critical behavior in the strength of the condensate fraction, see SM)

tribution at $\omega = 0$. For reference, we also show data points for a system that is initialized with the noninteracting steady state at a given value of g and then evolved as a closed system under magnon-magnon scattering. At $g > 1$ this closed system is positioned above the critical line for BEC in the \mathcal{N} - \mathcal{E} diagram in Fig. 2 (b). Therefore, in the thermodynamic limit this closed system necessarily develops a finite condensate fraction because this is the only possible thermalized solution to the closed-system kinetic equation. The comparison between the interacting driven-dissipative steady states and the closed-system thermalized states drives home our point that the interacting $g > 1$ system develops a nonvanishing condensate fraction in the thermodynamic limit⁶¹.

D. Static and dynamic criticality

Fig. 4 examines the nature of static and dynamic criticality occurring as g is tuned through $g = 1$. The main

panels show both the dependence of the static observable $d\mathcal{N}/dg$ [Fig. 4 (a)] and the dynamic decay rate $\lambda_{\mathcal{N}}$ [Fig. 4 (b)], as defined by

$$\mathcal{N}(t) = \mathcal{N}_{\text{final}} + \Delta\mathcal{N} \exp(-\lambda_{\mathcal{N}}t) \quad (6)$$

on the tuning parameter g . Equation (6) is the empirically observed long-time behavior of the excitation density in the system⁶². Data are shown for different system sizes. For both quantities there is a clear difference between $g < 1$ and $g > 1$ with weak system-size dependence for $g < 1$ and strong system-size dependence for $g > 1$. The inset shows an approximate data collapse that is consistent with a critical scaling as $g \rightarrow 1$ from above and $\ell \rightarrow \infty$. The implication of the data collapse is that

$$\frac{d\mathcal{N}}{dg} = f_1[(g-1)\ell] \sqrt{\ell}, \quad (7a)$$

$$\lambda_{\mathcal{N}} = \frac{f_2[(g-1)\ell]}{\sqrt{\ell}}. \quad (7b)$$

If $d\mathcal{N}/dg$ and $\lambda_{\mathcal{N}}$ are to be finite and non-zero as $\ell \rightarrow \infty$, the two functions $f_1(x)$ and $f_2(x)$ need to have the form $f_1(x) \propto (1/\sqrt{x})$ and $f_2(x) \propto \sqrt{x}$ as $x \rightarrow \infty$, implying that at $\ell = \infty$ $d\mathcal{N}/dg \sim \frac{1}{\sqrt{g-1}}$, i.e., a square-root singularity of $\mathcal{N}(g)$ in the thermodynamic limit, and $\lambda_{\mathcal{N}} \sim \sqrt{g-1}$ as $g \rightarrow 1^+$, i.e., a critical slowing down as $g \rightarrow 1$ from above. This asymmetric criticality is not present in the noninteracting theory and is a consequence of magnon-magnon interactions.

IV. DISCUSSION

A driven-dissipative system may exhibit two phase transitions as a function of drive strength. One is the nonequilibrium analogue of a conventional symmetry breaking transition, occurring because the drive creates excitations which push the system away from the ordered state. This transition has been previously studied^{8,10,12-15,42,43}. The other type, studied here, is that when the drive exceeds a critical value set by the linear dissipation mechanism, a kind of “order from disorder” transition may occur, with some fraction of the drive-induced excitations condensing into a zero-momentum ground state. Our finding bears an interesting relationship to the existing literature on Bose-Einstein condensation of magnons, where an evolution into a condensed state of a transiently induced magnon population is analysed.

Crucial to our analysis is a numerically exact solution of the Boltzmann equation derived by considering the interactions among excitations, which enables an analysis of the interplay between the frequency dependence of the dissipation mechanism and the tendency to condensation. This comprehensive numerical solution extends previously published theory which typically uses either a phenomenological relaxation rate or a simple approximation to the magnon-magnon scattering term. A key

finding is that the condensation occurs in a high-drive limit, where the drive induced energy density is large and the number of excited magnons is also large, and is associated with a dynamical (drive-strength driven) criticality. On the level of theory used here, this criticality is described by a new set of static and dynamic critical exponents.

Our work raises many important questions. First, while we have demonstrated a qualitative change in the magnon distribution consistent with the formation of a condensate, the physics of fluctuations around this state has not yet been studied, and therefore a full analysis of the criticality, beyond the Boltzmann approximation used here, cannot be undertaken. Understanding how to characterize the differences between the nonthermal symmetry breaking transition and the usual thermal one, how to understand transitions involving distribution functions and not conventional order parameters, and how to generalize the standard equilibrium theory of spatial and temporal fluctuations in a critical state to strongly nonequilibrium situations such as that considered here, are important open problems. The issues are of particular importance in two dimensions, where the obvious generalization of the Hohenberg-Mermin-Wagner theorem to nonequilibrium situations would suggest that the Bose-Einstein condensation we find signals a phase with power law correlations.

Observation of the nonthermal critical behavior predicted here is an important experimental challenge. Possible techniques include time-resolved second harmonic optical polarimetry or inelastic x-ray scattering⁶³. Our work also has a close connection to Bose-Einstein condensation in exciton-polariton systems, where interesting field-theory-based studies of criticality have appeared^{42,43}. Investigations of possible nonequilibrium-induced spatial structure, analogous to the structures observed in turbulence⁶⁴, and clarifying the relation of our work to nonthermal fixed points in closed systems after quenches⁶⁵⁻⁶⁷ are also important directions for future research.

V. ACKNOWLEDGEMENTS

We acknowledge discussions with S. Diehl and M. Mirano. This work was supported by the Max Planck-New York City Center for Nonequilibrium Quantum Phenomena. MAS acknowledges financial support through the Deutsche Forschungsgemeinschaft (DFG, German Research Foundation) via the Emmy Noether program (SE 2558/2). DMK acknowledges support by the Deutsche Forschungsgemeinschaft (DFG, German Research Foundation) via RTG 1995 and Germany’s Excellence Strategy – Cluster of Excellence Matter and Light for Quantum Computing (ML4Q) EXC 2004/1 – 390534769. A.J.M. is supported in part by Programmable Quantum Materials, an Energy Frontier Research Center funded by the U.S. Department of Energy (DOE), Office of Sci-

ence, Basic Energy Sciences (BES), under award DE-SC0019443. The Flatiron Institute is a division of the Simons Foundation.

VI. BIBLIOGRAPHY

- * mona.kalthoff@mpsd.mpg.de
† dante.kennes@rwth-aachen.de
‡ amillis@flatironinstitute.org
§ michael.sentef@mpsd.mpg.de
- ¹ Basov, D. N., Averitt, R. D. & Hsieh, D. Towards properties on demand in quantum materials. *Nature Materials* **16**, 1077–1088 (2017). URL <https://www.nature.com/articles/nmat5017>. Number: 11 Publisher: Nature Publishing Group.
 - ² de la Torre, A. et al. Colloquium: Nonthermal pathways to ultrafast control in quantum materials. *Rev. Mod. Phys.* **93**, 041002 (2021). URL <https://link.aps.org/doi/10.1103/RevModPhys.93.041002>.
 - ³ Tsuji, N., Eckstein, M. & Werner, P. Nonthermal Antiferromagnetic Order and Nonequilibrium Criticality in the Hubbard Model. *Phys. Rev. Lett.* **110**, 136404 (2013). URL <https://link.aps.org/doi/10.1103/PhysRevLett.110.136404>.
 - ⁴ Klinder, J., Keßler, H., Wolke, M., Mathey, L. & Hemmerich, A. Dynamical phase transition in the open Dicke model. *Proceedings of the National Academy of Sciences* **112**, 3290–3295 (2015). URL <https://www.pnas.org/content/112/11/3290>. <https://www.pnas.org/content/112/11/3290.full.pdf>.
 - ⁵ Kemper, A. F., Abdurazakov, O. & Freericks, J. K. General Principles for the Nonequilibrium Relaxation of Populations in Quantum Materials. *Phys. Rev. X* **8**, 041009 (2018). URL <https://link.aps.org/doi/10.1103/PhysRevX.8.041009>.
 - ⁶ Yarmohammadi, M., Meyer, C., Fauseweh, B., Normand, B. & Uhrig, G. S. Dynamical properties of a driven dissipative dimerized $S = \frac{1}{2}$ chain. *Phys. Rev. B* **103**, 045132 (2021). URL <https://link.aps.org/doi/10.1103/PhysRevB.103.045132>.
 - ⁷ Maghrebi, M. F. & Gorshkov, A. V. Nonequilibrium many-body steady states via keldysh formalism. *Phys. Rev. B* **93**, 014307 (2016). URL <https://link.aps.org/doi/10.1103/PhysRevB.93.014307>.
 - ⁸ Mitra, A., Takei, S., Kim, Y. B. & Millis, A. J. Nonequilibrium Quantum Criticality in Open Electronic Systems. *Phys. Rev. Lett.* **97**, 236808 (2006). URL <https://link.aps.org/doi/10.1103/PhysRevLett.97.236808>.
 - ⁹ Mitra, A. & Millis, A. J. Coulomb gas on the Keldysh contour: Anderson-Yuval-Hamann representation of the nonequilibrium two-level system. *Phys. Rev. B* **76**, 085342 (2007). URL <https://link.aps.org/doi/10.1103/PhysRevB.76.085342>.
 - ¹⁰ Mitra, A. & Millis, A. J. Current-driven quantum criticality in itinerant electron ferromagnets. *Phys. Rev. B* **77**, 220404 (2008). URL <https://link.aps.org/doi/10.1103/PhysRevB.77.220404>.
 - ¹¹ Mitra, A. & Millis, A. J. Current-driven defect-unbinding transition in an XY ferromagnet. *Phys. Rev. B* **84**, 054458 (2011). URL <https://link.aps.org/doi/10.1103/PhysRevB.84.054458>.
 - ¹² Brennecke, F. et al. Real-time observation of fluctuations at the driven-dissipative Dicke phase transition. *Proceedings of the National Academy of Sciences* **110**, 11763–11767 (2013). URL <https://www.pnas.org/content/110/29/11763>. Publisher: National Academy of Sciences Section: Physical Sciences.
 - ¹³ Rota, R., Minganti, F., Ciuti, C. & Savona, V. Quantum Critical Regime in a Quadratically Driven Nonlinear Photonic Lattice. *Phys. Rev. Lett.* **122**, 110405 (2019). URL <https://link.aps.org/doi/10.1103/PhysRevLett.122.110405>.
 - ¹⁴ Klöckner, C., Karrasch, C. & Kennes, D. M. Nonequilibrium Properties of Berezinskii-Kosterlitz-Thouless Phase Transitions. *Phys. Rev. Lett.* **125**, 147601 (2020). URL <https://link.aps.org/doi/10.1103/PhysRevLett.125.147601>.
 - ¹⁵ Marino, J. & Diehl, S. Driven markovian quantum criticality. *Phys. Rev. Lett.* **116**, 070407 (2016). URL <https://link.aps.org/doi/10.1103/PhysRevLett.116.070407>.
 - ¹⁶ The 2021 magnonics roadmap. *Journal of Physics: Condensed Matter* **33**, 413001 (2021). URL <https://doi.org/10.1088/1361-648x/abec1a>.
 - ¹⁷ Demokritov, S. O. et al. Bose-einstein condensation of quasi-equilibrium magnons at room temperature under pumping. *Nature* **443**, 430–433 (2006). URL <https://doi.org/10.1038/nature05117>.
 - ¹⁸ Bozhko, D. A. et al. Supercurrent in a room-temperature bose-einstein magnon condensate. *Nature Physics* **12**, 1057–1062 (2016). URL <https://doi.org/10.1038/nphys3838>.
 - ¹⁹ Nowik-Boltyk, P., Dzyapko, O., Demidov, V. E., Berloff, N. G. & Demokritov, S. O. Spatially non-uniform ground state and quantized vortices in a two-component bose-einstein condensate of magnons. *Scientific Reports* **2**, 482 (2012). URL <https://doi.org/10.1038/srep00482>.
 - ²⁰ Bender, S. A., Duine, R. A., Brataas, A. & Tserkovnyak, Y. Dynamic phase diagram of dc-pumped magnon condensates. *Phys. Rev. B* **90**, 094409 (2014). URL <https://link.aps.org/doi/10.1103/PhysRevB.90.094409>.
 - ²¹ Clausen, P. et al. Stimulated thermalization of a parametrically driven magnon gas as a prerequisite for bose-einstein magnon condensation. *Phys. Rev. B* **91**, 220402 (2015). URL <https://link.aps.org/doi/10.1103/PhysRevB.91.220402>.
 - ²² Demidov, V. E. et al. Magnon kinetics and bose-einstein condensation studied in phase space. *Phys. Rev. Lett.* **101**, 257201 (2008). URL <https://link.aps.org/doi/10.1103/PhysRevLett.101.257201>.
 - ²³ Serga, A. A., Chumak, A. V. & Hillebrands, B. YIG magnonics. *Journal of Physics D: Applied Physics* **43**, 264002 (2010). URL <https://doi.org/10.1088/0022-3727/43/26/264002>.
 - ²⁴ Kreil, A. J. E. et al. Tunable space-time crystal in room-temperature magnetodielectrics. *Phys. Rev. B* **100**, 020406 (2019). URL <https://link.aps.org/doi/10.1103/PhysRevB.100.020406>.
 - ²⁵ Sun, C., Nattermann, T. & Pokrovsky, V. L. Bose-einstein condensation and superfluidity of magnons in yttrium iron garnet films. *Journal of Physics D: Applied Physics* **50**, 143002 (2017). URL <https://doi.org/10.1088/1361-6463/aa5cfc>.
 - ²⁶ Bunkov, Y. M. et al. Discovery of the classical bose-einstein condensation of magnons in solid antiferromagnets. *JETP Letters* **94**, 68 (2011). URL <https://doi.org/10.1088/1361-6463/aa5cfc>.

- [org/10.1134/S0021364011130066](https://doi.org/10.1134/S0021364011130066).
- 27 Bunkov, Y. M. & Volovik, G. E. Magnon bose-einstein condensation and spin superfluidity. *Journal of Physics: Condensed Matter* **22**, 164210 (2010). URL <https://doi.org/10.1088/0953-8984/22/16/164210>.
 - 28 Autti, S. et al. Bose-einstein condensation of magnons and spin superfluidity in the polar phase of ^3He . *Phys. Rev. Lett.* **121**, 025303 (2018). URL <https://link.aps.org/doi/10.1103/PhysRevLett.121.025303>.
 - 29 Bunkov, Y. M. & Volovik, G. E. Magnon condensation into a q ball in $^3\text{He}-b$. *Phys. Rev. Lett.* **98**, 265302 (2007). URL <https://link.aps.org/doi/10.1103/PhysRevLett.98.265302>.
 - 30 Serga, A. A. et al. Bose-einstein condensation in an ultrahot gas of pumped magnons. *Nature Communications* **5**, 3452 (2014). URL <https://doi.org/10.1038/ncomms4452>.
 - 31 Kreil, A. J. E. et al. From kinetic instability to bose-einstein condensation and magnon supercurrents. *Phys. Rev. Lett.* **121**, 077203 (2018). URL <https://link.aps.org/doi/10.1103/PhysRevLett.121.077203>.
 - 32 Kinetic instability and bose condensation of nonequilibrium magnons. *Journal of Magnetism and Magnetic Materials* **132**, 180–184 (1994). URL <https://www.sciencedirect.com/science/article/pii/S0304885394903115>.
 - 33 Zapf, V., Jaime, M. & Batista, C. D. Bose-einstein condensation in quantum magnets. *Rev. Mod. Phys.* **86**, 563–614 (2014). URL <https://link.aps.org/doi/10.1103/RevModPhys.86.563>.
 - 34 Bunkov, Y. M. & Safonov, V. L. Magnon condensation and spin superfluidity. *Journal of Magnetism and Magnetic Materials* **452**, 30–34 (2018). URL <https://www.sciencedirect.com/science/article/pii/S0304885317326999>.
 - 35 Pirro, P., Vasyuchka, V. I., Serga, A. A. & Hillebrands, B. Advances in coherent magnonics. *Nature Reviews Materials* (2021). URL <https://doi.org/10.1038/s41578-021-00332-w>.
 - 36 Byrnes, T., Kim, N. Y. & Yamamoto, Y. Exciton-polariton condensates. *Nature Physics* **10**, 803–813 (2014). URL <https://doi.org/10.1038/nphys3143>.
 - 37 Plumhof, J. D., Stöferle, T., Mai, L., Scherf, U. & Mahrt, R. F. Room-temperature Bose-Einstein condensation of cavity exciton-polaritons in a polymer. *Nature Materials* **13**, 247–252 (2014). URL <https://doi.org/10.1038/nmat3825>.
 - 38 Walker, B. T. et al. Driven-dissipative non-equilibrium Bose-Einstein condensation of less than ten photons. *Nature Physics* **14**, 1173–1177 (2018). URL <https://doi.org/10.1038/s41567-018-0270-1>.
 - 39 Hakala, T. K. et al. Bose-Einstein condensation in a plasmonic lattice. *Nature Physics* **14**, 739–744 (2018). URL <https://www.nature.com/articles/s41567-018-0109-9>. Number: 7 Publisher: Nature Publishing Group.
 - 40 Väkeväinen, A. I. et al. Sub-picosecond thermalization dynamics in condensation of strongly coupled lattice plasmons. *Nature Communications* **11**, 3139 (2020). URL <https://doi.org/10.1038/s41467-020-16906-1>.
 - 41 Deng, H., Haug, H. & Yamamoto, Y. Exciton-polariton bose-einstein condensation. *Rev. Mod. Phys.* **82**, 1489–1537 (2010). URL <https://link.aps.org/doi/10.1103/RevModPhys.82.1489>.
 - 42 Sieberer, L. M., Huber, S. D., Altman, E. & Diehl, S. Dynamical Critical Phenomena in Driven-Dissipative Systems. *Physical Review Letters* **110**, 195301 (2013). URL <https://link.aps.org/doi/10.1103/PhysRevLett.110.195301>.
 - 43 Sieberer, L. M., Huber, S. D., Altman, E. & Diehl, S. Nonequilibrium functional renormalization for driven-dissipative Bose-Einstein condensation. *Phys. Rev. B* **89**, 134310 (2014). URL <https://link.aps.org/doi/10.1103/PhysRevB.89.134310>.
 - 44 Rückriegel, A. & Kopietz, P. Rayleigh-jeans condensation of pumped magnons in thin-film ferromagnets. *Phys. Rev. Lett.* **115**, 157203 (2015). URL <https://link.aps.org/doi/10.1103/PhysRevLett.115.157203>.
 - 45 Mohseni, M. et al. Bose-einstein condensation of nonequilibrium magnons in confined systems. *New Journal of Physics* **22**, 083080 (2020). URL <https://doi.org/10.1088/1367-2630/aba98c>.
 - 46 Zakharov, V. E., L'vov, V. S. & Starobinets, S. S. Spin-wave turbulence beyond the parametric excitation threshold. *Soviet Physics Uspekhi* **17**, 896–919 (1975). URL <https://doi.org/10.1070/pu1975v017n06abeh004404>.
 - 47 Rezende, S. M. Theory of coherence in bose-einstein condensation phenomena in a microwave-driven interacting magnon gas. *Phys. Rev. B* **79**, 174411 (2009). URL <https://link.aps.org/doi/10.1103/PhysRevB.79.174411>.
 - 48 Cornelissen, L. J., Peters, K. J. H., Bauer, G. E. W., Duine, R. A. & van Wees, B. J. Magnon spin transport driven by the magnon chemical potential in a magnetic insulator. *Phys. Rev. B* **94**, 014412 (2016). URL <https://link.aps.org/doi/10.1103/PhysRevB.94.014412>.
 - 49 Schneider, M. et al. Bose-einstein condensation of quasiparticles by rapid cooling. *Nature Nanotechnology* **15**, 457–461 (2020). URL <https://doi.org/10.1038/s41565-020-0671-z>.
 - 50 D'Alessio, L. & Rigol, M. Long-time Behavior of Isolated Periodically Driven Interacting Lattice Systems. *Phys. Rev. X* **4**, 041048 (2014). URL <https://link.aps.org/doi/10.1103/PhysRevX.4.041048>.
 - 51 Tindall, J., Buča, B., Coulthard, J. R. & Jaksch, D. Heating-Induced Long-Range η Pairing in the Hubbard Model. *Phys. Rev. Lett.* **123**, 030603 (2019). URL <https://link.aps.org/doi/10.1103/PhysRevLett.123.030603>.
 - 52 Abanin, D. A., De Roeck, W., Ho, W. W. & Huvneers, F. Effective Hamiltonians, prethermalization, and slow energy absorption in periodically driven many-body systems. *Phys. Rev. B* **95**, 014112 (2017). URL <https://link.aps.org/doi/10.1103/PhysRevB.95.014112>.
 - 53 Abanin, D., De Roeck, W., Ho, W. W. & Huvneers, F. A Rigorous Theory of Many-Body Prethermalization for Periodically Driven and Closed Quantum Systems. *Communications in Mathematical Physics* **354**, 809–827 (2017). URL <https://doi.org/10.1007/s00220-017-2930-x>.
 - 54 Ho, W. W., Protopopov, I. & Abanin, D. A. Bounds on Energy Absorption and Prethermalization in Quantum Systems with Long-Range Interactions. *Phys. Rev. Lett.* **120**, 200601 (2018). URL <https://link.aps.org/doi/10.1103/PhysRevLett.120.200601>.
 - 55 Kuwahara, T., Mori, T. & Saito, K. Floquet-Magnus theory and generic transient dynamics in periodically driven many-body quantum systems. *Annals of Physics* **367**, 96–124 (2016). URL <https://www.sciencedirect.com/>

- [science/article/pii/S0003491616000142](https://doi.org/10.1103/PhysRevLett.116.120401).
- ⁵⁶ Mori, T., Kuwahara, T. & Saito, K. Rigorous Bound on Energy Absorption and Generic Relaxation in Periodically Driven Quantum Systems. *Phys. Rev. Lett.* **116**, 120401 (2016). URL <https://link.aps.org/doi/10.1103/PhysRevLett.116.120401>.
- ⁵⁷ Mori, T., Ikeda, T. N., Kaminishi, E. & Ueda, M. Thermalization and prethermalization in isolated quantum systems: a theoretical overview. *Journal of Physics B: Atomic, Molecular and Optical Physics* **51**, 112001 (2018). URL <https://doi.org/10.1088/1361-6455/aabcdf>.
- ⁵⁸ Holstein, T. & Primakoff, H. Field Dependence of the Intrinsic Domain Magnetization of a Ferromagnet. *Phys. Rev.* **58**, 1098–1113 (1940). URL <https://link.aps.org/doi/10.1103/PhysRev.58.1098>.
- ⁵⁹ Walldorf, N., Kennes, D. M., Paaske, J. & Millis, A. J. The antiferromagnetic phase of the Floquet-driven Hubbard model. *Physical Review B* **100**, 121110 (2019). URL <https://link.aps.org/doi/10.1103/PhysRevB.100.121110>.
- ⁶⁰ Here all integrals are understood as properly normalized over the magnetic Brillouin zone.
- ⁶¹ For a corresponding analysis in the limit of weak driving, $g < 1$, see SM.
- ⁶² We have checked that this slow time scale that emerges in the critical system is observed not only for the dynamics of the magnon number, but also for the total energy as well as the magnon occupation at any given energy.
- ⁶³ Mazzone, D. G. et al. Laser-induced transient magnons in Sr3Ir2O7 throughout the Brillouin zone. *Proceedings of the National Academy of Sciences* **118** (2021). URL <https://www.pnas.org/content/118/22/e2103696118>. Publisher: National Academy of Sciences Section: Physical Sciences.
- ⁶⁴ Falkovich, G. & Sreenivasan, K. R. Lessons from hydrodynamic turbulence. *Physics Today* **59**, 43–49 (2006). URL <https://physicstoday.scitation.org/doi/10.1063/1.2207037>. Publisher: American Institute of Physics.
- ⁶⁵ Berges, J. Nonequilibrium Quantum Fields: From Cold Atoms to Cosmology. arXiv:1503.02907 [cond-mat, physics:hep-ph] (2015). URL <http://arxiv.org/abs/1503.02907>. ArXiv: 1503.02907.
- ⁶⁶ Erne, S., Bücken, R., Gasenzer, T., Berges, J. & Schmiedmayer, J. Universal dynamics in an isolated

one-dimensional Bose gas far from equilibrium. *Nature* **563**, 225–229 (2018). URL <https://www.nature.com/articles/s41586-018-0667-0>. Number: 7730 Publisher: Nature Publishing Group.

- ⁶⁷ Bhattacharyya, S., Rodriguez-Nieva, J. F. & Demler, E. Universal prethermal dynamics in heisenberg ferromagnets. *Phys. Rev. Lett.* **125**, 230601 (2020). URL <https://link.aps.org/doi/10.1103/PhysRevLett.125.230601>.

Appendix A: Methods

Interacting spin-wave theory We consider the isotropic Heisenberg antiferromagnet as given in Eq. (1) and apply standard Holstein-Primakoff spin-wave theory⁵⁸ resulting in

$$H_{\text{HP}} = E_0 + H_0 + V. \quad (\text{A1})$$

with an irrelevant ground state energy E_0 and bilinear Hamiltonian

$$H_0 = \sum_{\mathbf{k}} \hbar \omega_{\mathbf{k}} \left(\alpha_{\mathbf{k}}^\dagger \alpha_{\mathbf{k}} + \beta_{\mathbf{k}}^\dagger \beta_{\mathbf{k}} \right). \quad (\text{A2})$$

The magnon dispersion is

$$\omega_{\mathbf{k}} = \frac{JSz}{\hbar} \left[1 + \frac{1}{2S} \left(1 - \frac{2}{N} \sum_{\mathbf{k}'} \lambda_{\mathbf{k}'} \right) \right] \lambda_{\mathbf{k}} \quad (\text{A3})$$

with

$$\lambda_{\mathbf{k}} = \sqrt{1 - \gamma_{\mathbf{k}}^2} \quad (\text{A4a})$$

$$\gamma_{\mathbf{k}} = \frac{\cos(k_x) + \cos(k_y)}{2}. \quad (\text{A4b})$$

The interaction term for the kinematically allowed magnon energy and momentum conserving scattering processes is given by V with interaction vertices $V_{1_{\alpha}^{\dagger} 2_{\alpha}^{\dagger} 3_{\alpha}^{-} 4_{\alpha}^{-}}^{(2:2)}$ and $\tilde{V}_{1_{\alpha}^{\dagger} 2_{\beta}^{-} 3_{\alpha}^{-} 4_{\beta}^{\dagger}}^{(2:2)}$, namely

$$V = -J \frac{2z}{N} \sum_{\mathbf{k}_1 \mathbf{k}_2 \mathbf{k}_3 \mathbf{k}_4} \delta(\mathbf{k}_1 + \mathbf{k}_2 - \mathbf{k}_3 - \mathbf{k}_4) \left\{ V^{(2:2)} \left(\alpha_1^{\dagger} \alpha_2^{\dagger} \alpha_3 \alpha_4 + \beta_3^{\dagger} \beta_4^{\dagger} \beta_1 \beta_2 \right) + \tilde{V}^{(2:2)} \left(\alpha_1^{\dagger} \alpha_3 \beta_4^{\dagger} \beta_2 \right) \right\} \quad (\text{A5a})$$

$$V_{1_{\alpha}^{\dagger} 2_{\alpha}^{\dagger} 3_{\alpha}^{-} 4_{\alpha}^{-}}^{(2:2)} = \gamma_{(2-4)} u_1 u_3 v_2 v_4 + \frac{1}{4} [\gamma_1 u_1 v_2 v_3 v_4 + \gamma_2 u_1 u_3 u_4 v_2 + \gamma_3 u_3 v_1 v_2 v_4 + \gamma_4 u_1 u_2 u_3 v_4] \quad (\text{A5b})$$

$$\tilde{V}_{1_{\alpha}^{\dagger} 2_{\beta}^{-} 3_{\alpha}^{-} 4_{\beta}^{\dagger}}^{(2:2)} = \gamma_{(2-4)} [u_1 u_2 u_3 u_4 + v_1 v_2 v_3 v_4] + \gamma_{(2-3)} [u_1 u_2 v_3 v_4 + u_3 u_4 v_1 v_2] \quad (\text{A5c})$$

$$+ \frac{1}{2} \gamma_1 [u_3 v_1 v_2 v_4 + u_1 u_2 u_4 v_3] + \frac{1}{2} \gamma_2 [u_1 u_2 u_3 v_4 + u_4 v_1 v_2 v_3] \\ + \frac{1}{2} \gamma_3 [u_2 u_3 u_4 v_1 + u_1 v_2 v_3 v_4] + \frac{1}{2} \gamma_4 [u_2 v_1 v_3 v_4 + u_1 u_3 u_4 v_2].$$

Here we have used

$$u_{\mathbf{k}} = \sqrt{\frac{1 + \lambda_{\mathbf{k}}}{2\lambda_{\mathbf{k}}}} \quad (\text{A6a})$$

$$v_{\mathbf{k}} = -\text{sign}(\gamma_{\mathbf{k}}) \sqrt{\frac{1 - \lambda_{\mathbf{k}}}{2\lambda_{\mathbf{k}}}}. \quad (\text{A6b})$$

In Eq. (A5a), the momentum-conserving δ function is to be understood as modulo a reciprocal lattice vector of the standard two-dimensional antiferromagnetic Brillouin zone.

Boltzmann equation The semiclassical magnon Boltzmann equation for the magnon distribution in branch α

at a given momentum \mathbf{k}_1 is

$$\frac{dn^\alpha(\mathbf{k}_1)}{dt} = \frac{2\pi}{\hbar} \left(\frac{2Jz}{N}\right)^2 \left(\mathcal{S}_\alpha^{(2:2)}(\mathbf{k}_1) + \tilde{\mathcal{S}}_\alpha^{(2:2)}(\mathbf{k}_1)\right) \quad (\text{A7})$$

where \mathcal{S} are the relevant scattering integrals. To leading order in $1/S$, only scattering processes with two magnons scattering into two other magnons are kinematically allowed. Consequently, the scattering conserves the number of magnons term by term at this level of approximation. The corresponding scattering integrals are given by

$$\mathcal{S}_\alpha^{(2:2)}(\mathbf{k}_1) = \sum_{\mathbf{k}_2 \mathbf{k}_3 \mathbf{k}_4} \delta(\mathbf{k}_1 + \mathbf{k}_2 - \mathbf{k}_3 - \mathbf{k}_4) \delta(\omega_{\mathbf{k}_1} + \omega_{\mathbf{k}_2} - \omega_{\mathbf{k}_3} - \omega_{\mathbf{k}_4}) \mathcal{V}_{1_\alpha^+ 2_\alpha^+ 3_\alpha^- 4_\alpha^-}^{(2:2)} \mathcal{V}_{3_\alpha^+ 4_\alpha^+ 1_\alpha^- 2_\alpha^-}^{(2:2)} \times \quad (\text{A8})$$

$$[(1 + n^\alpha(\mathbf{k}_1))(1 + n^\alpha(\mathbf{k}_2))n^\alpha(\mathbf{k}_3)n^\alpha(\mathbf{k}_4) - n^\alpha(\mathbf{k}_1)n^\alpha(\mathbf{k}_2)(1 + n^\alpha(\mathbf{k}_3))(1 + n^\alpha(\mathbf{k}_4))]$$

$$\tilde{\mathcal{S}}_\alpha^{(2:2)}(\mathbf{k}_1) = \sum_{\mathbf{k}_2 \mathbf{k}_3 \mathbf{k}_4} \delta(\mathbf{k}_1 + \mathbf{k}_2 - \mathbf{k}_3 - \mathbf{k}_4) \delta(\omega_{\mathbf{k}_1} + \omega_{\mathbf{k}_2} - \omega_{\mathbf{k}_3} - \omega_{\mathbf{k}_4}) \tilde{\mathcal{V}}_{1_\alpha^+ 2_\beta^- 3_\alpha^- 4_\beta^+}^{(2:2)} \tilde{\mathcal{V}}_{3_\alpha^+ 4_\beta^- 1_\alpha^- 2_\beta^+}^{(2:2)} \times \quad (\text{A9})$$

$$[(1 + n^\alpha(\mathbf{k}_1))(1 + n^\beta(\mathbf{k}_4))n^\alpha(\mathbf{k}_3)n^\beta(\mathbf{k}_2) - n^\alpha(\mathbf{k}_3)n^\beta(\mathbf{k}_2)(1 + n^\alpha(\mathbf{k}_1))(1 + n^\beta(\mathbf{k}_4))].$$

Computational remarks We compute the time evolution on the two-dimensional antiferromagnetic Brillouin zone, that is discretized into square tiles and subsequently mapped onto an energy grid (see appendix D for details). The time propagation of the full kinetic equation in the main text is performed using the two-step Adams–Bashforth method. We have carefully checked convergence in the time step discretization.

The staggered magnetization is computed via

$$m(S, n(\omega)) = S + \frac{1}{2} - \omega_{\max} \sum_{m=1}^{\omega_{\max}} \frac{\rho(\omega_m)}{\omega_m} \left(n(\omega_m) + \frac{1}{2}\right). \quad (\text{A10})$$

Specifically, the black curve in Fig. 1 that separates the subthermal disordered phase from the subthermal ordered phase is computed by solving the equation $m(S, n(\omega)) = 0$ (with the noninteracting magnon distribution at given g inserted to compute m) for $1/S$.

Appendix B: Strength of the condensate fraction

The strength of the condensate fraction is determined by the ratio of the number of magnons \mathcal{N} to the system energy \mathcal{E} . Projecting each individual point in Fig. 2b) vertically onto the thermal distribution gives the number of magnons \mathcal{N}_{th} that can be accommodated by the thermal distribution. The excess of magnons determines the strength of the delta function, $\mathcal{D}_0 \equiv \mathcal{N} - \mathcal{N}_{\text{th}}$. Therefore

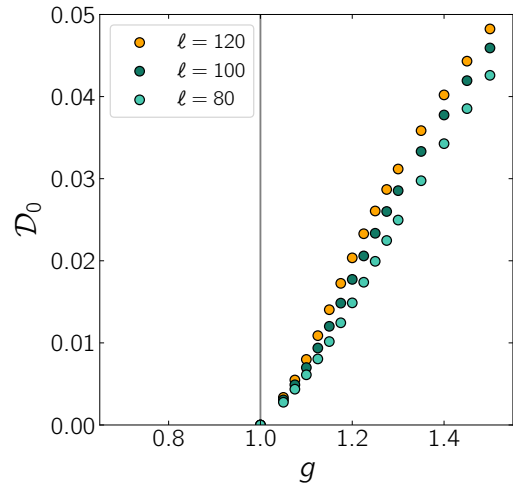


FIG. 5. Condensate fraction \mathcal{D}_0 as a function of dimensionless tuning parameter g for different linear system sizes as indicated.

the steady state has the form

$$\mathcal{N}(\omega) = \mathcal{D}_0 \mathcal{N}_\Delta(\omega) + \mathcal{N}_{\text{th}, T_\mathcal{E}}(\omega), \quad (\text{B1})$$

where $\mathcal{N}_\Delta(\omega)$ is a normalized function (integrating to unity) and, as discussed above, turns into a δ -function in the thermodynamic limit. Since the number of magnons only exceeds the number of magnons in a thermal distri-

bution at $g > 1$, the weight of the δ -function \mathcal{D}_0 vanishes for $g < 1$. The decrease of the weight of the delta function \mathcal{D}_0 to 0 at $g = 1$ is marking the phase transition [Fig. 5].

Appendix C: Scaling of the magnon number in the limit of weak driving

In the low driving phase $g < 1$ the scaling behavior is substantially different from the results in the strong

drive phase. As it is visible in Fig. 6 a) where the contribution of the lowest frequency in the interacting phase goes to zero as system size is increased, just as in the thermal system. So at $g < 1$ there are no indications for a condensate fraction at $\omega = 0$. Similarly, there is only a minimal shift from the non-interacting results in the ratio of the magnon density at the second lowest frequency and the lowest frequency, $\mathcal{N}_1/\mathcal{N}_0$. This is behavior in the low drive ordered phase is substantially different from the findings in the high drive, disordered phase.

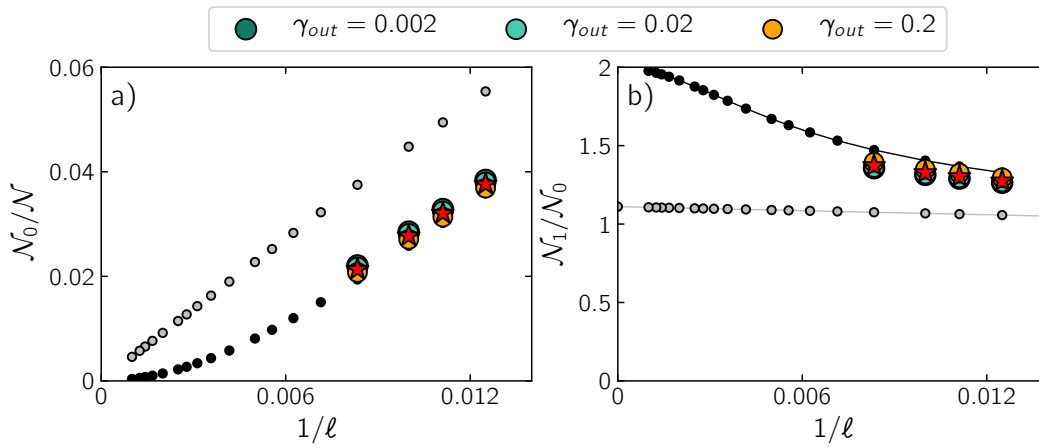


FIG. 6. Finite-size scaling analysis analogous to Fig. 4 for the subthermal regime ($g = 0.875$). (a) Ratio of the magnon density at the lowest frequency and the total number of magnons in the system, $\mathcal{N}_0/\mathcal{N}$, and (b) ratio of the magnon density at the second lowest frequency and the lowest frequency, $\mathcal{N}_1/\mathcal{N}_0$. Different colors correspond to different values of $\gamma_{out} = 0.002, 0.02, 0.2$ as indicated. Black points correspond to the non-interacting stationary state, gray points show thermal behavior ($g = 1$), and red stars correspond to the stationary state to which the interacting, closed system evolves when initialized with the respective non-interacting stationary state at given g .

Appendix D: Pseudocode

We numerically consider a quadratic lattice of momentum vectors as displayed in Fig 7 with linear dimension ℓ and ℓ^2 lattice sites. To make our computation numerically feasible even for comparatively large ℓ we then reduce this MBZ using symmetry relations to $(\ell^2 + 2\ell)/8$ lattice sites (green). These reduced MBZ vectors (k_{PZ}) are associated with different weights due to their multiplicity as indicated. Please note that in the following pseudocode # denotes the number of a quantity in an array while names like k_{PZ} without a # are the actual quantity. For example k_{PZ} without a # is the actual vector in the reduced MBZ.

1) Building the full (yellow) and reduced (green) MBZ as displayed in Fig. 7

- 1: Save MBZ vectors sorted by length in MBZ [# k_{MBZ}] [k_x, k_y]
 - 2: Save vectors within the reduced MBZ sorted by length in PZ [# k_{PZ}] [k_x, k_y]
 - 3: **for** $k \in PZ$ **do**
 - 4: save the precise Energy associated with this vector as Ω [# k_{PZ}]
 - 5: save the weight associated with this vector as k_{weight} [# k_{PZ}]
 - 6: **end for**
-

The scattering conserves both momentum and energy. This is implemented numerically by mapping the MBZ in momentum space on an energy grid as displayed in Fig. 8. To do so, we divide the interval $\{0, \Omega_{\max}\}$ into ℓ equidistant energy bins and determine with which bin the vectors in the momentum grid are associated. The different colors of the bins in Fig. 8 are simply to distinguish them from each other and have no further meaning. Since not all bins will have energies not all bins need to be taken into account. Note that in the example of $\ell = 8$ only 5 of the bins are occupied (purple ω). Each bin is then associated with the total weight of the MBZ vectors in it (red numbers).

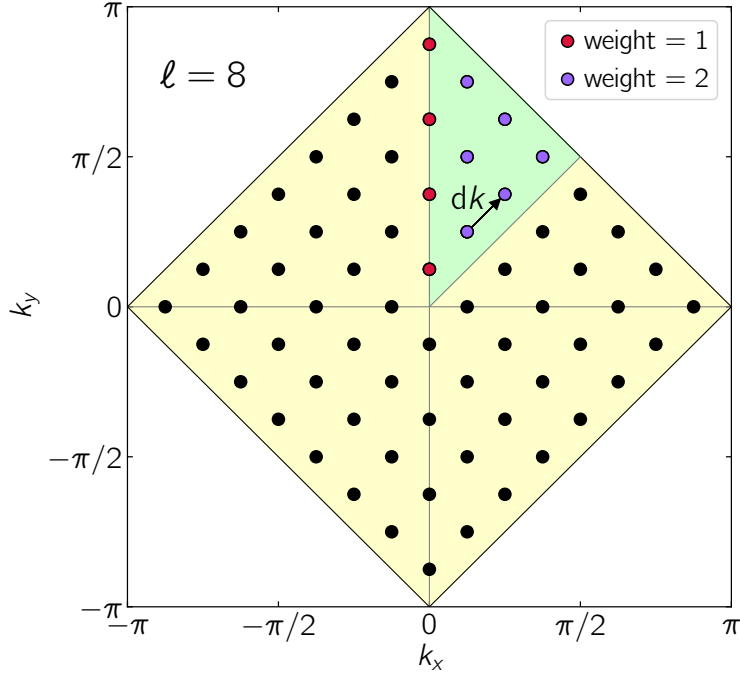


FIG. 7. Magnetic Brillouin zone (MBZ) for $\ell = 8$. The full MBZ (yellow) can be reduced to $(\ell^2 + 2\ell)/8$ lattice sites (green) due to the symmetry of the lattice. The multiplicity weights of these reduced lattice vectors that are sufficient to simulate the dynamics in the system is marked as indicated.

2) Map the reduced MBZ in \mathbf{k} space onto an energy grid as illustrated in Fig. 8

- 1: Divide the interval $\{0, \Omega_{\max}\}$ into ℓ equidistant energy bins
(see Fig. 8, blue and magenta boxes)
 - 2: **for** $k \in \text{PZ}$ **do**
 - 3: identify in which energy bin $\Omega[\#k]$ falls
 - 4: **end for**
 - 5: Discard empty energy bins
 - 6: Save the center of the remaining energy bins as energybin $[\#\omega]$
(see purple $\{\omega_1, \omega_2, \omega_3, \omega_4, \omega_5\}$ in Fig. 8)
 - 7: Save the numbers of the reduced MBZ vectors in each bin as kpz@energybin $[\#\omega][\#k_{\text{PZ}}]$
 - 8: Compute the total kweight in each bin and save it as kweight@energybin $[\#\omega][\#k_{\text{PZ}}]$
-

The next step is to find the quadruples in momentum space that satisfy momentum and energy conservation simultaneously. Note that we use the centers of the energy bins and not the precise energies of the momentum vectors to determine whether energy conservation is satisfied. The factor 4 in the cutoff is needed because each quadruple consists of 4 momentum vectors. Furthermore, all entries of the 2 dimensional array "integrals" are the same. Here the cutoff has to be divided by ℓ^4 because there are 4 free dimensions in the integration. The vertices are then

symmetrized by computing

$$(\mathcal{V}\mathcal{V})_{\text{sym}} = 0.125 \left[\mathcal{V}_{1\alpha^+ 2\alpha^+ 3\alpha^- 4\alpha^-} + \mathcal{V}_{3\alpha^+ 4\alpha^+ 1\alpha^- 2\alpha^-} \right] + 0.125 \left[\mathcal{V}_{1\alpha^+ 2\alpha^+ 4\alpha^- 3\alpha^-} + \mathcal{V}_{3\alpha^+ 4\alpha^+ 2\alpha^- 1\alpha^-} \right] \\ + 0.125 \left[\mathcal{V}_{2\alpha^+ 1\alpha^+ 3\alpha^- 4\alpha^-} + \mathcal{V}_{4\alpha^+ 3\alpha^+ 1\alpha^- 2\alpha^-} \right] + 0.125 \left[\mathcal{V}_{2\alpha^+ 1\alpha^+ 4\alpha^- 3\alpha^-} + \mathcal{V}_{4\alpha^+ 3\alpha^+ 2\alpha^- 1\alpha^-} \right] \quad (\text{D1})$$

and

$$(\tilde{\mathcal{V}}\tilde{\mathcal{V}})_{\text{sym}} = 0.25 \left[\tilde{\mathcal{V}}_{1\alpha^+ 4\beta^- 3\alpha^- 2\beta^+} + \tilde{\mathcal{V}}_{3\alpha^+ 2\beta^- 1\alpha^- 4\beta^+} \right] + 0.25 \left[\tilde{\mathcal{V}}_{2\alpha^+ 3\beta^- 4\alpha^- 1\beta^+} + \tilde{\mathcal{V}}_{4\alpha^+ 1\beta^- 2\alpha^- 3\beta^+} \right] \quad (\text{D2})$$

This vertex symmetrization ensures energy- and particle number conservation by enforcing detailed balance and is a necessary step in the energy-grid-representation.

3) Find Quadruples that satisfy momentum and energy conservation in momentum space

- 1: cutoff = $4 * \Omega_{\text{max}} / \ell$
 - 2: **for** $\mathbf{k}_1 \in \text{PZ}$ **do**
 - 3: **for** $\mathbf{k}_2 \in \text{MBZ}$ **do**
 - 4: **for** $\mathbf{k}_3 \in \text{MBZ}$ **do**
 - 5: $\mathbf{k}_4 = \mathbf{k}_1 + \mathbf{k}_2 - \mathbf{k}_3$
 - 6: Find bin energy ω_i associated with each of $\{\mathbf{k}_1, \mathbf{k}_2, \mathbf{k}_3, \mathbf{k}_4\} \rightarrow \{\omega_1, \omega_2, \omega_3, \omega_4\}$
 - 7: **if** $\omega_1 + \omega_2 - \omega_3 - \omega_4 < 0.05 * \text{cutoff}$ **then**
 - 8: Save quadruple as kquadruple [#k1] [#quadruple] $\{[\mathbf{k}_1, \mathbf{k}_2, \mathbf{k}_3, \mathbf{k}_4]\}$
 - 9: Compute $(\mathcal{V}\mathcal{V})_{\text{sym}} = \left(\text{symmetrize} \left[\mathcal{V}_{1\alpha^+ 2\alpha^+ 3\alpha^- 4\alpha^-} \right] \right)^2$
 - 10: Compute $(\tilde{\mathcal{V}}\tilde{\mathcal{V}})_{\text{sym}} = \left(\text{symmetrize} \left[\tilde{\mathcal{V}}_{1\alpha^+ 2\beta^- 3\alpha^- 4\beta^+} \right] \right)^2$
 - 11: Set vertices [#k1] [#quadruple] = $\mathcal{V}\mathcal{V}_{\text{sym}} + \tilde{\mathcal{V}}\tilde{\mathcal{V}}_{\text{sym}}$
 - 12: Set integrals [#k1] [#quadruple] = $\text{cutoff} / (\ell^4)$
 - 13: **end if**
 - 14: **end for**
 - 15: **end for**
 - 16: **end for**
-

Now we have found the quadruples in momentum space, but in order to compute the time evolution using the energy grid in Fig. 8 we need to turn the quadruple list into an energy list with $\omega_1, \omega_2, \omega_3$ and ω_4 and then average for each given ω_1 over the multiple entries. This gives a consolidated list of energy quadruples and their weights.

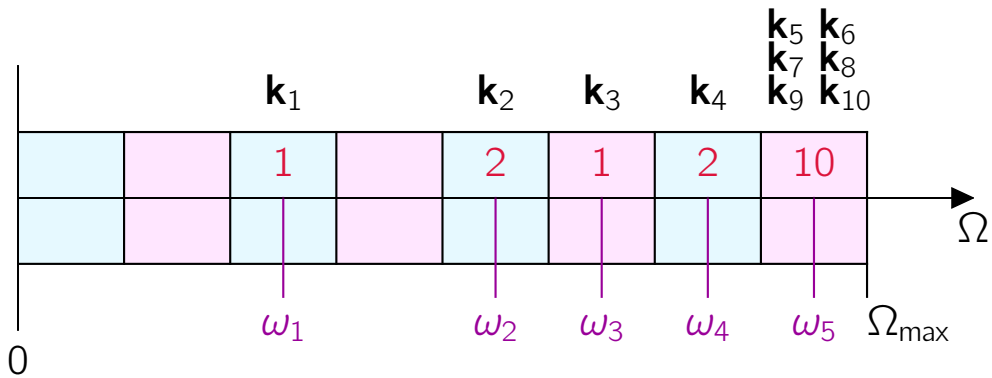


FIG. 8. Mapping of momentum grid onto an energy grid for $\ell = 8$. The Interval $\{0, \Omega_{\text{max}}\}$ into ℓ equidistant energy bins (blue and magenta) and for each momentum vector \mathbf{k}_{PZ} the associated bin is determined. The red numbers give the total weight of all vectors within the energy bin, so for example the energy bin ω_5 has the momentum vectors $\{\mathbf{k}_5, \mathbf{k}_6, \mathbf{k}_7, \mathbf{k}_8, \mathbf{k}_9, \mathbf{k}_{10}\}$ that have a total weight of 10.

4) Convert Momentum Quadruples into Energy Quadruples

```

1: for  $\omega \in$  energybins do
2:   for  $k \in$  kweight@energybin [# $\omega$ ] do
3:     for  $q \in$  kquadruple [# $k$ ] do
4:        $\{k_1, k_2, k_3, k_4\} =$  kquadruple[# $k$ ][# $q$ ]
5:       Find energy bins associated with  $k_1, k_2, k_3$  and  $k_4 \rightarrow \{\omega_1, \omega_2, \omega_3, \omega_4\}$ 
6:       Safe energyquadruples [# $\omega$ ] [#equadruple] [{ $\omega_1, \omega_2, \omega_3, \omega_4$ }]
7:       energyweight = integrals [# $k$ ] [# $q$ ] * vertices [# $k$ ] [# $q$ ] * kweight [# $k$ ]
8:       Set energyweights [# $\omega$ ] [#equadruple] = energyweight
9:     end for
10:  end for
11:  for equad  $\in$  energyquadruples [# $\omega$ ] do
12:    Check if the combination  $\{\omega_1, \omega_2, \omega_3, \omega_4\}$  has already been found
13:    if No then
14:      Save energyquadruples_consolidated [# $\omega$ ] [#equad.c] [{ $\omega_1, \omega_2, \omega_3, \omega_4$ }]
15:      energyweight_averaged = energyweights [# $\omega$ ] /kweight@energybin [# $\omega$ ]
16:      Save energyweights_consolidated [# $\omega$ ] [#equad.c] = energyweight_averaged
17:    else if Yes then
18:      energyweight_averaged = energyweights [# $\omega$ ] /kweight@energybin [# $\omega$ ]
19:      Add energyweights_consolidated [# $\omega$ ] [#equad.c] + = energyweight_averaged
20:    end if
21:  end for
22: end for

```

We then use the consolidated quadruples in energy space to compute the time evolution using the two-step Adams–Bashforth linear multistep method.

5.5 Linearized kinetic equation

The so far unpublished results in this chapter build on the results about the nonequilibrium phase transition and the nonequilibrium condensed phase in publication [II](#), focusing on the dynamics of the system that lead up to the steady state. In order to analyze the slow modes of the system in the limit of weak driving, we start from the full kinetic equation given by

$$\partial_t n_\omega = \gamma_{\text{in}}(1 + n_\omega) - \gamma_{\text{out}} \left(n_\omega + \frac{n_\omega^2}{n_{T_{\text{ni}}}} \right) + \mathcal{S}[\{n_\omega\}] \quad (5.102a)$$

$$\partial_t n_\omega = \gamma_{\text{in}} + (\gamma_{\text{in}} - \gamma_{\text{out}}) n_\omega - \gamma_{\text{out}} \left(\frac{n_\omega}{n_{T_{\text{ni}}}} \right)^2 + \mathcal{S}[\{n_\omega\}] \quad (5.102b)$$

with the full collision integral \mathcal{S} encoding the rearrangement of magnon occupations due to magnon-magnon interactions and $n_{T_{\text{ni}}}$ being a thermal distribution without a chemical potential at temperature T_{ni} (noninteracting temperature), as defined in Eq. (5.80). These scattering processes conserve both the number of magnons \mathcal{N} and the energy \mathcal{E} , which in the discretized system are given by

$$\mathcal{N} = \sum_{m=1}^{\omega_{\text{max}}} \rho(\omega_m) n(\omega_m) \quad (5.103a)$$

$$\mathcal{E} = \sum_{m=1}^{\omega_{\text{max}}} \rho(\omega_m) n(\omega_m) \omega_m, \quad (5.103b)$$

where $\rho(\omega_m)$ is the discretized density of states. We linearize the scattering matrix \mathcal{S} around a thermal distribution $n_{\text{th}}(T)$ at a given temperature T by initializing the system with a distribution where just one frequency deviates from the thermal distribution by a shift ν , i.e.

$$n(t_0) = n_{\text{th}}(T) + \nu \delta(\omega_i) \quad (5.104)$$

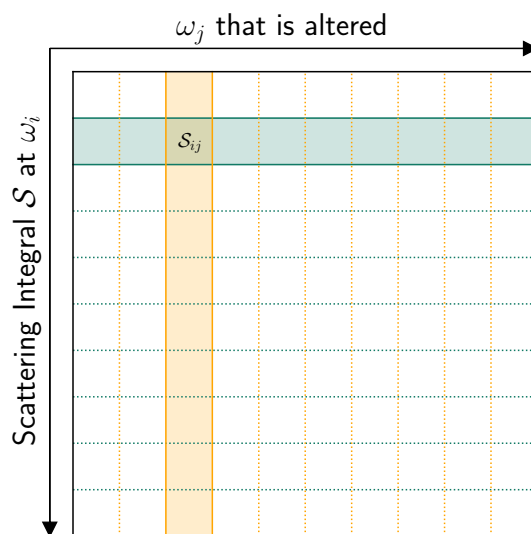


Figure 5.6: Schematic illustration of the linearized scattering matrix. Multiplying this matrix by a vector that only deviates from zero at a frequency ω_j will extract the orange column and therefore give the change within one timestep.

and then computing the scattering integrals for each frequency in the first timestep as the system evolves without drive or dissipation. By determining these scattering integrals for a deviation in all frequencies w_i and deviding the resulting matrix elements by the shift ν , we can build the full linearized scattering matrix \mathcal{S}_{lin} that satisfies the equation

$$n_i(dt) = n_i(t_0) + dt \sum_j \mathcal{S}_{\text{lin}}^{ij} \delta n_j \quad (5.105)$$

where we have defined δn to be a small deviation of the initial distribution $n(t_0)$ from the thermal distribution $n_{\text{th}}(T)$. The precise form of the linearized scattering matrix is displayed in Fig. 5.6. Note that the linearized scattering matrix is non-symmetric, but has real, nonnegative eigenvalues Γ which are directly related to the relaxation times to equilibrium when the system is initialized with a distribution that deviates slightly from the equilibrium distribution. We know that by construction every thermal distribution is an eigenfunction of the full scattering matrix \mathcal{S} , and that \mathcal{S} conserves both the energy \mathcal{E} and the number of magnons \mathcal{N} . The numerically extracted scattering matrices for different system sizes all show two zero modes. However, all other modes have eigenvalues, and therefore relaxation rates, that remain nonzero even in the infinite system size limit, meaning that there is not a continuum of relaxation rates going down to zero. The spectrum of eigenvalues for four different system sizes and the finite-size scaling analysis revealing that the smallest eigenvalue remains nonzero as $\ell \rightarrow \infty$ is displayed in Fig. 5.7.

It is due to the smallest eigenvalue remaining nonzero, that we can assume that for small γ_{in} and γ_{out} the distribution has relaxed to a distribution that is close to, though not identical to a thermal distribution, and that the remaining dynamics can be characterized by the slow variables. In this case, the stationary states of the kinetic equation have two degrees of freedom, the distribution is fully described by an energy \mathcal{E} and a number of magnons \mathcal{N} . Differentiating between the high drive and low drive phase, the distribution can also be fully characterized by a

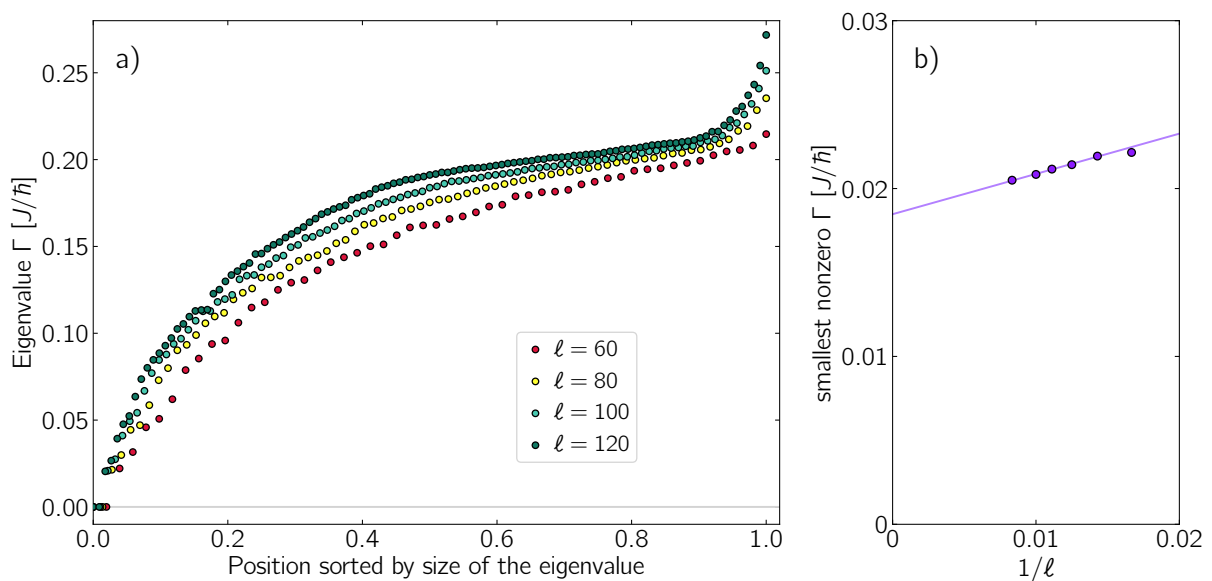


Figure 5.7: Analysis of the numerically extracted spectrum of eigenvalues: a) Eigenvalues Γ of the linearized scattering operator \mathcal{S}_{lin} for different system sizes ℓ sorted by magnitude, b) Scaling analysis for the smallest nonzero eigenvalue, revealing that the eigenvalue stays nonzero in the thermodynamic limit.

given temperature T and a chemical potential μ for $g < 1$ or a temperature T and a condensate fraction N_c for $g > 1$. So the two dimensional space of states that is stationary under the collision integral \mathcal{S} is spanned by either of these two sets of values and the most general form of the long time distribution is given by

$$n(\omega; T, \mu) = \mathcal{N}_c(t)\delta^{(2)}(\omega) + \frac{1}{e^{\frac{\omega-\mu(t)}{T(t)}} - 1}. \quad (5.106)$$

The two-dimensional delta-function $\delta^{(2)}(\omega)$ is defined as the limit of some integrable function whose area stays at one and which gets narrower and higher as the system size approaches the thermodynamic limit. Furthermore, it needs to satisfy $\int_0^\infty d\omega \rho(\omega)\delta^{(2)}(\omega) = 1$. For $\omega \rightarrow 0$ the density of states goes like $\rho(\omega) \sim \rho_0\omega$, thus

$$\delta^{(2)}(\omega) = \lim_{\sigma \rightarrow 0} \left[e^{-\frac{\omega^2}{2\sigma^2}} / (\rho_0\sigma^2) \right] \quad (5.107)$$

with

$$\frac{1}{\rho_0\sigma^2} \int_0^\infty \exp\left[-\frac{\omega^2}{2\sigma^2}\right] \rho_0\omega d\omega = 1 \quad (5.108)$$

is a possible definition that matches all criteria. The steady state for $g > 1$, in which there is no chemical potential and the condensate fraction is given by $\mathcal{N}_c(t_{\text{final}}) = \mathcal{D}_0$, is discussed in detail in publication [II](#). Due to the diverging magnon occupation at $\omega \rightarrow 0$, which can not be directly treated numerically, the condensate fraction needs to be extracted via a careful finite-size analysis. However, the distribution for $g < 1$ remains finite for all frequencies, so we can directly fit the interacting steady state with a negative chemical potential and a temperature T to the numerical data. This fit is displayed in [Fig. 5.8](#), where it is visible that the thermal fit very accurately corresponds to the steady state distribution.

5.5.1 The nonequilibrium condensed steady state

Starting from [Eq. \(5.103\)](#) we remember that the collision integral \mathcal{S} conserves both the number of magnons and the energy and use [Eq. \(5.102b\)](#) to write

$$\partial_t \mathcal{N} = \gamma_{\text{in}} \left(\sum_{\omega} \rho(\omega) \right) + (\gamma_{\text{in}} - \gamma_{\text{out}}) \mathcal{N} - \gamma_{\text{out}} \sum_{\omega} \rho(\omega) \left(\frac{n(\omega)}{n_{T_{\text{ni}}}(\omega)} \right)^2 \quad (5.109a)$$

$$\partial_t \mathcal{E} = \gamma_{\text{in}} \left(\sum_{\omega} \omega \rho(\omega) \right) + (\gamma_{\text{in}} - \gamma_{\text{out}}) \mathcal{E} - \gamma_{\text{out}} \sum_{\omega} \omega \rho(\omega) \left(\frac{n(\omega)}{n_{T_{\text{ni}}}(\omega)} \right)^2. \quad (5.109b)$$

At $\gamma_{\text{in}} = \gamma_{\text{out}} = 0$ the distribution $n(\omega)$ is thermal with a possible condensate fraction and chemical potential (depending on the initial values of \mathcal{E} and \mathcal{N}), because a thermal distribution is a fix point of the scattering operator \mathcal{S} . Therefore, we expect in the limit of weak driving, meaning γ_{in} and γ_{out} being small compared to the smallest eigenvalue Γ , that the distribution is given by thermal distribution with corrections $\gamma_{\text{out}}/\Gamma$. This justifies to consider [Eq. \(5.109\)](#) at $(g-1) > 0$ and to replace the general distribution $n(\omega)$ with a thermal distribution at $T = T_{\text{ni}} + T_{\Delta}$, where T_{Δ} is small and $\mu = 0$, plus a condensate fraction which has no effect on

the system energy. In order to facilitate notation we define

$$\mathcal{N}_0 = \sum_{\omega} \rho(\omega) \quad \mathcal{E}_0 = \sum_{\omega} \omega \rho(\omega) \quad (5.110a)$$

$$\mathcal{N}_T = \sum_{\omega} \rho(\omega) n_T(\omega) \quad \mathcal{E}_T = \sum_{\omega} \omega \rho(\omega) n_T(\omega) \quad (5.110b)$$

where $n_T(\omega)$ is a thermal distribution at temperature T . Using these definitions to reformulate Eq. (5.109b) in the stationary state, we obtain

$$0 = \gamma_{\text{in}} \mathcal{E}_0 + (\gamma_{\text{in}} - \gamma_{\text{out}}) \mathcal{E}_T - \gamma_{\text{out}} \sum_{\omega} \omega \rho(\omega) \left(\frac{\exp\left[\frac{\omega}{T_{\text{ni}}}\right] - 1}{\exp\left[\frac{\omega}{T_{\text{ni}} + T_{\Delta}}\right] - 1} \right)^2. \quad (5.111)$$

We can now Taylor expand

$$f(T_{\Delta}) = \left(\exp\left[\frac{\omega}{T_{\text{ni}} + T_{\Delta}}\right] - 1 \right)^{-2} \quad (5.112)$$

using the derivative

$$f'(T_{\Delta}) = -2 \left(\exp\left[\frac{\omega}{T_{\text{ni}} + T_{\Delta}}\right] - 1 \right)^{-3} \left[\frac{-\omega}{(T_{\text{ni}} + T_{\Delta})^2} \right] \exp\left[\frac{\omega}{T_{\text{ni}} + T_{\Delta}}\right], \quad (5.113)$$

so the leading order of $f(T_{\Delta})$ is given by

$$\text{Taylor}[f(T_{\Delta})]|_{T_{\Delta}=0} = \frac{1}{\left(\exp\left[\frac{\omega}{T_{\text{ni}}}\right] - 1\right)^2} + \frac{2 \frac{\omega}{T_{\text{ni}}^2} \exp\left[\frac{\omega}{T_{\text{ni}}}\right]}{\left(\exp\left[\frac{\omega}{T_{\text{ni}}}\right] - 1\right)^3} T_{\Delta} + \mathcal{O}[T_{\Delta}^2]. \quad (5.114)$$

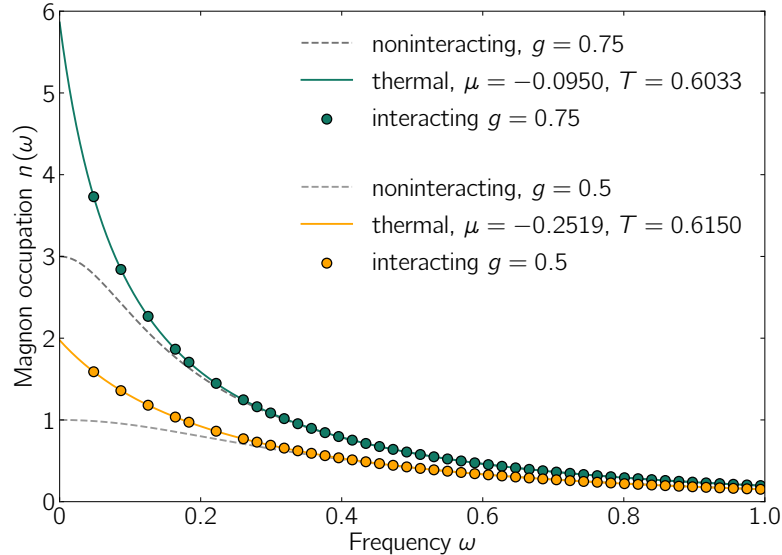


Figure 5.8: Steady state analysis for the subthermal regime ($g < 1$) in the limit of small γ_{in} and γ_{out} (here: $\gamma_{\text{out}} = 0.002$). The dashed lines indicate the noninteracting results for $g = \{0.5, 0.75\}$ and the dots show the interacting results. The solid green and orange lines are fits for thermal distributions with a negative chemical potential μ and a temperature T . The errors of both quantities are on the order of 0.0001.

5 Nonequilibrium phase transition

Linearizing in T_Δ we have

$$0 = \gamma_{\text{in}}\mathcal{E}_0 + (\gamma_{\text{in}} - \gamma_{\text{out}})\mathcal{E}_T - \gamma_{\text{out}} \sum_{\omega} \rho(\omega) \omega \left(1 + \frac{2 \frac{\omega}{T_{\text{ni}}} \exp\left[\frac{\omega}{T_{\text{ni}}}\right]}{\exp\left[\frac{\omega}{T_{\text{ni}}}\right] - 1} T_\Delta \right) \quad (5.115a)$$

$$0 = (\gamma_{\text{in}} - \gamma_{\text{out}})(\mathcal{E}_0 + \mathcal{E}_T) - 2T_\Delta \gamma_{\text{out}} \sum_{\omega} \rho(\omega) \left[\frac{\omega}{T_{\text{ni}}}\right]^2 \frac{\exp\left[\frac{\omega}{T_{\text{ni}}}\right]}{\exp\left[\frac{\omega}{T_{\text{ni}}}\right] - 1} \quad (5.115b)$$

and solving for T_Δ yields

$$T_\Delta = \frac{(g-1)(\mathcal{E}_0 + \mathcal{E}_T) T_{\text{ni}}^2}{2 \sum_{\omega} \rho(\omega) \omega^2 \exp\left[\frac{\omega}{T_{\text{ni}}}\right] \left(\exp\left[\frac{\omega}{T_{\text{ni}}}\right] - 1\right)^{-1}}. \quad (5.116)$$

Analogous to the energy analysis of the stationary state, we can analyze the stationary state of the magnon number for small driving. However, while the condensate fraction does not contribute to the system energy, it does contribute to the number of magnons in the system. We consider the stationary state with $\mathcal{N}_c(t_{\text{final}}) = \mathcal{D}_0$ and write

$$0 = \gamma_{\text{in}}\mathcal{N}_0 - \gamma_{\text{out}} \sum_{\omega} \rho(\omega) \left(e^{\frac{\omega}{T_{\text{ni}}}} - 1\right)^2 \left(\mathcal{D}_0 \delta^{(2)}(\omega) + \frac{1}{e^{\frac{\omega}{T}} - 1}\right)^2 + (\gamma_{\text{in}} - \gamma_{\text{out}})(\mathcal{D}_0 + \mathcal{N}_T) \quad (5.117a)$$

$$0 = \gamma_{\text{in}}\mathcal{N}_0 + (\gamma_{\text{in}} - \gamma_{\text{out}})(\mathcal{D}_0 + \mathcal{N}_T) - \gamma_{\text{out}} \sum_{\omega} \left\{ \rho(\omega) \frac{\left(e^{\frac{\omega}{T_{\text{ni}}}} - 1\right)^2}{\left(e^{\frac{\omega}{T}} - 1\right)^2} \right\} - \gamma_{\text{out}} \sum_{\omega} \left\{ \rho(\omega) \left(\mathcal{D}_0 \delta^{(2)}(\omega)\right)^2 \left(e^{\frac{\omega}{T_{\text{ni}}}} - 1\right)^2 + 2\rho(\omega) \mathcal{D}_0 \delta^{(2)}(\omega) \frac{\left(e^{\frac{\omega}{T_{\text{ni}}}} - 1\right)^2}{e^{\frac{\omega}{T}} - 1} \right\}. \quad (5.117b)$$

Here, we need to remember our definition of the two-dimensional delta-function as the limit of a Gaussian function in Eq. (5.107). For small frequencies we know that

$$\text{Taylor} \left[\left(e^{\frac{\omega}{T_{\text{ni}}}} - 1\right)^2 \right] \Big|_{\omega=0} = \left(\frac{\omega}{T_{\text{ni}}}\right)^2 + \mathcal{O} \left[\left(\frac{\omega}{T_{\text{ni}}}\right)^3 \right]. \quad (5.118)$$

Using

$$\left(\mathcal{D}_0 \delta^{(2)}\right)^2 \sim \frac{\mathcal{D}_0^2 e^{-\frac{\omega^2}{\sigma^2}}}{\rho_0^2 \sigma^4} \quad (5.119)$$

we can now write the blue term in Eq. (5.117b) as

$$\frac{\mathcal{D}_0^2}{T_{\text{ni}}^2 \rho_0^2 \sigma^4} \int_0^\infty d\omega \rho_0 \omega^3 e^{-\frac{\omega^2}{\sigma^2}} = \frac{\mathcal{D}_0^2}{2 T_{\text{ni}}^2 \rho_0} \quad (5.120)$$

where we have used Eq. (5.118) to express the integrand. The green term in Eq. (5.117b) becomes

$$\frac{2T}{T_{\text{ni}}\rho_0\sigma^2} \int_0^\infty \rho_0\omega^2 e^{-\frac{1}{2}\left(\frac{\omega}{\sigma}\right)^2} = \sigma\sqrt{2\pi} \left(\frac{T}{T_{\text{ni}}}\right). \quad (5.121)$$

In this form it is visible that the green term vanishes as $\sigma \rightarrow 0$. Keeping this in mind, we can write Eq. (5.117b) as

$$0 = \gamma_{\text{in}}\mathcal{N}_0 - \frac{\gamma_{\text{out}}}{2\rho_0 T_{\text{ni}}^2} \mathcal{D}_0^2 - \gamma_{\text{out}} \sum_{\omega} \rho(\omega) \frac{\left(e^{\frac{\omega}{T_{\text{ni}}}} - 1\right)^2}{\left(e^{\frac{\omega}{T}} - 1\right)^2} + (\gamma_{\text{in}} - \gamma_{\text{out}})(\mathcal{D}_0 + \mathcal{N}_T). \quad (5.122)$$

Linearizing in $T - T_{\text{ni}}$ in the same way as in the energy analysis we get

$$0 = (\gamma_{\text{in}} - \gamma_{\text{out}})(\mathcal{D}_0 + \mathcal{N}_T + \mathcal{N}_0) - \frac{\gamma_{\text{out}}}{2\rho_0 T_{\text{ni}}^2} \mathcal{D}_0^2 - \gamma_{\text{out}} \sum_{\omega} \rho(\omega) \left(\frac{2\frac{\omega}{T_W} \exp\left[\frac{\omega}{T_W}\right] T_{\Delta}}{\exp\left[\frac{\omega}{T_W}\right] - 1} \right) \quad (5.123)$$

$$0 = (\gamma_{\text{in}} - \gamma_{\text{out}})(\mathcal{D}_0 + \mathcal{N}_T + \mathcal{N}_0) - \frac{\gamma_{\text{out}}}{2\rho_0 T_{\text{ni}}^2} \mathcal{D}_0^2 - 2\frac{T_{\Delta}\gamma_{\text{out}}}{T_W^2} \sum_{\omega} \rho(\omega) \omega \left(1 + \frac{1}{\exp\left[\frac{\omega}{T_W}\right] - 1} \right) \quad (5.124)$$

$$0 = (\gamma_{\text{in}} - \gamma_{\text{out}})(\mathcal{D}_0 + \mathcal{N}_T + \mathcal{N}_0) - \frac{\gamma_{\text{out}}}{2\rho_0 T_{\text{ni}}^2} \mathcal{D}_0^2 - 2\frac{T_{\Delta}\gamma_{\text{out}}}{T_W^2} (\mathcal{E}_0 + \mathcal{E}_T), \quad (5.125)$$

where dropping the part linear in \mathcal{D}_0 and solving for \mathcal{D}_0^2 yields

$$\mathcal{D}_0^2 = 2\rho_0 T_{\text{ni}}^2 \left[(g-1)(\mathcal{N}_T + \mathcal{N}_0) - \frac{2}{T_W^2} (\mathcal{E}_0 + \mathcal{E}_T) T_{\Delta} \right]. \quad (5.126)$$

Finally we can use Eq. (5.116) for T_{Δ} to obtain

$$\mathcal{D}_0^2 = 2\rho_0 T_{\text{ni}}^2 (g-1) \left[(\mathcal{N}_T + \mathcal{N}_0) - \frac{(\mathcal{E}_0 + \mathcal{E}_T)^2}{\sum_{\omega} \rho(\omega) \omega^2 \left(1 + \frac{1}{\exp\left[\frac{\omega}{T_{\text{ni}}}\right] - 1} \right)} \right]. \quad (5.127)$$

Equation (5.127) states, that the squared condensate fraction \mathcal{D}_0^2 in the stationary state of a system with $g > 1$ and weak drive/dissipation is proportional to $(g-1)$. Figure 5.9 shows that scaling the y-axis with the square root of the linear system size and the x-axis with the linear system size collapses the curves for three different system sizes onto one function. Similar to the discussion of the finite-size scaling of the magnon number \mathcal{N} and the decay rate $\lambda_{\mathcal{N}}$ in publication II, the data-collapse of the condensate fraction implies that there is a function $f(x)$, such that

$$\mathcal{D}_0 = \frac{f((g-1)\ell)}{\sqrt{\ell}}. \quad (5.128)$$

Since we can assume that the condensate fraction is finite and nonzero in the thermodynamic limit, the function $f(x)$ needs to satisfy $f(x) \propto \sqrt{x}$, which means that in the thermodynamic

limit the condensate fraction satisfies $\mathcal{D}_0 \propto \sqrt{g-1}$, which is in agreement with Eq. (5.127).

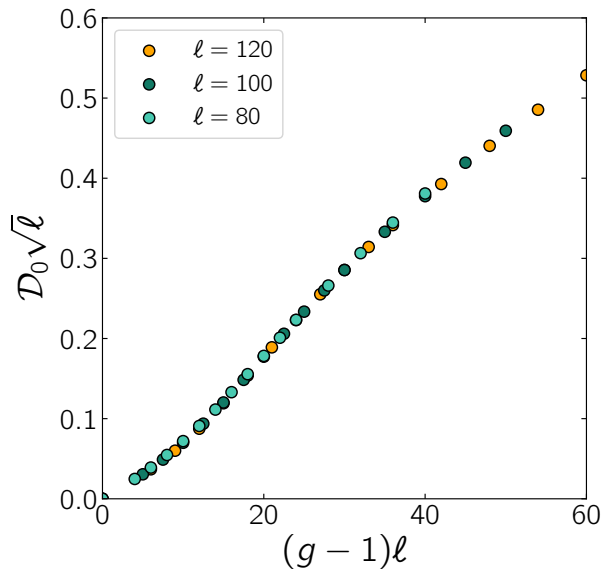


Figure 5.9: Finite size scaling analysis of the condensate fraction \mathcal{D}_0 as a function of the dimensionless tuning parameter g . It is visible that a scaling with $\mathcal{D}_0\sqrt{\ell}$ and $(g-1)\ell$ collapses the curves for three different linear system sizes ℓ onto one function, which is in agreement with the analysis of the linearized kinetic equation.

5.5.2 Long time limit of the kinetic equation

Up to now, we have been concentrating on the behavior in the nonequilibrium steady state, where it was advantageous to consider the discrete notation of the system energy as well as the kinetic equation in terms of γ_{in} and γ_{out} . We now focus on the dynamics that lead to the stationary state. Numerically, we find that at fixed γ_{out} and g there is a short, initial decay which depends on the observable, followed by an exponential decay which has the same decay rate for all observables. This observation confirms our analysis of the spectrum of eigenvalues, revealing that there is a smallest nonzero eigenvalue and therefore a smallest decay rate, which dominates the decay at long times.

Figure 5.10 shows the dynamics of the magnon distribution function $n(\omega)$ for two different magnitudes of γ_{out} at a fixed tuning parameter $g = 1.25$ at seven different magnon mode energies ω . In the left panel, it is visible that for large values of γ_{in} and γ_{out} , i.e. a system with strong drive and dissipation, the decay time is comparatively short, meaning the decay rate is large, and that the initial decay makes up a large part of the overall decay towards the stationary state. However, in the limit of small drive and dissipation, which is displayed in the right panel, the initial decay is short and the majority of the decay is dominated by a universal decay rate λ . For the displayed system size of $\ell = 120$, the difference between the magnitude of the smallest eigenvalues of \mathcal{S} ($\Gamma \approx 0.05$) is one order of magnitude larger than the decay rates in the system with drive and dissipation ($\lambda < 0.005$).

One explanation for the two different decay regimes with the universal decay rate λ in the long time limit would be, that the system first evolves on a fast time scale mainly under \mathcal{S} until

the two-dimensional space spanned by T and μ is reached and then evolves on a much smaller timescale within this space, where the decay rate is determined by drive and dissipation while \mathcal{S} can be neglected. However, if this was the case, the decay rate on the long time scale should be independent of the system size ℓ since the noninteracting distribution is independent at each frequency. However, the decay rate depends majorly on ℓ (see publication II). So while it is likely that \mathcal{S} indeed determines the relaxation on short time scales and brings the distribution close to the space spanned by T and μ , the assumption that \mathcal{S} can be neglected in the long time behavior seems to be wrong. Drive and dissipation are likely to cause the system to leave the subspace where \mathcal{S} can be neglected, such that the long time decay rate is an interplay of the decay rate determined by the eigenvalues Γ and the decay rates determined by g .

In order to gain further insight on the dynamics of the system in leading up to the steady state in the limit of weak driving, we write the kinetic equation in Eq. (5.102b) in units of γ_{out}^{-1} to obtain the dynamics in terms of the tuning parameter g , which yields

$$\frac{\partial n(\omega; T, \mu)}{\partial (\gamma_{\text{out}} t)} = g + (g - 1) n(\omega; T, \mu) - \left(\frac{n(\omega; T, \mu)^2}{n_{T_{\text{ni}}}^2} \right) + \frac{1}{\gamma_{\text{out}}} \mathcal{S}[\{n_\omega\}], \quad (5.129)$$

and consider the integral representation of the magnon number and the energy, which is given by

$$\mathcal{N} = \int d\omega \rho(\omega) n(\omega; T, \mu) \quad (5.130a)$$

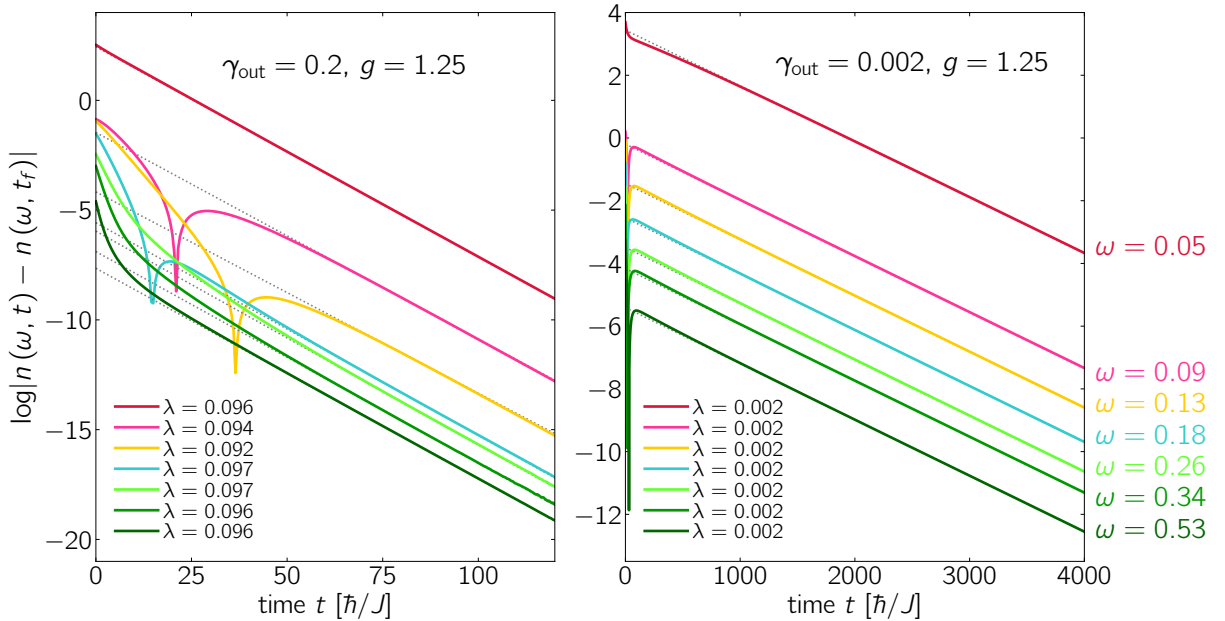


Figure 5.10: Decay of the magnon distribution function $n(\omega)$ at different magnon mode energies ω as a function of time. Displayed is the natural logarithm of the difference between the occupation at a time t and the occupation at the final time t_f in the stationary state. The dashed, grey lines are linear fits to the long time decay, which are used to extract the decay rate λ , the system size is $\ell = 120$. While the initial decay with individual decay rates for each frequency makes up a major part of the decay at $\gamma_{\text{out}} = 0.2$, the initial decay is very short for $\gamma_{\text{out}} = 0.002$ and the decay rate of the long term relaxation is independent of the frequency ω .

$$\mathcal{E} = \int d\omega \omega \rho(\omega) n(\omega; T, \mu). \quad (5.130b)$$

Using that both quantities are conserved under the scattering integral \mathcal{S} but are time dependent through drive and dissipation, the derivative of the magnon number \mathcal{N} yields

$$\frac{\partial \mathcal{N}}{\partial (\gamma_{\text{out}} t)} = \int d\omega \rho(\omega) \left(g + (g-1) n(\omega; T, \mu) - \left(\frac{n(\omega; T, \mu)^2}{n_{T_{\text{ni}}}^2} \right) \right) \quad (5.131a)$$

$$= g \left[\int d\omega \rho(\omega) \right] + (g-1) \left[\int d\omega \rho(\omega) n(\omega; T, \mu) \right] - \int d\omega \rho(\omega) \frac{n(\omega; T, \mu)^2}{n_{T_{\text{ni}}}^2} \quad (5.131b)$$

$$= (g-1) (\mathcal{N} + \mathcal{N}_0) + \mathcal{N}_0 - \int d\omega \rho(\omega) \frac{n(\omega; T, \mu)^2}{n_{T_{\text{ni}}}^2} \quad (5.131c)$$

and the derivative of the system energy \mathcal{E} yields

$$\frac{\partial \mathcal{E}}{\partial (\gamma_{\text{out}} t)} = (g-1) (\mathcal{E} + \mathcal{E}_0) + \mathcal{E}_0 - \int d\omega \omega \rho(\omega) \frac{n(\omega; T, \mu)^2}{n_{T_{\text{ni}}}^2}, \quad (5.132)$$

where we have defined the constants

$$\mathcal{N}_0 = \int d\omega \rho(\omega) \quad (5.133a)$$

$$\mathcal{E}_0 = \int d\omega \omega \rho(\omega). \quad (5.133b)$$

In order to derive the time dependence of the condensate fraction, we now need to consider the low drive regime ($g < 1$) and the high drive regime ($g > 1$) in the limit of weak driving ($\gamma_{\text{in}} < \Gamma$ and $\gamma_{\text{out}} < \Gamma$) separately. To do so, we use the same argumentation as before, namely that in the long time limit the dynamics are such, that the distribution $n(\omega)$ is close, but not identical to a thermal distribution with an a priori unknown temperature and either a chemical potential for $g < 1$, or a condensate fraction for $g > 1$.

In the subthermal phase the chemical potential is negative ($\mu < 0$) and there is no condensate ($N_c = 0$), meaning we can use Eq. (5.106) to define

$$I_{\mathcal{N}}(T, \mu) = \int d\omega \rho(\omega) \left(\frac{\exp\left[\frac{\omega}{T_{\text{ni}}}\right] - 1}{\exp\left[\frac{\omega - \mu}{T}\right] - 1} \right)^2 \quad (5.134a)$$

$$I_{\mathcal{E}}(T, \mu) = \int d\omega \omega \rho(\omega) \left(\frac{\exp\left[\frac{\omega}{T_{\text{ni}}}\right] - 1}{\exp\left[\frac{\omega - \mu}{T}\right] - 1} \right)^2 \quad (5.134b)$$

and use $I_{\mathcal{N}}(T_{\text{ni}}, 0) = \mathcal{N}_0$ and $I_{\mathcal{E}}(T_{\text{ni}}, 0) = \mathcal{E}_0$ to rewrite Eq. (5.131) and Eq. (5.132) as

$$\frac{\partial \mathcal{N}}{\partial (\gamma_{\text{out}} t)} = (g-1) (\mathcal{N}_0 + \mathcal{N}(T, \mu)) - [I_{\mathcal{N}}(T, \mu) - I_{\mathcal{N}}(T_{\text{ni}}, 0)] \quad (5.135a)$$

$$\frac{\partial \mathcal{E}}{\partial (\gamma_{\text{out}} t)} = (g-1) (\mathcal{E}_0 + \mathcal{E}(T, \mu)) - [I_{\mathcal{E}}(T, \mu) - I_{\mathcal{E}}(T_{\text{ni}}, 0)]. \quad (5.135b)$$

Since \mathcal{N} and \mathcal{E} are dependent on the time t only via the chemical potential μ and the temperature

T , we can define

$$A_{\mathcal{N}}^{\mu}(T, \mu) = \frac{\partial \mathcal{N}}{\partial \mu} = \int d\omega \frac{\rho(\omega) e^{\frac{\omega-\mu}{T}}}{T \left(e^{\frac{\omega-\mu}{T}} - 1 \right)^2} \quad (5.136a)$$

$$A_{\mathcal{N}}^T(T, \mu) = \frac{\partial \mathcal{N}}{\partial T} = \int d\omega \frac{\rho(\omega) (\omega - \mu) e^{\frac{\omega-\mu}{T}}}{T^2 \left(e^{\frac{\omega-\mu}{T}} - 1 \right)^2} \quad (5.136b)$$

$$A_{\mathcal{E}}^{\mu}(T, \mu) = \frac{\partial \mathcal{E}}{\partial \mu} = \int d\omega \frac{\rho(\omega) \omega e^{\frac{\omega-\mu}{T}}}{T \left(e^{\frac{\omega-\mu}{T}} - 1 \right)^2} \quad (5.136c)$$

$$A_{\mathcal{E}}^T(T, \mu) = \frac{\partial \mathcal{E}}{\partial T} = \int d\omega \frac{\rho(\omega) \omega (\omega - \mu) e^{\frac{\omega-\mu}{T}}}{T^2 \left(e^{\frac{\omega-\mu}{T}} - 1 \right)^2} \quad (5.136d)$$

and rewrite Eq. (5.135) as

$$\frac{1}{\gamma_{\text{out}}} \left(A_{\mathcal{N}}^{\mu}(T, \mu) \partial_t \mu + A_{\mathcal{N}}^T(T, \mu) \partial_t T \right) = (g - 1) (\mathcal{N}_0 + \mathcal{N}(T, \mu)) - [I_{\mathcal{N}}(T, \mu) - I_{\mathcal{N}}(T_{\text{ni}}, 0)] \quad (5.137a)$$

$$\frac{1}{\gamma_{\text{out}}} \left(A_{\mathcal{E}}^{\mu}(T, \mu) \partial_t \mu + A_{\mathcal{E}}^T(T, \mu) \partial_t T \right) = (g - 1) (\mathcal{E}_0 + \mathcal{E}(T, \mu)) - [I_{\mathcal{E}}(T, \mu) - I_{\mathcal{E}}(T_{\text{ni}}, 0)] . \quad (5.137b)$$

Given that μ is negative when $g < 1$, all derivatives in Eq. (5.136) except for Eq. (5.136a) are finite when $T \rightarrow T_{\text{ni}}$ and $\mu \rightarrow 0^-$. However, $A_{\mathcal{N}}^{\mu}$ diverges as $\mu \rightarrow 0^-$. Using $\rho(\omega) \sim \rho_0 \omega$ we can write the integral as

$$A_{\mathcal{N}}^{\mu}(T_{\text{ni}}, \mu) \sim \frac{\rho_0}{T_{\text{ni}}} \int_0^{\omega_{\text{max}}} d\omega \frac{\omega e^{\frac{\omega-\mu}{T_{\text{ni}}}}}{\left(e^{\frac{\omega-\mu}{T_{\text{ni}}}} - 1 \right)^2} \quad (5.138a)$$

$$= \omega_{\text{max}} \left(\frac{1}{1 - e^{\frac{\omega_{\text{max}} + |\mu|}{T_{\text{ni}}}}} - 1 \right) + T_{\text{ni}} \ln \left[\frac{e^{\frac{\omega_{\text{max}} + |\mu|}{T_{\text{ni}}}} - 1}{e^{\frac{|\mu|}{T_{\text{ni}}}} - 1} \right] . \quad (5.138b)$$

So for a chemical potential going to zero from the negative side ($\mu \rightarrow 0^-$), this integral diverges like

$$A_{\mathcal{N}}^{\mu}(T_{\text{ni}}, \mu) \xrightarrow{\mu \rightarrow 0^-} T_{\text{ni}} \ln \left[\frac{T_{\text{ni}}}{|\mu|} \right] . \quad (5.139)$$

The steady state distribution at $g < 1$ has a temperature that satisfies $T = T_{\text{ni}} - T_{\Delta}$, so we can linearize the right hand side of Eq. (5.137) by writing

$$\text{Taylor } [I_{\mathcal{N}}(T, \mu) - I_{\mathcal{N}}(T_{\text{ni}}, 0)]|_{\mu=0, T=T_{\text{ni}}} = I_{\mathcal{N}}^{\mu}(T_{\text{ni}}, 0) \mu + I_{\mathcal{N}}^T(T_{\text{ni}}, 0) (T - T_{\text{ni}}) \quad (5.140a)$$

$$= I_{\mathcal{N}}^{\mu}(T_{\text{ni}}, 0) \mu - I_{\mathcal{N}}^T(T_{\text{ni}}, 0) T_{\Delta} \quad (5.140b)$$

$$\text{Taylor } [I_{\mathcal{E}}(T, \mu) - I_{\mathcal{E}}(T_{\text{ni}}, 0)]|_{\mu=0, T=T_{\text{ni}}} = I_{\mathcal{E}}^{\mu}(T_{\text{ni}}, 0) \mu - I_{\mathcal{E}}^T(T_{\text{ni}}, 0) T_{\Delta} \quad (5.140c)$$

5 Nonequilibrium phase transition

with

$$I_{\mathcal{N}}^{\mu}(T_{\text{ni}}, 0) = \left. \frac{\partial I_{\mathcal{N}}}{\partial \mu} \right|_{\mu=0, T=T_{\text{ni}}} = \frac{2}{T_{\text{ni}}} \int d\omega \frac{\rho(\omega) e^{\frac{\omega}{T_{\text{ni}}}}}{\left(e^{\frac{\omega}{T_{\text{ni}}}} - 1 \right)} = \frac{2(\mathcal{N}_0 + \mathcal{N}(T_{\text{ni}}, 0))}{T_{\text{ni}}} \quad (5.141\text{a})$$

$$I_{\mathcal{N}}^T(T_{\text{ni}}, 0) = \left. \frac{\partial I_{\mathcal{N}}}{\partial T} \right|_{\mu=0, T=T_{\text{ni}}} = \frac{2}{T_{\text{ni}}^2} \int d\omega \frac{\rho(\omega) \omega e^{\frac{\omega}{T_{\text{ni}}}}}{\left(e^{\frac{\omega}{T_{\text{ni}}}} - 1 \right)} = \frac{2(\mathcal{E}_0 + \mathcal{E}(T_{\text{ni}}, 0))}{T_{\text{ni}}^2} \quad (5.141\text{b})$$

and

$$I_{\mathcal{E}}^{\mu}(T_{\text{ni}}, 0) = \left. \frac{\partial I_{\mathcal{E}}}{\partial \mu} \right|_{\mu=0, T=T_{\text{ni}}} = \frac{2}{T_{\text{ni}}} \int d\omega \frac{\rho(\omega) \omega e^{\frac{\omega}{T_{\text{ni}}}}}{\left(e^{\frac{\omega}{T_{\text{ni}}}} - 1 \right)} = \frac{2(\mathcal{E}_0 + \mathcal{E}(T_{\text{ni}}, 0))}{T_{\text{ni}}} \quad (5.142\text{a})$$

$$I_{\mathcal{E}}^T(T_{\text{ni}}, 0) = \left. \frac{\partial I_{\mathcal{E}}}{\partial T} \right|_{\mu=0, T=T_{\text{ni}}} = \frac{2}{T_{\text{ni}}^2} \int d\omega \rho(\omega) \omega^2 \left(\frac{1}{e^{\frac{\omega}{T_{\text{ni}}}} - 1} + 1 \right), \quad (5.142\text{b})$$

where all terms are finite. Equation (5.137) can now be written as

$$\frac{1}{\gamma_{\text{out}}} \left(A_{\mathcal{N}}^{\mu}(T_{\text{ni}}, 0) \partial_t \mu + A_{\mathcal{N}}^T(T_{\text{ni}}, 0) \partial_t T \right) = (g-1) [\mathcal{N}_0 + \mathcal{N}(T_{\text{ni}}, 0)] - I_{\mathcal{N}}^{\mu}(T_{\text{ni}}, 0) \mu + I_{\mathcal{N}}^T(T_{\text{ni}}, 0) T_{\Delta} \quad (5.143\text{a})$$

$$\frac{1}{\gamma_{\text{out}}} \left(A_{\mathcal{E}}^{\mu}(T_{\text{ni}}, 0) \partial_t \mu + A_{\mathcal{E}}^T(T_{\text{ni}}, 0) \partial_t T \right) = (g-1) (\mathcal{E}_0 + \mathcal{E}(T_{\text{ni}}, 0)) - I_{\mathcal{E}}^{\mu}(T_{\text{ni}}, 0) \mu + I_{\mathcal{E}}^T(T_{\text{ni}}, 0) T_{\Delta}, \quad (5.143\text{b})$$

or, in matrix notation

$$\frac{1}{\gamma_{\text{out}}} \begin{bmatrix} A_{\mathcal{N}}^{\mu}(T_{\text{ni}}, 0) & A_{\mathcal{N}}^T(T_{\text{ni}}, 0) \\ A_{\mathcal{E}}^{\mu}(T_{\text{ni}}, 0) & A_{\mathcal{E}}^T(T_{\text{ni}}, 0) \end{bmatrix} \begin{pmatrix} \partial_t \mu \\ \partial_t T \end{pmatrix} = (g-1) \begin{pmatrix} \mathcal{N}_0 + \mathcal{N}(T_{\text{ni}}, 0) \\ \mathcal{E}_0 + \mathcal{E}(T_{\text{ni}}, 0) \end{pmatrix} + \begin{bmatrix} -I_{\mathcal{N}}^{\mu}(T_{\text{ni}}, 0) & I_{\mathcal{N}}^T(T_{\text{ni}}, 0) \\ -I_{\mathcal{E}}^{\mu}(T_{\text{ni}}, 0) & I_{\mathcal{E}}^T(T_{\text{ni}}, 0) \end{bmatrix} \begin{pmatrix} \mu \\ T_{\Delta} \end{pmatrix}. \quad (5.144)$$

This is an intrinsically nonlinear equation because the matrix element $A_{\mathcal{N}}^{\mu}(T_{\text{ni}}, 0)$, here marked in green, is diverging like $A_{\mathcal{N}}^{\mu}(T_{\text{ni}}, 0) \sim T_{\text{ni}} \ln [T_{\text{ni}}/|\mu|]$ and the coefficients of the matrices on both sides depend upon T and μ , so the general time evolution is complicated. However, we numerically find that the long time value of μ is different from zero for $g < 1$, so to analyze the equation it is useful to first consider the steady state in which the stationary values are $T_{\Delta}(t_{\text{final}}) = T_{\Delta}^*$ and $\mu(t_{\text{final}}) = \mu^*$ and the derivatives on the left side of Eq. (5.144) are zero. The steady state equation is

$$(g-1) \begin{pmatrix} \mathcal{N}_0 + \mathcal{N}(T_{\text{ni}}, 0) \\ \mathcal{E}_0 + \mathcal{E}(T_{\text{ni}}, 0) \end{pmatrix} = - \begin{bmatrix} -I_{\mathcal{N}}^{\mu}(T_{\text{ni}}, 0) & I_{\mathcal{N}}^T(T_{\text{ni}}, 0) \\ -I_{\mathcal{E}}^{\mu}(T_{\text{ni}}, 0) & I_{\mathcal{E}}^T(T_{\text{ni}}, 0) \end{bmatrix} \begin{pmatrix} \mu^* \\ T_{\Delta}^* \end{pmatrix}, \quad (5.145)$$

and there is an implicit dependence on $(g-1)$ in both μ^* and T^* . With this, we can write

Eq. (5.144) in terms of the stationary values, yielding

$$\frac{1}{\gamma_{\text{out}}} \begin{bmatrix} A_{\mathcal{N}}^{\mu}(T_{\text{ni}}, 0) & A_{\mathcal{N}}^T(T_{\text{ni}}, 0) \\ A_{\mathcal{E}}^{\mu}(T_{\text{ni}}, 0) & A_{\mathcal{E}}^T(T_{\text{ni}}, 0) \end{bmatrix} \begin{pmatrix} \partial_t \mu \\ \partial_t T \end{pmatrix} = \begin{bmatrix} -I_{\mathcal{N}}^{\mu}(T_{\text{ni}}, 0) & I_{\mathcal{N}}^T(T_{\text{ni}}, 0) \\ -I_{\mathcal{E}}^{\mu}(T_{\text{ni}}, 0) & I_{\mathcal{E}}^T(T_{\text{ni}}, 0) \end{bmatrix} \left(\begin{pmatrix} \mu \\ T_{\Delta} \end{pmatrix} - \begin{pmatrix} \mu^* \\ T_{\Delta}^* \end{pmatrix} \right). \quad (5.146)$$

This equation has no direct dependence on $(g - 1)$, meaning the relaxation for $g < 1$ is not explicitly dependent on the distance from criticality. Yet, there is the implicit dependence on $(g - 1)$ through the values of μ^* and T_{Δ}^* , and we now consider the very long time limit in which the chemical potential μ is close to μ^* and the temperature T_{Δ} is close to T_{Δ}^* . Given that $A_{\mathcal{N}}^T$, $A_{\mathcal{E}}^{\mu}$ and $A_{\mathcal{E}}^T$ are smooth functions we can simply set $\mu = 0$ when evaluating these three integrals, but we need to explicitly denote the dependence on the chemical potential in the diverging function $A_{\mathcal{N}}^{\mu}$, which is marked green in Eq. (5.146). This diverging factor multiplies the time derivative of the chemical potential, which will make the relaxation of $\mu(t)$ slow, and we can solve for the temperature T assuming $\mu - \mu^*$ is varying very slowly in time, meaning that $T(t)$ will depend on the deviation of the chemical potential from its final value. Under the assumption that $\mu - \mu^*$ is constant in time, we get

$$T(t) \propto \exp \left[-\gamma_{\text{out}} t \frac{I_{\mathcal{E}}^T}{A_{\mathcal{E}}^T} \right] + \frac{I_{\mathcal{E}}^{\mu}}{I_{\mathcal{E}}^T} (\mu - \mu^*) + (T_{\text{ni}} - T_{\Delta}^*). \quad (5.147)$$

Given the rapid relaxation of $T(t)$ (rapid meaning on the scale of γ_{out}) we can now study the time dependence of $\mu(t)$ and find that due to the divergence of $A_{\mathcal{N}}^{\mu}$ the differential equation goes like

$$\frac{1}{\gamma_{\text{out}}} \log \left[\frac{T_{\text{ni}}}{\mu^*} \right] \mu \propto (\mu - \mu^*) \quad (5.148)$$

which means that there is a logarithmic divergence of the time constant as the coupling approaches the critical value from the subthermal side. Due to the implicit dependence of the stationary state value of the chemical potential on distance from criticality $\mu^* \sim (1 - g)$ from Eq. (5.145), these analytics predict the relaxation time to diverge like $\log [1/(1 - g)]$, meaning a weak divergence which is difficult to extract from finite-size data.

At $g > 1$ the chemical potential is zero and there is a time dependent condensate fraction $\mathcal{N}_c(t)$. In this case, Eq. (5.131c) becomes

$$\frac{1}{\gamma_{\text{out}}} A_{\mathcal{E}}^T(T_{\text{ni}}, 0) \partial_t T = g\mathcal{E}_0 + (g - 1) \mathcal{E}(T, 0) - I_{\mathcal{E}}(T, 0) \quad (5.149a)$$

$$= (g - 1) (\mathcal{E}_0 + \mathcal{E}(T, 0)) - [I_{\mathcal{E}}(T, 0) - I_{\mathcal{E}}(T_{\text{ni}}, 0)]. \quad (5.149b)$$

Linearizing around $T = T_{\text{ni}} + T_{\Delta}$ yields

$$\text{Taylor } [I_{\mathcal{E}}(T, 0) - I_{\mathcal{E}}(T_{\text{ni}}, 0)]|_{T=T_{\text{ni}}} = I_{\mathcal{E}}^T(T_{\text{ni}}, 0) (T - T_{\text{ni}}) \quad (5.150a)$$

$$= I_{\mathcal{E}}^T(T_{\text{ni}}, 0) T_{\Delta}, \quad (5.150b)$$

here with the opposite sign of the previous analysis because the steady state temperature is larger than the noninteracting temperature T_{ni} for $g > 1$. This allows to write a linearized form

5 Nonequilibrium phase transition

of Eq. (5.149b), namely

$$\frac{1}{\gamma_{\text{out}}} \left(\frac{A_{\mathcal{E}}^T(T_{\text{ni}}, 0)}{I_{\mathcal{E}}^T(T_{\text{ni}}, 0)} \right) \partial_t T_{\Delta} = (g - 1) \left(\frac{\mathcal{E}_0 + \mathcal{E}(T, 0)}{I_{\mathcal{E}}^T(T_{\text{ni}}, 0)} \right) - T_{\Delta}, \quad (5.151)$$

which means that the relaxation rate towards the steady state remains nonzero as $g \rightarrow 1$. In order to compute $\partial_t \mathcal{N}$, we need to consider the condensate fraction and write

$$\mathcal{N} = \mathcal{N}_c + \int d\omega \rho(\omega) n(\omega; T). \quad (5.152)$$

Following the same steps as in section 5.5.1 up to Eq. 5.125, but this time keeping the derivative of \mathcal{N} on the left side, we obtain

$$\frac{\partial \mathcal{N}}{\partial (\gamma_{\text{out}} t)} = (g - 1)(\mathcal{N}_c + \mathcal{N} + \mathcal{N}_0) - 2 \frac{T_{\Delta}}{T_{\text{ni}}^2} (\mathcal{E}_0 + \mathcal{E}) - \frac{1}{2\rho_0 T_{\text{ni}}^2} \mathcal{N}_c^2, \quad (5.153)$$

where the time dependence is in the temperature T and the condensate fraction \mathcal{N}_c , which means the left side yields

$$\frac{1}{\gamma_{\text{out}}} \left(\frac{\partial \mathcal{N}}{\partial \mathcal{N}_c} \partial_t \mathcal{N}_c + \frac{\partial \mathcal{N}}{\partial T} \partial_t T \right) = (g - 1)(\mathcal{N}_c + \mathcal{N} + \mathcal{N}_0) - 2 \frac{T_{\Delta}}{T_{\text{ni}}^2} (\mathcal{E}_0 + \mathcal{E}) - \frac{1}{2\rho_0 T_{\text{ni}}^2} \mathcal{N}_c^2. \quad (5.154)$$

On timescales such that T_{Δ} has relaxed to its final value, this simplifies to

$$\frac{1}{\gamma_{\text{out}}} \partial_t \mathcal{N}_c = (g - 1)(\mathcal{N}_c + \mathcal{N} + \mathcal{N}_0) - 2 \frac{T_{\Delta}}{T_{\text{ni}}^2} (\mathcal{E}_0 + \mathcal{E}) - \frac{1}{2\rho_0 T_{\text{ni}}^2} (\mathcal{N}_c)^2. \quad (5.155)$$

From Eq. (5.116) we know that T_{Δ} is proportional to $g - 1$, and the steady state analysis in section 5.5.1 revealed that $\mathcal{N}_c^2 \sim (g - 1)$, so to leading order in $g - 1$ we can drop \mathcal{N}_c in Eq. (5.155), yielding an equation of the form

$$\frac{1}{\gamma_{\text{out}}} \partial_t \mathcal{N}_c = (g - 1) C_1 - C_2 (\mathcal{N}_c)^2, \quad (5.156)$$

meaning the relaxation time diverges as $\sqrt{g - 1}$.

So in both the subthermal phase at $g < 1$ and the high drive phase at $g > 1$, the slow time dependence is driven by the slow time dependence of the chemical potential $\mu(t)$ and respectively the condensate fraction $\mathcal{N}_c(t)$, while the temperature $T(t)$ relaxes on a faster timescale. Due to the comparatively strong divergence ($\sim \sqrt{g - 1}$) in the high drive phase, the divergence of the relaxation time is in agreement with the numerical data and can be shown through an appropriate finite-size scaling analysis, as it is presented in publication II. However, the divergence is weak in the subthermal phase ($\sim \log[1/(1 - g)]$), and while we perceive a small dependence of the relaxation rate on the distance from criticality in publication II, it is difficult to extract the logarithmic divergence from our finite-size data. Hence the analysis presented in this chapter is consistent with the numeric computations, but the exponent of the critical slowing down can only be verified numerically for the condensed phase at $g > 1$.

6 | Light-cone spreading of correlations

Over the last two decades, there has been a variety of time-resolved spectroscopy experiments which measure the transient physical response of strongly correlated systems [7]. One powerful experimental technique is time- and angle-resolved photoemission spectroscopy (trARPES), which measures the single-particle spectral properties of quantum systems [3, 104–107]. Most other groups of spectroscopy experiments directly or indirectly measure two-point correlation functions, prominent examples being time resolved X-ray diffraction measuring equal time density-density correlations of the electron cloud as well as the nuclear lattice [108–112], time-resolved resonant inelastic X-ray scattering (tr-RIXS) gaining information about short-range spin correlations as well as valence density-density and charge-density correlations [113, 114] and a vast variety of optical methods (infrared spectroscopy, time-resolved Raman spectroscopy etc.) measuring, amongst others, current correlation functions [115, 116]. In publication I, we investigate the spread of density-density correlations in a one-dimensional correlated chain of spinless fermions under the influence of an electromagnetic field by using t-DMRG calculations [47]. In this chapter, we provide an introduction to the theory behind publication I by elucidating the duality between the Hamiltonian of the half-filled chain of spinless fermions and the XXZ-spin chain, as well as explaining the concept of dynamical localization.

6.1 The dual charge/spin Hamiltonian and dynamical localization

The Hamiltonian of the chain at half filling and with nearest neighbor Coulomb interactions is given by

$$H_{\text{ferm}}(t) = \sum_j \left[-\frac{J(t)}{2} (c_j^\dagger c_{j+1} + c_{j+1}^\dagger c_j) + U \left(n_j - \frac{1}{2} \right) \left(n_{j+1} - \frac{1}{2} \right) \right]. \quad (6.1)$$

The fermionic creation operator c_j^\dagger creates a fermion at lattice site j and the annihilation operator c_j destroys an electron at lattice site j . The particle number conserving local number operator is given by $n_j = c_j^\dagger c_j$. Here, the nearest neighbor Coulomb interaction $U > 0$ is constant in time, while the hopping amplitude $J(t)$ is time dependent once the chain is driven by an electromagnetic field. This *charge Hamiltonian* can be mapped onto a *fermionic Hamiltonian* by the Jordan-Wigner transformation [117], namely

$$c_j^\dagger = S_j^+ e^{-i\Phi_j} \quad (6.2a)$$

$$c_j = S_j^- e^{i\Phi_j} \quad (6.2b)$$

$$c_j^\dagger c_j = S_j^z + \frac{1}{2}, \quad (6.2c)$$

where the phase Φ is given by

$$\Phi_j = \pi \sum_{l < j} S_l^+ S_l^-. \quad (6.3)$$

6 Light-cone spreading of correlations

In order to write the charge Hamiltonian in terms of the spin-operators, we compute

$$c_j^\dagger c_{j+1} = S_j^+ S_{j+1}^- e^{i\pi n_j} \quad (6.4a)$$

$$= S_j^+ S_{j+1}^- \left(1 + n_j \sum_{m=1}^{\infty} \frac{(i\pi)^m}{m} \right) \quad (6.4b)$$

$$= S_j^+ S_{j+1}^- (1 - 2n_j) \quad (6.4c)$$

$$c_{j+1}^\dagger c_j = (1 - 2n_j) S_{j+1}^+ S_j^- \quad (6.4d)$$

such that the Hamiltonian in Eq. (6.1) becomes

$$H_{\text{XXZ}}(t) = \sum_j \left[-\frac{J(t)}{2} (S_j^+ S_{j+1} + S_{j+1}^+ S_j^-) + U S_j^z S_{j+1}^z \right]. \quad (6.5)$$

Here we have made use of the fact that we can write

$$S_j^+ (1 - 2n_j) \begin{pmatrix} |\uparrow\rangle \\ |\downarrow\rangle \end{pmatrix} = S_j^+ \left(\begin{pmatrix} |\uparrow\rangle \\ |\downarrow\rangle \end{pmatrix} - 2 \begin{pmatrix} |\uparrow\rangle \\ 0 \end{pmatrix} \right) = \begin{pmatrix} 0 \\ |\uparrow\rangle \end{pmatrix} = S_j^+ \begin{pmatrix} |\uparrow\rangle \\ |\downarrow\rangle \end{pmatrix} \quad (6.6a)$$

$$(1 - 2n_j) S_j^- \begin{pmatrix} |\uparrow\rangle \\ |\downarrow\rangle \end{pmatrix} = (1 - 2n_j) \begin{pmatrix} \downarrow \\ 0 \end{pmatrix} = \begin{pmatrix} \downarrow \\ 0 \end{pmatrix} = S_j^- \begin{pmatrix} |\uparrow\rangle \\ |\downarrow\rangle \end{pmatrix}, \quad (6.6b)$$

which implies that $S_j^+ (1 - 2n_j) = S_j^+$ and $(1 - 2n_j) S_j^- = S_j^-$. It is useful to keep in mind that the formulation in terms of the spin operators and the charge picture are equivalent, since some observations are more intuitive considering one of them. The interaction U between two neighboring occupied lattice sites in the charge picture corresponds to the Ising-type coupling between two spins, and the hopping J between two lattice sites is equivalent to a spin-flip. The Hamiltonian in Eq. (6.1) is schematically displayed in Fig. 6.1. Note that the Hubbard interaction is defined relative to half filling, so two neighboring filled (empty) sites, as displayed by the two neighboring red dots, mean an energy penalty of $U/2$.

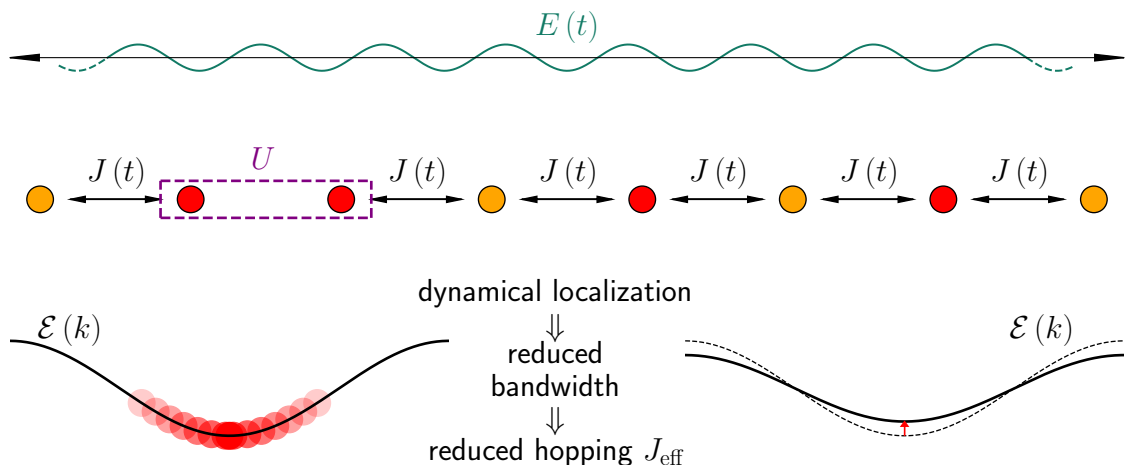


Figure 6.1: Schematic illustration of the influence of a periodic driving field on a half-filled chain of spinless fermions with hopping amplitude $J(t)$ and nearest neighbor Coulomb interaction U . The drive (top panel) adds a time dependence to the hopping J , which drives the the electron along the band (displayed in the bottom panel) such that the hopping is effectively reduced.

Two ways to add energy to the system are a quench or, as displayed in the upper panel of Fig. 6.1, a spatially uniform, time-periodic electric field. The field adds a time dependence to the hopping J which can be taken into account via the Peierls substitution [118], yielding

$$J(t) = J_0 e^{iA(t)} \quad (6.7a)$$

$$E(t) = -\partial_t A(t), \quad (6.7b)$$

where $E(t)$ is the electric driving field and $A(t)$ is the corresponding vector potential. Since we consider the drive to be uniform, we can assume both to be scalar functions. For simplicity, we now consider an infinite sinusoidal driving protocol with $E(t) = E_0 \sin(\Omega t)$ where E_0 is the field strength and Ω is the driving frequency. In the high frequency limit also known as Magnus limit, in which $\Omega \gg J, U$, meaning the driving frequency is larger than the intrinsic time and energy scales in the system [3], the steady state can be defined in a parametrically long intermediate time regime and the long time behavior can be characterized using a renormalized Hamiltonian, i.e. a Hamiltonian that is averaged over a period of the drive ($2\pi/\Omega$). In this case, the time dependent hopping $J(t)$ gets replaced with an effective hopping J_{eff} given by

$$J_{\text{eff}} = J_0 \mathcal{J}_0 \left(\frac{E_0}{\Omega} \right), \quad (6.8)$$

where \mathcal{J}_α is the Bessel function of first kind. Note that the argument of the Bessel function is smaller or equal to one, meaning the hopping is smaller than in equilibrium. This is schematically displayed in the bottom panel of Fig. 6.1, which displays the single particle band energy. In equilibrium, when both the hopping and the interaction are constant in time, the electron is at the bottom of the band. Once a periodic drive adds energy to the system and the hopping becomes time dependent, the electron is driven along the band and *sees* a band with reduced bandwidth. This effectively leads to a reduced hopping, which is known as dynamical localization. While we study a more complex drive, namely a drive that is ramped up over a certain time interval and a drive which is modulated with a Gaussian, in publication I, the general concept of dynamical localization in the Magnus limit is still applicable.

In equilibrium, the system displays a well defined phase transition at $U/J = 1$. If U/J is smaller than one, meaning the interaction is small compared to the hopping, the system is a Luttinger liquid, which is a gapless metal and does not display long range order. In this phase, the comparatively large hopping causes the charge density to be almost evenly distributed. In contrast, in the charge-density wave phase at $U/J > 1$, the interaction dominates, so the system does display long range correlations and the charge alternates between the lattice sites. In this case, the system is insulating and could be described as an antiferromagnet in the spin picture.

The metric or characterization tool of the phase transition is the density-density correlation function

$$C_{\text{ferm}}(\ell, t) = \left\langle \left(n_0(t) - \frac{1}{2} \right) \left(n_\ell(t) - \frac{1}{2} \right) \right\rangle, \quad (6.9)$$

whose equivalent in the spin picture is given by

$$C_{\text{XXZ}}(\ell, t) = \langle S_0^z(t) S_\ell^z(t) \rangle. \quad (6.10)$$

The correlation function states to what extent a spin at a certain lattice site ℓ is correlated with

the spin at a certain distance. Considering two spins that are far away from each other, the correlation function is zero in the Luttinger liquid, while there is a finite offset in the charge-density wave phase, since only the charge-density wave phase displays long range order. The equilibrium correlation function for two spins which are separated by 49 sites is displayed in Fig. 6.2 (orange), where it is visible that $C(t_0)$ is nonzero only in the charge-density wave phase at $U/J > 1$, where there are staggered long-range density-density correlations.

In contrast to the correlation function, the fluctuations which are computed by subtracting the classical part $\langle S_0^z(t) \rangle \langle S_\ell^z(t) \rangle$ off the correlation function, and therefore are given by

$$F_{\text{XXZ}}(\ell, t) = \langle S_0^z(t) S_\ell^z(t) \rangle - \langle S_0^z(t) \rangle \langle S_\ell^z(t) \rangle, \quad (6.11)$$

are largest around the phase transition, as it is visible in Fig. 6.2 (purple). While we focus on the spread of density-density correlations through the quantum chain upon laser driving in publication I, the fluctuations become important in manuscript III when extracting information about the entanglement in the driven system.

In an exact calculation for two infinitely distant spins, we would expect the fluctuations to diverge at the phase transition and the correlations to be exactly zero in the Luttinger liquid [119]. However, the DMRG-data in Fig 6.2 shows a peak which is not diverging and is slightly shifted towards $U/J > 1$ as well as a correlation function that has small deviations from zero in the Luttinger liquid phase. Despite our use of the t-DMRG method in the infinite system size limit [47], we can only evaluate fluctuations and correlations between two spins which are a finite distance apart from each other, which causes the fluctuations to be finite and the slight offset in the correlations at $U/J < 1$.

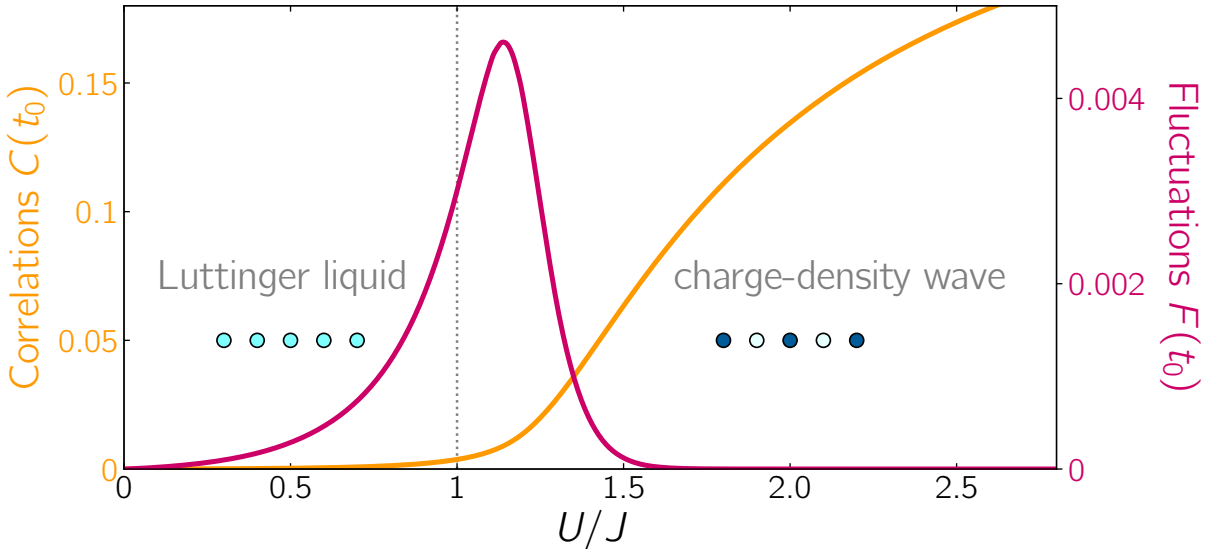


Figure 6.2: Equilibrium correlations and fluctuations of two lattice sites which are 49 sites apart in a half-filled chain of spinless fermions. The density-density correlation function $C(t)$ (orange, left y-axis) is zero in the Luttinger liquid, because the charge-density is evenly distributed (as indicated by the light blue points) and nonzero in the charge-density wave phase at $U/J > 1$, where there are long range correlations and the charge alternates (visualized through alternating blue points). The fluctuations (purple, right y-axis) peak at the phase transition at $U/J = 1$

Floquet-engineered light-cone spreading of correlations in a driven quantum chain

Mona H. Kalthoff,^{1,*} Dante M. Kennes,² and Michael A. Sentef^{1,†}

¹Max Planck Institute for the Structure and Dynamics of Matter, Luruper Chaussee 149, 22761 Hamburg, Germany

²Institut für Theorie der Statistischen Physik, RWTH Aachen University, 52056 Aachen, Germany



(Received 30 July 2019; revised manuscript received 4 October 2019; published 16 October 2019)

We investigate the light-cone-like spread of electronic correlations in a laser-driven quantum chain. Using the time-dependent density matrix renormalization group, we show that high-frequency driving leads to a Floquet-engineered spread velocity that determines the enhancement of density-density correlations when the ratio of potential and kinetic energies is effectively increased both by either a continuous or a pulsed drive. For large times we numerically show the existence of a Floquet steady state at not too long distances on the lattice with minimal heating. Intriguingly, we find a discontinuity of dynamically scaled correlations at the edge of the light cone, akin to the discontinuity known to exist for quantum quenches in Luttinger liquids. Our work demonstrates the potential of pump-probe experiments for investigating light-induced correlations in low-dimensional materials and puts quantitative speed limits on the manipulation of long-ranged correlations through Floquet engineering.

DOI: [10.1103/PhysRevB.100.165125](https://doi.org/10.1103/PhysRevB.100.165125)

I. INTRODUCTION

The control of materials properties with light is a growing research field [1]. Theoretical proposals for using light to change properties of interacting-electron systems range from spin systems [2–5] via one-dimensional Luttinger liquids and charge-density waves [6,7] and nonequilibrium superconductors [8–21] to correlated insulators [22–27]. However, in practice one often has to deal with heating effects that can blur Floquet-engineered properties [28,29].

A sweet spot in laser-driven correlated systems was identified in Ref. [6], where it was shown that high-frequency driving avoids runaway heating and tunes the system across a phase transition. Similarly, resonant laser excitation with phonons [30] has been demonstrated experimentally to lead to light-induced phases with enhanced interactions and induced order parameters [31–33]. However, in ultrafast materials science it is difficult to assess the actual correlation lengths involved in the buildup of correlations in real time. This is drastically different, for instance, in cold atoms in optical lattices, where light-cone-like spreading of correlations was demonstrated [34].

Here we show how light-cone spreading of correlations can also be triggered by high-frequency laser driving. By investigating a laser-driven one-dimensional quantum chain with real-time density matrix renormalization group (t-DMRG) calculations, we demonstrate how the spread of correlations is dictated by an instantaneous effective mode velocity that can be understood in terms of Floquet-renormalized effective Hamiltonian parameters. Moreover, we investigate the buildup of a Floquet steady-state for continuous laser driving and compare against thermal states. Finally, we find that a sufficiently fast switch-on of the drive leads to a kink at the edge of the

light cone, reminiscent of a dynamical phase transition after a quantum quench. Our combined results demonstrate the rich opportunities to tune correlations in periodically driven systems, provided that adequate off-resonant driving regimes can be identified.

II. MODEL AND METHOD

To analyze the influence of an electromagnetic driving field on a one-dimensional correlated chain of spinless fermions, we consider the Hamiltonian

$$H(t) = \sum_j \left[-\frac{J(t)}{2} c_j^\dagger c_{j+1} + \text{H.c.} + U \left(n_j - \frac{1}{2} \right) \left(n_{j+1} - \frac{1}{2} \right) \right]. \quad (1)$$

Here $U > 0$ is the nearest-neighbor Coulomb interaction and $J(t)$ the hopping amplitude, which becomes time-dependent in the driven case (see below). The operator $c_j^{(\dagger)}$ annihilates (creates) a fermion on lattice site j , and $n_j = c_j^\dagger c_j$ is the local number operator. Throughout this paper we assume an infinite chain at half filling. The influence of a spatially uniform, time-dependent electric field is taken into account by performing the Peierls substitution [35], yielding the time-dependent hopping $J(t) = J_0 \exp[iA(t)]$, where $A(t)$ is the vector potential corresponding to an electric field $E(t) = -\partial_t A(t)$. In the following we use $J_0 = 1$ as our unit of energy.

To set the stage for the nonequilibrium dynamics, we first characterize the well-known equilibrium phase diagram. The system has a quantum phase transition at $U/J = 1$. To characterize this phase transition, we compute the density-density correlation function

$$C(\ell, t) = \langle (n_0(t) - \frac{1}{2})(n_\ell(t) - \frac{1}{2}) \rangle. \quad (2)$$

This correlation function is shown for the ground state ($t = 0$) in Fig. 1 for the tenth (red) and the 50th (blue) lattice site

*mona.kalthoff@mpsd.mpg.de

†michael.sentef@mpsd.mpg.de

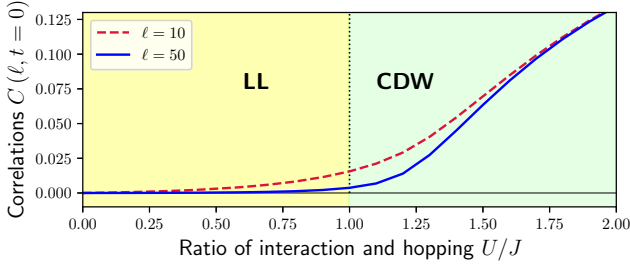


FIG. 1. Equilibrium quantum phase transition showing the transition from a Luttinger liquid (LL) to a charge-density wave (CDW) at $U/J = 1$ with nonzero long-ranged correlations.

as a function of U/J . When $U/J < 1$ the system is a gapless Luttinger liquid (LL), which does not display long-range charge density wave order. For $U/J > 1$ a gapped charge density wave (CDW) phase emerges with staggered long-range density-density correlations.

We now turn to the nonequilibrium dynamics. In the following we consider two different harmonic drives with frequency Ω in the high-frequency (Magnus) limit $\Omega \gg J, U$. The first is a drive that is ramped on over a time interval τ , with vector potential

$$A_D(t) = \frac{E_0}{\Omega} \sin(\Omega t) \left[0.5 + 0.5 \tanh\left(\frac{t - 5\tau}{\tau}\right) \right]. \quad (3)$$

This continuous-wave drive (CW-Drive) has previously been studied with the same DMRG method that we use in this paper [6]. Hence, it is known that in the Magnus regime the growth of entanglement limiting the DMRG calculations remains manageable due to the absence of runaway heating, and the long-time limit is accessible.

For high driving frequencies, it is known that a steady state can be defined in a parametrically long intermediate time regime [4,6,36]. Therefore, long-time physics can be described by a renormalized Hamiltonian, i.e., by a Hamiltonian that is averaged over a period of the drive. Averaging the time-dependent hopping $J(t)$ over the $2\pi/\Omega$ period yields the effective hopping

$$J_{\text{eff}} = J_0 \mathcal{J}_0\left(\frac{E_0}{\Omega}\right), \quad (4)$$

where \mathcal{J}_α is the Bessel function of the first kind [37]. Because the absolute value of the Bessel function is smaller than unity for any nonzero argument, the effective hopping is generically reduced compared to the equilibrium hopping. This implies that U/J is increased by the drive. Therefore the laser drive moves the system to the right in the phase diagram shown in Fig. 1, provided that the renormalization of U/J is the dominant effect of the laser. Below we will show that this is indeed the case provided that the parameters of the problem are carefully chosen.

Floquet theory [38] allows for an effective analytical study of periodically driven systems, but is restricted to time-periodic systems in analogy to Bloch theory for spatially periodic systems. Therefore most theoretical studies of Floquet-driven systems [4,39–56] assume the limit in which the drive was turned on in the infinitely distant past, which is impossible

to realize within an experiment. Nevertheless it has been shown that Floquet theory still captures the essential spectral features for a system driven by laser pulses of finite duration [57,58] if the system is probed on timescales sufficiently longer than the period of the driving field [59], and if the pulse envelope is even longer than the probe duration. We therefore also consider a periodic drive that is modulated with a Gaussian envelope, given by

$$A_G(t) = \frac{E_0}{\Omega} \sin(\Omega t) \exp\left[-\frac{(t - t_0)^2}{2\sigma^2}\right], \quad (5)$$

and compare our results to the system where the driving field is switched on and is kept switched on for long times.

The spread of correlations within a quantum many-body system is restricted by a maximal velocity, known as the Lieb-Robinson bound [60]. This bound is similar to the speed of light for the propagation of information in a relativistic quantum field theory. The corresponding light-cone effect has been demonstrated experimentally by quenching a one-dimensional quantum gas in an optical lattice [34]. The spread of correlations can be visualized as modes departing from two lattice sites and the information being propagated when the modes interfere in the middle [61]. Therefore the velocity with which correlations spread through the lattice after it is excited by a quench is given by twice the maximal mode velocity [62]. In the case of a LL, this means the expected velocity is given by

$$2v_{\text{LL}} = \frac{J\pi}{\hbar} \cdot \frac{\sin[\arccos(-U/J)]}{\pi - \arccos(-U/J)}. \quad (6)$$

To compare this velocity to our numerical data, where the system is not excited by a sudden quench, but rather an oscillatory laser drive that is turned on smoothly, we define a time-dependent effective hopping $J_{\text{eff}}(t)$, which is calculated via the envelope functions of the drives. For the ramped case and the Gaussian pulse, this effective time-dependent hopping is given by

$$J_{\text{eff}}^D(t) = J_0 \mathcal{J}_0 \left\{ \frac{E_0}{\Omega} \left[0.5 + 0.5 \tanh\left(\frac{t - 5\tau}{\tau}\right) \right] \right\}, \quad (7a)$$

$$J_{\text{eff}}^G(t) = J_0 \mathcal{J}_0 \left[\frac{E_0}{\Omega} \exp\left(-\frac{(t - t_0)^2}{2\sigma^2}\right) \right], \quad (7b)$$

respectively. Replacing J in Eq. (6) with $J_{\text{eff}}(t)$ yields the spread velocity

$$2v_{\text{LL}}(t) = \frac{J_{\text{eff}}(t)\pi}{\hbar} \cdot \frac{\sin\{\arccos[-U/J_{\text{eff}}(t)]\}}{\pi - \arccos[-U/J_{\text{eff}}(t)]}. \quad (8)$$

Note that this implies that $J_{\text{eff}}(t)$ decreases as the amplitude of the drive increases, and the velocity, which is dominated not by U/J but by J , decreases because J_{eff} is smaller than 1. This is illustrated in Fig. 2, which displays the vector potential $A_G(t)$, the corresponding renormalized hopping $J_{\text{eff}}(t)$, and the spread velocity $2v_{\text{LL}}(t)$ as a function of time. Below we will investigate to which extent the spread of correlations is indeed captured by the effective spread velocity given in Eq. (8) by comparing against the numerical data.

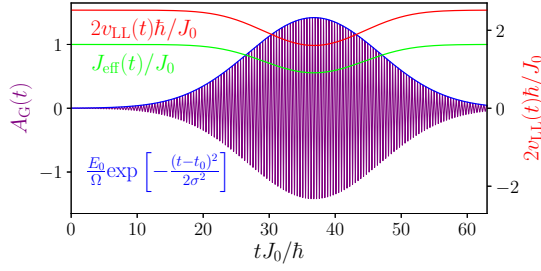


FIG. 2. Vector potential $A_G(t)$ as a function of time with driving frequency $\Omega/J_0 = 15$, maximal amplitude $E_0/\Omega = 1.421$, width $\sigma J_0/\hbar = 10$, and $t_0 J_0/\hbar = 36.77$ (purple, left y axis). The Gaussian envelope is displayed in blue, and the resulting Floquet-engineered hopping J_{eff}/J_0 is displayed in green. The right y axis refers to the time-dependent spread velocity $2v_{\text{LL}}(t)\hbar/J_0$ (twice the Luttinger velocity), which is displayed in red.

III. RESULTS

In this paper we consider three different interactions in the LL phase $U/J_0 = \{0.429, 0.500, 0.643\}$ and three different maximal amplitudes $E_0/\Omega = \{0.835, 1.111, 1.421\}$, which we found to be representative. This yields values of U/J_{eff} between 0.52 (LL) and 1.16 (CDW) at the maximal driving amplitude. The corresponding driving field profiles are shown in the upper panels of Figs. 3 and 4, respectively. Note that the values for the interaction and the driving amplitudes are chosen such that even though nine different combinations of

U/J_0 and E_0/Ω are given, there are only six corresponding values of U/J_{eff} . Thus the pairs Figs. 3(g) and 3(e), 3(f) and 3(j), as well as 3(i) and 3(k), and analogously for the corresponding pairs of panels in Fig. 4, have the same U/J_{eff} . The driving frequency is chosen to be $\Omega = 15J_0$, the ramp time of the ramped drive is $\tau J_0/\hbar = 5$ unless denoted otherwise, and the parameters of the Gaussian pulse are given by $\sigma J_0/\hbar = 10$ and $t_0 J_0/\hbar = 36.77$. The lower panels in Figs. 3 and 4 display the heat maps of the light-induced changes of correlations at even distances ℓ (odd distances have opposite sign) as a function of time t . Here we subtract off the initial correlations, and $C(\ell, t) - C(\ell, 0)$ is displayed on a logarithmic scale.

The green lines show the expected spread of correlations, with twice the largest possible mode velocity in the LL, as defined in Eq. (4), integrated from $t_{\text{start}} J_0/\hbar = 22.2$ for the CW-Drive and $t_{\text{start}} J_0/\hbar = 23.0$ to t for the pulse

$$\ell_{\text{eff}}(t, t_{\text{start}}) = \int_{t_{\text{start}}}^t 2v_{\text{LL}}(t') dt'. \quad (9)$$

The starting time t_{start} is chosen to best match the onset of enhanced correlations in the numerical data. Note that we tried to automatize the extraction of the wave front position as well as of t_{start} from the numerical data. However, we found that this requires the introduction of a somewhat arbitrary threshold value for the signal, which is why we prefer to not use an automatic extraction method to analyze the results. Nevertheless we find that, especially for small distances on the lattice, the wave front of the correlations computed with t-DMRG matches the green curves quite well. This

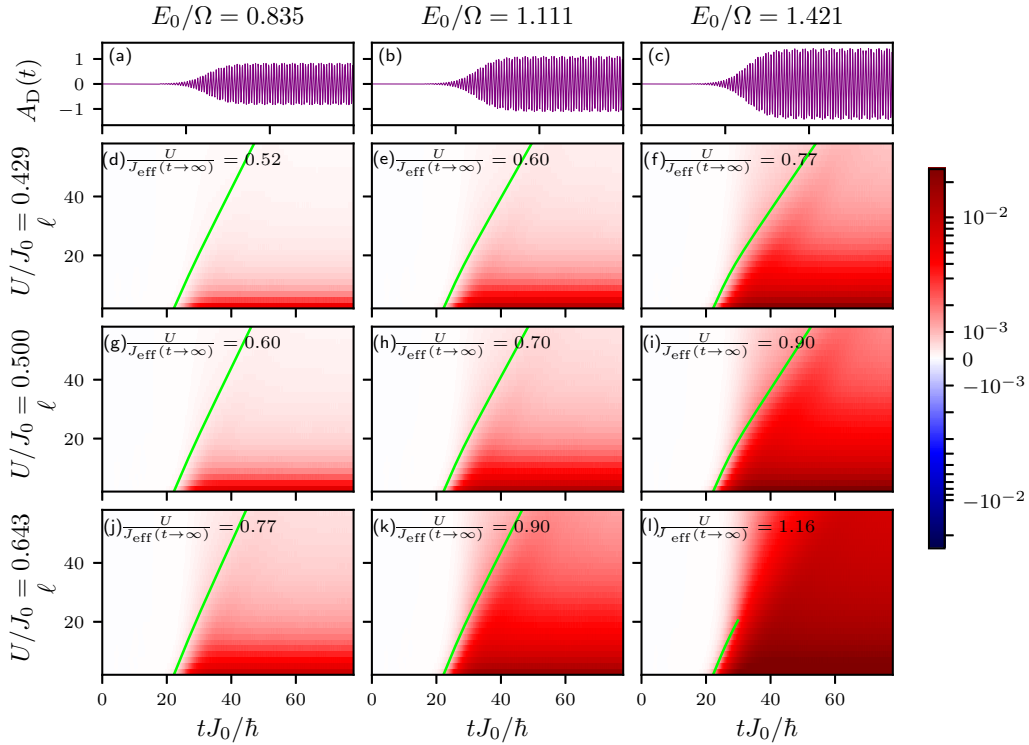


FIG. 3. Spread of correlations in the continuously driven chain. (a)–(c) Vector potential $A_D(t)$ of the ramped drives as a function of time with driving frequency $\Omega/J_0 = 15$ and ramp time $\tau J_0/\hbar = 5$. (d)–(l) Heatmaps of correlation changes $C(\ell, t) - C(\ell, 0)$ as a function of time t for even distances ℓ and three different values of U and E_0/Ω , as indicated. $J_{\text{eff}}(t_0)$ is the maximal amplitude of $A_D(t)$.

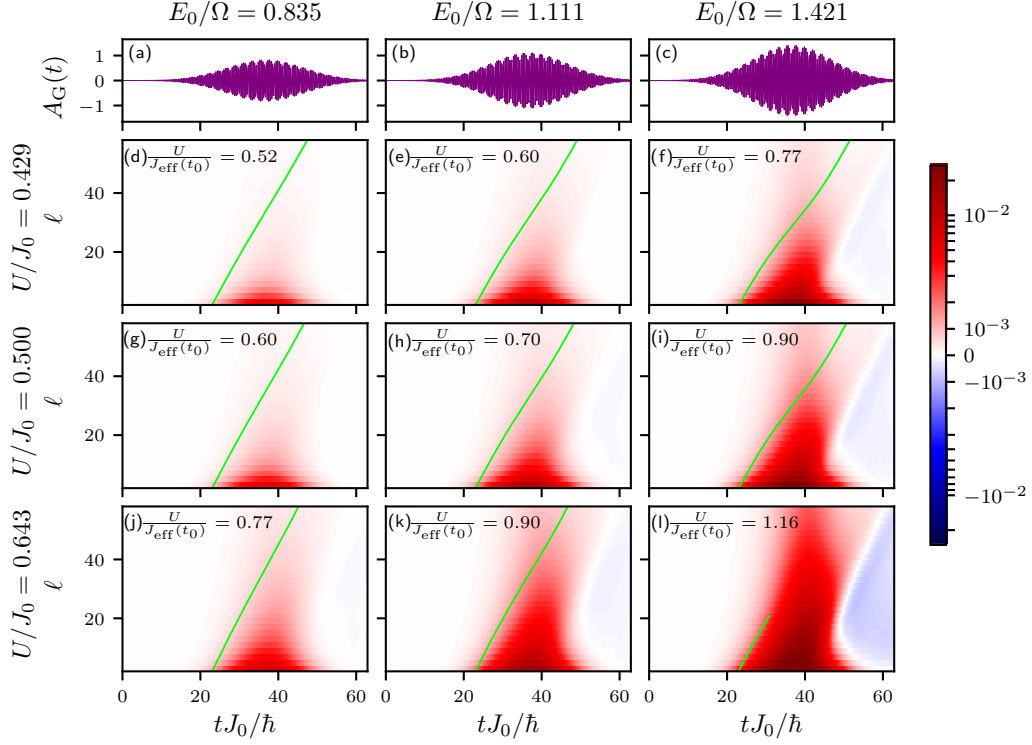


FIG. 4. Spread of correlations in the pulse-driven chain. (a)–(c) Vector potential $A_G(t)$ of the Gaussian drives as a function of time with driving frequency $\Omega/J_0 = 15$, width $\sigma J_0/\hbar = 10$, and $t_0 J_0/\hbar = 36.77$. (d)–(l) Heatmaps of correlation changes $C(\ell, t) - C(\ell, 0)$ as a function of time t at even distances ℓ for three different values of U and E_0/Ω , as indicated.

hints towards the validity of the concept of a time-dependent Floquet-engineered spread velocity. Moreover, the magnitude of the correlations increases as U/J_{eff} increases.

At the maximal drive envelope amplitude ($t \rightarrow \infty$), only the cases in Figs. 3(d) to 3(k) correspond entirely to the LL phase with $(U/J_{\text{eff}}(t_0)) = \{0.52, 0.6, 0.7, 0.77, 0.9\}$. The green curves match the data to a large extent in all of the shown cases. However, there are tails of correlations that exceed the $2v_{\text{LL}}$ limit, which have a suppressed magnitude compared to the major wave front that spreads with $2v_{\text{LL}}$ to a good approximation.

To compare more closely against time-resolved experiments, which typically employ a pump-probe setup with a pulsed driving envelope, we consider a sinusoidal field that is modulated with a Gaussian envelope. The correlation changes for such a Gaussian drive are displayed in Fig. 4. Here the time-dependent effective velocity also matches the major wave front. For the pulse we can also observe the relaxation dynamics after the pulse. While $C(\ell, t) - C(\ell, 0)$ is always nonnegative for the ramped drive, it does take slightly negative values when the field is switched off after the peak of the Gaussian pulse (see slightly blue areas in Fig. 4). This effect can be understood as a consequence of heating (see discussion below and Appendix), with reduced correlations at effective nonzero temperatures compared to zero temperature. Moreover, we find that enhanced correlations last longer at larger distances, as can be seen from the red areas bending over to the right in Fig. 4. This implies slower relaxation dynamics at larger distances, which is in accordance with

the same light-cone effect that causes slower enhancement of correlations at longer distances when the drive is first switched on.

According to Floquet theory, a periodic drive with a driving frequency in the high-frequency Magnus regime should induce a Floquet steady state at sufficiently long times. In Fig. 5 the correlations for three different distances on the lattice are displayed as a function of time. The panels on the left [Figs. 5(a), 5(c), and 5(e)] display the correlations for a pulsed system, and the panels on the right (Figs. 5(b), 5(d), and 5(f)) display the correlations for the ramped drive. Note that the scale of the y axis is different for all three distances (three rows) since the correlations are roughly ten times larger at $\ell = 6$ than at $\ell = 26$.

For the ramped case, the correlations are stabilized to a steady state at short [Fig. 5(b)] and intermediate [Fig. 5(d)] distances, but as expected we find longer thermalization times for larger distances in the lattice [Fig. 5(f)]. For the pulsed case, we find that the correlations at short [Fig. 5(a)] and intermediate [Fig. 5(d)] distances basically follow the driving pulse profile and return to the initial value almost perfectly shortly after the pulse, whereas for the longest distance shown here [Fig. 5(e)] the correlations are slightly suppressed below the initial value before thermalizing at longer times.

The dashed grey lines in the panels on the right indicate the correlations at thermal equilibrium for the U/J_{eff} (whose value is indicated by the arrows on the right) corresponding to the curves. The magnitude of these equilibrium correlations does not depend on U/J_0 and E_0/Ω separately, but is solely

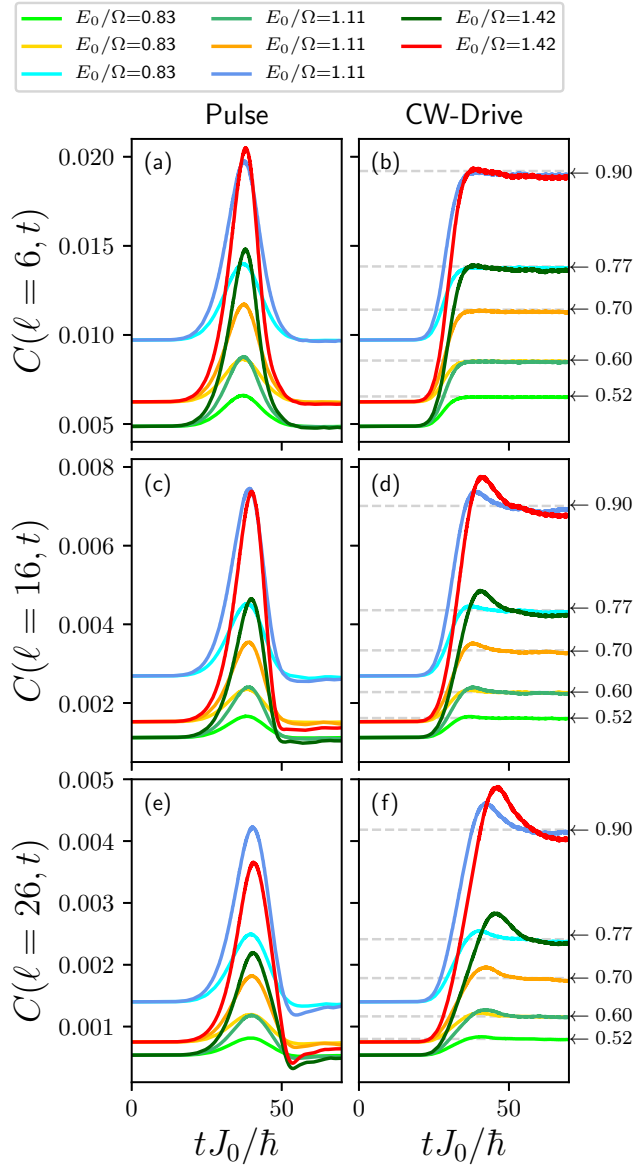


FIG. 5. Temporal evolution of correlations at short, intermediate, and long distances. Correlations $C(\ell, t)$ for a continuously driven system (left panels) and a pulsed system (right panels) with $\Omega/J_0 = 15$ and $\ell = 6$ (top), $\ell = 16$ (middle), and $\ell = 26$ (bottom). Note the different scale on the y axis for each ℓ . Driving: $\tau J_0/\hbar = 5$. Pulse: $\sigma J_0/\hbar = 10$, $t_0 J_0/\hbar = 36.77$. The grey lines indicate the correlations at thermal equilibrium (zero temperature) for the values of U/J_{eff} that are indicated with the arrows on the right.

determined by the value of $U/J_{\text{eff}}(t \rightarrow \infty)$. Note that due to the fact that three combinations of interaction strengths U/J_0 and maximal driving amplitudes E_0/Ω yield the same $U/J_{\text{eff}}(t \rightarrow \infty)$, there are only five different equilibrium correlations and corresponding steady-state values for the eight different cases shown. Indeed, we show in the Appendix that heating is negligible by computing the time-dependent energy absorption. The system evolves essentially adiabatically despite the fact that the LL phase is gapless and adiabaticity is not well defined in this case [63–65].

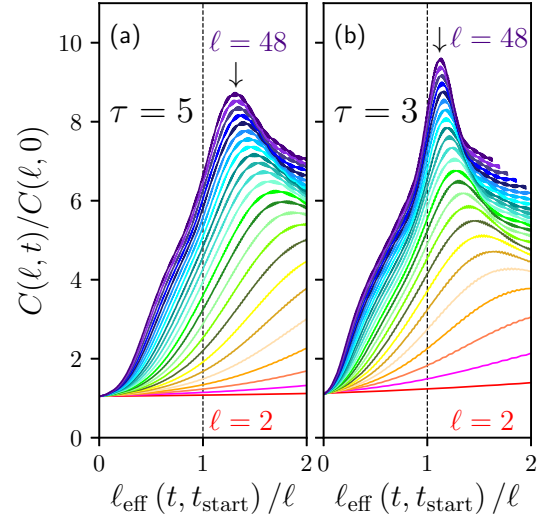


FIG. 6. Renormalized correlations as a function of dimensionless distance at increasing distances ℓ in the lattice for ramp times (a) $\tau J_0/\hbar = 5$ [same parameters as Fig. 3(i)], and (b) $\tau J_0/\hbar = 3$. Here $U/J_0 = 0.5$ and $U/J_{\text{eff}}(t \rightarrow \infty) = 0.9$. Different curves correspond to increasing even lattice distances as indicated.

We finally turn to the question of dynamical critical behavior when the system is driven between states with different correlation power laws. Within the LL phase, a scaling analysis shows that the correlations after a quench follow a different power law inside compared to outside the light cone, which necessarily leads to a kink in the renormalized correlation function at the edge of the light cone. This can be shown analytically for quenched systems, for example, in the interacting Tomonaga-Luttinger model [66,67]. In the following we identify an analogous kink at the edge of the light cone in our numerical data for driven systems.

To this end we show in Fig. 6 the correlation function $C(\ell, t)/C(\ell, t=0)$, for two different switch-on times of the ramped drive, as a function of the effective dimensionless spreading distance, given by $\ell_{\text{eff}}(t, t_{\text{start}})/\ell$. The initial and final values of U/J are within the LL phase in both cases. For large distances, where a power-law decay of correlations is expected, the kink should be located at $\ell_{\text{eff}}(t, t_{\text{start}})/\ell = 1$, i.e., at the edge of the light cone, which is indicated by the dashed line in Fig. 6.

Indeed no clear peak can be identified at short distances in both cases, but a peak emerges and moves towards the edge of the cone at intermediate distances. At large distances the peak is well defined and approaches a kink-like discontinuity. As expected, the peak develops more clearly when the ramp time is shorter [Fig. 6(b)] compared to the slower ramp [Fig. 6(a)]. Interestingly this result proves that dynamical quantum criticality with nonanalytic behavior can indeed not only be observed for quantum quenches but also for Floquet-driven systems, paving the way for the potential observation of such critical behavior in pump-probe experiments on solids.

IV. SUMMARY AND OUTLOOK

In this work we investigated in detail the Floquet-engineered spread of correlations in a driven quantum chain

with Luttinger liquid and charge-density wave phases. In particular, we showed that light-cone effects exist even in driven systems with finite ramp times and finite laser pulses when the velocity renormalization due to the driving field is properly taken into account. Our findings prove that thermalization of correlations at moderate distances happens relatively quickly, provided that heating can be largely avoided in the first place. In our study heating is effectively suppressed although the Luttinger liquid is gapless and the switch-on timescale of the laser drive is relatively fast. The suppression of heating is enabled by the choice of an off-resonant, large driving frequency.

The upshot from our results for laser-driven materials is that light-induced phase transitions and nonequilibrium materials engineering can be rationalized. In analogy with experiments on cold atomic gases [34] the effective correlation length that can be induced by nonequilibrium engineering of microscopic interactions is speed-limited only by the largest available relevant mode velocity. For example, for velocities on the order of 10^6 ms^{-1} , which is a typical scale for the Fermi velocity in graphene, a correlation length on the order of 10^{-6} m is established within half a picosecond. Correspondingly, for slower modes like phonons, magnons, or plasmons, the times for correlations on the micrometer level are longer. It would be highly intriguing to devise experiments that are able to measure such timescales for the buildup of correlations in Floquet-engineered materials, which might be possible with time-resolved scattering at x-ray free-electron lasers [68–70].

ACKNOWLEDGMENTS

We acknowledge helpful discussions with Andrew Millis and Michael Sekania. M.H.K. acknowledges financial support by the IMPRS-UFAST Program. Financial support by the DFG through the Emmy Noether program is gratefully acknowledged (D.M.K.: KA 3360/2-1; M.A.S.:SE 2558/2-1).

APPENDIX: ENERGY ABSORPTION

Here we briefly comment on the extraction of a Floquet steady-state energy in comparison to the ground-state energy of the Floquet-renormalized Hamiltonian, which proves that energy absorption is minimal and heating is avoided in the high-frequency driving regime. The upper two panels in Fig. 7 display the energy $h(t)$ as a function of time. The values of U/J_0 and E_0/Ω are chosen such that $U/J_{\text{eff}}(t \rightarrow \infty) = 0.60$ for both panels [analogous to Figs. 3(e) and 3(g)]. The numerically extracted period duration of the time-dependent energy, $h^{\text{av}}(t) = 0.838$, equals twice the period of the drive. By comparison to the ground-state energy for the Floquet-renormalized parameters with $U/J_{\text{eff}} = 0.60$, it becomes evident that the time-averaged energy of the driven system approaches exactly this ground-state energy in the long-time limit. This proves that heating is indeed minimal, as discussed in the main text in the context of Fig. 5.

Finally we illustrate that the energies corresponding to parameters that have the same $U/J_{\text{eff}}(t \rightarrow \infty) = 0.60$ are directly related to each other. Figure 7(c) displays the energy as a function of the inverse temperature β and shows that they are simply related by rescaling of all energies in the problem

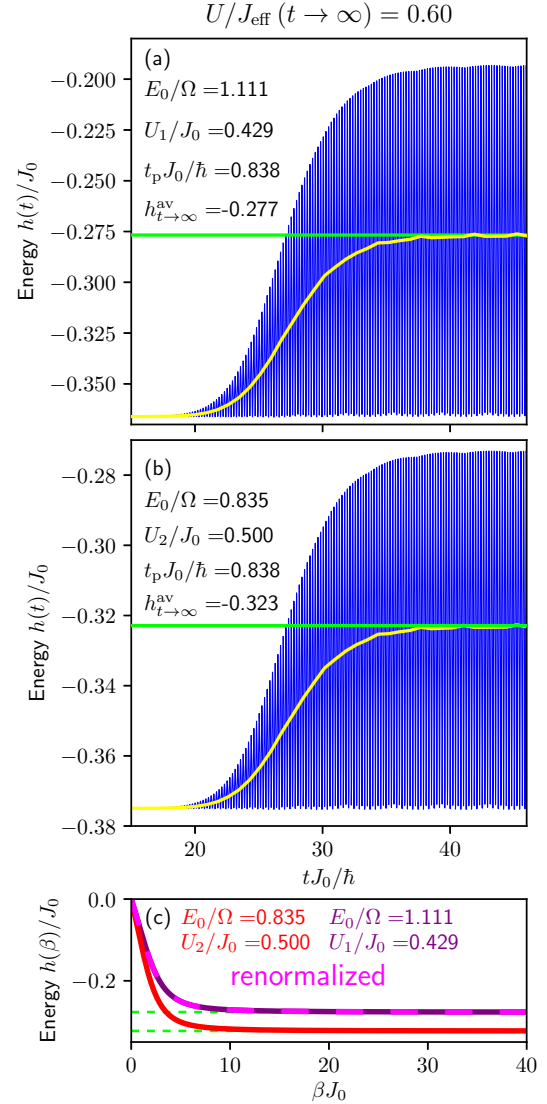


FIG. 7. Energy $h(t)$ as a function of time for (a) $U_1/J_0 = 0.429$ and $E_0/J_0 = 1.111$ and (b) $U_2/J_0 = 0.500$ and $E_0/J_0 = 0.835$, respectively, shown as rapidly oscillating blue curves. Averaging over the numerically determined period duration $t_p J_0/\hbar$ leads to the period-averaged energy $h^{\text{av}}(t)$ (yellow). In addition, we indicate in the legend the long-time limit $h^{\text{av}}_{t \rightarrow \infty}$. Green lines indicate the respective equilibrium energies of the Floquet-renormalized Hamiltonian at zero temperature. The frequency of the drive is $\Omega/J_0 = 15$ and the ramp time is $\tau J_0/\hbar = 5$. (c) Energy $h(\beta)$ as a function of inverse temperature for $U_1/J_0 = 0.429$ and $E_0/J_0 = 1.111$ [purple, same parameters as Fig. 3(g)] and $U_2/J_0 = 0.500$ and $E_0/J_0 = 0.835$ [red, same parameters as Fig. 3(e)]. A renormalization of $h(\beta)$ for the red curve ($U_1/J_0 = 0.500$, $E_0/J_0 = 0.835$) of both the x axis and the y axis with the ratio of energy scales, namely $U_1/U_2 = 0.858$, leads to the dashed magenta curve, which is identical to the purple curve ($U_1/J_0 = 0.429$ and $E_0/J_0 = 1.111$), showing that the curves are related by simple rescaling of all energies, as they should.

for the two cases shown. The nonequilibrium parameter E_0/Ω enters the equilibrium calculation as a parameter that renormalizes the effective hopping $J_{\text{eff}}(E_0/\Omega)$ [cf. Eq. (4) in the main text]. We show this parameter as a label in Fig. 7(c)

to allow for a direct comparison to the nonequilibrium cases shown in Figs. 7(a) and 7(b). Figure 7(c) indeed shows that the dashed magenta curve, which is the red curve rescaled by

the ratio of respective J_{eff} values for the two cases discussed here, is identical to the purple curve, confirming the expected behavior.

-
- [1] D. N. Basov, R. D. Averitt, and D. Hsieh, Towards properties on demand in quantum materials, *Nat. Mater.* **16**, 1077 (2017).
- [2] J. H. Mentink, K. Balzer, and M. Eckstein, Ultrafast and reversible control of the exchange interaction in Mott insulators, *Nat. Commun.* **6**, 6708 (2015).
- [3] M. Eckstein, J. H. Mentink, and P. Werner, Designing spin and orbital exchange Hamiltonians with ultrashort electric field transients, [arXiv:1703.03269](https://arxiv.org/abs/1703.03269).
- [4] M. Claassen, H.-C. Jiang, B. Moritz, and T. P. Devereaux, Dynamical time-reversal symmetry breaking and photo-induced chiral spin liquids in frustrated Mott insulators, *Nat. Commun.* **8**, 1192 (2017).
- [5] T. Oka and S. Kitamura, Floquet engineering of quantum materials, *Annu. Rev. Condens. Matter Phys.* **10**, 387 (2019).
- [6] D. M. Kennes, A. de la Torre, A. Ron, D. Hsieh, and A. J. Millis, Floquet Engineering in Quantum Chains, *Phys. Rev. Lett.* **120**, 127601 (2018).
- [7] D. M. Kennes, Transport through periodically driven correlated quantum wires, [arXiv:1801.02866](https://arxiv.org/abs/1801.02866).
- [8] Z. M. Raines, V. Stanev, and V. M. Galitski, Enhancement of superconductivity via periodic modulation in a three-dimensional model of cuprates, *Phys. Rev. B* **91**, 184506 (2015).
- [9] R. Höppner, B. Zhu, T. Rexin, A. Cavalleri, and L. Mathey, Redistribution of phase fluctuations in a periodically driven cuprate superconductor, *Phys. Rev. B* **91**, 104507 (2015).
- [10] F. Peronaci, M. Schiró, and M. Capone, Transient Dynamics of *d*-Wave Superconductors after a Sudden Excitation, *Phys. Rev. Lett.* **115**, 257001 (2015).
- [11] M. A. Sentef, A. F. Kemper, A. Georges, and C. Kollath, Theory of light-enhanced phonon-mediated superconductivity, *Phys. Rev. B* **93**, 144506 (2016).
- [12] M. Knap, M. Babadi, G. Refael, I. Martin, and E. Demler, Dynamical cooper pairing in nonequilibrium electron-phonon systems, *Phys. Rev. B* **94**, 214504 (2016).
- [13] D. M. Kennes, E. Y. Wilner, D. R. Reichman, and A. J. Millis, Transient superconductivity from electronic squeezing of optically pumped phonons, *Nat. Phys.* **13**, 479 (2017).
- [14] M. A. Sentef, Light-enhanced electron-phonon coupling from nonlinear electron-phonon coupling, *Phys. Rev. B* **95**, 205111 (2017).
- [15] Y. Murakami, N. Tsuji, M. Eckstein, and P. Werner, Nonequilibrium steady states and transient dynamics of conventional superconductors under phonon driving, *Phys. Rev. B* **96**, 045125 (2017).
- [16] Y. Wang, C.-C. Chen, B. Moritz, and T. P. Devereaux, Light-Enhanced Spin Fluctuations and *d*-Wave Superconductivity at a Phase Boundary, *Phys. Rev. Lett.* **120**, 246402 (2018).
- [17] D. M. Kennes, M. Claassen, M. A. Sentef, and C. Karrasch, Light-induced *d*-wave superconductivity through Floquet-engineered Fermi surfaces in cuprates, *Phys. Rev. B* **100**, 075115 (2019).
- [18] N. Dasari and M. Eckstein, Transient Floquet engineering of superconductivity, *Phys. Rev. B* **98**, 235149 (2018).
- [19] O. Hart, G. Goldstein, C. Chamon, and C. Castellano, Steady-state superconductivity in electronic materials with repulsive interactions, *Phys. Rev. B* **100**, 060508(R) (2019).
- [20] A. Sheikhan and C. Kollath, Dynamically enhanced unconventional superconducting correlations in a Hubbard ladder, [arXiv:1902.07947](https://arxiv.org/abs/1902.07947).
- [21] M. Claassen, D. M. Kennes, M. Zingl, M. A. Sentef, and A. Rubio, Universal optical control of chiral superconductors and Majorana modes, *Nat. Phys.* **15**, 766 (2019).
- [22] Y. Wang, M. Claassen, B. Moritz, and T. P. Devereaux, Producing coherent excitations in pumped Mott antiferromagnetic insulators, *Phys. Rev. B* **96**, 235142 (2017).
- [23] N. Tancogne-Dejean, M. A. Sentef, and A. Rubio, Ultrafast Modification of Hubbard U in a Strongly Correlated Material: *Ab initio* High-Harmonic Generation in NiO, *Phys. Rev. Lett.* **121**, 097402 (2018).
- [24] N. Walldorf, D. M. Kennes, J. Paaske, and A. J. Millis, The antiferromagnetic phase of the Floquet-driven Hubbard model, *Phys. Rev. B* **100**, 121110(R) (2019).
- [25] G. E. Topp, N. Tancogne-Dejean, A. F. Kemper, A. Rubio, and M. A. Sentef, All-optical nonequilibrium pathway to stabilising magnetic Weyl semimetals in pyrochlore iridates, *Nat. Commun.* **9**, 4452 (2018).
- [26] F. Peronaci, M. Schiró, and O. Parcollet, Resonant Thermalization of Periodically Driven Strongly Correlated Electrons, *Phys. Rev. Lett.* **120**, 197601 (2018).
- [27] D. Golez, M. Eckstein, and P. Werner, Multi-band nonequilibrium GW+EDMFT formalism for correlated insulators, [arXiv:1903.08713](https://arxiv.org/abs/1903.08713).
- [28] J. W. McIver, B. Schulte, F.-U. Stein, T. Matsuyama, G. Jotzu, G. Meier, and A. Cavalleri, Light-induced anomalous Hall effect in graphene, [arXiv:1811.03522](https://arxiv.org/abs/1811.03522).
- [29] S. A. Sato, J. W. McIver, M. Nuske, P. Tang, G. Jotzu, B. Schulte, H. Hübener, U. De Giovannini, L. Mathey, M. A. Sentef, A. Cavalleri, and A. Rubio, Microscopic theory for the light-induced anomalous Hall effect in graphene, *Phys. Rev. B* **99**, 214302 (2019).
- [30] M. Först, C. Manzoni, S. Kaiser, Y. Tomioka, Y. Tokura, R. Merlin, and A. Cavalleri, Nonlinear phononics as an ultrafast route to lattice control, *Nat. Phys.* **7**, 854 (2011).
- [31] D. Fausti, R. I. Tobey, N. Dean, S. Kaiser, A. Dienst, M. C. Hoffmann, S. Pyon, T. Takayama, H. Takagi, and A. Cavalleri, Light-induced superconductivity in a stripe-ordered cuprate, *Science* **331**, 189 (2011).
- [32] M. Mitrano, A. Cantaluppi, D. Nicoletti, S. Kaiser, A. Perucchi, S. Lupi, P. Di Pietro, D. Pontiroli, M. Riccò, S. R. Clark, D. Jaksch, and A. Cavalleri, Possible light-induced superconductivity in K_3C_{60} at high temperature, *Nature* **530**, 461 (2016).
- [33] E. Pomarico, M. Mitrano, H. Bromberger, M. A. Sentef, A. Al-Temimy, C. Coletti, A. Stöhr, S. Link, U. Starke, C. Cacho, R. Chapman, E. Springate, A. Cavalleri, and I. Gierz, Enhanced electron-phonon coupling in graphene with periodically distorted lattice, *Phys. Rev. B* **95**, 024304 (2017).

- [34] M. Cheneau, P. Barmettler, D. Poletti, M. Endres, P. Schauß, T. Fukuhara, C. Gross, I. Bloch, C. Kollath, and S. Kuhr, Light-cone-like spreading of correlations in a quantum many-body system, *Nature* **481**, 484 (2012).
- [35] A. P. Jauho and J. W. Wilkins, Theory of high-electric-field quantum transport for electron-resonant impurity systems, *Phys. Rev. B* **29**, 1919 (1984).
- [36] S. A. Weidinger and M. Knap, Floquet prethermalization and regimes of heating in a periodically driven, interacting quantum system, *Sci. Rep.* **7**, 45382 (2017).
- [37] W. Magnus, On the exponential solution of differential equations for a linear operator, *Commun. Pure Appl. Math.* **7**, 649 (1954).
- [38] G. Floquet, Sur les équations différentielles linéaires à coefficients périodiques, *Ann. Scient. Ec. Norm. Sup.* **12**, 47 (1883).
- [39] J. H. Shirley, Solution of the schrödinger equation with a Hamiltonian periodic in time, *Phys. Rev.* **138**, B979 (1965).
- [40] H. Sambe, Steady states and quasienergies of a quantum-mechanical system in an oscillating field, *Phys. Rev. A* **7**, 2203 (1973).
- [41] T. Oka and H. Aoki, Photovoltaic Hall effect in graphene, *Phys. Rev. B* **79**, 081406(R) (2009).
- [42] A. Hemmerich, Effective time-independent description of optical lattices with periodic driving, *Phys. Rev. A* **81**, 063626 (2010).
- [43] T. Kitagawa, T. Oka, A. Brataas, L. Fu, and E. Demler, Transport properties of nonequilibrium systems under the application of light: Photoinduced quantum Hall insulators without Landau levels, *Phys. Rev. B* **84**, 235108 (2011).
- [44] N. H. Lindner, G. Refael, and V. Galitski, Floquet topological insulator in semiconductor quantum wells, *Nat. Phys.* **7**, 490 (2011).
- [45] M. S. Rudner, N. H. Lindner, E. Berg, and M. Levin, Anomalous Edge States and the Bulk-Edge Correspondence for Periodically Driven Two-Dimensional Systems, *Phys. Rev. X* **3**, 031005 (2013).
- [46] T. Iadecola, D. Campbell, C. Chamon, Chang-Yu Hou, R. Jackiw, So-Young Pi, and S. V. Kusminskiy, Materials Design from Nonequilibrium Steady States: Driven Graphene as a Tunable Semiconductor with Topological Properties, *Phys. Rev. Lett.* **110**, 176603 (2013).
- [47] G. Usaj, P. M. Perez-Piskunow, L. E. F. Foa Torres, and C. A. Balseiro, Irradiated graphene as a tunable Floquet topological insulator, *Phys. Rev. B* **90**, 115423 (2014).
- [48] A. G. Grushin, Á. Gómez-León, and T. Neupert, Floquet Fractional Chern Insulators, *Phys. Rev. Lett.* **112**, 156801 (2014).
- [49] H. Dehghani, T. Oka, and A. Mitra, Dissipative Floquet topological systems, *Phys. Rev. B* **90**, 195429 (2014).
- [50] H. Dehghani, T. Oka, and A. Mitra, Out-of-equilibrium electrons and the Hall conductance of a Floquet topological insulator, *Phys. Rev. B* **91**, 155422 (2015).
- [51] M. Bukov, L. D'Alessio, and A. Polkovnikov, Universal high-frequency behavior of periodically driven systems: from dynamical stabilization to Floquet engineering, *Adv. Phys.* **64**, 139 (2015).
- [52] L. D'Alessio and M. Rigol, Dynamical preparation of Floquet Chern insulators, *Nat. Commun.* **6**, 8336 (2015).
- [53] A. Eckardt and E. Anisimovas, High-frequency approximation for periodically driven quantum systems from a Floquet-space perspective, *New J. Phys.* **17**, 093039 (2015).
- [54] T. Mikami, S. Kitamura, K. Yasuda, N. Tsuji, T. Oka, and H. Aoki, Brillouin-Wigner theory for high-frequency expansion in periodically driven systems: Application to Floquet topological insulators, *Phys. Rev. B* **93**, 144307 (2016).
- [55] A. Eckardt, *Colloquium: Atomic quantum gases in periodically driven optical lattices*, *Rev. Mod. Phys.* **89**, 011004 (2017).
- [56] G. S. Uhrig, M. H. Kalthoff, and J. K. Freericks, Positivity of the Spectral Densities of Retarded Floquet Green Functions, *Phys. Rev. Lett.* **122**, 130604 (2019).
- [57] M. A. Sentef, M. Claassen, A. F. Kemper, B. Moritz, T. Oka, J. K. Freericks, and T. P. Devereaux, Theory of Floquet band formation and local pseudospin textures in pump-probe photoemission of graphene, *Nat. Commun.* **6**, 7047 (2015).
- [58] M. H. Kalthoff, G. S. Uhrig, and J. K. Freericks, Emergence of Floquet behavior for lattice fermions driven by light pulses, *Phys. Rev. B* **98**, 035138 (2018).
- [59] Y. H. Wang, H. Steinberg, P. Jarillo-Herrero, and N. Gedik, Observation of Floquet-Bloch states on the surface of a topological insulator, *Science* **342**, 453 (2013).
- [60] E. H. Lieb and D. W. Robinson, The finite group velocity of quantum spin systems, *Commun. Math. Phys.* **28**, 251 (1972).
- [61] A. M. Läuchli and C. Kollath, Spreading of correlations and entanglement after a quench in the one-dimensional Bose-Hubbard model, *J. Stat. Mech.* (2008) P05018.
- [62] P. Calabrese and J. Cardy, Time Dependence of Correlation Functions Following a Quantum Quench, *Phys. Rev. Lett.* **96**, 136801 (2006).
- [63] B. Dóra, M. Haque, and G. Zaránd, Crossover from Adiabatic to Sudden Interaction Quench in a Luttinger Liquid, *Phys. Rev. Lett.* **106**, 156406 (2011).
- [64] D. M. Kennes, Adiabatically deformed ensemble: Engineering nonthermal states of matter, *Phys. Rev. B* **96**, 024302 (2017).
- [65] G. Mazza, From sudden quench to adiabatic dynamics in the attractive hubbard model, *Phys. Rev. B* **96**, 205110 (2017).
- [66] P. Chudzinski and D. Schuricht, Time evolution during and after finite-time quantum quenches in Luttinger liquids, *Phys. Rev. B* **94**, 075129 (2016).
- [67] M. Collura, P. Calabrese, and F. H. L. Essler, Quantum quench within the gapless phase of the spin $- \frac{1}{2}$ Heisenberg XXZ spin chain, *Phys. Rev. B* **92**, 125131 (2015).
- [68] M. Trigo, M. Fuchs, J. Chen, M. P. Jiang, M. Cammarata, S. Fahy, D. M. Fritz, K. Gaffney, S. Ghimire, A. Higginbotham, S. L. Johnson, M. E. Kozina, J. Larsson, H. Lemke, A. M. Lindenberg, G. Ndabashimiye, F. Quirin, K. Sokolowski-Tinten, C. Uher, G. Wang, J. S. Wark, D. Zhu, and D. A. Reis, Fourier-transform inelastic X-ray scattering from time- and momentum-dependent phonon-phonon correlations, *Nat. Phys.* **9**, 790 (2013).
- [69] S. Wall, S. Yang, L. Vidas, M. Chollet, J. M. Glowia, M. Kozina, T. Katayama, T. Henighan, M. Jiang, T. A. Miller, D. A. Reis, L. A. Boatner, O. Delaire, and M. Trigo, Ultrafast disordering of vanadium dimers in photoexcited VO₂, *Science* **362**, 572 (2018).
- [70] Y. Chen, Y. Wang, C. Jia, B. Moritz, A. M. Shvaika, J. K. Freericks, and T. P. Devereaux, Theory for time-resolved resonant inelastic x-ray scattering, *Phys. Rev. B* **99**, 104306 (2019).

7 | Entanglement dynamics

Strongly correlated materials in and out of equilibrium may feature phases that are characterized through short- or long-ranged many body entanglement and the identification of these phases requires knowledge of the entanglement content [120, 121]. Understanding and measuring this entanglement through quantities commonly referred to as *entanglement witnesses* is therefore essential for gaining a deeper insight of emergent phases of matter, especially in a nonequilibrium context where a quantification of the entanglement would allow for the distinction between thermal and nonthermal photoinduced states. The quantum Fisher information has been identified as a dynamic measure for entanglement, which is accessible through Bragg or neutron scattering experiments and can be used to detect multipartite entanglement in complex condensed-matter systems [122, 123]. In manuscript III we study the quantum Fisher information in a half filled chain of spinless fermions, as it is introduced in section 6.1. However, instead of considering a driven chain with a Floquet engineered hopping $J(t)$, we focus on a quench of the Coulomb repulsion $U(t)$ with a varying ramp speed v , i.e.

$$U(t) = vt. \quad (7.1)$$

This excitation protocol is experimentally relevant because interaction-quenches can effectively be achieved through laser driving of correlated materials [124, 125].

The quantum Fisher information can then be extracted from the t-DMRG data by taking the Fourier transformation of the fluctuations introduced in Eq. (6.11), namely

$$\mathcal{F}(q, t) = \frac{2L}{N} \sum_{\ell} e^{iq\ell} \{ \langle S_0^z(t) S_{\ell}^z(t) \rangle - \langle S_0^z(t) \rangle \langle S_{\ell}^z(t) \rangle \} \quad (7.2)$$

and evaluating the resulting function at $q = \pi$, i.e.

$$\mathcal{F}_Q(t) = \mathcal{F}(\pi, t). \quad (7.3)$$

Although the t-DMRG simulations are performed on an infinite chain [47, 126, 127], the Fourier transformation in Eq. (7.2) is computed over a finite number of lattice sites ($L = 198$ if not denoted differently), so there are weak finite-size effects in the data presented in this chapter. In addition to the t-DMRG data, we present exact diagonalization (ED) data ¹ for spin-chains up to 24 lattice sites, using the python QuSpin package [128]. However, due to the comparatively small system size accessible through ED, the ground state features nearly degenerate states and the computations require an infinitesimal staggered magnetic field. It is important to keep in mind that this staggered magnetic field noticeably influences both the height and the shape of the ED quantum Fisher information, while the quantum Fisher information extracted from the t-DMRG data is not computed using an additional field.

Figure 7.1 displays the quantum Fisher information both in equilibrium setup and in the quenched chain. The equilibrium curve computed with t-DMRG is given by the solid black

¹The ED computations were performed by Denitsa R. Baykusheva

line, which in the gapless phase is continuously increasing with distance to criticality at $U = 1$, reaches a maximum at the critical point and decays to zero in the antiferromagnetic phase. The equilibrium ED data, given by the dashed dark blue line, qualitatively agrees with the equilibrium DMRG data, but the exact height and the position of the maximum computed via ED is dependent on the staggered magnetic field. The four solid multicolored curves show the time evolution of the quantum Fisher information following an interaction quench starting at $U = 0$. The t-DMRG data displayed for different ramp velocities $v \in \{0.6, 0.8, 1.0, 1.2\}$ reveals that the quench generally increases the quantum Fisher information, and that the increase is larger for smaller ramp velocities. In contrast to the equilibrium curve, the dynamical quantum Fisher information shows not only a global first maximum, but also multiple local maxima at $U > 1$, and the position of the global maximum moves to the right upon increasing the ramp velocity.

The inset shows that the dynamical quantum Fisher information computed via ED for the same ramp velocities (dashed, shades of blue), approximately agrees with the t-DMRG data at $U(t) < 2$. After this initial increase, ED finite-size effects become important and the curves start to differ. However, while the bond dimension rapidly grows in the t-DMRG computations and restricts our simulation to shorter time scales, the ground state wavefunction is computed individually at each time step with ED, which allows to simulate comparatively large time spans. Overall, the enhancement of the quantum Fisher information following a quench shows that the quantum Fisher information is indeed a sensitive probe for criticality and phase transitions out of equilibrium.

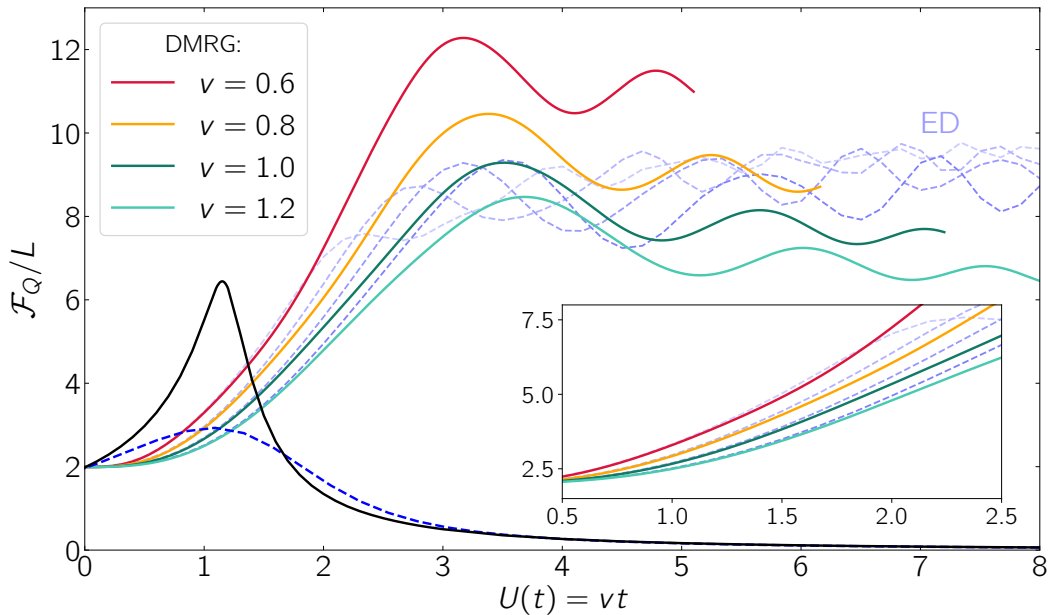


Figure 7.1: Dynamical quantum Fisher information for an interaction quenched chain computed via ED (blue lines, dashed) and t-DMRG (solid black and multicoloured lines). The solid black line is the DMRG equilibrium curve and the dashed dark blue curve is the ED equilibrium result. Both equilibrium curves feature a local maximum at $U(t) = 1$ and approach zero in the antiferromagnetic phase at $U > 1$. Note that the exact shape of the ED equilibrium curve depends on the staggered magnetic field, which is here given by $h_z = 0.05$. The multicolored solid lines (t-DMRG) for the quenched system at different ramp speeds v show an enhancement of the quantum Fisher information upon laser driving. The dashed lines in shades of blue are the corresponding ED results and the inset shows that the ED data qualitatively agrees with the t-DMRG data (computed for an infinite chain) below $U(t) = 2$.

Manuscript: Witnessing Nonequilibrium Entanglement Dynamics in a Quenched Quantum Chain

Denitsa R. Baykusheva,¹ Mona H. Kalthoff,² Damian Hofmann,² Martin Claassen,³ Dante M. Kennes,^{4,2} Michael A. Sentef,² and Matteo Mitrano¹

¹*Department of Physics, Harvard University, Cambridge, Massachusetts 02138, USA*

²*Max Planck Institute for the Structure and Dynamics of Matter, Center for Free-Electron Laser Science (CFEL), Luruper Chaussee 149, 22761 Hamburg, Germany*

³*Department of Physics and Astronomy, University of Pennsylvania, Philadelphia, PA 19104, USA*

⁴*Institut für Theorie der Statistischen Physik, RWTH Aachen University, 52056 Aachen, Germany and JARA-Fundamentals of Future Information Technology, 52056 Aachen, Germany*

(Dated: April 24, 2022)

Quantum materials driven out of equilibrium can host highly-entangled emergent states. The experimental detection of these many-body states requires the identification of entanglement signatures in the measured response functions both in and out of equilibrium. A possible protocol relies on the use of entanglement witnesses, such as the Quantum Fisher Information, in tandem with operator-specific quantum bounds. However, this method hinges upon the validity of the fluctuation-dissipation theorem and has not yet been applied to the physical response of nonequilibrium systems. Here, we investigate the entanglement dynamics in an XXZ quantum chain following an interaction quench. By linearly ramping the spin anisotropy, we observe an enhancement of multipartite entanglement, which manifests itself as a peak and subsequent oscillations of the dynamical quantum Fisher information. These features are nonadiabatic, i.e., not connected to the equilibrium XXZ phase diagram, and resilient to the introduction of different decoherence channels. We finally map our findings onto the experimentally relevant scenario of a quenched Hubbard U in a dual charge chain and discuss implications for time-resolved spectroscopic probes of both charge and spin degrees of freedom.

Introduction.— Many-body entanglement is a ubiquitous phenomenon in condensed matter physics [1–5]. Superconductors, quantum spin liquids, and certain quantum magnets, all feature complex wavefunctions involving entangled building blocks with either short- or long-ranged correlations [6–8]. Examples of such states include resonating valence-bond states comprised of dimerized singlet excitations [9], which have recently been experimentally realized in a programmable quantum simulator [10, 11], anyonic excitations in the Kitaev toric code model [12], or suggested wavefunctions potentially at the root of the strange metal that is observed in high-temperature superconductors [13]. While typically considered a *microscopic* phenomenon best observed in small atomic ensembles [13], quantum entanglement can persist in the thermodynamic limit and can have significant effects on the finite-temperature behavior of *macroscopic* systems [14–16]. This realization ignited an intense experimental and theoretical interest in devising means to probe many-body entanglement in quantum materials.

Entangled states in thermodynamic equilibrium can be diagnosed from response functions through the use of “entanglement witnesses” [1, 17], such as one- [18–20] and two-tangles [14, 20, 21], or the Quantum Fisher Information (QFI) [22–24]. In particular, the QFI is rigorously related to a sum-rule integral of the imaginary dynamical susceptibility [25] and has been recently used to quantify multipartite entanglement in neutron scattering experiments on low-dimensional spin systems [16, 26]. Crucially, by extracting information about quantum correlations encoded in the dynamical response of a mate-

rial, the QFI is able to discriminate quantum criticality at non-zero temperatures from thermal phase transitions [1, 25]. The QFI with respect to nonlocal operators can be used to detect topological quantum phase transitions in models such as the Kitaev chain [27], the Kitaev honeycomb model [28], and the toric code [29].

A particularly intriguing new application of entanglement witnesses, such as the QFI, would be the detection of entanglement correlations in driven quantum materials. Intense laser pulses have recently enabled the observation of emergent topological Floquet [30–32] and superconducting-like [33–35] states of matter, thus paving the way to the synthesis of coherent light-matter hybrids with novel electronic properties [36–39]. Certifying the presence of quantum entanglement far from equilibrium would allow the distinction between thermal and nonthermal photoinduced states [40, 41] and the identification of entangled nonequilibrium states without obvious order parameters. However, whether entanglement witnesses can detect and characterize nonequilibrium phase transitions in driven quantum materials through time-resolved response functions is still an open problem.

In this Letter, we tackle this challenge by witnessing the time-dependent entanglement dynamics in a quantum chain undergoing an interaction quench. We consider the experimentally relevant case of a quench of the Coulomb repulsion [42–45] in a dual spinless fermion (charge) chain, or anisotropic Heisenberg (spin) chain, and calculate the time-dependent QFI in both the charge and spin sectors. Upon globally ramping the interaction

strength, both models exhibit a time-dependent increase of the QFI, which is robust against decoherence and the presence of additional interactions that break integrability in the thermodynamic limit. The QFI dynamics qualitatively changes from an adiabatic to a diabatic quench regime with varying ramping speed, thus indicating that the quench speed crucially influences the multipartite entanglement of a quantum system. Our results indicate that the QFI is able to witness nonequilibrium entanglement dynamics and could be used to distinguish different dynamical regimes in driven materials.

Model.— We consider a half-filled chain of spinless fermions interacting through nearest neighbor Coulomb repulsion. The model Hamiltonian is given by

$$\hat{\mathcal{H}}_{\text{ch}}(t) = -\frac{J_{xy}}{2} \sum_j (\hat{c}_j^\dagger \hat{c}_{j+1} + \text{H.c.}) + U(t) \sum_j \tilde{n}_j \tilde{n}_{j+1}, \quad (1)$$

where \hat{c}_j^\dagger (\hat{c}_j) is a fermionic creation (annihilation) operator at site j , $\tilde{n}_j = \hat{c}_j^\dagger \hat{c}_j - 1/2$ is the number operator relative to half filling, and J_{xy} is a constant hopping amplitude which determines the energy scale of our model. The nearest-neighbor Coulomb interaction $U(t) = vt$ is time-dependent and ramped up at constant velocity v starting at $t = 0$. By applying a Jordan-Wigner transformation [46], this charge Hamiltonian maps onto an equivalent spin-1/2 anisotropic Heisenberg (XXZ) chain (Fig. 1a)

$$\hat{\mathcal{H}}_{\text{sp}}(t) = \sum_j \left[-\frac{J_{xy}}{2} (\hat{S}_j^+ \hat{S}_{j+1}^- + \text{H.c.}) + U(t) \hat{S}_j^z \hat{S}_{j+1}^z \right], \quad (2)$$

where $\hat{S}_j^\pm = \frac{1}{2} (\hat{S}_j^x \pm \hat{S}_j^y)$ and \hat{S}_j^α ($\alpha = x, y, z$) are the usual spin operators defined in terms of the Pauli matrices $\hat{S}^\alpha = \frac{1}{2} \hat{\sigma}^\alpha$. In this picture, the hopping amplitude J_{xy} becomes the exchange coupling while $\Delta(t) = U(t)/J_{xy}$ quantifies the anisotropy of the spin interactions.

At equilibrium, this dual quantum chain exhibits well-known quantum phase transitions. Upon increasing Δ , the fermionic chain evolves from a gapless Luttinger Liquid (LL) phase with short-range correlations to a charge density wave (CDW) phase with long-range correlations. The XXZ chain instead undergoes two separate transitions into an Ising ferromagnet ($\Delta < -1$) and antiferromagnet ($\Delta > 1$), while for ($|\Delta| < 1$) it exhibits an XY phase.

Since the dual charge and spin formulations are one-to-one equivalent, we choose to study the time-dependent dynamics of the quantum spin chain by using the QuSpin package [47, 48]. We diagonalize Eq. 2 and calculate the ground state wavefunction at each time step for finite-size chains up to $L = 24$ sites. The antiferromagnetic XXZ ground state in a finite-size system contains a mixture of nearly-degenerate states (notably $|\uparrow\downarrow \dots \uparrow\downarrow\rangle \pm |\downarrow\uparrow \dots \downarrow\uparrow\rangle$). In order to break this near degeneracy, which vanishes in the thermodynamic limit, we also introduce an infinitesimal staggered magnetic field

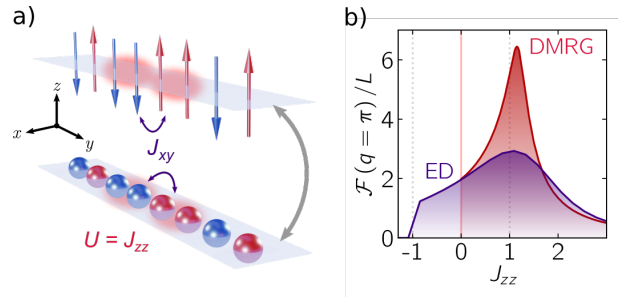


FIG. 1. Equilibrium phase diagram of the XXZ chain. (a) Sketch of half-filled chain of spinless fermions with Coulomb-type nearest-neighbor interaction [Eq. (1)] (lower part). Via the Jordan-Wigner transform, this is equivalent to a spin-1/2 XXZ chain [Eq. (2)] (upper part) where the fermionic hopping amplitude corresponds to the exchange coupling J_{xy} and the Hubbard interaction constant becomes the z -direction exchange coupling J_{zz} . Note that since the Hubbard interaction in Eq. (1) is defined relative to half-filling, pairs of adjacent sites incur an energy penalty of $J_{zz}/2$ when they are both occupied and when they are both unoccupied, matching the physics of the $\hat{S}^z \hat{S}^z$ coupling in the XXZ chain. (b) Equilibrium QFI density, calculated as a function of the spin anisotropy response. Coulomb interaction for the spin-1/2 chain system of length $L = 10$ computed using ED (purple) and for an infinite chain computed using i-DMRG (red), respectively. The bound of f_Q for detecting entanglement is given by $f_Q = 1$.

$\hat{\mathcal{H}}_{\text{ext}} = \sum_j (-1)^j h_z \hat{S}_j^z$ to select a specific spin configuration. This ensures that the disconnected part of the spin correlation function in Eq. (3) attains a finite value in the limit $\Delta \rightarrow \infty$. Our spin sector quench dynamics is then benchmarked for selected conditions against real-time density matrix renormalization group (t-DMRG) calculations [49] of the time evolution of an infinite chain.

To witness the *multipartite* entanglement content, we directly calculate the QFI of our system. For a pure state $|\tilde{\psi}_0\rangle$, the QFI, defined in terms of the generator $\hat{\mathcal{O}}_q$ assumes the particularly simple form of the connected correlation function:

$$\mathcal{F}_Q = 4\Delta \left(\hat{\mathcal{O}}_q \right)^2 = 4 \left(\langle \tilde{\psi}_0 | \hat{\mathcal{O}}_q^2 | \tilde{\psi}_0 \rangle - \langle \tilde{\psi}_0 | \hat{\mathcal{O}}_q | \tilde{\psi}_0 \rangle^2 \right). \quad (3)$$

Here we focus on the gapless and the antiferromagnetic regions of the quantum XXZ chain phase diagram (resp. the LL/CDW regions of the spinless fermion counterpart). These phase transitions are characterized by a divergent correlation function at $q = \pi$, identifying the onset of staggered spin (charge) order [46]. Hence, we choose $\hat{\mathcal{O}}_\pi = \sum_l (-1)^l \hat{S}_l^z$ to interrogate the entanglement content of these quantum chains. In the presence of genuine multipartite entanglement, a value of the QFI density $f_Q \equiv \mathcal{F}_Q/L > m$, where m is a divisor of the system size L , signals that the state $|\tilde{\psi}_0\rangle$ must be at least $m + 1$ -partite entangled.

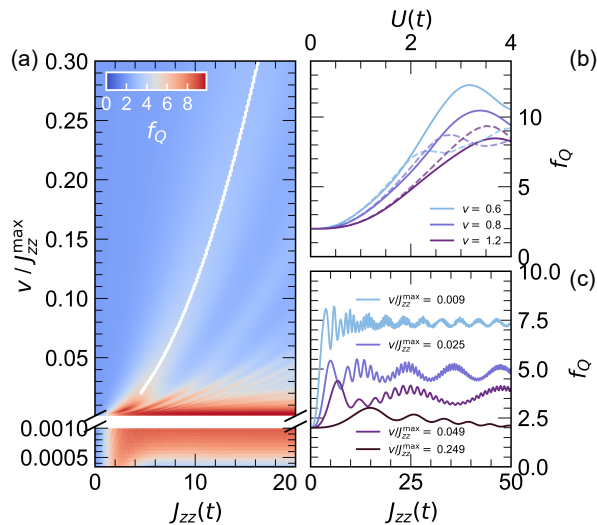


FIG. 2. **Nonequilibrium QFI in the driven XXZ chain.** (a) Dynamical QFI density $f_Q = \mathcal{F}_Q/L$ as a function of time and ramp velocity. The lower part represents a zoom on the dynamics for low ramp velocities, emphasizing the adiabatic region and the region of superextensive QFI density. (b) Selected one-dimensional line cuts of the time-dependent QFI density for various ramp velocities.

QFI in and out of equilibrium.— In Fig. 1b, we show the equilibrium QFI density f_Q as a function of the anisotropy parameter Δ for both spin (ED, blue) and charge (t-DMRG, red) sectors. Focusing on the $\Delta > 0$ portion of the phase diagram, the QFI density shows critical behavior in the vicinity of $\Delta = 1$, manifested in the appearance of a local maximum of the QFI where f_Q exceeds the classical bounds. On approaching the critical point, the spin (charge) system becomes three (seven)-partite entangled, and both systems exhibit a robust region of an enhanced QFI throughout the entire critical gapless (LL) phase. The fine details of the phase diagram in the spin sector also feature a dependence on the additional staggered magnetic field h_z , as elaborated in the supplementary material. Deep into the AFM regime, the QFI becomes featureless. For the ED calculations, we also extend the phase diagram mapped by the equilibrium QFI to the ferromagnetic region, which is the result of a $q = 0$ instability. f_Q features a discontinuity at the phase boundary point $\Delta = -1$. These findings establish the QFI density as a sensitive probe of quantum phase transitions in both spin and charge sectors at equilibrium.

Having discussed the multipartite entanglement in the static limit, we now turn to the nonequilibrium case. Unless stated otherwise, we focus entirely on the spin sector, and validate our results through comparison with t-DMRG. In Fig. 2a, we present the main result of this work, namely the unitary time evolution of the QFI density following an interaction quench. We start

from the XY limit $\Delta = 0$, with ramp velocities ranging from $5 \cdot 10^{-4} J_{zz}^{\max}$ to $0.3 J_{zz}^{\max}$ (with J_{zz}^{\max} ranging up to $200 J_{xy}$), and calculate the QFI using Eq. (3) for the time-evolved pure initial ground state $|\tilde{\psi}_0(t)\rangle = \mathcal{T} \exp[-i \int_{t_0}^t \hat{\mathcal{H}}_{XXZ}(t) dt] |\tilde{\psi}_0(t_0)\rangle$.

While the QFI density generally decreases upon increasing ramp speed, a region with extensive QFI density scaling (i.e. $f_Q \sim L$, thus saturating the upper bound) emerges at low-to-intermediate ramp velocities $v/J_{\text{eff,max}}^z \sim 0.005 - 0.025$. On further analysis, this highly entangled state features low-energy excitations giving rise to a “Schrödinger-cat”-like state featuring a superposition of nearly-degenerate Néel states.

At sufficiently high ramp speeds ($v > 0.01 J_{zz}^{\max}$), the temporal evolution of the QFI assumes a more regular structure, characterized by the emergence of a pronounced broad main peak encoding a region of enhanced entanglement content with respect to the static case. This main front is robust with respect to the inclusion of decoherence terms or additional interactions, that break integrability in the infinite system. The position of the main propagation front (marked with a white line in Fig. 2a) moves towards larger values of the effective spin anisotropy $J_{zz}(t)$ with increasing ramp speed v , which corresponds to earlier times in the time evolution in the SM for analysis in the time domain. Moreover, its position is essentially size-independent. The analysis in the supplementary material reveals that the main front bears no link with the specific details of the equilibrium model (i.e. presence of additional interaction terms), making it a generic feature that emerges out of thermal equilibrium. Instead, its origin can be associated with the existence of a critical ramp speed v^* separating the dynamical evolution of the QFI into an adiabatic regime ($v < v^*$) where the time-dependent f_Q essentially traces out the equilibrium phase diagram (cp. Fig. 1b) as a function of time, and a nonadiabatic, “impulsive” region. Before discussing the physical origin of the nonadiabatic phase and its implication for nonequilibrium entanglement spectroscopy, we first examine the temporal features of the QFI density at $v > v^*$ in more detail.

Apart from the main “jet”, the time-dependent QFI exhibits a rich dynamical texture, as revealed by selected the 1D “cuts” presented in Fig. 2b. A detailed time-frequency analysis performed with the aid sliding-window Fourier transform offers additional insight into the origin of the various dynamical features. Both the system-size-dependent slow “revivals” following the main peak and the size-independent rapid oscillations (dominating the dynamics for slower ramps at short time scales) can be linked to the energy level structure of the ground state and the separation between the states dominating the formed wave packet in the nonadiabatic limit.

Stability of the QFI dynamics.— Realistic protocols aimed at an experimental detection of macroscopic entanglement face the problem of coupling to an external

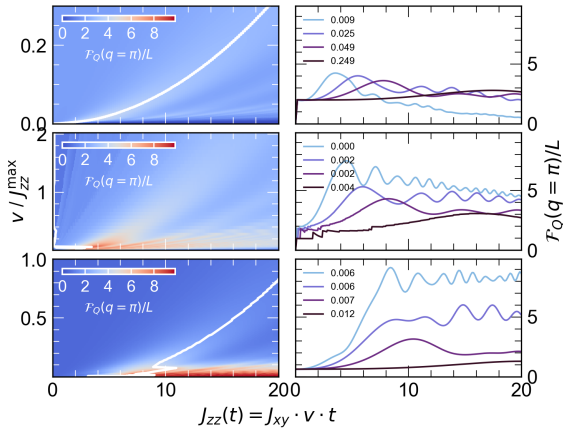


FIG. 3. **Stability of the nonequilibrium QFI.** Effect of decoherence and additional interactions on the nonequilibrium QFI. The QFI density $f_Q = \mathcal{F}_Q/L$ is plotted as a function of time and ramp velocity as 2D maps (left) as well as selected 1D cuts (right). Panels (a) and (b) show the evolution of f_Q in the presence of the Lindbladian jump operators $\hat{\mathcal{L}}_z$ and $\hat{\mathcal{L}}_{+-}$, whereas panel (c) shows the unitarily evolved f_Q for a Hamiltonian featuring a static second-order interaction term $\hat{\mathcal{H}}_{(2)}$ (see text for more details).

environment, usually detrimental for the presence of entanglement. To investigate the QFI dynamics in presence of quantum dissipation, we evolve the density matrix $\hat{\rho}(t) = |\psi_0(t)\rangle\langle\psi_0(t)|$ according to a Lindblad master equation with a decoherence rate γ :

$$\dot{\hat{\rho}}(t) = -i \left[\hat{\mathcal{H}}_{\text{sp}}(t), \hat{\rho}(t) \right] + 2\gamma \left(\hat{\mathcal{L}}\hat{\rho}(t)\hat{\mathcal{L}}^\dagger - \frac{1}{2} \left\{ \hat{\mathcal{L}}^\dagger\hat{\mathcal{L}}, \hat{\rho}(t) \right\} \right). \quad (4)$$

The temporal evolution of the QFI following the linear ramp protocol in the presence of decoherence is displayed in Fig. 3 a and b for two different choices of the Lindbladian jump operator, $\hat{\mathcal{L}}_z \equiv \sum_l (-1)^l \hat{\sigma}_l^z$ and $\hat{\mathcal{L}}_{+-} \equiv \sum_l \hat{\sigma}_l^+ \hat{\sigma}_{l+1}^-$, respectively, and for a fixed decoherence rate of $\gamma = 0.005$. As anticipated, the decoherence term eradicates the highly entangled ‘‘Schrödinger-cat’’-like region located at low ramp speeds barely exceeding the adiabatic limit, reducing the temporal profile of f_Q in this region to a single main peak followed by a slow decay as the effective anisotropy increases. At higher ramp velocities, the effect of decoherence is mainly discernible at longer times, where it quenches the dynamical f_Q to values below the classical bound $f_Q = 1$, in contrast to the case of unitary evolution. The latter is consistent with the equilibrium evolution of the QFI density for increasing anisotropy. The most striking aspect that emerges on examining Fig. 3, however, is the fact that the main nonequilibrium feature identified in the unitary case - the ‘‘entanglement fan’’ at $v > v^*$, is preserved throughout the entire region, and persists up to significant coupling

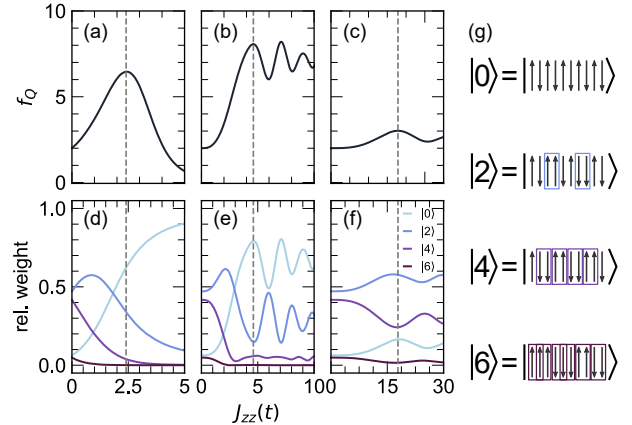


FIG. 4. **QFI and defect density.** Nonequilibrium QFI (upper row) and time-dependent density of defects (bottom row) for three different velocities: panel (a): $v = 0.005$; (b): $v = 2$; (c): $v = 50$. Dashed grey lines indicate the position of the first QFI maximum. The density of defects is quantified by the sum of the weights of the spin configurations featuring zero to three domain walls (cf. color legend) comprising the time-evolved ground state $\tilde{\psi}_0(t)$.

rates of $\gamma \approx 0.1$, only undergoing minor shifts in the exact location of the maximum as well as its magnitude.

Finally, we take a step to further corroborate the stability (or universality) of the nonequilibrium features by also considering the role of additional interactions, that break integrability in the infinite system, and study the dynamical QFI for a spin-1/2 XXZ chain (Eq. (2)) featuring next-nearest-neighbor interactions of the form $\hat{\mathcal{H}}_{(2)} = J_{zz}^{(2)} \sum_l \hat{S}_l^z \hat{S}_{l+2}^z$. The results presented in Fig. 3c for an exchange coupling of $J_{zz}^{(2)} = 2J_{xy}$ illustrate that the main traits of the nonequilibrium QFI dynamics are preserved also in this case. Importantly, this observation further demonstrates the generic character and robustness of our main findings and suggests that they should be observable across many different experimental platforms, irrespective of microscopic details.

The formation of the extended entanglement ‘‘jet’’, its spreading out and suppression at progressively higher velocities, and its stability against decoherence, constitute the main features of the nonequilibrium entanglement dynamics. We now provide a rationalization for these observations. We plot the temporal evolution of the weights of the various spin configurations comprising the ground state of the quantum chain, classified according to the relative number of domain walls (or *defects*) separating Néel-like phases within each configuration. The zero-defect spin arrangements correspond to the pure Néel states. In the AFM limit, the two possible superpositions of the latter form the doubly degenerate (in the thermodynamic limit) ground state, whereas states with two domain walls constitute the low-energy excitations.

The equally-weighted superposition of Néel states in fact constitutes a maximally entangled state and saturates the QFI ($f_Q \geq 5$) as the underlying wavefunction cannot be represented as a product state. With this information, we can not only explain formation of the “entanglement jet” but also delineate two distinctly different regimes of the buildup of entanglement: adiabatic versus impulsive. At $t_0 = 0$, the system is initialized in the critical regime $\Delta = 0$, where the ground state $\tilde{\psi}_0(t_0)$ has a complex form interpolating between the AFM and FM limits, and exhibits a high density of defects. During an adiabatic ramp-up of the spin anisotropy $v < 0.005J_{zz}^{\max}$, $\tilde{\psi}_0(t)$ essentially follows the GS of the XXZ Hamiltonian with the effective anisotropy $J_{\text{eff}}^z = J_{xy}vt$, thus increasing the proportion of the the zero-defect Néel superposition in the time-evolved wavefunction $\tilde{\psi}_0(t)$. This is reflected in an initial rise of the QFI density f_Q , which is followed by a steady decay as the staggered magnetic field term favors one of the Néel configurations as J_{eff}^z grows, quenching the created entanglement. At finite but still sufficiently small ramp velocities ($0.05 < v/J_{zz}^{\max} < 30$), the entanglement dynamics take a nonadiabatic course and proceed via coherent (?) excitations to a cluster of states with lower defect density at higher energies with respect to the GS configuration at $\Delta = 0$. These excitations also lead to a net growth of the weight of the zero-defect configuration (and thus of the QFI) Finite (but still sufficiently small) ramp speeds $v > v^*$ also lead to a net growth of the weight of the zero-defect configuration (and thus of the QFI), however, after the initial maximum of the zero-defect configuration (coinciding with the maximum of f_Q), the temporal defect redistribution develops a highly oscillatory structure. As we show in the supplement, the frequency content of these oscillations can be traced back to the energy separations between the states composing the wave packet. At very high ramp velocities ($v > 30$), the defect creation and the QFI dynamics are situated deep in the nonadiabatic regime. As shown in the Kibble-Zurek scal-

ing analysis in the SM, the domain wall density follows the power law. In this regime, the peak of the QFI coincides with the emergence of low-defect states (mainly exhibiting two domain walls) in the GS configuration. The maximally achievable entanglement in this regime is lower ($2 < f_Q < 3$), thus suppressing the amplitude of the entanglement fan at higher ramp velocities.

Conclusions.— We have investigated the nonequilibrium evolution of a driven quantum chain in terms of its many-body entanglement properties. By using an experimentally accessible quantity, the QFI, we find that multipartite entanglement grows across a quantum phase transition both in and out of equilibrium, with distinct dynamical behavior for adiabatic and nonadiabatic regimes. Owing to the dual nature of our model, such dynamics is expected to occur both in the spin and charge sectors, thus underscoring the possibility to measure multipartite entanglement through multiple time-resolved experimental probes. While experimental studies of entanglement in quantum materials at equilibrium have mainly focused on spin systems, where quantum operators are local and inelastic neutron scattering is an established method to interrogate the spin-spin correlation function, our conclusions could be tested with time-resolved resonant inelastic x-ray scattering (sensitive to both spin and charge degrees of freedom), or via optical methods (mainly charge-sensitive).

Our findings are immediately relevant to the study of photoinduced phase transitions in quasi-one-dimensional correlated materials [49] and to the search for dynamical coherence in higher dimensions. By establishing a direct relationship between the instantaneous response function of a material and the time-dependent QFI, we anticipate the possibility to identify dynamical criticality and nonequilibrium long-range ordered states, such as photoinduced superconductivity and quantum spin liquidity. More generally, the use of entanglement witnesses provides an opportunity to detect coherent states in light-driven quantum materials without the need for well-defined order parameters.

-
- [1] L. Amico, R. Fazio, A. Osterloh, and V. Vedral, *Reviews of Modern Physics* **80**, 517 (2008).
 - [2] V. Vedral, *Nature* **453**, 1004 (2008).
 - [3] N. Laflorencie, *Physics Reports-Review Section of Physics Letters* **646**, 1 (2016).
 - [4] C. Gogolin and J. Eisert, *Reports on Progress in Physics* **79**, 056001 (2016).
 - [5] M. Ueda, *Nature Reviews Physics* **2**, 669 (2020).
 - [6] L. Balents, *Nature* **464**, 199 (2010).
 - [7] L. Savary and L. Balents, *Reports on Progress in Physics* **80**, 016502 (2016).
 - [8] X.-G. Wen, *Reviews of Modern Physics* **89** (2017), 10.1103/revmodphys.89.041004.
 - [9] P. Anderson, *Materials Research Bulletin* **8**, 153 (1973).
 - [10] R. Verresen, M. D. Lukin, and A. Vishwanath, *Physical Review X* **11** (2021), 10.1103/physrevx.11.031005.
 - [11] G. Semeghini, H. Levine, A. Keesling, S. Ebadi, T. T. Wang, D. Bluvstein, R. Verresen, H. Pichler, M. Kalinowski, R. Samajdar, A. Omran, S. Sachdev, A. Vishwanath, M. Greiner, V. Vuletić, and M. D. Lukin, *Science* **374**, 1242 (2021).
 - [12] A. Kitaev, *Annals of Physics* **303**, 2 (2003).
 - [13] R. Islam, R. Ma, P. M. Preiss, M. Eric Tai, A. Lukin, M. Rispoli, and M. Greiner, *Nature* **528**, 77 (2015).
 - [14] Č. Brukner, V. Vedral, and A. Zeilinger, *Physical review. A, Atomic, molecular, and optical physics* **73**, 195 (2006).
 - [15] S. Ghosh, T. F. Rosenbaum, G. Aeppli, and S. N. Coppersmith, *Nature* **425**, 48 (2003).
 - [16] P. Laurell, A. Scheie, C. J. Mukherjee, M. M. Koza, M. Enderle, Z. Tylczynski, S. Okamoto, R. Coldea, D. A. Tennant, and G. Alvarez, *Physical Review Letters* **127**, 037201 (2021).

- [17] O. Ghne and G. Tth, *Physics Reports* **474**, 1 (2009).
- [18] V. Coffman, J. Kundu, and W. K. Wootters, *Phys. Rev. A* **61**, 052306 (2000).
- [19] L. Amico, A. Osterloh, F. Plastina, R. Fazio, and G. Massimo Palma, *Phys. Rev. A* **69**, 022304 (2004).
- [20] T. Roscilde, P. Verrucchi, A. Fubini, S. Haas, and V. Tognetti, *Phys. Rev. Lett.* **93**, 167203 (2004).
- [21] L. Amico, F. Baroni, A. Fubini, D. Patanè, V. Tognetti, and P. Verrucchi, *Phys. Rev. A* **74**, 022322 (2006).
- [22] L. Pezzé and A. Smerzi, *Physical Review Letters* **102** (2009), 10.1103/physrevlett.102.100401.
- [23] P. Hyllus, W. Laskowski, R. Krischek, C. Schwemmer, W. Wieczorek, H. Weinfurter, L. Pezzé, and A. Smerzi, *Physical Review A* **85** (2012), 10.1103/physreva.85.022321.
- [24] G. Tóth and I. Apellaniz, *Journal of Physics A: Mathematical and Theoretical* **47**, 424006 (2014).
- [25] P. Hauke, M. Heyl, L. Tagliacozzo, and P. Zoller, *Nature Publishing Group* **12**, 778 (2016).
- [26] G. Mathew, S. L. L. Silva, A. Jain, A. Mohan, D. T. Adroja, V. G. Sakai, C. V. Tomy, A. Banerjee, R. Goreti, A. V. N, R. Singh, and D. Jaiswal-Nagar, *Physical Review Research* **2**, 043329 (2020).
- [27] L. Pezzè, M. Gabbriellini, L. Lepori, and A. Smerzi, *Phys. Rev. Lett* **119**, 250401 (2017).
- [28] Y.-R. Zhang, Y. Zeng, H. Fan, J. Q. You, and F. Nori, *Phys. Rev. Lett.* **120**, 250501 (2018).
- [29] Y.-R. Zhang, Y. Zeng, T. Liu, H. Fan, J. Q. You, and F. Nori, “Multipartite entanglement of the topologically ordered state in a perturbed toric code,” (2021), [arXiv:2109.03315](https://arxiv.org/abs/2109.03315) [quant-ph].
- [30] Y. H. Wang, H. Steinberg, P. Jarillo-Herrero, and N. Gedik, *Science* **342**, 453 (2013).
- [31] F. Mahmood, C.-K. Chan, Z. Alpichshev, D. Gardner, Y. Lee, P. A. Lee, and N. Gedik, *Nature Physics* **12**, 306 (2016).
- [32] J. W. McIver, B. Schulte, F. U. Stein, T. Matsuyama, G. Jotzu, G. Meier, and A. Cavalleri, *Nature Physics* **16**, 38 (2020).
- [33] W. Hu, S. Kaiser, D. Nicoletti, C. R. Hunt, I. Gierz, M. C. Hoffmann, M. Le Tacon, T. Loew, B. Keimer, and A. Cavalleri, *Nature Materials* **13**, 705 (2014).
- [34] S. Kaiser, C. R. Hunt, D. Nicoletti, W. Hu, I. Gierz, H. Y. Liu, M. Le Tacon, T. Loew, D. Haug, B. Keimer, and A. Cavalleri, *Phys. Rev. B* **89**, 184516 (2014).
- [35] M. Mitrano, A. Cantaluppi, D. Nicoletti, S. Kaiser, A. Perucchi, S. Lupi, P. Di Pietro, D. Pontiroli, M. Riccò, S. R. Clark, D. Jaksch, and A. Cavalleri, *Nature* **530**, 461 (2016).
- [36] M. Claassen, H.-C. Jiang, B. Moritz, and T. P. Devereaux, *Nat. Comm.* **8**, 1192 (2017).
- [37] T. Kaneko, T. Shirakawa, S. Sorella, and S. Yunoki, *Phys. Rev. Lett.* **122**, 077002 (2019).
- [38] F. Peronaci, O. Parcollet, and M. Schiró, *Phys. Rev. B* **101**, 161101 (2020).
- [39] J. Li, D. Golez, P. Werner, and M. Eckstein, *Phys. Rev. B* **102**, 165136 (2020).
- [40] N. Tsuji, M. Eckstein, and P. Werner, *Phys. Rev. Lett.* **110**, 136404 (2013).
- [41] A. de la Torre, D. M. Kennes, M. Claassen, S. Gerber, J. W. McIver, and M. A. Sentef, *Rev. Mod. Phys.* **93**, 041002 (2021).
- [42] R. Singla, G. Cotugno, S. Kaiser, M. Först, M. Mitrano, H. Y. Liu, A. Cartella, C. Manzoni, H. Okamoto, T. Hasegawa, S. R. Clark, D. Jaksch, and A. Cavalleri, *Phys. Rev. Lett.* **115**, 187401 (2015).
- [43] N. Tancogne-Dejean, M. A. Sentef, and A. Rubio, *Phys. Rev. Lett.* **121**, 097402 (2018).
- [44] S. Beaulieu, S. Dong, N. Tancogne-Dejean, M. Dendzik, T. Pincelli, J. Maklar, R. P. Xian, M. A. Sentef, M. Wolf, A. Rubio, L. Rettig, and R. Ernstorfer, *Science Advances* **7**, eabd9275 (2021), <https://www.science.org/doi/pdf/10.1126/sciadv.abd9275>.
- [45] D. R. Baykusheva, H. Jang, A. A. Husain, S. Lee, S. F. R. TenHuisen, P. Zhou, S. Park, H. Kim, J.-K. Kim, H.-D. Kim, M. Kim, S.-Y. Park, P. Abbamonte, B. J. Kim, G. D. Gu, Y. Wang, and M. Mitrano, *Phys. Rev. X* **12**, 011013 (2022).
- [46] T. Giamarchi, *Quantum physics in one dimension*, International series of monographs on physics (Clarendon Press, Oxford, 2004).
- [47] P. Weinberg and M. Bukov, *SciPost Phys.* **2**, 003 (2017).
- [48] P. Weinberg and M. Bukov, *SciPost Phys.* **7**, 20 (2019).
- [49] D. M. Kennes, A. de la Torre, A. Ron, D. Hsieh, and A. J. Millis, *Phys. Rev. Lett.* **120**, 127601 (2018).

8 | Comprehensive discussion

In this thesis, we aimed at shedding light on the nature of nonequilibrium steady states in correlated materials and the phase transitions between them. To do so, we studied criticality from different angles, namely by simulating an interacting, two-dimensional, driven-dissipative magnon system using a Boltzmann formalism, by analyzing the Floquet-engineered spread of density-density correlations in a driven quantum chain with Luttinger liquid and charge-density wave phases, and by investigating the multipartite entanglement that is created through an interaction-quench in a spin-1/2 XXZ chain. The presented results help with understanding different aspects of driving systems out of equilibrium and achieving nonequilibrium steady-states with distinct phase properties. Throughout these projects, we aimed at maintaining close relation to experimental pump-probe spectroscopy by choosing realistic driving protocols and discussing experimentally accessible dynamic quantities.

Investigating the spread of electronic correlations in a one-dimensional correlated chain of spinless fermions driven by a high frequency laser, we find that the velocity with which the correlations spread through the system, is restricted by an upper bound that is renormalized with respect to the driving field. This renormalized upper bound causes light-cone effects, which can be shown even if the periodic drive is ramped up over a finite time and when the drive is modulated with a Gaussian. The modulation of the drive is chosen in order to connect our results to time-resolved experiments, which typically use pulsed driving envelopes and require the drive to be ramped up over a given time [53, 54]. In this context, the renormalized bound to the spread of correlations sets the time that is required for experimentally realizing a nonequilibrium phase transition, given that the correlations need to build up over macroscopic distances [46]. Despite the modulation, we find that heating is suppressed as long as the high-frequency, off resonant driving protocol is employed. For the quenched Luttinger liquid, it is known that the correlations follow a different power law behavior inside and outside of the light-cone, leading to a discontinuity in the form of a kink at the edge of the light-cone [129–131]. This dynamical critical behavior in the form of a discontinuity is also present in the correlation function of the Floquet-driven system, making the observation of Floquet-engineered spreading of correlations in time-resolved spectroscopy experiments a thrilling future perspective.

Investigating the same equilibrium model, namely a half-filled chain of spinless fermions, but introducing a quench in the Coulomb repulsion [125, 132] instead of an external driving field, we identify the quantum Fisher information as a dynamical witness of multipartite entanglement which can be used to characterize nonequilibrium phase transitions. Both t-DMRG and ED calculations reveal that the quantum Fisher information shows critical behavior at the phase transition between a gapless and an antiferromagnetic phase, and reaches its maximum value at the critical point. The entanglement is generally enhanced in the interaction quenched system and continues to show distinct critical features out of equilibrium. Upon increasing the ramp speed, we find a qualitative change from adiabatic to nonadiabatic behavior, meaning that the entanglement is sensitive to the ramp-time of the quench. Due to the accessibility of the quantum Fisher information through inelastic neutron scattering [122, 123] and time-resolved resonant inelastic X-ray scattering [113, 114] as well as various optical methods, it is a promising candidate for identifying dynamical criticality and nonequilibrium long-range order in photoinduced

nonequilibrium states [3].

In the project presented in publication II, we move from studying criticality in one-dimensional systems to a two-dimensional quantum magnet. Simulating a driven-dissipative Heisenberg anti-ferromagnet, we find two distinct phase transitions that are determined through the interplay of drive, dissipation and interactions amongst excitations (magnons). In the subthermal regime the driving term is small compared to the parameter that regulates the dissipation into a reservoir, and we find a nonequilibrium steady state which is ordered for sufficiently large spin-length. The Holstein-Primakoff expansion allows us to mathematically decrease the spin-length and find a transition where at sufficiently short spin length, the number of fluctuations is large enough to destabilize the ordered state, and spin rotation invariance is broken. Due to the employed large spin expansion, the precise location of the ordered subthermal to disordered subthermal phase boundary will be different from the curve presented in publication II, but the qualitative aspects of this order-to-disorder transition are captured by our theory. This nonequilibrium phase transition is closely related to equilibrium transitions where a magnetic order parameter vanishes as temperature is raised, and similar nonequilibrium transitions have been studied in previous literature [66, 73, 133–135]. Furthermore, the subthermal population of magnons indicates that nonthermal situations in perturbed magnetic materials exist in which low energy excitations are less populated than one would a priori expect. This could lead to interesting effects such as avoiding the Mermin-Wagner-Hohenberg theorem. Although this subthermal phase transition is contained in our theory, it is not the main focus of our results.

However, in addition to the phase transition that is characterized by the disappearance of an order parameter, there is a conceptually different phase transition where the functional form of the distribution of excitations changes. This phase transition occurs when the drive exceeds a critical value set by the dissipation mechanism and causes an excess of magnons with regard to the system energy, which in the interacting system condenses at zero momentum. To determine the precise properties of the condensed phase, we perform a careful finite-size scaling analysis, and find that the high drive phase is given by a thermal distribution with a condensate fraction and it can therefore be fully characterized by a temperature and the excitation density in the condensate. Importantly, the condensation is a direct consequence of the inclusion of magnon interactions; there is no condensate in the noninteracting driven-dissipative system, as has been shown for various other nonequilibrium phenomena in magnetic materials [79, 91, 92]. Our results are fully consistent with the known occurrence of Bose-Einstein condensates in particle-number conserving systems with an excess number of particles [101, 136], but differ in various ways. At the nonequilibrium phase transition, the system shows characteristic critical scaling behavior in static and dynamic observables. We show a discontinuity of the magnon number with respect to the tuning parameter and a critical slowing down in all computed dynamic quantities. On the level of the Boltzmann approximation, we extract the corresponding critical exponents and further analyze the behavior close to criticality by considering the linearized kinetic equation and its eigenvalues. The spectrum of eigenvalues reveals two zero modes corresponding to the conserved quantities as well as a smallest eigenvalue that remains nonzero in the thermodynamic limit. The existence of a smallest nonzero eigenvalue is not only consistent with the existence of a smallest relaxation rate that dominates the long term decay of the occupation function, but also justifies a hydrodynamic approach to the slow modes close to criticality. Therefore, the derivation of a hydrodynamic nonequilibrium theory of this critical behavior in close relation to the derivation of the Navier-Stokes equation from the Boltzmann equation [137] is an exciting point of future research.

The condensed nonequilibrium phase we find numerically, shows interesting similarities to the phenomena studied in largely experimental literature on Bose-Einstein condensation of magnons in systems with long relaxation times, where a population of magnons is transiently introduced and evolves into a coherent quantum state where the lowest energy state is macroscopically populated [81–83]. The most prominent materials in which such a condensation of magnons is observed are ferromagnetic yttrium iron garnet (YIG) films [83–90], and a modification of our Boltzmann approach to simulate ferromagnetic materials could possibly help understand the mechanisms of the evolution into the condensed state. Similarly, our results bear a close relationship to exciton-polariton condensates [98, 138–141], which are bosonic systems and can be modeled by a Boltzmann equation as well. Because we consider a spatially uniform drive, our approach in its current form does not answer the question as to whether there can be an interesting spacial structure to the nonequilibrium phase transition. And importantly, our numerical observation of a high-drive condensed phase in a Heisenberg antiferromagnet requires further study because we used a large spin expansion around the ordered Néel state to find a condensed phase with a distribution function that is at least thermal for any nonzero momentum, meaning long-range order is necessarily destroyed. This implicit contradiction could be avoided using the Schwinger representation of the antiferromagnet [101, 142, 143], which would require implementing a change in the dispersion in every time step. Furthermore, it would be fascinating to see a full quantum critical analysis revealing the physics beyond the Boltzmann formalism, including a connection of nonequilibrium critical exponents to a possible new universality class. Another point of relevance is that our computations are based on a theory up to leading order in the magnon expansion. We believe, although we have not investigated in detail, that if we included terms to higher order (which are not necessarily particle number conserving) the system would eventually thermalize at much longer time scales. The critical behavior in our analysis could therefore possibly be interpreted as intermediate time asymptotics of the magnon system.

Observing the nonthermal behavior and particularly measuring a nonequilibrium phase transition in the distribution function rather than in a conventional order parameter, would be highly intriguing. Promising experimental setups for probing such a transition are time-resolved second harmonic optical polarimetry or inelastic x-ray scattering [144, 145], especially given that at the level of the Boltzmann approximation, we find different critical exponents when approaching the phase transition from the subthermal phase and from the nonequilibrium condensed phase. While the determined spin condensate occurs in the limit of low energy spin waves, a measurement of the dynamical excitations approaching the phase transition from both sides could reveal the critical slowing down in proximity of the critical point. Possible probe-candidates for such measurements would be for example antiferromagnetic, two-dimensional transition metal oxides [146] because of their large magnetic exchange energy and strong spin-orbit coupling.

Summarizing, the projects presented in this thesis contribute to our understanding of the versatile physical mechanisms involved in inducing nonequilibrium phase transitions and criticality through light-matter interaction. This is important given that the enormous progress in the field of time-resolved spectroscopy goes hand in hand with the need for the development of out-of-equilibrium computational methods. Furthermore, improving our understanding of the control knobs for achieving nonequilibrium steady states is essential to optically control emergent states of strongly correlated materials, and thus achieving engineered quantum materials with distinct desired system properties. This deterministic engineering of quantum materials and phases presents a rich new landscape of technological applications.

Bibliography

1. Feliciano Giustino, Jin Hong Lee, Felix Trier, Manuel Bibes, Stephen M. Winter, Roser Valentí, Young Woo Son, Louis Taillefer, Christoph Heil, Adriana I. Figueroa, Bernard Plaçais, Quan Sheng Wu, Oleg V. Yazyev, Erik P.A.M. Bakkers, Jesper Nygård, Pol Forn-Díaz, Silvano de Franceschi, J. W. McIver, L. E.F. Foa Torres, Tony Low, Anshuman Kumar, Regina Galceran, Sergio O. Valenzuela, Marius V. Costache, Aurélien Manchon, Eun Ah Kim, Gabriel R. Schleder, Adalberto Fazzio, and Stephan Roche. The 2021 quantum materials roadmap. *JPhys Materials*, 3(4), October 2020. URL <https://iopscience.iop.org/article/10.1088/2515-7639/abb74e>.
2. Anatoli Polkovnikov, Krishnendu Sengupta, Alessandro Silva, and Mukund Vengalattore. Colloquium: Nonequilibrium dynamics of closed interacting quantum systems. *Rev. Mod. Phys.*, 83:863–883, Aug 2011. URL <https://link.aps.org/doi/10.1103/RevModPhys.83.863>.
3. Alberto de la Torre, Dante M. Kennes, Martin Claassen, Simon Gerber, James W. McIver, and Michael A. Sentef. Colloquium: Nonthermal pathways to ultrafast control in quantum materials. *Rev. Mod. Phys.*, 93:041002, Oct 2021. URL <https://link.aps.org/doi/10.1103/RevModPhys.93.041002>.
4. Masatoshi Imada, Atsushi Fujimori, and Yoshinori Tokura. Metal-insulator transitions. *Rev. Mod. Phys.*, 70:1039–1263, Oct 1998. URL <https://link.aps.org/doi/10.1103/RevModPhys.70.1039>.
5. Kenneth G. Wilson. The renormalization group and critical phenomena. *Rev. Mod. Phys.*, 55:583–600, Jul 1983. URL <https://link.aps.org/doi/10.1103/RevModPhys.55.583>.
6. Gerald D. Mahan. *Many-Particle Physics*. Springer US, 2000. URL <https://doi.org/10.1007%2F978-1-4757-5714-9>.
7. D. N. Basov, Richard D. Averitt, Dirk van der Marel, Martin Dressel, and Kristjan Haule. Electrodynamics of correlated electron materials. *Rev. Mod. Phys.*, 83:471–541, Jun 2011. URL <https://link.aps.org/doi/10.1103/RevModPhys.83.471>.
8. Jens Klinder, Hans Keßler, Matthias Wolke, Ludwig Mathey, and Andreas Hemmerich. Dynamical phase transition in the open dicke model. *Proceedings of the National Academy of Sciences*, 112(11):3290–3295, 2015. URL <https://www.pnas.org/content/112/11/3290>.
9. Tilman Esslinger. Fermi-hubbard physics with atoms in an optical lattice. *Annual Review of Condensed Matter Physics*, 1(1):129–152, 2010. URL <https://doi.org/10.1146/annurev-conmatphys-070909-104059>.
10. Immanuel Bloch, Jean Dalibard, and Wilhelm Zwerger. Many-body physics with ultracold gases. *Rev. Mod. Phys.*, 80:885–964, Jul 2008. URL <https://link.aps.org/doi/10.1103/>

RevModPhys.80.885.

11. A. L. Cavalieri, N. Müller, Th. Uphues, V. S. Yakovlev, A. Baltuška, B. Horvath, B. Schmidt, L. Blümel, R. Holzwarth, S. Hendel, M. Drescher, U. Kleineberg, P. M. Echenique, R. Kienberger, F. Krausz, and U. Heinzmann. Attosecond spectroscopy in condensed matter. *Nature*, 449(7165):1029–1032, Oct 2007. URL <https://doi.org/10.1038/nature06229>.
12. D. Nicoletti and A. Cavalleri. Nonlinear light–matter interaction at terahertz frequencies. *Adv. Opt. Photon.*, 8(3):401–464, Sep 2016. URL <http://opg.optica.org/aop/abstract.cfm?URI=aop-8-3-401>.
13. Andrei Kirilyuk, Alexey V. Kimel, and Theo Rasing. Ultrafast optical manipulation of magnetic order. *Rev. Mod. Phys.*, 82:2731–2784, Sep 2010. URL <https://link.aps.org/doi/10.1103/RevModPhys.82.2731>.
14. M. Mitrano, A. Cantaluppi, D. Nicoletti, S. Kaiser, A. Perucchi, S. Lupi, P. Di Pietro, D. Pontiroli, M. Riccò, S. R. Clark, D. Jaksch, and A. Cavalleri. Possible light-induced superconductivity in $\text{K}_3\text{C}_6\text{O}$ at high temperature. *Nature*, 530(7591):461–464, Feb 2016. URL <https://doi.org/10.1038/nature16522>.
15. R. Mankowsky, A. Subedi, M. Först, S. O. Mariager, M. Chollet, H. T. Lemke, J. S. Robinson, J. M. Glowia, M. P. Minitti, A. Frano, M. Fechner, N. A. Spaldin, T. Loew, B. Keimer, A. Georges, and A. Cavalleri. Nonlinear lattice dynamics as a basis for enhanced superconductivity in $\text{YBa}_2\text{Cu}_3\text{O}_{6.5}$. *Nature*, 516(7529):71–73, Dec 2014. URL <https://doi.org/10.1038/nature13875>.
16. R. D. Averitt, G. Rodriguez, A. I. Lobad, J. L. W. Siders, S. A. Trugman, and A. J. Taylor. Nonequilibrium superconductivity and quasiparticle dynamics in $\text{YBa}_2\text{Cu}_3\text{O}_{7-\delta}$. *Phys. Rev. B*, 63:140502, Mar 2001. URL <https://link.aps.org/doi/10.1103/PhysRevB.63.140502>.
17. D. Fausti, R. I. Tobey, N. Dean, S. Kaiser, A. Dienst, M. C. Hoffmann, S. Pyon, T. Takayama, H. Takagi, and A. Cavalleri. Light-induced superconductivity in a stripe-ordered cuprate. *Science*, 331:189–191, Jan 2011. URL <https://www.science.org/doi/10.1126/science.1197294>.
18. A. Cavalleri, Th. Dekorsy, H. H. W. Chong, J. C. Kieffer, and R. W. Schoenlein. Evidence for a structurally-driven insulator-to-metal transition in VO_2 : A view from the ultrafast timescale. *Phys. Rev. B*, 70:161102, Oct 2004. URL <https://link.aps.org/doi/10.1103/PhysRevB.70.161102>.
19. Mengkun Liu, Harold Y. Hwang, Hu Tao, Andrew C. Strikwerda, Kebin Fan, George R. Keiser, Aaron J. Sternbach, Kevin G. West, Salinporn Kittiwatanakul, Jiwei Lu, Stuart A. Wolf, Fiorenzo G. Omenetto, Xin Zhang, Keith A. Nelson, and Richard D. Averitt. Terahertz-field-induced insulator-to-metal transition in vanadium dioxide metamaterial. *Nature*, 487(7407):345–348, Jul 2012. URL <https://doi.org/10.1038/nature11231>.
20. M. Zahradnik, M. Kiaba, S. Espinoza, M. Rebarz, J. Andreasson, O. Caha, F. Abadizaman, D. Munzar, and A. Dubroka. Photo-induced insulator-to-metal transition and coherent

- acoustic phonon propagation in LaCoO_3 thin films explored by femtosecond pump-probe ellipsometry, 2022.
21. A. Cavalleri, Cs. Tóth, C. W. Siders, J. A. Squier, F. Ráksi, P. Forget, and J. C. Kieffer. Femtosecond structural dynamics in VO_2 during an ultrafast solid-solid phase transition. *Phys. Rev. Lett.*, 87:237401, Nov 2001. URL <https://link.aps.org/doi/10.1103/PhysRevLett.87.237401>.
 22. R. Singla, A. Simoncig, M. Först, D. Prabhakaran, A. L. Cavalieri, and A. Cavalleri. Photoinduced melting of the orbital order in $\text{La}_{0.5}\text{Sr}_{1.5}\text{MnO}_4$ measured with 4-fs laser pulses. *Phys. Rev. B*, 88:075107, Aug 2013. URL <https://link.aps.org/doi/10.1103/PhysRevB.88.075107>.
 23. R. I. Tobey, D. Prabhakaran, A. T. Boothroyd, and A. Cavalleri. Ultrafast electronic phase transition in $\text{La}_{1/2}\text{Sr}_{3/2}\text{MnO}_4$ by coherent vibrational excitation: Evidence for non-thermal melting of orbital order. *Phys. Rev. Lett.*, 101:197404, Nov 2008. URL <https://link.aps.org/doi/10.1103/PhysRevLett.101.197404>.
 24. J. Eisert, M. Friesdorf, and C. Gogolin. Quantum many-body systems out of equilibrium. *Nature Physics*, 11(2):124–130, Feb 2015. URL <https://doi.org/10.1038/nphys3215>.
 25. J.A. Sobota, S.-L. Yang, D. Leuenberger, A.F. Kemper, J.G. Analytis, I.R. Fisher, P.S. Kirchmann, T.P. Devereaux, and Z.-X. Shen. Ultrafast electron dynamics in the topological insulator Bi_2Se_3 studied by time-resolved photoemission spectroscopy. *Journal of Electron Spectroscopy and Related Phenomena*, 195:249–257, 2014. URL <https://www.sciencedirect.com/science/article/pii/S0368204814000231>.
 26. Herbert F. Fotsos, Eric Dohner, Alexander Kemper, and James K. Freericks. Bridging the gap between the transient and the steady state of a nonequilibrium quantum system, 2021.
 27. Naoto Tsuji, Martin Eckstein, and Philipp Werner. Nonthermal antiferromagnetic order and nonequilibrium criticality in the hubbard model. *Phys. Rev. Lett.*, 110:136404, Mar 2013. URL <https://link.aps.org/doi/10.1103/PhysRevLett.110.136404>.
 28. Philipp Werner and Yuta Murakami. Nonthermal excitonic condensation near a spin-state transition. *Phys. Rev. B*, 102:241103, Dec 2020. URL <https://link.aps.org/doi/10.1103/PhysRevB.102.241103>.
 29. Bojan Žunkovič, Markus Heyl, Michael Knap, and Alessandro Silva. Dynamical quantum phase transitions in spin chains with long-range interactions: Merging different concepts of nonequilibrium criticality. *Phys. Rev. Lett.*, 120:130601, Mar 2018. URL <https://link.aps.org/doi/10.1103/PhysRevLett.120.130601>.
 30. Alfred Zong, Pavel E. Dolgirev, Anshul Kogar, Emre Ergeçen, Mehmet B. Yilmaz, Ya-Qing Bie, Timm Rohwer, I-eg Tung, Joshua Straquadine, Xirui Wang, Yafang Yang, Xiaozhe Shen, Renkai Li, Jie Yang, Suji Park, Matthias C. Hoffmann, Benjamin K. Ofori-Okai, Michael E. Kozina, Haidan Wen, Xijie Wang, Ian R. Fisher, Pablo Jarillo-Herrero, and Nuh Gedik. Dynamical slowing-down in an ultrafast photoinduced phase transition. *Phys. Rev. Lett.*, 123:097601, Aug 2019. URL <https://link.aps.org/doi/10.1103/>

- PhysRevLett.123.097601.
31. Wojciech H. Zurek, Uwe Dorner, and Peter Zoller. Dynamics of a quantum phase transition. *Phys. Rev. Lett.*, 95:105701, Sep 2005. URL <https://link.aps.org/doi/10.1103/PhysRevLett.95.105701>.
 32. Fahad Mahmood, Ching-Kit Chan, Zhanybek Alpichshev, Dillon Gardner, Young Lee, Patrick A. Lee, and Nuh Gedik. Selective scattering between floquet–bloch and volkov states in a topological insulator. *Nature Physics*, 12(4):306–310, Apr 2016. URL <https://doi.org/10.1038/nphys3609>.
 33. Takashi Oka and Sota Kitamura. Floquet engineering of quantum materials. *Annual Review of Condensed Matter Physics*, 10(1):387–408, 2019. URL <https://doi.org/10.1146/annurev-conmatphys-031218-013423>.
 34. D. N. Basov, R. D. Averitt, and D. Hsieh. Towards properties on demand in quantum materials. *Nature Materials*, 16(11):1077–1088, Nov 2017. URL <https://doi.org/10.1038/nmat5017>.
 35. Jun-Yi Shan, M. Ye, H. Chu, Sungmin Lee, Je-Geun Park, L. Balents, and D. Hsieh. Giant modulation of optical nonlinearity by floquet engineering. *Nature*, 600(7888):235–239, Dec 2021. URL <https://doi.org/10.1038/s41586-021-04051-8>.
 36. Götz S. Uhrig, Mona H. Kalthoff, and James K. Freericks. Positivity of the spectral densities of retarded floquet green functions. *Phys. Rev. Lett.*, 122:130604, Apr 2019. URL <https://link.aps.org/doi/10.1103/PhysRevLett.122.130604>.
 37. Luca D’Alessio and Anatoli Polkovnikov. Many-body energy localization transition in periodically driven systems. *Annals of Physics*, 333:19–33, 2013. URL <https://www.sciencedirect.com/science/article/pii/S0003491613000389>.
 38. Adhip Agarwala, Utso Bhattacharya, Amit Dutta, and Diptiman Sen. Effects of periodic kicking on dispersion and wave packet dynamics in graphene. *Phys. Rev. B*, 93:174301, May 2016. URL <https://link.aps.org/doi/10.1103/PhysRevB.93.174301>.
 39. G. Floquet. Sur les équations différentielles linéaires à coefficients périodiques. *Annales scientifiques de l’École Normale Supérieure*, 12:47–88, 1883. URL <http://www.numdam.org/articles/10.24033/asens.220/>.
 40. Mark S. Rudner and Netanel H Lindner. The floquet engineer’s handbook. *arXiv*, 2020. URL <https://arxiv.org/abs/2003.08252>.
 41. Y. H. Wang, H. Steinberg, P. Jarillo-Herrero, and N. Gedik. Observation of floquet-bloch states on the surface of a topological insulator. *Science*, 342:453–457, Oct 2013. URL <https://www.science.org/doi/10.1126/science.1239834>.
 42. J. W. McIver, B. Schulte, F.-U. Stein, T. Matsuyama, G. Jotzu, G. Meier, and A. Cavalleri. Light-induced anomalous hall effect in graphene. *Nature Physics*, 16(1):38–41, Jan 2020. URL <https://doi.org/10.1038/s41567-019-0698-y>.

Bibliography

43. Sven Aeschlimann, Shunsuke A. Sato, Razvan Krause, Mariana Chávez-Cervantes, Umberto De Giovannini, Hannes Hübener, Stiven Forti, Camilla Coletti, Kerstin Hanff, Kai Rossnagel, Angel Rubio, and Isabella Gierz. Survival of floquet–bloch states in the presence of scattering. *Nano Letters*, 21(12):5028–5035, 2021. URL <https://doi.org/10.1021/acs.nanolett.1c00801>. PMID: 34082532.
44. Mark S. Rudner and Netanel H. Lindner. Band structure engineering and non-equilibrium dynamics in floquet topological insulators. *Nature Reviews Physics*, 2(5):229–244, May 2020. URL <https://doi.org/10.1038/s42254-020-0170-z>.
45. Sein Park, Wonjun Lee, Seong Jang, Yong-Bin Choi, Jinho Park, Woonchan Jung, Kenji Watanabe, Takashi Taniguchi, Gil Young Cho, and Gil-Ho Lee. Steady floquet–andreev states in graphene josephson junctions. *Nature*, 603(7901):421–426, Mar 2022. URL <https://doi.org/10.1038/s41586-021-04364-8>.
46. Marc Cheneau, Peter Barmettler, Dario Poletti, Manuel Endres, Peter Schauß, Takeshi Fukuhara, Christian Gross, Immanuel Bloch, Corinna Kollath, and Stefan Kuhr. Light-cone-like spreading of correlations in a quantum many-body system. *Nature*, 481(7382):484–487, Jan 2012. URL <https://doi.org/10.1038/nature10748>.
47. D. M. Kennes, A. de la Torre, A. Ron, D. Hsieh, and A. J. Millis. Floquet engineering in quantum chains. *Phys. Rev. Lett.*, 120:127601, Mar 2018. URL <https://link.aps.org/doi/10.1103/PhysRevLett.120.127601>.
48. Pedro Ponte, Z. Papić, Fran çois Huveneers, and Dmitry A. Abanin. Many-body localization in periodically driven systems. *Phys. Rev. Lett.*, 114:140401, Apr 2015. URL <https://link.aps.org/doi/10.1103/PhysRevLett.114.140401>.
49. Dmitry A. Abanin, Wojciech De Roeck, Wen Wei Ho, and Fran çois Huveneers. Effective hamiltonians, prethermalization, and slow energy absorption in periodically driven many-body systems. *Phys. Rev. B*, 95:014112, Jan 2017. URL <https://link.aps.org/doi/10.1103/PhysRevB.95.014112>.
50. Philipp T. Dumitrescu, Romain Vasseur, and Andrew C. Potter. Logarithmically slow relaxation in quasiperiodically driven random spin chains. *Phys. Rev. Lett.*, 120:070602, Feb 2018. URL <https://link.aps.org/doi/10.1103/PhysRevLett.120.070602>.
51. Marin Bukov, Luca D’Alessio, and Anatoli Polkovnikov. Universal high-frequency behavior of periodically driven systems: from dynamical stabilization to floquet engineering. *Advances in Physics*, 64(2):139–226, 2015. URL <https://doi.org/10.1080/00018732.2015.1055918>.
52. André Eckardt and Egidijus Anisimovas. High-frequency approximation for periodically driven quantum systems from a floquet-space perspective. *New Journal of Physics*, 17(9):093039, sep 2015. URL <https://doi.org/10.1088/1367-2630/17/9/093039>.
53. Mona H. Kalthoff, Götz S. Uhrig, and J. K. Freericks. Emergence of floquet behavior for lattice fermions driven by light pulses. *Phys. Rev. B*, 98:035138, Jul 2018. URL <https://link.aps.org/doi/10.1103/PhysRevB.98.035138>.

54. M. A. Sentef, M. Claassen, A. F. Kemper, B. Moritz, T. Oka, J. K. Freericks, and T. P. Devereaux. Theory of floquet band formation and local pseudospin textures in pump-probe photoemission of graphene. *Nature Communications*, 6(1):7047, May 2015. URL <https://doi.org/10.1038/ncomms8047>.
55. U. Schollwöck. The density-matrix renormalization group. *Rev. Mod. Phys.*, 77:259–315, Apr 2005. URL <https://link.aps.org/doi/10.1103/RevModPhys.77.259>.
56. Elliott H. Lieb and Derek W. Robinson. The finite group velocity of quantum spin systems. *Communications in Mathematical Physics*, 28(3):251–257, Sep 1972. URL <https://doi.org/10.1007/BF01645779>.
57. Daniel A. Roberts and Brian Swingle. Lieb-robinson bound and the butterfly effect in quantum field theories. *Phys. Rev. Lett.*, 117:091602, Aug 2016. URL <https://link.aps.org/doi/10.1103/PhysRevLett.117.091602>.
58. John Sous, Benedikt Kloss, Dante M. Kennes, David R. Reichman, and Andrew J. Millis. Phonon-induced disorder in dynamics of optically pumped metals from nonlinear electron-phonon coupling. *Nature Communications*, 12(1):5803, Oct 2021. URL <https://doi.org/10.1038/s41467-021-26030-3>.
59. Tatsuhiko N. Ikeda and Masahiro Sato. General description for nonequilibrium steady states in periodically driven dissipative quantum systems. *Science Advances*, 6(27): eabb4019, 2020. URL <https://www.science.org/doi/abs/10.1126/sciadv.abb4019>.
60. M. Yarmohammadi, C. Meyer, B. Fauseweh, B. Normand, and G. S. Uhrig. Dynamical properties of a driven dissipative dimerized $s = \frac{1}{2}$ chain. *Phys. Rev. B*, 103:045132, Jan 2021. URL <https://link.aps.org/doi/10.1103/PhysRevB.103.045132>.
61. A. F. Kemper, O. Abdurazakov, and J. K. Freericks. General principles for the nonequilibrium relaxation of populations in quantum materials. *Phys. Rev. X*, 8:041009, Oct 2018. URL <https://link.aps.org/doi/10.1103/PhysRevX.8.041009>.
62. Daniel Vorberg, Waltraut Wustmann, Roland Ketzmerick, and André Eckardt. Generalized bose-einstein condensation into multiple states in driven-dissipative systems. *Phys. Rev. Lett.*, 111:240405, Dec 2013. URL <https://link.aps.org/doi/10.1103/PhysRevLett.111.240405>.
63. E. M. Kessler, G. Giedke, A. Imamoglu, S. F. Yelin, M. D. Lukin, and J. I. Cirac. Dissipative phase transition in a central spin system. *Phys. Rev. A*, 86:012116, Jul 2012. URL <https://link.aps.org/doi/10.1103/PhysRevA.86.012116>.
64. L. Landau. The theory of phase transitions. *Nature*, 138(3498), Nov 1936. URL <https://doi.org/10.1038/138840a0>.
65. Ferdinand Brennecke, Rafael Mottl, Kristian Baumann, Renate Landig, Tobias Donner, and Tilman Esslinger. Real-time observation of fluctuations at the driven-dissipative dicke phase transition. *Proceedings of the National Academy of Sciences*, 110(29):11763–11767, 2013. URL <https://www.pnas.org/doi/abs/10.1073/pnas.1306993110>.

Bibliography

66. Aditi Mitra, So Takei, Yong Baek Kim, and A. J. Millis. Nonequilibrium quantum criticality in open electronic systems. *Phys. Rev. Lett.*, 97:236808, Dec 2006. URL <https://link.aps.org/doi/10.1103/PhysRevLett.97.236808>.
67. Aditi Mitra and Andrew J. Millis. Current-driven quantum criticality in itinerant electron ferromagnets. *Phys. Rev. B*, 77:220404, Jun 2008. URL <https://link.aps.org/doi/10.1103/PhysRevB.77.220404>.
68. Nicklas Walldorf, Dante M. Kennes, Jens Paaske, and Andrew J. Millis. The antiferromagnetic phase of the floquet-driven hubbard model. *Phys. Rev. B*, 100:121110, Sep 2019. URL <https://link.aps.org/doi/10.1103/PhysRevB.100.121110>.
69. Subir Sachdev. *Quantum Phase Transitions*. Cambridge University Press, 2 edition, 2011.
70. Piers Coleman. *Introduction to Many-Body Physics*. Cambridge University Press, 2015.
71. Baoquan Feng, Shuai Yin, and Fan Zhong. Theory of driven nonequilibrium critical phenomena. *Phys. Rev. B*, 94:144103, Oct 2016. URL <https://link.aps.org/doi/10.1103/PhysRevB.94.144103>.
72. P. V. Prudnikov, V. V. Prudnikov, and E. A. Pospelov. Calculation of the fluctuation-dissipation ratio for the nonequilibrium critical behavior of disordered systems. *JETP Letters*, 98(10):619–625, Jan 2014. URL <https://doi.org/10.1134/S0021364013230100>.
73. L. M. Sieberer, S. D. Huber, E. Altman, and S. Diehl. Dynamical critical phenomena in driven-dissipative systems. *Phys. Rev. Lett.*, 110:195301, May 2013. URL <https://link.aps.org/doi/10.1103/PhysRevLett.110.195301>.
74. Emanuele G. Dalla Torre, Eugene Demler, Thierry Giamarchi, and Ehud Altman. Quantum critical states and phase transitions in the presence of non-equilibrium noise. *Nature Physics*, 6(10):806–810, Oct 2010. URL <https://doi.org/10.1038/nphys1754>.
75. Jamir Marino and Sebastian Diehl. Driven markovian quantum criticality. *Phys. Rev. Lett.*, 116:070407, Feb 2016. URL <https://link.aps.org/doi/10.1103/PhysRevLett.116.070407>.
76. Adolfo del Campo and Wojciech H. Zurek. Universality of phase transition dynamics: Topological defects from symmetry breaking. *International Journal of Modern Physics A*, 29(08), 2014. URL <https://www.worldscientific.com/doi/abs/10.1142/S0217751X1430018X>.
77. Charles Kittel. *Introduction to solid state physics eighth edition*. 2021.
78. Sergio M. Rezende, Antonio Azevedo, and Roberto L. Rodríguez-Suárez. Introduction to antiferromagnetic magnons. *Journal of Applied Physics*, 126(15):151101, 2019. URL <https://doi.org/10.1063/1.5109132>.
79. Philipp Pirro, Vitaliy I. Vasyuchka, Alexander A. Serga, and Burkard Hillebrands. Advances in coherent magnonics. *Nature Reviews Materials*, Jul 2021. URL <https://doi.org/10.1038/s41578-021-00332-w>.

80. The 2021 magnonics roadmap. *Journal of Physics: Condensed Matter*, 33(41):413001, aug 2021. URL <https://doi.org/10.1088/1361-648x/abec1a>.
81. V. Zapf, M. Jaime, and C. D. Batista. Bose-einstein condensation in quantum magnets. *Rev. Mod. Phys.*, 86:563–614, May 2014. URL <https://link.aps.org/doi/10.1103/RevModPhys.86.563>.
82. Yu. M. Bunkov, E. M. Alakshin, R. R. Gazizulin, A. V. Klochkov, V. V. Kuzmin, T. R. Safin, and M. S. Tagirov. Discovery of the classical bose-einstein condensation of magnons in solid antiferromagnets. *JETP Letters*, 94(1):68, Sep 2011. URL <https://doi.org/10.1134/S0021364011130066>.
83. S. O. Demokritov, V. E. Demidov, O. Dzyapko, G. A. Melkov, A. A. Serga, B. Hillebrands, and A. N. Slavin. Bose-einstein condensation of quasi-equilibrium magnons at room temperature under pumping. *Nature*, 443(7110):430–433, Sep 2006. URL <https://doi.org/10.1038/nature05117>.
84. D. A. Bozhko, A. A. Serga, P. Clausen, V. I. Vasyuchka, F. Heussner, G. A. Melkov, A. Pomyalov, V. S. L’vov, and B. Hillebrands. Supercurrent in a room-temperature bose-einstein magnon condensate. *Nature Physics*, 12(11):1057–1062, Nov 2016. URL <https://doi.org/10.1038/nphys3838>.
85. P. Nowik-Boltyk, O. Dzyapko, V. E. Demidov, N. G. Berloff, and S. O. Demokritov. Spatially non-uniform ground state and quantized vortices in a two-component bose-einstein condensate of magnons. *Scientific Reports*, 2(1):482, Jun 2012. URL <https://doi.org/10.1038/srep00482>.
86. S. A. Bender, R. A. Duine, A. Brataas, and Y. Tserkovnyak. Dynamic phase diagram of dc-pumped magnon condensates. *Phys. Rev. B*, 90:094409, Sep 2014. URL <https://link.aps.org/doi/10.1103/PhysRevB.90.094409>.
87. P. Clausen, D. A. Bozhko, V. I. Vasyuchka, B. Hillebrands, G. A. Melkov, and A. A. Serga. Stimulated thermalization of a parametrically driven magnon gas as a prerequisite for bose-einstein magnon condensation. *Phys. Rev. B*, 91:220402, Jun 2015. URL <https://link.aps.org/doi/10.1103/PhysRevB.91.220402>.
88. V. E. Demidov, O. Dzyapko, M. Buchmeier, T. Stockhoff, G. Schmitz, G. A. Melkov, and S. O. Demokritov. Magnon kinetics and bose-einstein condensation studied in phase space. *Phys. Rev. Lett.*, 101:257201, Dec 2008. URL <https://link.aps.org/doi/10.1103/PhysRevLett.101.257201>.
89. A A Serga, A V Chumak, and B Hillebrands. YIG magnonics. *Journal of Physics D: Applied Physics*, 43(26):264002, jun 2010. URL <https://doi.org/10.1088/0022-3727/43/26/264002>.
90. Chen Sun, Thomas Nattermann, and Valery L Pokrovsky. Bose-einstein condensation and superfluidity of magnons in yttrium iron garnet films. *Journal of Physics D: Applied Physics*, 50(14):143002, mar 2017. URL <https://doi.org/10.1088/1361-6463/aa5cfc>.
91. Michael Schneider, Thomas Brächer, David Breitbach, Viktor Lauer, Philipp Pirro,

- Dmytro A. Bozhko, Halyna Yu. Musiienko-Shmarova, Björn Heinz, Qi Wang, Thomas Meyer, Frank Heussner, Sascha Keller, Evangelos Th. Papaioannou, Bert Lägél, Thomas Löber, Carsten Dubs, Andrei N. Slavin, Vasyl S. Tiberkevich, Alexander A. Serga, Burkard Hillebrands, and Andrii V. Chumak. Bose–einstein condensation of quasiparticles by rapid cooling. *Nature Nanotechnology*, 15(6):457–461, Jun 2020. URL <https://doi.org/10.1038/s41565-020-0671-z>.
92. L. J. Cornelissen, K. J. H. Peters, G. E. W. Bauer, R. A. Duine, and B. J. van Wees. Magnon spin transport driven by the magnon chemical potential in a magnetic insulator. *Phys. Rev. B*, 94:014412, Jul 2016. URL <https://link.aps.org/doi/10.1103/PhysRevB.94.014412>.
93. Steven S.-L. Zhang and Shufeng Zhang. Magnon mediated electric current drag across a ferromagnetic insulator layer. *Phys. Rev. Lett.*, 109:096603, Aug 2012. URL <https://link.aps.org/doi/10.1103/PhysRevLett.109.096603>.
94. Rico Schmidt, Francis Wilken, Tamara S. Nunner, and Piet W. Brouwer. Boltzmann approach to the longitudinal spin seebeck effect. *Phys. Rev. B*, 98:134421, Oct 2018. URL <https://link.aps.org/doi/10.1103/PhysRevB.98.134421>.
95. Andreas Rückriegel and Peter Kopietz. Rayleigh-jeans condensation of pumped magnons in thin-film ferromagnets. *Phys. Rev. Lett.*, 115:157203, Oct 2015. URL <https://link.aps.org/doi/10.1103/PhysRevLett.115.157203>.
96. Morteza Mohseni, Alireza Qaiumzadeh, Alexander A Serga, Arne Brataas, Burkard Hillebrands, and Philipp Pirro. Bose–einstein condensation of nonequilibrium magnons in confined systems. *New Journal of Physics*, 22(8):083080, aug 2020. URL <https://doi.org/10.1088/1367-2630/aba98c>.
97. Yuriy M Bunkov and Grigory E Volovik. Magnon bose–einstein condensation and spin superfluidity. *Journal of Physics: Condensed Matter*, 22(16):164210, mar 2010. URL <https://doi.org/10.1088/0953-8984/22/16/164210>.
98. Hui Deng, Hartmut Haug, and Yoshihisa Yamamoto. Exciton-polariton bose-einstein condensation. *Rev. Mod. Phys.*, 82:1489–1537, May 2010. URL <https://link.aps.org/doi/10.1103/RevModPhys.82.1489>.
99. L. M. Sieberer, S. D. Huber, E. Altman, and S. Diehl. Nonequilibrium functional renormalization for driven-dissipative bose-einstein condensation. *Phys. Rev. B*, 89:134310, Apr 2014. URL <https://link.aps.org/doi/10.1103/PhysRevB.89.134310>.
100. E. Manousakis. The spin- $\frac{1}{2}$ heisenberg antiferromagnet on a square lattice and its application to the cuprous oxides. *Rev. Mod. Phys.*, 63:1–62, Jan 1991. URL <https://link.aps.org/doi/10.1103/RevModPhys.63.1>.
101. A. Auerbach. *Interacting Electrons and Quantum Magnetism*. Springer-Verlag, 1994. URL <https://doi.org/10.1007/978-1-4612-0869-3>.
102. T. Oguchi. Theory of spin-wave interactions in ferro- and antiferromagnetism. *Phys. Rev.*, 117:117–123, Jan 1960. URL <https://link.aps.org/doi/10.1103/PhysRev.117.117>.

103. C. J. Hamer, Z. Weihong, and P. Arndt. Third-order spin-wave theory for the heisenberg antiferromagnet. *Phys. Rev. B*, 46:6276–6292, Sep 1992. URL <https://link.aps.org/doi/10.1103/PhysRevB.46.6276>.
104. Nuh Gedik and Inna Vishik. Photoemission of quantum materials. *Nature Physics*, 13(11): 1029–1033, Nov 2017. URL <https://doi.org/10.1038/nphys4273>.
105. Baiqing Lv, Tian Qian, and Hong Ding. Angle-resolved photoemission spectroscopy and its application to topological materials. *Nature Reviews Physics*, 1(10):609–626, Oct 2019. URL <https://doi.org/10.1038/s42254-019-0088-5>.
106. Stephan Hüfner. *Photoelectron spectroscopy: principles and applications*. Springer Science & Business Media, 2013.
107. Timm Rohwer, Stefan Hellmann, Martin Wiesenmayer, Christian Sohr, Ankatrin Stange, Bartosz Slomski, Adra Carr, Yanwei Liu, Luis Miaja Avila, Matthias Kalläne, Stefan Mathias, Lutz Kipp, Kai Rossnagel, and Michael Bauer. Collapse of long-range charge order tracked by time-resolved photoemission at high momenta. *Nature*, 471(7339):490–493, Mar 2011. URL <https://doi.org/10.1038/nature09829>.
108. P. Beaud, A. Caviezel, S. O. Mariager, L. Rettig, G. Ingold, C. Dornes, S.-W. Huang, J. A. Johnson, M. Radovic, T. Huber, T. Kubacka, A. Ferrer, H. T. Lemke, M. Chollet, D. Zhu, J. M. Glowina, M. Sikorski, A. Robert, H. Wadati, M. Nakamura, M. Kawasaki, Y. Tokura, S. L. Johnson, and U. Staub. A time-dependent order parameter for ultrafast photoinduced phase transitions. *Nature Materials*, 13(10):923–927, Oct 2014. URL <https://doi.org/10.1038/nmat4046>.
109. L. Perfetti, P. A. Loukakos, M. Lisowski, U. Bovensiepen, H. Berger, S. Biermann, P. S. Cornaglia, A. Georges, and M. Wolf. Time evolution of the electronic structure of $1t\text{-}2a_2$ through the insulator-metal transition. *Phys. Rev. Lett.*, 97:067402, Aug 2006. URL <https://link.aps.org/doi/10.1103/PhysRevLett.97.067402>.
110. Maria C Abramo, Dino Costa, Gianpietro Malescio, Gianmarco Munaò, Giuseppe Pelliscane, Santi Prestipino, and Carlo Caccamo. Structure factors and x-ray diffraction intensities in molten alkali halides. *Journal of Physics Communications*, 4(7):075017, jul 2020. URL <https://doi.org/10.1088/2399-6528/aba2b8>.
111. D. Starodub, A. Aquila, S. Bajt, M. Barthelmess, A. Barty, C. Bostedt, J. D. Bozek, N. Coppola, R. B. Doak, S. W. Epp, B. Erk, L. Foucar, L. Gumprecht, C. Y. Hampton, A. Hartmann, R. Hartmann, P. Holl, S. Kassemeyer, N. Kimmel, H. Laksmono, M. Liang, N. D. Loh, L. Lomb, A. V. Martin, K. Nass, C. Reich, D. Rolles, B. Rudek, A. Rudenko, J. Schulz, R. L. Shoeman, R. G. Sierra, H. Soltau, J. Steinbrener, F. Stellato, S. Stern, G. Weidenspointner, M. Frank, J. Ullrich, L. Strüder, I. Schlichting, H. N. Chapman, J. C. H. Spence, and M. J. Bogan. Single-particle structure determination by correlations of snapshot x-ray diffraction patterns. *Nature Communications*, 3(1):1276, Dec 2012. URL <https://doi.org/10.1038/ncomms2288>.
112. T. Kubacka, J. A. Johnson, M. C. Hoffmann, C. Vicario, S. de Jong, P. Beaud, S. Grübel, S.-W. Huang, L. Huber, L. Patthey, Y.-D. Chuang, J. J. Turner, G. L. Dakovski, W.-S.

- Lee, M. P. Minitti, W. Schlotter, R. G. Moore, C. P. Hauri, S. M. Koochpayeh, V. Scagnoli, G. Ingold, S. L. Johnson, and U. Staub. Large-amplitude spin dynamics driven by a thz pulse in resonance with an electromagnon. *Science*, 343(6177):1333–1336, 2014. URL <https://www.science.org/doi/abs/10.1126/science.1242862>.
113. E. Paris, C. W. Nicholson, S. Johnston, Y. Tseng, M. Rumo, G. Coslovich, S. Zohar, M. F. Lin, V. N. Strocov, R. Saint-Martin, A. Revcolevschi, A. Kemper, W. Schlotter, G. L. Dakovski, C. Monney, and T. Schmitt. Probing the interplay between lattice dynamics and short-range magnetic correlations in cugeo3 with femtosecond rixs. *npj Quantum Materials*, 6(1):51, May 2021. URL <https://doi.org/10.1038/s41535-021-00350-5>.
114. Matteo Mitrano and Yao Wang. Probing light-driven quantum materials with ultrafast resonant inelastic x-ray scattering. *Communications Physics*, 3(1):184, Oct 2020. URL <https://doi.org/10.1038/s42005-020-00447-6>.
115. Claudio Giannetti, Massimo Capone, Daniele Fausti, Michele Fabrizio, Fulvio Parmigiani, and Dragan Mihailovic. Ultrafast optical spectroscopy of strongly correlated materials and high-temperature superconductors: a non-equilibrium approach. *Advances in Physics*, 65(2):58–238, 2016. URL <https://doi.org/10.1080/00018732.2016.1194044>.
116. Daniele Nicoletti and Andrea Cavalleri. Nonlinear light–matter interaction at terahertz frequencies. *Adv. Opt. Photon.*, 8(3):401–464, Sep 2016. URL <http://opg.optica.org/aop/abstract.cfm?URI=aop-8-3-401>.
117. Thierry Giamarchi. *Quantum physics in one dimension*. International series of monographs on physics. Clarendon Press, Oxford, 2004. URL <https://cds.cern.ch/record/743140>.
118. R. Peierls. Zur theorie des diamagnetismus von leitungselektronen. *Zeitschrift für Physik*, 80(11):763–791, Nov 1933. URL <https://doi.org/10.1007/BF01342591>.
119. Thomas Vojta. *Quantum Phase Transitions*, pages 211–226. Springer Berlin Heidelberg, Berlin, Heidelberg, 2002. ISBN 978-3-662-04804-7. URL https://doi.org/10.1007/978-3-662-04804-7_13.
120. Otfried Gühne and Géza Tóth. Entanglement detection. *Physics Reports*, 474(1):1–75, 2009. URL <https://www.sciencedirect.com/science/article/pii/S0370157309000623>.
121. Martin Gärttner, Philipp Hauke, and Ana Maria Rey. Relating out-of-time-order correlations to entanglement via multiple-quantum coherences. *Phys. Rev. Lett.*, 120:040402, Jan 2018. URL <https://link.aps.org/doi/10.1103/PhysRevLett.120.040402>.
122. George Mathew, Saulo L. L. Silva, Anil Jain, Arya Mohan, D. T. Adroja, V. G. Sakai, C. V. Tomy, Alok Banerjee, Rajendar Goreti, Aswathi V. N., Ranjit Singh, and D. Jaiswal-Nagar. Experimental realization of multipartite entanglement via quantum fisher information in a uniform antiferromagnetic quantum spin chain. *Phys. Rev. Research*, 2:043329, Dec 2020. URL <https://link.aps.org/doi/10.1103/PhysRevResearch.2.043329>.
123. Philipp Hauke, Markus Heyl, Luca Tagliacozzo, and Peter Zoller. Measuring multipartite entanglement through dynamic susceptibilities. *Nature Physics*, 12(8):778–782, Aug 2016.

- URL <https://doi.org/10.1038/nphys3700>.
124. Denitsa R. Baykusheva, Hoyoung Jang, Ali A. Husain, Sangjun Lee, Sophia F. R. Ten-Huisen, Preston Zhou, Sunwook Park, Hoon Kim, Jin-Kwang Kim, Hyeong-Do Kim, Min-seok Kim, Sang-Youn Park, Peter Abbamonte, B. J. Kim, G. D. Gu, Yao Wang, and Matteo Mitrano. Ultrafast renormalization of the on-site coulomb repulsion in a cuprate superconductor. *Phys. Rev. X*, 12:011013, Jan 2022. URL <https://link.aps.org/doi/10.1103/PhysRevX.12.011013>.
 125. R. Singla, G. Cotugno, S. Kaiser, M. Först, M. Mitrano, H. Y. Liu, A. Cartella, C. Manzoni, H. Okamoto, T. Hasegawa, S. R. Clark, D. Jaksch, and A. Cavalleri. Thz-frequency modulation of the hubbard u in an organic mott insulator. *Phys. Rev. Lett.*, 115:187401, Oct 2015. URL <https://link.aps.org/doi/10.1103/PhysRevLett.115.187401>.
 126. Steven R. White. Density matrix formulation for quantum renormalization groups. *Phys. Rev. Lett.*, 69:2863–2866, Nov 1992. URL <https://link.aps.org/doi/10.1103/PhysRevLett.69.2863>.
 127. C. Karrasch and J. E. Moore. Luttinger liquid physics from the infinite-system density matrix renormalization group. *Phys. Rev. B*, 86:155156, Oct 2012. URL <https://link.aps.org/doi/10.1103/PhysRevB.86.155156>.
 128. Phillip Weinberg and Marin Bukov. QuSpin: a Python Package for Dynamics and Exact Diagonalisation of Quantum Many Body Systems part I: spin chains. *SciPost Phys.*, 2:003, 2017. URL <https://scipost.org/10.21468/SciPostPhys.2.1.003>.
 129. Piotr Chudzinski and Dirk Schuricht. Time evolution during and after finite-time quantum quenches in luttinger liquids. *Phys. Rev. B*, 94:075129, Aug 2016. URL <https://link.aps.org/doi/10.1103/PhysRevB.94.075129>.
 130. Mario Collura, Pasquale Calabrese, and Fabian H. L. Essler. Quantum quench within the gapless phase of the spin $- \frac{1}{2}$ heisenberg xxz spin chain. *Phys. Rev. B*, 92:125131, Sep 2015. URL <https://link.aps.org/doi/10.1103/PhysRevB.92.125131>.
 131. M. A. Cazalilla. Effect of suddenly turning on interactions in the luttinger model. *Phys. Rev. Lett.*, 97:156403, Oct 2006. URL <https://link.aps.org/doi/10.1103/PhysRevLett.97.156403>.
 132. S. Kaiser, S. R. Clark, D. Nicoletti, G. Cotugno, R. I. Tobey, N. Dean, S. Lupi, H. Okamoto, T. Hasegawa, D. Jaksch, and A. Cavalleri. Optical properties of a vibrationally modulated solid state mott insulator. *Scientific Reports*, 4(1):3823, Jan 2014. URL <https://doi.org/10.1038/srep03823>.
 133. Riccardo Rota, Fabrizio Minganti, Cristiano Ciuti, and Vincenzo Savona. Quantum critical regime in a quadratically driven nonlinear photonic lattice. *Phys. Rev. Lett.*, 122:110405, Mar 2019. URL <https://link.aps.org/doi/10.1103/PhysRevLett.122.110405>.
 134. C. Klöckner, C. Karrasch, and D. M. Kennes. Nonequilibrium properties of berezinskii-kosterlitz-thouless phase transitions. *Phys. Rev. Lett.*, 125:147601, Oct 2020. URL <https://link.aps.org/doi/10.1103/PhysRevLett.125.147601>.

Bibliography

135. Guo-Qiang Zhang, Zhen Chen, Wei Xiong, Chi-Hang Lam, and J. Q. You. Parity-symmetry-breaking quantum phase transition via parametric drive in a cavity magnonic system. *Phys. Rev. B*, 104:064423, Aug 2021. URL <https://link.aps.org/doi/10.1103/PhysRevB.104.064423>.
136. A. Griffin, D. W. Snoke, and S. Stringari. *Bose-Einstein Condensation*. Cambridge University Press, 1995.
137. François Golse. From the boltzmann equation to the euler equations in the presence of boundaries. *Computers & Mathematics with Applications*, 65(6):815–830, Mar 2013. URL <https://www.sciencedirect.com/science/article/pii/S089812211200123X>.
138. Johannes D. Plumhof, Thilo Stöferle, Lijian Mai, Ullrich Scherf, and Rainer F. Mahrt. Room-temperature bose–einstein condensation of cavity exciton–polaritons in a polymer. *Nature Materials*, 13(3):247–252, Mar 2014. URL <https://doi.org/10.1038/nmat3825>.
139. Tim Byrnes, Na Young Kim, and Yoshihisa Yamamoto. Exciton–polariton condensates. *Nature Physics*, 10(11):803–813, Nov 2014. URL <https://doi.org/10.1038/nphys3143>.
140. Hui Deng, Gregor Weihs, Charles Santori, Jacqueline Bloch, and Yoshihisa Yamamoto. Condensation of semiconductor microcavity exciton polaritons. *Science*, 298(5591):199–202, 2002. URL <https://www.science.org/doi/abs/10.1126/science.1074464>.
141. Fabio Scafirimuto, Darius Urbonas, Michael A. Becker, Ullrich Scherf, Rainer F. Mahrt, and Thilo Stöferle. Tunable exciton–polariton condensation in a two-dimensional lieb lattice at room temperature. *Communications Physics*, 4(1):39, Mar 2021. URL <https://doi.org/10.1038/s42005-021-00548-w>.
142. Daniel P. Arovas and Assa Auerbach. Functional integral theories of low-dimensional quantum heisenberg models. *Phys. Rev. B*, 38:316–332, Jul 1988. URL <https://link.aps.org/doi/10.1103/PhysRevB.38.316>.
143. Assa Auerbach and Daniel P Arovas. New approaches to the quantum heisenberg models: Schwinger boson representations. *Journal of applied physics*, 67(9):5734–5739, 1990. URL <https://doi.org/10.1063/1.345947>.
144. Daniel G. Mazzone, Derek Meyers, Yue Cao, James G. Vale, Cameron D. Dashwood, Youguo Shi, Andrew J. A. James, Neil J. Robinson, Jiaqi Lin, Vivek Thampy, Yoshikazu Tanaka, Allan S. Johnson, Hu Miao, Ruitang Wang, Tadesse A. Assefa, Jungho Kim, Diego Casa, Roman Mankowsky, Diling Zhu, Roberto Alonso-Mori, Sanghoon Song, Hasan Yavas, Tetsuo Katayama, Makina Yabashi, Yuya Kubota, Shigeki Owada, Jian Liu, Junji Yang, Robert M. Konik, Ian K. Robinson, John P. Hill, Desmond F. McMorrow, Michael Först, Simon Wall, Xuerong Liu, and Mark P. M. Dean. Laser-induced transient magnons in sr3ir2o7 throughout the brillouin zone. *Proceedings of the National Academy of Sciences*, 118(22):e2103696118, 2021. URL <https://www.pnas.org/doi/abs/10.1073/pnas.2103696118>.
145. M. P. M. Dean, Y. Cao, X. Liu, S. Wall, D. Zhu, R. Mankowsky, V. Thampy, X. M. Chen, J. G. Vale, D. Casa, Jungho Kim, A. H. Said, P. Juhas, R. Alonso-Mori, J. M. Glowia, A. Robert, J. Robinson, M. Sikorski, S. Song, M. Kozina, H. Lemke, L. Patthey,

- S. Owada, T. Katayama, M. Yabashi, Yoshikazu Tanaka, T. Togashi, J. Liu, C. Rayan Serrao, B. J. Kim, L. Huber, C.-L. Chang, D. F. McMorrow, M. Först, and J. P. Hill. Ultrafast energy- and momentum-resolved dynamics of magnetic correlations in the photo-doped mott insulator SrTiO_3 . *Nature Materials*, 15(6):601–605, Jun 2016. URL <https://doi.org/10.1038/nmat4641>.
146. J. Zhang and R.D. Averitt. Dynamics and control in complex transition metal oxides. *Annual Review of Materials Research*, 44(1):19–43, 2014. URL <https://doi.org/10.1146/annurev-matsci-070813-113258>.

Appendix

A Mathematical details of the magnon interactions

The two-operator products in this Eq. (5.43) and Eq. (5.44) are given by

$$a_1^\dagger a_3 = v_1^2 \delta(\mathbf{k}_1 - \mathbf{k}_3) + u_1 u_3 \alpha_1^\dagger \alpha_3 + v_1 v_3 \beta_3^\dagger \beta_1 + u_1 v_3 \alpha_1^\dagger \beta_3^\dagger + u_3 v_1 \alpha_3 \beta_1 \quad (\text{A.1a})$$

$$b_4^\dagger b_2 = v_2^2 \delta(\mathbf{k}_2 - \mathbf{k}_4) + u_2 u_4 \beta_4^\dagger \beta_2 + v_2 v_4 \alpha_2^\dagger \alpha_4 + u_4 v_2 \alpha_2^\dagger \beta_4^\dagger + u_2 v_4 \alpha_4 \beta_2 \quad (\text{A.1b})$$

$$a_4 b_2 = u_2 v_2 \delta(\mathbf{k}_2 - \mathbf{k}_4) + u_4 v_2 \alpha_2^\dagger \alpha_4 + u_2 v_4 \beta_4^\dagger \beta_2 + v_2 v_4 \alpha_2^\dagger \beta_4^\dagger + u_2 u_4 \alpha_4 \beta_2 \quad (\text{A.1c})$$

$$a_1^\dagger b_3^\dagger = u_1 v_1 \delta(\mathbf{k}_1 - \mathbf{k}_3) + u_1 v_3 \alpha_1^\dagger \alpha_3 + u_3 v_1 \beta_3^\dagger \beta_1 + u_1 u_3 \alpha_1^\dagger \beta_3^\dagger + v_1 v_3 \alpha_3 \beta_1. \quad (\text{A.1d})$$

With this, we can evaluate the four operator products that appear both in the Holstein-Primakoff and the Dyson-Maleev formalism, namely

$$\begin{aligned} a_1^\dagger a_3 b_4^\dagger b_2 &= v_1^2 v_2^2 \delta(\mathbf{k}_1 - \mathbf{k}_3) \delta(\mathbf{k}_2 - \mathbf{k}_4) + u_1 u_2 v_1 v_2 \delta(\mathbf{k}_1 - \mathbf{k}_4) \delta(\mathbf{k}_2 - \mathbf{k}_3) \quad (\text{A.2}) \\ &+ v_1^2 \delta(\mathbf{k}_1 - \mathbf{k}_3) \left(u_2 u_4 \beta_4^\dagger \beta_2 + v_2 v_4 \alpha_2^\dagger \alpha_4 + u_4 v_2 \alpha_2^\dagger \beta_4^\dagger + u_2 v_4 \alpha_4 \beta_2 \right) \\ &+ v_2^2 \delta(\mathbf{k}_2 - \mathbf{k}_4) \left(u_1 u_3 \alpha_1^\dagger \alpha_3 + v_1 v_3 \beta_3^\dagger \beta_1 + u_1 v_3 \alpha_1^\dagger \beta_3^\dagger + u_3 v_1 \alpha_3 \beta_1 \right) \\ &+ u_2 v_2 \delta(\mathbf{k}_2 - \mathbf{k}_3) \left(u_1 v_4 \alpha_1^\dagger \alpha_4 + u_1 u_4 \alpha_1^\dagger \beta_4^\dagger + v_1 v_4 \alpha_4 \beta_1 + u_4 v_1 \beta_4^\dagger \beta_1 \right) \\ &+ u_1 v_1 \delta(\mathbf{k}_1 - \mathbf{k}_4) \left(u_2 v_3 \beta_3^\dagger \beta_2 + v_2 v_3 \alpha_2^\dagger \beta_3^\dagger + u_2 u_3 \alpha_3 \beta_2 + u_3 v_2 \alpha_2^\dagger \alpha_3 \right) \\ &+ u_1 u_2 u_3 u_4 \alpha_1^\dagger \alpha_3 \beta_4^\dagger \beta_2 + v_1 v_2 v_3 v_4 \alpha_2^\dagger \alpha_4 \beta_3^\dagger \beta_1 \\ &+ u_1 u_2 v_3 v_4 \alpha_1^\dagger \alpha_4 \beta_3^\dagger \beta_2 + u_3 u_4 v_1 v_2 \alpha_2^\dagger \alpha_3 \beta_4^\dagger \beta_1 \\ &+ u_1 u_3 v_2 v_4 \alpha_1^\dagger \alpha_2^\dagger \alpha_3 \alpha_4 + u_2 u_4 v_1 v_3 \beta_3^\dagger \beta_4^\dagger \beta_1 \beta_2 \\ &+ u_1 u_4 v_2 v_3 \alpha_1^\dagger \alpha_2^\dagger \beta_3^\dagger \beta_4^\dagger + u_3 u_2 v_1 v_4 \alpha_3 \alpha_4 \beta_1 \beta_2 \\ &+ u_1 u_3 u_4 v_2 \alpha_1^\dagger \alpha_2^\dagger \alpha_3 \beta_4^\dagger + u_1 v_2 v_3 v_4 \alpha_1^\dagger \alpha_2^\dagger \alpha_4 \beta_3^\dagger \\ &+ u_1 u_2 u_3 v_4 \alpha_1^\dagger \alpha_3 \alpha_4 \beta_2 + u_3 v_1 v_2 v_4 \alpha_2^\dagger \alpha_3 \alpha_4 \beta_1 \\ &+ u_4 v_1 v_2 v_3 \alpha_2^\dagger \beta_3^\dagger \beta_4^\dagger \beta_1 + u_1 u_2 u_4 v_3 \alpha_1^\dagger \beta_3^\dagger \beta_4^\dagger \beta_2 \\ &+ u_2 u_3 u_4 v_1 \alpha_3 \beta_4^\dagger \beta_1 \beta_2 + u_2 v_1 v_3 v_4 \alpha_4 \beta_3^\dagger \beta_1 \beta_2, \end{aligned}$$

which is the only term dependent on the anisotropy parameter Δ , as well as

$$\begin{aligned} a_1^\dagger a_3 a_4 b_2 &= v_1^2 u_2 v_2 [\delta(\mathbf{k}_1 - \mathbf{k}_3) \delta(\mathbf{k}_2 - \mathbf{k}_4) + \delta(\mathbf{k}_2 - \mathbf{k}_3) \delta(\mathbf{k}_1 - \mathbf{k}_4)] \quad (\text{A.3}) \\ &+ v_1^2 \delta(\mathbf{k}_1 - \mathbf{k}_3) \left(u_4 v_2 \alpha_2^\dagger \alpha_4 + u_2 v_4 \beta_4^\dagger \beta_2 + v_2 v_4 \alpha_2^\dagger \beta_4^\dagger + u_2 u_4 \alpha_4 \beta_2 \right) \\ &+ u_2 v_2 \delta(\mathbf{k}_2 - \mathbf{k}_4) \left(u_1 u_3 \alpha_1^\dagger \alpha_3 + v_1 v_3 \beta_3^\dagger \beta_1 + u_1 v_3 \alpha_1^\dagger \beta_3^\dagger + u_3 v_1 \alpha_3 \beta_1 \right) \\ &+ u_2 v_2 \delta(\mathbf{k}_2 - \mathbf{k}_3) \left(u_1 u_4 \alpha_1^\dagger \alpha_4 + v_1 v_4 \beta_4^\dagger \beta_1 + u_1 v_4 \alpha_1^\dagger \beta_4^\dagger + u_4 v_1 \alpha_4 \beta_1 \right) \\ &+ v_1^2 \delta(\mathbf{k}_1 - \mathbf{k}_4) \left(u_3 v_2 \alpha_2^\dagger \alpha_3 + u_2 v_3 \beta_3^\dagger \beta_2 + v_2 v_3 \alpha_2^\dagger \beta_3^\dagger + u_3 u_2 \alpha_3 \beta_2 \right) \\ &+ u_1 u_2 u_3 v_4 \alpha_1^\dagger \alpha_3 \beta_4^\dagger \beta_2 + u_4 v_1 v_3 v_2 \alpha_2^\dagger \alpha_4 \beta_3^\dagger \beta_1 \end{aligned}$$

$$\begin{aligned}
& + u_1 u_2 u_4 v_3 \alpha_1^\dagger \alpha_4 \beta_3^\dagger \beta_2 + u_3 v_1 v_2 v_4 \alpha_2^\dagger \alpha_3 \beta_4^\dagger \beta_1 \\
& + u_1 u_3 u_4 v_2 \alpha_1^\dagger \alpha_2^\dagger \alpha_3 \alpha_4 + u_2 v_1 v_3 v_4 \beta_3^\dagger \beta_4^\dagger \beta_1 \beta_2 \\
& + u_1 v_3 v_2 v_4 \alpha_1^\dagger \alpha_2^\dagger \beta_3^\dagger \beta_4^\dagger + u_3 u_2 u_4 v_1 \alpha_3 \beta_1 \alpha_4 \beta_2 \\
& + u_1 u_3 v_2 v_4 \alpha_1^\dagger \alpha_2^\dagger \alpha_3 \beta_4^\dagger + u_1 u_4 v_3 v_2 \alpha_1^\dagger \alpha_2^\dagger \alpha_4 \beta_3^\dagger \\
& + u_1 u_2 u_3 u_4 \alpha_1^\dagger \alpha_3 \alpha_4 \beta_2 + u_3 u_4 v_1 v_2 \alpha_2^\dagger \alpha_3 \alpha_4 \beta_1 \\
& + v_1 v_2 v_3 v_4 \alpha_2^\dagger \beta_3^\dagger \beta_4^\dagger \beta_1 + u_1 u_2 v_3 v_4 \alpha_1^\dagger \beta_3^\dagger \beta_4^\dagger \beta_2 \\
& + u_2 u_4 v_1 v_3 \alpha_4 \beta_3^\dagger \beta_1 \beta_2 + u_3 u_2 v_1 v_4 \alpha_3 \beta_4^\dagger \beta_1 \beta_2
\end{aligned}$$

and

$$\begin{aligned}
a_1^\dagger b_3^\dagger b_4^\dagger b_2 &= v_2^2 u_1 v_1 \delta(\mathbf{k}_1 - \mathbf{k}_3) \delta(\mathbf{k}_2 - \mathbf{k}_4) + v_2^2 u_1 v_1 (\mathbf{k}_2 - \mathbf{k}_3) \delta(\mathbf{k}_1 - \mathbf{k}_4) \quad (\text{A.4}) \\
& + u_1 v_1 \delta(\mathbf{k}_1 - \mathbf{k}_3) \left(v_2 v_4 \alpha_2^\dagger \alpha_4 + u_2 u_4 \beta_4^\dagger \beta_2 + u_4 v_2 \alpha_2^\dagger \beta_4^\dagger + u_2 v_4 \alpha_4 \beta_2 \right) \\
& + v_2^2 \delta(\mathbf{k}_2 - \mathbf{k}_4) \left(u_1 v_3 \alpha_1^\dagger \alpha_3 + u_3 v_1 \beta_3^\dagger \beta_1 + u_1 u_3 \alpha_1^\dagger \beta_3^\dagger + v_1 v_3 \alpha_3 \beta_1 \right) \\
& + v_2^2 \delta(\mathbf{k}_2 - \mathbf{k}_3) \left(u_1 v_4 \alpha_1^\dagger \alpha_4 + u_4 v_1 \beta_4^\dagger \beta_1 + u_1 u_4 \alpha_1^\dagger \beta_4^\dagger + v_1 v_4 \alpha_4 \beta_1 \right) \\
& + u_1 v_1 \delta(\mathbf{k}_1 - \mathbf{k}_4) \left(v_2 v_3 \alpha_2^\dagger \alpha_3 + u_2 u_3 \beta_3^\dagger \beta_2 + u_3 v_2 \alpha_2^\dagger \beta_3^\dagger + u_2 v_3 \alpha_3 \beta_2 \right) \\
& + u_1 u_2 u_4 v_3 \alpha_1^\dagger \alpha_3 \beta_4^\dagger \beta_2 + u_3 v_1 v_2 v_4 \alpha_2^\dagger \alpha_4 \beta_3^\dagger \beta_1 \\
& + u_1 u_2 u_3 v_4 \alpha_1^\dagger \alpha_4 \beta_3^\dagger \beta_2 + u_4 v_1 v_2 v_3 \alpha_2^\dagger \alpha_3 \beta_4^\dagger \beta_1 \\
& + u_1 v_2 v_3 v_4 \alpha_1^\dagger \alpha_2^\dagger \alpha_3 \alpha_4 + u_2 u_3 u_4 v_1 \beta_3^\dagger \beta_4^\dagger \beta_1 \beta_2 \\
& + u_1 u_3 u_4 v_2 \alpha_1^\dagger \alpha_2^\dagger \beta_3^\dagger \beta_4^\dagger + u_2 v_1 v_3 v_4 \alpha_3 \alpha_4 \beta_1 \beta_2 \\
& + u_1 v_2 u_4 v_3 \alpha_1^\dagger \alpha_2^\dagger \alpha_3 \beta_4^\dagger + u_1 u_3 v_2 v_4 \alpha_1^\dagger \alpha_2^\dagger \alpha_4 \beta_3^\dagger \\
& + u_1 u_2 v_3 v_4 \alpha_1^\dagger \alpha_3 \alpha_4 \beta_2 + v_1 v_2 v_3 v_4 \alpha_2^\dagger \alpha_3 \alpha_4 \beta_1 \\
& + u_3 u_4 v_1 v_2 \alpha_2^\dagger \beta_3^\dagger \beta_4^\dagger \beta_1 + u_1 u_2 u_3 u_4 \alpha_1^\dagger \beta_3^\dagger \beta_4^\dagger \beta_2 \\
& + u_2 u_3 v_1 v_4 \alpha_4 \beta_3^\dagger \beta_1 \beta_2 + u_2 u_4 v_1 v_3 \alpha_3 \beta_4^\dagger \beta_1 \beta_2 .
\end{aligned}$$

The products that only appear in the Hollstein Primakoff formalism are

$$\begin{aligned}
a_1^\dagger b_4^\dagger a_2^\dagger a_3 &= u_1 v_1 v_2^2 \delta(\mathbf{k}_1 - \mathbf{k}_4) \delta(\mathbf{k}_2 - \mathbf{k}_3) + v_1^2 u_2 v_2 \delta(\mathbf{k}_1 - \mathbf{k}_3) \delta(\mathbf{k}_2 - \mathbf{k}_4) \quad (\text{A.5}) \\
& + v_1^2 \delta(\mathbf{k}_1 - \mathbf{k}_3) \left(u_2 v_4 \alpha_2^\dagger \alpha_4 + u_4 v_2 \beta_4^\dagger \beta_2 + u_2 u_4 \alpha_2^\dagger \beta_4^\dagger + v_2 v_4 \alpha_4 \beta_2 \right) \\
& + u_2 v_2 \delta(\mathbf{k}_2 - \mathbf{k}_4) \left(u_1 u_3 \alpha_1^\dagger \alpha_3 + v_1 v_3 \beta_3^\dagger \beta_1 + u_1 v_3 \alpha_1^\dagger \beta_3^\dagger + u_3 v_1 \alpha_3 \beta_1 \right) \\
& + v_2^2 \delta(\mathbf{k}_2 - \mathbf{k}_3) \left(u_1 v_4 \alpha_1^\dagger \alpha_4 + u_4 v_1 \beta_4^\dagger \beta_1 + u_1 u_4 \alpha_1^\dagger \beta_4^\dagger + v_1 v_4 \alpha_4 \beta_1 \right) \\
& + u_1 v_1 \delta(\mathbf{k}_1 - \mathbf{k}_4) \left(u_2 u_3 \alpha_2^\dagger \alpha_3 + v_2 v_3 \beta_3^\dagger \beta_2 + u_2 v_3 \alpha_2^\dagger \beta_3^\dagger + u_3 v_2 \alpha_3 \beta_2 \right) \\
& + u_1 v_2 v_3 v_4 \alpha_1^\dagger \alpha_4 \beta_3^\dagger \beta_2 + u_4 u_2 u_3 v_1 \alpha_2^\dagger \alpha_3 \beta_4^\dagger \beta_1 \\
& + u_1 u_3 u_4 v_2 \alpha_1^\dagger \alpha_3 \beta_4^\dagger \beta_2 + u_2 v_1 v_3 v_4 \alpha_2^\dagger \alpha_4 \beta_3^\dagger \beta_1 \\
& + u_1 u_2 u_3 v_4 \alpha_1^\dagger \alpha_2^\dagger \alpha_4 \alpha_3 + u_4 v_1 v_2 v_3 \beta_4^\dagger \beta_3^\dagger \beta_1 \beta_2 \\
& + u_1 u_2 u_4 v_3 \alpha_1^\dagger \alpha_2^\dagger \beta_3^\dagger \beta_4^\dagger + u_3 v_1 v_2 v_4 \alpha_3 \alpha_4 \beta_1 \beta_2 \\
& + u_1 u_2 v_3 v_4 \alpha_1^\dagger \alpha_2^\dagger \alpha_4 \beta_3^\dagger + u_1 u_2 u_3 u_4 \alpha_1^\dagger \alpha_2^\dagger \alpha_3 \beta_4^\dagger \\
& + u_3 u_4 v_1 v_2 \alpha_3 \beta_4^\dagger \beta_1 \beta_2 + v_1 v_2 v_3 v_4 \alpha_4 \beta_3^\dagger \beta_1 \beta_2 \\
& + u_1 u_3 v_2 v_4 \alpha_1^\dagger \alpha_3 \alpha_4 \beta_2 + u_2 u_3 v_1 v_4 \alpha_2^\dagger \alpha_3 \alpha_4 \beta_1
\end{aligned}$$

$$+ u_2 u_4 v_1 v_3 \alpha_2^\dagger \beta_3^\dagger \beta_4^\dagger \beta_1 + u_1 u_4 v_2 v_3 \alpha_1^\dagger \beta_3^\dagger \beta_4^\dagger \beta_2$$

and

$$\begin{aligned}
 b_2^\dagger b_3 a_1 b_4 = & u_1 v_1 v_2^2 \delta(\mathbf{k}_1 - \mathbf{k}_4) \delta(\mathbf{k}_2 - \mathbf{k}_3) + u_1 v_1 v_2^2 \delta(\mathbf{k}_1 - \mathbf{k}_3) \delta(\mathbf{k}_2 - \mathbf{k}_4) \quad (\text{A.6}) \\
 & + u_1 v_1 \delta(\mathbf{k}_1 - \mathbf{k}_3) \left(v_2 v_4 \alpha_4^\dagger \alpha_2 + u_2 u_4 \beta_2^\dagger \beta_4 + u_2 v_4 \alpha_4^\dagger \beta_2^\dagger + u_4 v_2 \alpha_2 \beta_4 \right) \\
 & + v_2^2 \delta(\mathbf{k}_2 - \mathbf{k}_4) \left(u_1 v_3 \alpha_3^\dagger \alpha_1 + u_3 v_1 \beta_1^\dagger \beta_3 + v_1 v_3 \alpha_3^\dagger \beta_1^\dagger + u_1 u_3 \alpha_1 \beta_3 \right) \\
 & + v_2^2 \delta(\mathbf{k}_2 - \mathbf{k}_3) \left(u_1 v_4 \alpha_4^\dagger \alpha_1 + u_4 v_1 \beta_1^\dagger \beta_4 + v_1 v_4 \alpha_4^\dagger \beta_1^\dagger + u_1 u_4 \alpha_1 \beta_4 \right) \\
 & + u_1 v_1 \delta(\mathbf{k}_1 - \mathbf{k}_4) \left(v_2 v_3 \alpha_3^\dagger \alpha_2 + u_2 u_3 \beta_2^\dagger \beta_3 + u_2 v_3 \alpha_3^\dagger \beta_2^\dagger + u_3 v_2 \alpha_2 \beta_3 \right) \\
 & + u_1 u_2 u_3 v_4 \alpha_4^\dagger \alpha_1 \beta_2^\dagger \beta_3 + u_4 v_1 v_2 v_3 \alpha_3^\dagger \alpha_2 \beta_1^\dagger \beta_4 \\
 & + u_1 u_2 u_4 v_3 \alpha_3^\dagger \beta_2^\dagger \alpha_1 \beta_4 + u_3 v_1 v_2 v_4 \alpha_4^\dagger \alpha_2 \beta_1^\dagger \beta_3 \\
 & + u_3 u_2 u_4 v_1 \beta_2^\dagger \beta_1^\dagger \beta_3 \beta_4 + u_1 v_2 v_3 v_4 \alpha_3^\dagger \alpha_4^\dagger \alpha_2 \alpha_1 \\
 & + u_2 v_1 v_3 v_4 \alpha_3^\dagger \alpha_4^\dagger \beta_1^\dagger \beta_2^\dagger + u_1 u_3 u_4 v_2 \alpha_1 \alpha_2 \beta_3 \beta_4 \\
 & + u_1 u_2 v_3 v_4 \alpha_3^\dagger \alpha_4^\dagger \alpha_1 \beta_2^\dagger + v_1 v_2 v_3 v_4 \alpha_3^\dagger \alpha_4^\dagger \alpha_2 \beta_1^\dagger \\
 & + u_1 u_2 u_3 u_4 \alpha_1 \beta_2^\dagger \beta_3 \beta_4 + u_3 u_4 v_1 v_2 \alpha_2 \beta_1^\dagger \beta_3 \beta_4 \\
 & + u_1 u_4 v_2 v_3 \alpha_3^\dagger \alpha_1 \alpha_2 \beta_4 + u_1 u_3 v_2 v_4 \alpha_4^\dagger \alpha_1 \alpha_2 \beta_3 \\
 & + u_2 u_4 v_1 v_3 \alpha_3^\dagger \beta_1^\dagger \beta_2^\dagger \beta_4 + u_2 u_3 v_1 v_4 \alpha_4^\dagger \beta_1^\dagger \beta_2^\dagger \beta_3,
 \end{aligned}$$

where the scattering terms that conserve the number of magnons are marked in blue. In order to simplify notation we will write the delta function as

$$\delta_{(1+2-3-4)} = \delta_{(1+2-3-4)} \quad (\text{A.7})$$

in this appendix. The component of the product of four operators that encode the magnon interactions as defined in Eq. (5.45) is given by

$$\begin{aligned}
 \mathcal{P}_1 = & \sum_{\mathbf{k}_1 \mathbf{k}_2 \mathbf{k}_3 \mathbf{k}_4} \Delta \delta_{(1+2-3-4)} \left[\gamma_{(2-4)} (u_1 u_2 u_3 u_4 + v_1 v_2 v_3 v_4) \right] \alpha_1^\dagger \alpha_3 \beta_4^\dagger \beta_2 \quad (\text{A.8}) \\
 & + \sum_{\mathbf{k}_1 \mathbf{k}_2 \mathbf{k}_3 \mathbf{k}_4} \Delta \delta_{(1+2-3-4)} \left[\gamma_{(2-3)} (u_1 u_2 v_3 v_4 + u_3 u_4 v_1 v_2) \right] \alpha_1^\dagger \alpha_3 \beta_4^\dagger \beta_2 \\
 & + \sum_{\mathbf{k}_1 \mathbf{k}_2 \mathbf{k}_3 \mathbf{k}_4} \Delta \delta_{(1+2-3-4)} \left[\gamma_{(2-4)} u_1 u_3 v_2 v_4 \right] \left(\alpha_1^\dagger \alpha_2^\dagger \alpha_3 \alpha_4 + \beta_3^\dagger \beta_4^\dagger \beta_1 \beta_2 \right) \\
 & + \sum_{\mathbf{k}_1 \mathbf{k}_2 \mathbf{k}_3 \mathbf{k}_4} \Delta \delta_{(1+2-3-4)} \gamma_{(2-3)} [u_1 u_3 u_4 v_2 + u_2 v_1 v_3 v_4] \left(\alpha_1^\dagger \alpha_2^\dagger \alpha_4 \beta_3^\dagger + \alpha_3 \beta_4^\dagger \beta_1 \beta_2 \right) \\
 & + \sum_{\mathbf{k}_1 \mathbf{k}_2 \mathbf{k}_3 \mathbf{k}_4} \Delta \delta_{(1+2-3-4)} \gamma_{(2-4)} [u_4 v_1 v_2 v_3 + u_1 u_2 u_3 v_4] \left(\alpha_1^\dagger \alpha_3 \alpha_4 \beta_2 + \alpha_2^\dagger \beta_3^\dagger \beta_4^\dagger \beta_1 \right) \\
 & + \sum_{\mathbf{k}_1 \mathbf{k}_2 \mathbf{k}_3 \mathbf{k}_4} \Delta \delta_{(1+2-3-4)} \gamma_{(2-4)} u_1 u_4 v_2 v_3 \left(\alpha_1^\dagger \alpha_2^\dagger \beta_3^\dagger \beta_4^\dagger + \alpha_1 \alpha_2 \beta_3 \beta_4 \right),
 \end{aligned}$$

where we have used that due to the delta-function we can write $\gamma_{(2-4)} = \gamma_{(1-3)}$. The remaining components from Eq. (5.46) that are the same in both the Hollstein-Primakoff and the Dyson-Maleev formalism are given by

$$\mathcal{P}_2 = 2 \sum_{\mathbf{k}_1 \mathbf{k}_2 \mathbf{k}_3 \mathbf{k}_4} \delta_{(1+2-3-4)} \left[\gamma_{(2)} u_1 u_2 u_3 v_4 + \gamma_{(1)} u_3 v_1 v_2 v_4 \right] \alpha_1^\dagger \alpha_3 \beta_4^\dagger \beta_2 \quad (\text{A.9})$$

$$\begin{aligned}
& + \sum_{\mathbf{k}_1 \mathbf{k}_2 \mathbf{k}_3 \mathbf{k}_4} \delta_{(1+2-3-4)} \gamma_{(2)} \left[u_1 u_3 u_4 v_2 \alpha_1^\dagger \alpha_2^\dagger \alpha_3 \alpha_4 + u_2 v_1 v_3 v_4 \beta_3^\dagger \beta_4^\dagger \beta_1 \beta_2 \right] \\
& + 2 \sum_{\mathbf{k}_1 \mathbf{k}_2 \mathbf{k}_3 \mathbf{k}_4} \delta_{(1+2-3-4)} \left[\gamma_{(2)} u_1 u_4 v_2 v_3 \right] \alpha_1^\dagger \alpha_2^\dagger \alpha_4 \beta_3^\dagger \\
& + 2 \sum_{\mathbf{k}_1 \mathbf{k}_2 \mathbf{k}_3 \mathbf{k}_4} \delta_{(1+2-3-4)} \left[\gamma_{(2)} u_2 u_3 v_1 v_4 \right] \alpha_3 \beta_4^\dagger \beta_1 \beta_2 \\
& + \sum_{\mathbf{k}_1 \mathbf{k}_2 \mathbf{k}_3 \mathbf{k}_4} \delta_{(1+2-3-4)} \left[\gamma_{(2)} u_1 u_2 u_3 u_4 + \gamma_{(1)} u_3 u_4 v_1 v_2 \right] \alpha_1^\dagger \alpha_3 \alpha_4 \beta_2 \\
& + \sum_{\mathbf{k}_1 \mathbf{k}_2 \mathbf{k}_3 \mathbf{k}_4} \delta_{(1+2-3-4)} \left[\gamma_{(2)} v_1 v_2 v_3 v_4 + \gamma_{(1)} u_1 u_2 v_3 v_4 \right] \alpha_2^\dagger \beta_3^\dagger \beta_4^\dagger \beta_1 \\
& + \sum_{\mathbf{k}_1 \mathbf{k}_2 \mathbf{k}_3 \mathbf{k}_4} \delta_{(1+2-3-4)} \gamma_{(2)} \left[u_1 v_2 v_3 v_4 \alpha_1^\dagger \alpha_2^\dagger \beta_3^\dagger \beta_4^\dagger + u_2 u_3 u_4 v_1 \alpha_3 \alpha_4 \beta_1 \beta_2 \right]
\end{aligned}$$

$$\begin{aligned}
\mathcal{P}_3 = & 2 \sum_{\mathbf{k}_1 \mathbf{k}_2 \mathbf{k}_3 \mathbf{k}_4} \delta_{(1+2-3-4)} \left[\gamma_{(1)} u_1 u_2 u_4 v_3 + \gamma_{(2)} u_4 v_1 v_2 v_3 \right] \alpha_1^\dagger \alpha_3 \beta_4^\dagger \beta_2 \quad (\text{A.10}) \\
& + \sum_{\mathbf{k}_1 \mathbf{k}_2 \mathbf{k}_3 \mathbf{k}_4} \delta_{(1+2-3-4)} \gamma_{(2)} \left[u_2 v_1 v_3 v_4 \alpha_1^\dagger \alpha_2^\dagger \alpha_3 \alpha_4 + u_1 u_3 u_4 v_2 \beta_3^\dagger \beta_4^\dagger \beta_1 \beta_2 \right] \\
& + 2 \sum_{\mathbf{k}_1 \mathbf{k}_2 \mathbf{k}_3 \mathbf{k}_4} \delta_{(1+2-3-4)} \left[\gamma_{(2)} u_2 u_3 v_1 v_4 \right] \alpha_1^\dagger \alpha_2^\dagger \alpha_4 \beta_3^\dagger \\
& + 2 \sum_{\mathbf{k}_1 \mathbf{k}_2 \mathbf{k}_3 \mathbf{k}_4} \delta_{(1+2-3-4)} \left[\gamma_{(2)} u_1 u_4 v_2 v_3 \right] \alpha_3 \beta_4^\dagger \beta_1 \beta_2 \\
& + \sum_{\mathbf{k}_1 \mathbf{k}_2 \mathbf{k}_3 \mathbf{k}_4} \delta_{(1+2-3-4)} \left[\gamma_{(2)} v_1 v_2 v_3 v_4 + \gamma_{(1)} u_1 u_2 v_3 v_4 \right] \alpha_1^\dagger \alpha_3 \alpha_4 \beta_2 \\
& + \sum_{\mathbf{k}_1 \mathbf{k}_2 \mathbf{k}_3 \mathbf{k}_4} \delta_{(1+2-3-4)} \left[\gamma_{(2)} u_1 u_2 u_3 u_4 + \gamma_{(1)} u_3 u_4 v_1 v_2 \right] \alpha_2^\dagger \beta_3^\dagger \beta_4^\dagger \beta_1 \\
& + \sum_{\mathbf{k}_1 \mathbf{k}_2 \mathbf{k}_3 \mathbf{k}_4} \delta_{(1+2-3-4)} \gamma_{(2)} \left[u_2 u_3 u_4 v_1 \alpha_1^\dagger \alpha_2^\dagger \beta_3^\dagger \beta_4^\dagger + u_1 v_2 v_3 v_4 \alpha_3 \alpha_4 \beta_1 \beta_2 \right].
\end{aligned}$$

The products that are unique to the Holstein-Primakoff formalism yield

$$\begin{aligned}
\mathcal{P}_4 = & 2 \sum_{\mathbf{k}_1 \mathbf{k}_2 \mathbf{k}_3 \mathbf{k}_4} \delta_{(1+2-3-4)} \left[\gamma_{(3)} u_1 v_2 v_3 v_4 + \gamma_{(4)} u_1 u_3 u_4 v_2 \right] \alpha_1^\dagger \alpha_3 \beta_4^\dagger \beta_2 \quad (\text{A.11}) \\
& + \sum_{\mathbf{k}_1 \mathbf{k}_2 \mathbf{k}_3 \mathbf{k}_4} \delta_{(1+2-3-4)} \gamma_{(4)} \left[u_1 u_2 u_3 v_4 \alpha_1^\dagger \alpha_2^\dagger \alpha_4 \alpha_3 + u_4 v_1 v_2 v_3 \beta_3^\dagger \beta_4^\dagger \beta_1 \beta_2 \right] \\
& + \sum_{\mathbf{k}_1 \mathbf{k}_2 \mathbf{k}_3 \mathbf{k}_4} \delta_{(1+2-3-4)} \left[\gamma_{(4)} u_1 u_2 v_3 v_4 + \gamma_{(3)} u_1 u_2 u_3 u_4 \right] \alpha_1^\dagger \alpha_2^\dagger \alpha_4 \beta_3^\dagger \\
& + \sum_{\mathbf{k}_1 \mathbf{k}_2 \mathbf{k}_3 \mathbf{k}_4} \delta_{(1+2-3-4)} \left[\gamma_{(4)} u_3 u_4 v_1 v_2 + \gamma_{(3)} v_1 v_2 v_3 v_4 \right] \alpha_3 \beta_4^\dagger \beta_1 \beta_2 \\
& + 2 \sum_{\mathbf{k}_1 \mathbf{k}_2 \mathbf{k}_3 \mathbf{k}_4} \delta_{(1+2-3-4)} \left[\gamma_{(4)} u_1 u_3 v_2 v_4 \right] \alpha_1^\dagger \alpha_3 \alpha_4 \beta_2 \\
& + 2 \sum_{\mathbf{k}_1 \mathbf{k}_2 \mathbf{k}_3 \mathbf{k}_4} \delta_{(1+2-3-4)} \left[\gamma_{(4)} u_2 u_4 v_1 v_3 \right] \alpha_2^\dagger \beta_3^\dagger \beta_4^\dagger \beta_1 \\
& + \sum_{\mathbf{k}_1 \mathbf{k}_2 \mathbf{k}_3 \mathbf{k}_4} \delta_{(1+2-3-4)} \gamma_{(4)} \left[u_1 u_2 u_4 v_3 \alpha_1^\dagger \alpha_2^\dagger \beta_3^\dagger \beta_4^\dagger + u_3 v_1 v_2 v_4 \alpha_3 \alpha_4 \beta_1 \beta_2 \right]
\end{aligned}$$

$$\mathcal{P}_5 = 2 \sum_{\mathbf{k}_1 \mathbf{k}_2 \mathbf{k}_3 \mathbf{k}_4} \delta_{(1+2-3-4)} \left[\gamma_{(3)} u_2 u_3 u_4 v_1 + \gamma_{(4)} u_2 v_1 v_3 v_4 \right] \alpha_1^\dagger \alpha_3 \beta_4^\dagger \beta_2 \quad (\text{A.12})$$

$$\begin{aligned}
 & + \sum_{\mathbf{k}_1 \mathbf{k}_2 \mathbf{k}_3 \mathbf{k}_4} \delta_{(1+2-3-4)} \gamma_{(4)} \left[u_1 u_2 u_3 v_4 \beta_3^\dagger \beta_4^\dagger \beta_1 \beta_2 + u_4 v_1 v_2 v_3 \alpha_1^\dagger \alpha_2^\dagger \alpha_3 \alpha_4 \right] \\
 & + \sum_{\mathbf{k}_1 \mathbf{k}_2 \mathbf{k}_3 \mathbf{k}_4} \delta_{(1+2-3-4)} \left[\gamma_{(4)} u_3 u_4 v_1 v_2 + \gamma_{(3)} v_1 v_2 v_3 v_4 \right] \alpha_1^\dagger \alpha_2^\dagger \alpha_4 \beta_3^\dagger \\
 & + \sum_{\mathbf{k}_1 \mathbf{k}_2 \mathbf{k}_3 \mathbf{k}_4} \delta_{(1+2-3-4)} \left[\gamma_{(4)} u_1 u_2 v_3 v_4 + \gamma_{(3)} u_1 u_2 u_3 u_4 \right] \alpha_3 \beta_4^\dagger \beta_1 \beta_2 \\
 & + 2 \sum_{\mathbf{k}_1 \mathbf{k}_2 \mathbf{k}_3 \mathbf{k}_4} \delta_{(1+2-3-4)} \left[\gamma_{(4)} u_2 u_4 v_1 v_3 \right] \alpha_1^\dagger \alpha_3 \alpha_4 \beta_2 \\
 & + 2 \sum_{\mathbf{k}_1 \mathbf{k}_2 \mathbf{k}_3 \mathbf{k}_4} \delta_{(1+2-3-4)} \left[\gamma_{(4)} u_1 u_3 v_2 v_4 \right] \alpha_2^\dagger \beta_3^\dagger \beta_4^\dagger \beta_1 \\
 & + \sum_{\mathbf{k}_1 \mathbf{k}_2 \mathbf{k}_3 \mathbf{k}_4} \delta_{(1+2-3-4)} \gamma_{(4)} \left[u_3 v_1 v_2 v_4 \alpha_1^\dagger \alpha_2^\dagger \beta_3^\dagger \beta_4^\dagger + u_1 u_2 u_4 v_3 \alpha_3 \alpha_4 \beta_1 \beta_2 \right]
 \end{aligned}$$

B Numerical implementation of the density of states

Due to the mapping of the momentum grid onto an energy grid, as presented in the appendix of publication [II](#), the numerically extracted density of states shows major finite size effects (see figure [B.1](#)). While this is less of a problem when analyzing quantities that are summed over the entire Brillouin zone, it presents complications when determining frequency dependent quantities like the energy density $\mathcal{U}(t)$ given by

$$\mathcal{U}(\omega, t) = \omega n(\omega, t) \rho(\omega) . \quad (\text{B.13})$$

We therefore compute a smoothed density of states by averaging over intervals of the density of states extracted from a system with $\ell = 2000$, as presented in figure [B.1](#), and read in the averaged density of states for the various system sizes. The files containing this density of states are available at the github repository mentioned in section [5.4](#).

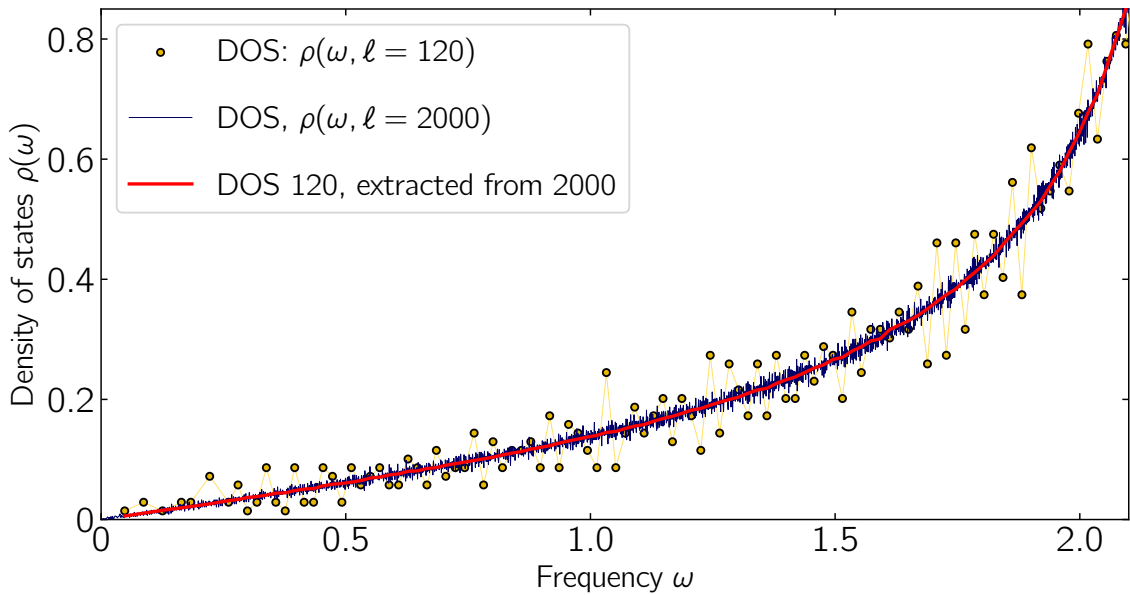


Figure B.1: Numerically extracted density of states for $\ell = 120$ (orange) and $\ell = 2000$ (blue) as well as smoothed density of states (red) that is implemented in the code.

Acknowledgements

Throughout my PhD, I consider myself very lucky to have worked with outstanding people whose guidance, experience and support have shaped this dissertation. In particular I'd like to express my gratitude towards my supervisors Michael Sentef and Dante Kennes. Thank you for patiently answering my questions, for believing in our projects even when I did not and for the vivid discussions from which I learned so much. Stumbling into the field of computational physics, it was your expertise and your dedication that enabled me to overcome the obstacles I encountered with developing my own code and producing reliable data.

Furthermore, I am deeply grateful to Andrew Millis for igniting my interest in nonequilibrium phase transitions and for inviting me to New York, even though I was so nervous that I was barely able to pronounce my own name when I first met him. Andy, you taught me how to keep the big picture in mind when I was focused on a single aspect of our results, how to think of our simulations as exciting numerical experiments and how to grow as a physicist.

My work benefited greatly from a collaboration with Matteo Mitrano, who introduced me to the intriguing field of time-resolved spectroscopy (despite my unreasonable fear of laser-labs) and even patiently guided me around his experimental setup at Harvard University. It was exciting to see possible applications and realizations of the systems that we try to simulate, and the close relation to experiment was a major motivation, especially during the second half of my PhD.

I would also like to thank Michael Potthoff and the members of my committee for sacrificing their time, examining this thesis and assessing my defense.

The path towards this thesis was paved more than a decade ago by two physics teachers, Henning Geyer and Kieran Hackett, who taught physics with enthusiasm and fascination. It was due to you that I realized how thrilling and vast the field of physics is, and that I became so curious that I decided to continue in this direction. Speaking about the last decade, I am truly grateful for the friendship with Leona Flohr, your encouragement, reliability and empathy really helped me through the darker days.

At MPSD I owe a big thanks to my wonderful colleagues Damian Hofmann, Lukas Windgätter and Christian Eckhardt, for scientific and computational help as well as for the many shared laughs, coffee breaks and personal advice. I truly enjoyed working with you. Moving to Hamburg in 2018, I would have not imagined the extraordinary friendships that awaited me. Meredith Henstridge, Alexandra Göbel and Miguel Silva Toledo, thanks for nights of dancing in the kitchen, thanks for your emotional support, thank you for making this time so special. In New York, I would also like to thank my awesome office mates Denis Golež, Bo Xiao and Artem Strashko, as well as all the other great scientists who made me feel welcome, were always eager to discuss and who make CCQ such an amazing work environment. Artem, I will never forget how you rescued my leather jacket.

I am immensely grateful to my parents Petra and Rolf for giving me the freedom to pursue my dreams, for their unconditional support, for giving me the perseverance to keep on going and for always having an open ear as well as an open door for me. Mum, thank you for being my emotional anchor.

Finally, Kevin my love, thank you for your patience, your loyalty, your companionship and your strong arms.